Dynamic Properties of Bimodal Polyethylene: Crystallization and Flow Instabilities

Mohammadali Sattari

A Thesis

In the Department

of

Mechanical, Industrial and Aerospace Engineering

Presented in Partial Fulfillment of Requirements

For the Degree of

Doctor of Philosophy (Mechanical Engineering) at

Concordia University

Montreal, Québec, Canada

February 2024

CONCORDIA UNIVERSITY

SCHOOL OF GRADUATE STUDIES

This is to certify that the thesis prepared

By: Mohammadali Sattari

Entitled: Dynamic Properties of Bimodal polyethylene: Crystallization and Flow Instabilities

and submitted in partial fulfillment of the requirements for the degree of:

DOCTOR OF PHILOSOPHY (MECHANICAL ENGINEERING)

complies with the regulations of the University and meets the accepted standards with respect to originality and quality.

Signed by the final examining committee:

_____ Chair

Dr. Mamoun Medraj

_____ External Examiner

Dr. Savvas G. Hatzikiriakos

_____ External to Program

Dr. Zhibin Ye

_____ Examiner

Dr. Mehdi Hojjati

_____ Examiner

Dr. Martin Pugh

_____ Thesis Supervisor

Dr. Paula Wood-Adams

Approved by _____

Dr. Muthukumaran Packirisamy, Graduate Program Director

March 18, 2024 _____

Dr. Mourad Debbabi, Dean Gina

Cody School of Engineering

Abstract

Dynamic properties of bimodal polyethylene: Crystallization and flow instabilities

Mohammadali Sattari, Ph.D.

Concordia University, 2024

The emergence of new single-reactor technologies has enabled the production of bimodal polyethylene at reduced capital costs, prompting a need for deeper investigations into the characterization and property-structure relationships of these materials. In this thesis, we are looking at how the molecular structure affects both the solid-state and the melt-state properties of polyethylene.

This study employs a material set featuring systematic variations in molecular weight distribution and short chain branching distribution. The initial step involves extracting the fundamental molecular parameters of the materials by utilizing statistical modelling to acquire the ethylene sequence length distribution and its features. Subsequently, we identify the key parameters governing our materials' environmental stress crack resistance, a crucial concern, particularly for solid-state properties in pipe applications of bimodal polyethylene. We showed that many mechanical properties from strain hardening tests correlate with features of ethylene sequence length distribution, showing that this distribution is the most meaningful in describing the structure of bimodal polyethylene in terms of solid-state properties. An approach to studying the critical correlations between structure, crystallization, and mechanical properties is presented.

In the latter part of this study, we investigate the effect of molecular weight distribution on the wall-slip behavior of bimodal polyethylene melt under simple shear. The study under simple shear is important as it eliminates the confounding effects of pressure and shear rate gradient. We examine the impact of low molecular weight content on various slip regimes. We showed that the stress level at which the slip velocity becomes independent of molecular weight distribution decreases with an increase in short-chain content. The degree of entanglement

between the interfacial and bulk chains drops sharply in the transition region based on the friction of coefficient investigations.

Throughout our investigations, we frequently observe melt rupture in our materials, prompting further exploration of this instability using visualization techniques. Melt rupture is critical as it limits the industrial applications of these materials. We showed that melt rupture is a time-dependent phenomenon that can occur after a stress and slip velocity plateau is reached, inviting additional studies on the effects of interfacial structural changes during slip.

Acknowledgment

I want to truly thank my supervisor, Dr. Paula Wood-Adams, for her tremendous support, brilliant ideas, and excellent supervision throughout my Ph.D. journey. Thank you for keeping us motivated all the time. Your commitment to our success is inspiring.

I thank Dr. Inn and Dr. Karimi for their outstanding scientific input, support, and contributions to this research.

I want to express my appreciation to my committee, Dr. Hatzikiriakos, Dr. Ye, Dr. Pugh, and Dr. Hojjati, for allocating their valuable time in their busy schedule to review this thesis.

I want to thank my colleagues, Bianca and Nimo, for being there for me during this journey; you made this manageable for me.

I thank all the technicians and lab managers who helped me with my research: Heng, Robert, Henry, Gilles, Peter, Mathieu, and Marie-Helene. I thank Harriet for her efforts to keep us safe.

My research groupmates helped me on many occasions, and I would like to thank Kero, Nonso, Elham, Cindy, Milad, Mina, Hai, and Mostafa.

My special appreciation goes to Chevron Philips Chemical for providing funding and the materials for this study.

Dedication

This thesis is dedicated to my parents for their support and sacrifices in all stages of my life. I am grateful for everything you have done for me.

To, Aida, thank you for standing beside me throughout this journey!

Contribution of Authors

Chapter 3 is a manuscript co-authored with S. Kwakye-Nimo, E. C. M. J. Ehounou, Y. W. Inn, P. Karimineghlani, and P. M. Wood-Adams. I conceptualized the project, designed the experiments, analyzed the data, wrote the manuscript, and conducted the SSA and part of non-isothermal crystallization experiments, all with the guidance of Y. W. Inn, P. Karimineghlani, and P. M. Wood-Adams. Dr. Nimo conducted feature selection analysis and SSA peak deconvolution and helped with the initial efforts to apply statistical modelling to experimental data. Ms. Ehounou conducted part of the non-isothermal crystallization and their data analysis and initial literature review on the non-isothermal crystallization. Chevron Philips Chemical provided the GPC and strain hardening data. This long manuscript will split into two shorter manuscripts that will be submitted to scientific journals.

Chapter 4 is an article published in Macromolecules co-authored with Y. Inn and P. Wood-Adams. I have conceptualized the project, designed and conducted the experiments, analyzed the data, and written the manuscript, all with the guidance and supervision of the co-authors above.

Chapter 5 is a manuscript (submitted to Polymer) co-authored with Y. Inn and P. Wood-Adams. I have conceptualized the project, designed and conducted the experiments, analyzed the data, and written the manuscript, all with the guidance and supervision of the co-authors above.

All authors mentioned above have approved representation of their work in this thesis.

Table of Contents

List of Figures

List of Tables

Chapter 1. Introduction

The relationship between the structure and properties of polyethylene can be divided into two main categories: solid-state and melt-state properties. Solid-state properties dictate how functional the materials are in various applications[1], while melt-state properties affect the cost and speed of processing[2–4]. For a material to be valuable in industry, it needs to have favorable properties in both states. This thesis explores both aspects together, as it is possible for polymers to have characteristics that might be advantageous in solid-state properties but problematic in melt-state properties and vice versa[5]. While most research focuses on either solid or melt-state properties separately, this thesis aims to bridge this gap by presenting a comprehensive analysis encompassing both aspects.

The beauty and complexity of polymers originate from their molecular structure, which exists in various distributions[6]. This complexity makes it challenging to understand and establish simple structure-property relationships[6,7]. However, it also offers opportunities to manipulate these aspects for designing and developing a broad range of properties[6]. In this work, we utilized statistical modelling of the structure[6] to explore relationships between structure and properties in polyethylene.

Polyethylene is a semi-crystalline material[1], and its crystallization behavior depends on various aspects of the molecular structure[1,6]. This behavior governs the solid-state properties of the material[1]. To optimize the structure of polyethylene, it is essential to identify the parameters controlling its properties. For instance, in this thesis, we investigated materials specifically designed for pipe applications. Our focus was on the major limiting factor, which in this case, is the cracking[8–10] of the pipes. We examined a mechanical property linked to pipe cracking[8–10] and correlated it with the molecular structure. The methodology we employed is applicable to other polymers and applications.

The properties in the melt-state are crucial as they define the processing conditions and their limitations for polyethylene[2–4,11]. This thesis examined two important instabilities in the melt-state: slip[11] and melt rupture[12]. Slip can be advantageous as it enhances processing output volume[2–4]. However, it can also result in defects[2–4,13]. Melt rupture[12] is a bulk defect that may

occur during the flow. This instability is a limiting factor in polyethylene processing, constraining the output volume[2–4,11]. We employed visualization techniques to gain a deeper understanding of this phenomenon. While the behavior of materials regarding melt rupture and slip has been studied previously[11,12,14–18], the occurrence and degree of these instabilities in our particular material structure are surprising, exposing potential directions for future research.

The results of this study assist the industry and researchers in designing a polyethylene structure that addresses the industrial needs concerning both solid and melt-state properties.

1. 1. Scope of study

This study aims to understand the critical structural parameters influencing polyethylene solid and melt-state properties. The thesis is structured as follows: **Chapter 3** represents a manuscript with theoretical structure modelling[6] of our materials. We study the structure-solid-state property relations and examine crystallization experimentally. **Chapter 4** contains an article that looks into the wall slip behavior of polyethylene melt and its relation to the material structure. **Chapter 5** comprises a manuscript that investigates the instability of melt rupture using visualization techniques. This thesis comprehensively discusses various aspects of polyethylene properties and highlights numerous critical structural parameters.

Chapter 2. Basics and literature review

This chapter reviews the fundamental concepts and methodologies used in this thesis, in addition to conducting a literature review and justifying the aim of the study.

2. 1. Structure of bimodal polyethylene

2. 1. 1. Molecular weight distribution and short chain branching

A polymer is made of long chains[5,19], with each chain consisting of a high number of repeat units called monomers linked together via covalent bonding[5,19]. The monomers are bonded together through the polymerization process[5,19]. These long-chain molecules have varying numbers of monomers, resulting in different molecular weights (the mass of a mole of the chain)[5,19]. This diversity is shown by the molecular weight distribution (MWD), which displays the proportion of molecules versus their molecular weight[5,19]. **Figure 2.1** illustrates an example of MWD. From MWD, different average values can be calculated, such as number[5,19] (M_n) and weight-averaged[5,19] (M_w) molecular weights, and their ratio, known as polydispersity index[5,19] (M_w/M_n), which indicates the breadth of the distribution[5,19]. If there is a single peak in the molecular weight distribution, it is called unimodal MWD[5,19].

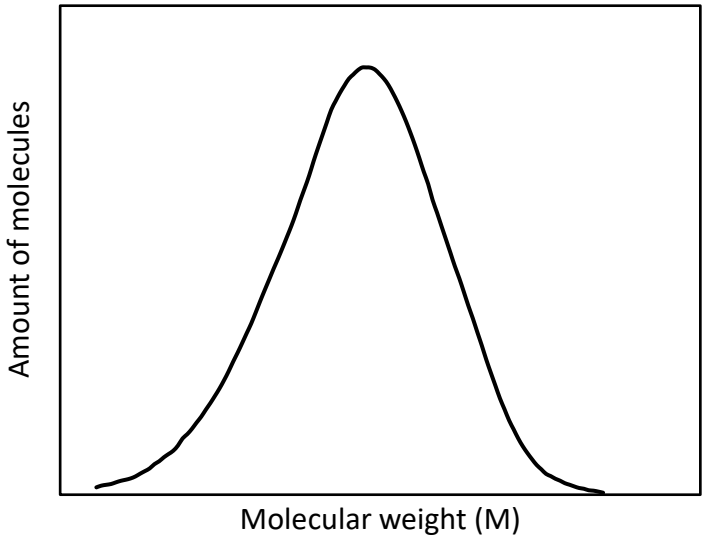

Figure 2.1. An example of molecular weight distribution of a unimodal polyethylene

Each polymer chain can be made of a single type of monomer, called a homopolymer, or it can consist of two different monomers, known as copolymers[5,19]. In the case of polyethylene homopolymer, the repeat unit is ethylene[5,19]. Copolymerization[20] involves the combination of two types of monomers during the polymerization process[5,19]. For instance, ethylene and hexene (**Figure 2.2**) can be polymerized together to form a polymeric chain, resulting in an ethylene-hexene copolymer[5,19]. The presence of hexene in the copolymer introduces side branches to the chains, referred to as short chain branching (SCB). The term "short" indicates a branch length consisting of only a few carbons, much shorter than the whole chain[1,5,19,21].

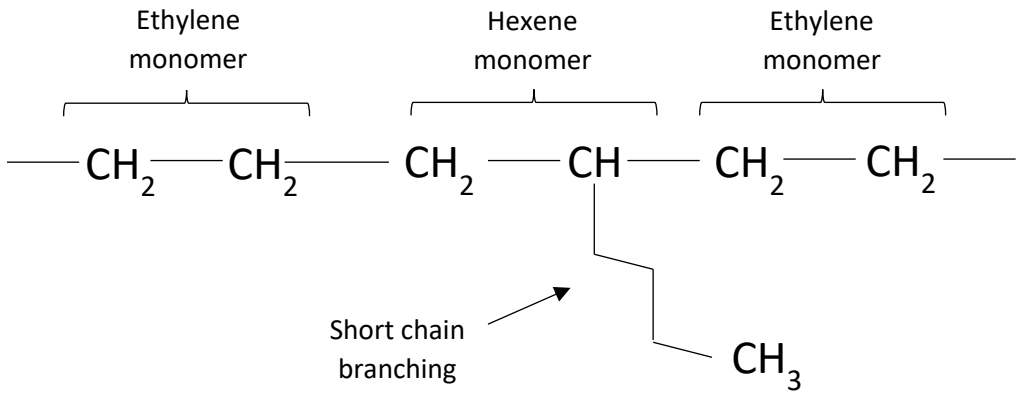

Figure 2.2. Short chain branching in copolymerization of ethylene and hexene. Inspired from[22].

The branch population is typically reported as the number of branches per 1000 carbon atoms[21]. Just like we define the distribution of molecular weights, we can also describe the distribution of short chain branching. We can display short chain branching versus molecular weight, revealing the average short chain branching for chains with particular molecular weights[5,19,21].

Altering the short chain branching is a way to engineer polymer properties[5]. Depending on the targeted property, the effect of SCB can vary. For instance, while approximately up to 20 wt.% of butene branches do not affect the rheological behavior of polyethylene (linear viscoelastic behavior)[23], it affects the crystallization behavior of polyethylene[24].

2. 1. 2. Bimodal polyethylene

If there are two peaks in the molecular weight distribution of polyethylene, it is called bimodal MWD polyethylene[5]. This type of polyethylene has two populations: high molecular weight (HMW) and low molecular weight (LMW)[2,5]. Each population has its structural features that can affect the overall behavior of the polymer[5]. This provides opportunities for designing materials with properties that rely on both high and low molecular populations[5,25]. If the two populations have different short chain branching distributions, we will have a material that has both bimodal molecular weight and short chain branching distributions[5,25].

One advantage of bimodal molecular weight distribution in polyethylene is its ability to allocate different levels of short-branch content to the preferred chain population[5]. It is possible to have a bimodal polyethylene with an equal quantity of short chain branches on both the HMW and LMW populations, or deliberately position a higher content of short branches on either the LMW or HMW populations[5]. An example of MWD and short chain branching distribution (SCBD) of this type of material[5,25] is presented in **Figure 2.3**. Please note that in this example, the HMW population has a higher content of short chain branching[25] as it is the case for the materials of this study.

The bimodal distribution can be achieved by having two catalysts simultaneously conducting the polymerization or having two reactors in series[20]. Polyethylene with a bimodal short chain branching distribution exhibits enhanced properties, such as increased toughness[20] or crack resistance[25].

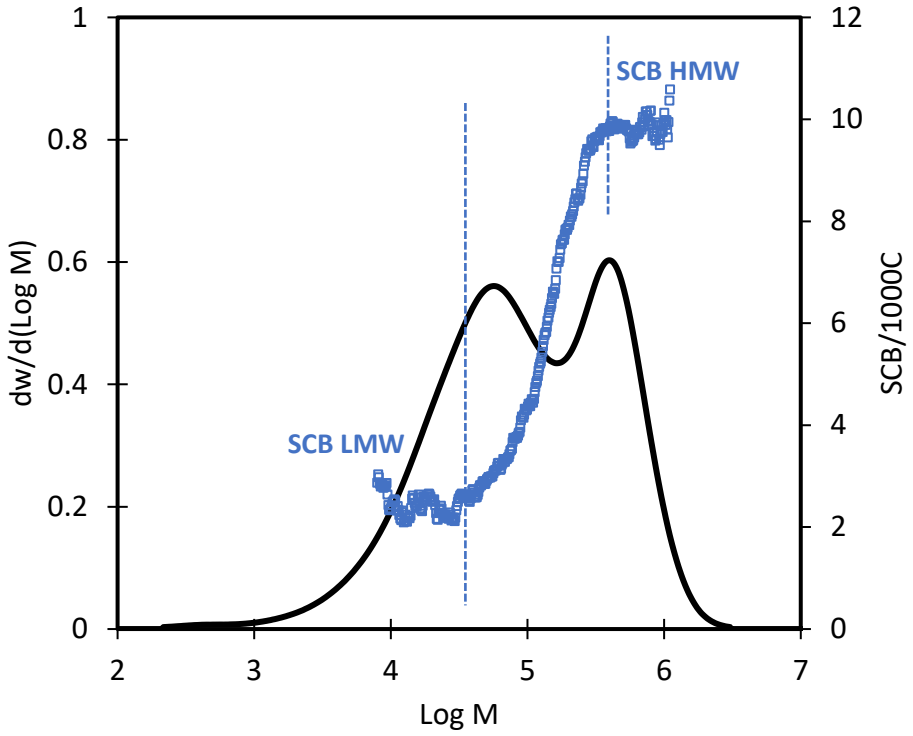

Figure 2.3. An example of molecular weight and short chain branching distributions of a bimodal polyethylene in which HMW population has a higher content of short chain branching.

Bimodal polyethylene has garnered significant attention from both industry and academia due to its outstanding mechanical properties[5,25]. The mechanical properties are rooted in the high-molecular-weight population, while the processing comes from the low-molecular-weight population[5,25]. These properties are a result of engineered molecular weight and short chain branching distributions[5,25].

This study focuses on metallocene-catalyzed polyethylene, which is characterized by a well-controlled, narrow (in the case of unimodal MWD type) and homogeneous MWD, as well as SCBD[26]. The precise control over its structure has facilitated the customization of this type of polymer for various applications[27]. In the case of metallocene-catalyzed bimodal polyethylene, the uniform and controllable structure enables the development of numerous materials having a broad range of molecular features[5].

The molecular structure plays a significant role in determining the physical and mechanical properties of polyethylene[28,29]. As discussed, we have two distributions of MWD and SCBD, each describing specific aspects of the molecular structure and representing particular information about it[5]. Discovering the most meaningful distribution to describe the structure is crucial for optimizing it for a target application[30]. In the following section, we present the ethylene sequence length distribution[31] that reflects both MWD and SCBD aspects. This information is very helpful in studying properties of polyethylene that rely on both distributions, such as crystallization[31].

2. 1. 3. Ethylene sequence length distribution

A chain of polyethylene without branches theoretically has the potential to incorporate the entire length of the chain into the formation of the crystal structure[31,32]. However, when a branch, such as butyl[33] (resulting from the co-polymerization of ethylene and hexene[33]), is introduced into the chain, it hinders crystallization[34]. Only the segment of the chain between the branches can be easily integrated into the crystal structure[31,32,34]. This segment consists of a series of consecutive ethylene monomers, where the number of ethylene units in the series is called the ethylene sequence length[31]. Similar to molecular weight and short chain branching, the ethylene sequence length also exists in a distribution known as the ethylene sequence length distribution (ESLD)[6,31]. Short chain branching distribution alone cannot provide us with information about the ethylene sequence lengths since it does not include the molecular weight distribution (MWD) information[6,31].

While SCBD and ESLD are related through the MWD, they describe different structural aspects of polymer chains[6,31]. The SCBD is typically characterized in relation to molecular weight, indicating the average SCB for chains with specific molecular weights (**Figure 2.4a**)[31]. The ESLD shows the weight fraction of each ethylene sequence length within the entire system (**Figure 2.4b**) [6,31].

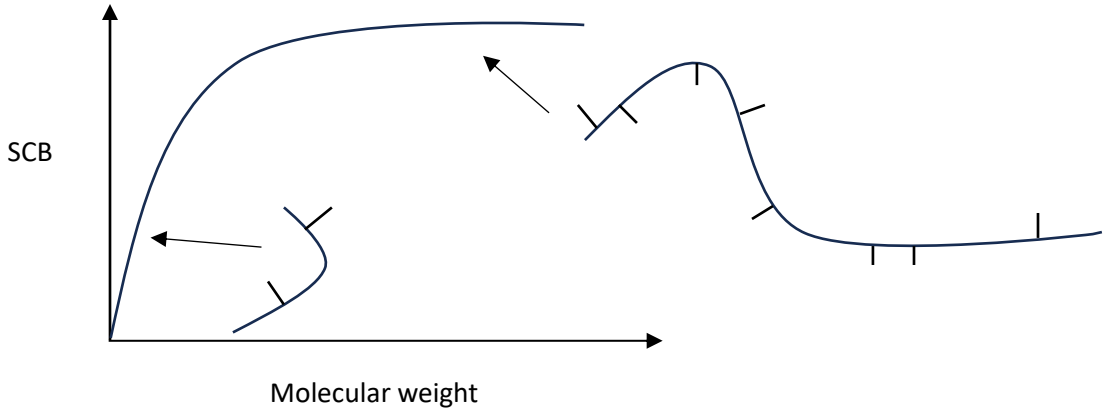

a.

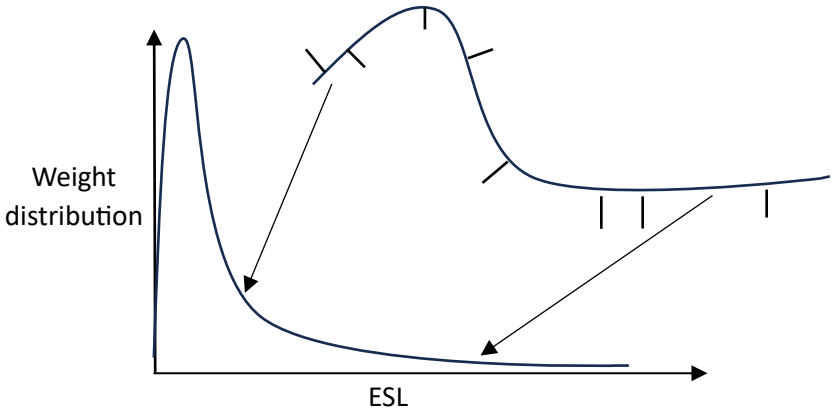

b.

Figure 2.4. ESL and SCB distributions for unimodal metallocene-catalyzed polyethylene. a. Typical SCB versus molecular weight b. Typical weight distribution versus ESL. Inspired from[31].

The question of whether ESLD or SCBD features serve as the key molecular parameters for the thermal and mechanical properties of bimodal polyethylene[6,31] remains open. One complexity arises from the lack of access to materials having a systematic variation in their MWD and SCBD. In this study, we addressed this gap by utilizing a unique set of such materials.

2. 1. 4. Tie chains

As previously discussed, the presence of short branches on the chain hinders crystallization. When a crystal is forming and the ethylene sequence length is incorporated into it, it encounters these short branches that hinder the process[31,32,34]. Consequently, different chain configurations may occur for the rest of the chain if it reaches the amorphous region after being integrated into the crystalline region[35]. One possibility is that the rest of the chain remains freely in the amorphous region[35]. Another possibility is when the polymer chain returns to the same lamellae, known as chain folding[35]. Additionally, if the chain incorporates in the formation of adjacent crystallites, a tie chain or covalent bridging occurs (**Figure 2.5**). In this case, the chain becomes involved in forming more than one crystallite[35,36].

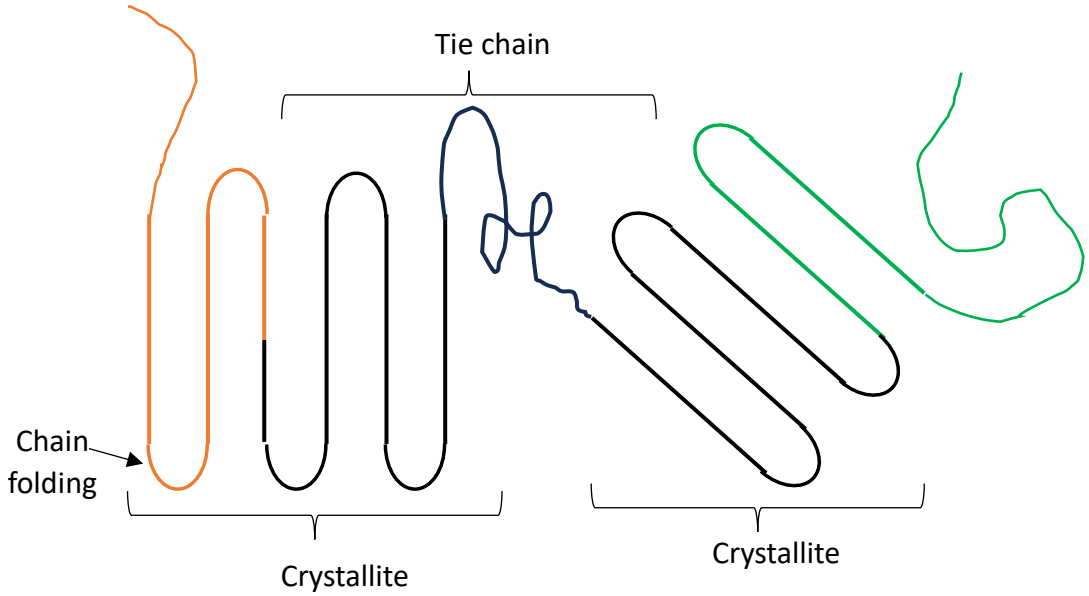

Figure 2.5. Chain folding and tie chains. Each color represents a different chain. Inspired from[37]

Tie chains are believed to play a crucial role in enhancing the toughness and crack resistance of polyethylene[35,38,39] as they act as load transfer bridges[40]. The number of tie chains increases with an increase in short branches[39] at the expense of reducing the overall crystallinity[41]. The presence of more short branches on the chain increases the likelihood that crystallization is hindered, and the chain may be incorporated into the formation of another

crystallite, forming tie chains[41]. This is more probable to occur for high molecular weight chains since they are longer and may contain more sites available (ESL) to be incorporated into other crystallites[41]. However, due to the hindered crystallization process caused by the increase in short chain branching, the overall crystallinity decreases[41].

Studying tie chains with analytical techniques is challenging[35,37]. In this study, we have established a protocol using differential scanning calorimetry (DSC) and statistical modelling[6] to investigate the combined crystallization of low and high molecular populations. We assumed that an increase in the contribution of the high molecular weight population to crystallization leads to more tie chain formations in our materials. To test this assumption, we looked into the correlation between the contribution of high molecular weight population to crystallization, and a mechanical property that is affected by the tie chains.

Hu et al.[41] investigated the impact of SCB (up to 8 SCB/1000C) on the crystallization of bimodal polyethylene through molecular dynamic simulation[41]. Their findings indicated a decrease in crystallinity with an increasing average SCB content, irrespective of whether these SCBs were placed on short or long chains[41]. At SCB levels up to 5/1000, no significant difference in crystallinity was observed between placing the short branches on either short or long chains, maintaining the same average SCB content[41]. However, at higher SCB content, placing the SCBs on the long chains resulted in a more pronounced decrease in crystallinity compared to placing them on the short chains[41].

The same study[41] also explored the influence of SCBs on tie chain formation, specifically when the short branches were exclusively located on the longer chains[41]. It was concluded that higher SCB content and positioning the branches on the long chains led to increased tie chain formation[41]. This increase in the number of tie chains was attributed to the varying growth velocity during crystallization between LMW chains and short-branched HMW chains[41]. The growth velocity is the rate at which the chains are deposited into the crystal. LMW chains have a higher growth velocity than branched HMW chains[41]. Consequently, when formation of a crystallite is initiated by an HMW chain, the higher growth velocity of LMW chains lead them to join the crystallization ahead of the HMW branched chain. As a result, the HMW chain was

deposited on another crystallite, forming tie chains[41]. They concluded that[41] the placement of a higher quantity of short branches on longer chains leads to superior mechanical properties[41]. However, a comprehensive study addressing the multiple features of the MWD and SCBD has not been conducted due to limited access to materials with systematic changes in MWD and SCBD. We aim to bridge this gap through our research.

2. 2. Slow crack growth and environmental stress crack

The materials used in this thesis are designed for pipe applications. This section introduces a common concern related to pipe cracking. This section reviews the significant role that tie chains play in resisting cracking[42,43].

Polyethylene failure can be categorized into three modes: ductile, rapid crack propagation, and slow crack growth (SCG)[9]. Among these modes, SCG is the primary concern in pipe applications[8–10]. This brittle failure mode, which is dependent on time, occurs at stresses below the yield stress of polyethylene and within the stress range typically experienced in pipe applications[7–9]. Usually, the duration to failure under such low-stress conditions spans decades[9]. However, some applications, such as pipes[9,44], often require materials capable of enduring without failure for more than 100 years[9], even when exposed to higher loads during installation[44–46], and to challenging environments such as oil[47] during use. SGC can occur in a standard environment, and the material response is called environmental stress cracking (ESC)[9].

2. 2. 1. SCG mechanisms

The mechanism of SCG in the absence of a harsh environment operates mainly through craze and crack formation, known as the craze-crack mechanism[43]. Imperfections and defects act as stress concentrators[43]. Within the amorphous regions, small holes develop in front of the crack tips due to localized plastic deformation and changes in the chains' orientation on a small scale[43]. These holes gradually enlarge, merge, and create craze structures perpendicular to the direction of applied stress[43]. Under load, the craze structure makes oriented fibrils that are elongated in the direction of the load[43].

The elongated fibrils within these craze structures, aligned with the force direction, impede crack propagation until their further extension results in pullout[42], scission[48], or disentanglements[42]. This progression leads to crack-craze growth, as shown in **Figure 2.6**, culminating in the eventual failure of the material[43]. Tie chains are believed to play a crucial role in SCG[42,43] since they transfer the load between the crystallites and increase the SCG resistance[42]. The tie chains serve to connect the two (or more) crystallites. When subjected to a load, these tie chains transfer the force between the crystallites and strengthen the crystal structure[7]. Moreover, these chains can either extend or disentangle from other chains, relaxing stress[7].

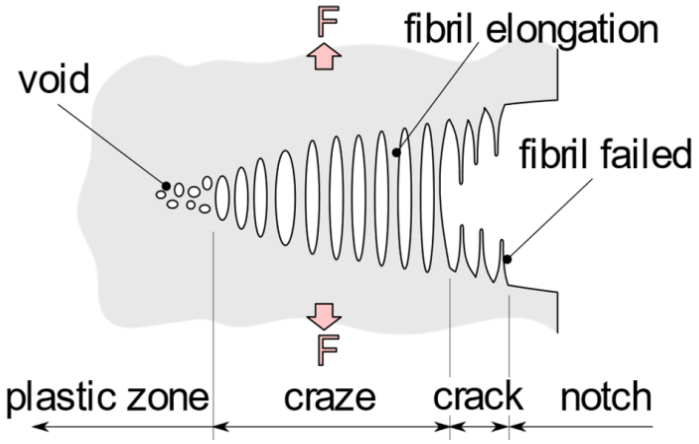

Figure 2.6. Crack-graze mechanism[43]

A great deal of effort has been made to enhance ESC resistance (ESCR) by manipulating the molecular structure[18]. These modifications aim to facilitate the formation of more effective tie chains within the polymer structure[18]. Various features of MWD and SCBD influence the overall behavior of ESCR[9,44]. This complexity necessitates a comprehensive study where both MWD and SCBD are investigated. In this thesis, we aim to address this gap.

Two common industrial structural modifications involve the placement of short branches on the HMW population[9,44] and transitioning from the more common butene comonomer (found in most pipe resins) to hexene[28]. The justification for the effectiveness of these changes lies in their impact on tie chains[8,42]. Hexene comonomer exhibits greater effectiveness compared to butene, as its use results in longer branches in the polyethylene chain[42].

Challenges in the investigation of the ESCR include: many structural parameters[7], a lack of appropriate materials, and experimental complexity to obtain SCBD and MWD[25]. In this thesis, we aim to address this gap. We utilize a set of hexene-ethylene co-polymers with systematic variations in MWD and SCBD. We focus on materials with short branches placed on the HMW chains. By focusing on these materials, we look into the most recent technological advancements and exclude certain structural parameters whose effects have already been reported and studied.

Furthermore, we investigate the correlation between a DSC heat treatment process results and the mechanical properties linked to ESCR. Our objective is to facilitate the efficient ranking of materials based on ESCR using DSC.

2. 3. Natural draw ratio

Experimental analysis of SCG is challenging due to its inherently slow process[9]. Such experiments are typically conducted using tests like Pennsylvania notched or full-notch creep[9]. These tests can endure up to 10,000 hours (over a year)[8,44]. Accelerated tests, employing low-energy liquids to expedite the creation of new surfaces and elevated temperatures[9], can reduce the experimental time by one-sixth[8]; however, they still require a substantial time (more than two months). Furthermore, there are concerns about changes in the failure mechanism and antioxidant consumption due to elevated temperatures[9]. These changes may alter the material's behavior compared to normal conditions[9], and potentially mislead researchers in designing materials. To address this issue, looking into other mechanical properties that correlate well with SCG properties is suggested[9].

Extensive research has been conducted to determine the best parameters representing ESCR, concluding that natural draw ratio (NDR)[50,8,51,42] and strain hardening modulus[50,8,51,42,44] from strain hardening tests are two potential parameters[9]. The strain hardening test, a modified tensile test performed at 80°C using a relatively thin sample[52], offers an effective method to select between polyethylenes with different structures for superior environmental crack resistance[52]. These correlations have been established for both ethylene-hexene and ethylene-butene copolymers[9].

The NDR[51,53] can be defined as the engineering strain when strain hardening begins in the plot of engineering stress against the engineering strain[51,53]. NDR reflects the capacity of the crystalline network to extend under load[51]. The formation of tie chains affects NDR. A reduction in NDR leads to an increase in ESCR[51].

The strain hardening modulus (SHM) is defined as the slope of strain hardening[42,51,54] (between strains higher than eight and lower than 12) in the true stress versus draw ratio (instantaneous length divided by the original length) curve[42,51]. This parameter is correlated with ESCR and is associated with the tie chains and dynamics of trapped entanglements and their disentanglement[51]. A higher SHM value corresponds to a higher ESCR[42,51,55,56].

Zhang et al. reported that higher crystallinity results in a greater strain hardening modulus[49]. Fawaz et al.[7] investigated the impact of molecular and microstructure parameters on the SCG. They concluded that an increase in molecular weight and comonomer content enhances the likelihood of tie chain formation, thereby improving SCG resistance[7]. Higher comonomer content increases the possibility of a single chain being incorporated into two lamellae[7]. Additionally, they highlighted the significance of high crystallinity and molecular weight in ensuring acceptable ESCR behavior[7]. They noted the complexity of multiple factors simultaneously influencing behavior, making it challenging to reach a universal conclusion[7].

In our studies, we addressed this issue by limiting the parameters under investigation. Specifically, our focus was on hexene-ethylene copolymers (widely recognized as the best industrial choice for pipe applications[10,49]) having a higher amount of comonomer content in longer chains, coupled with our systematic resins.

2. 4. Non-isothermal crystallization

The crystallization behavior controls the solid-state properties of polyethylene[1]. Non-isothermal crystallization studies provide a practical and quick method to investigate the crystallization behavior of polymers[57]. Non-isothermal studies might be preferred over isothermal studies due to two reasons: first, standard industrial processes involve non-isothermal procedures[57], and second, achieving an ideal isothermal process for polyethylene poses challenges as it is a rapidly nucleating polymer[58]. Non-isothermal behavior is commonly studied

using DSC[59]. Parameters such as relative crystallinity and peak crystallization temperature can be extracted from non-isothermal studies[57]. In this study, we aim to identify the molecular parameters governing these thermal properties of polyethylene. The identification of these parameters would then facilitate the process of developing new polyethylene structures. Furthermore, we try to establish correlations between these parameters and the results of the strain-hardening test. Such correlations aid in ranking developmental resins based on the desired properties quickly using DSC.

2. 5. Successive self-nucleation and annealing (SSA)

Polyethylene has a semi-crystalline structure comprising regions of amorphous and crystalline materials[35,38,50]. A crystalline phase forms a lamellar structure[60]. The lamellar thickness varies depending upon the molecular structure and crystallization temperature[60]. The successive self-nucleation and annealing (SSA) method is a heat treatment technique used on polymers to fractionate the crystal structure based on lamellar thickness[61–63]. The distribution of lamellar thickness (the relative amount of lamellae versus the lamellar thickness) is an outcome of this process[61–63]. This heat treatment can be conducted using a DSC[61–63]. The process involves five steps[61–63] shown in **Figure 2.7**:

1. Thermal history removal: In this step, the sample is heated to a temperature higher than its melting point and then held for a specific time to eliminate any thermal history[61–63].
2. Cooling to room temperature: The molten material is cooled at a constant rate to attain a standard crystal structure[61–63].
3. Self-nucleation: The sample temperature is raised to the self-nucleation temperature ($T_{s,\ ideal}$). At this temperature, all crystals are melted, but the chain arrangement from the former crystal structure persists, acting as self-nucleation agents[61–63]. Precise determination of this temperature is crucial for the success of the SSA treatment[61–63]. The procedure to determine this temperature is detailed in **Chapter 3**.
4. Annealing steps: The sample will undergo annealing in consecutive steps, each step is set to 5 °C (as an example) lower than the previous step[61–63].

5. Final melting step: During this stage, the annealed sample will undergo melting, and the melting curve will display fractionated peaks. Each peak corresponds to the melting of a lamellar population[61–63].

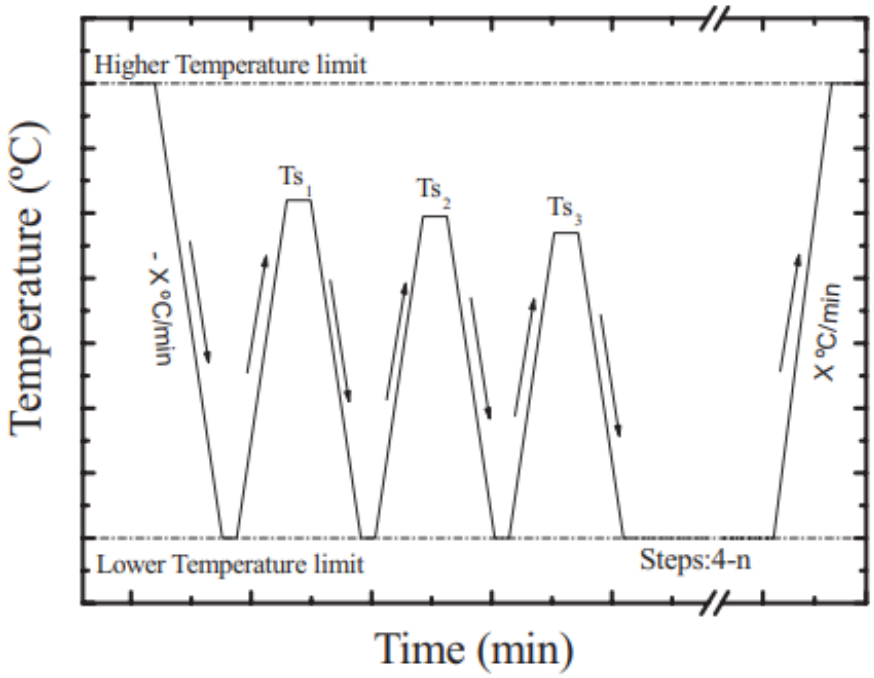

Figure 2.7. SSA heat treatment. Ts_1 is the $T_{s,\,ideal}$. [61]

The final melting step yields peaks at various temperatures and relative areas[61–63]. The higher the peak melting temperature, the greater the lamellar thickness, which corresponds to fewer crystal defects[61–63]. It is important to consider both the comonomer content and chain length throughout the ethylene sequence length analysis when analyzing the data[6].

There has been a prolonged debate regarding the interpretation of SSA results and the extent to which these results are meaningful[61–63]. The challenge arises from the numerous parameters that impact SSA results[61–63], as well as the limited accessibility to comprehensive microstructure analysis due to experimental complexities[25]. The correct determination of SSA experimental factors, such as $T_{s,\,ideal}$, further adds to this complexity[63]. In this study, we aim to address this gap by utilizing a set of samples exhibiting systematic changes in their MWD and SCBD. We obtained the MWD and SCBD through gel permeation chromatography (GPC)[25] and

then converted them into ESLD via statistical modeling[6]. We evaluate how SSA results reflect the structure of our materials[63]. The objective is to attain a satisfactory comprehension of the microstructure more quickly using DSC[61–63], as opposed to other challenging techniques[25] like temperature rising elution fractionation (TREF)[64,65] and crystallization analysis fractionation (CRYSTAF)[64,65].

We further continue our analysis to examine any correlation between the SSA results and the mechanical properties linked to ESCR. Previous studies have noted some relationship between SSA and ESCR[51,66]; however, comprehensive investigations integrating MWD and SCBD data, mechanical properties, and SSA data are lacking. Our study aims to address this gap by conducting a thorough analysis and verifying the correlations among these factors.

In **Chapter 3** we apply statistical modeling[6] to obtain the ethylene sequence length distribution from experimental data of molecular weight distribution and short chain branching distribution. We will explore the molecular parameters that control bimodal polyethylene environmental stress crack resistance and propose a quick and efficient protocol to study the structure of bimodal polyethylene and rank the developmental materials in terms of environmental stress crack resistance.

2. 6. Melt-state studies

This section reviews the fundamentals and methodology used to characterize bimodal polyethylene melts under simple shear. These studies are important in terms of understanding their processing behavior[2–4,11].

2. 6. 1. Slip and melt rupture

The no-slip boundary condition at the wall had been used for fluid dynamic analysis until it was found that many polymer melts behave differently. The observation of a decrease in the wall shear stress, the dependency of the wall shear stress on the gap, and the non-continuous flow curve in non-Newtonian fluids raised questions about the zero-velocity boundary condition. Despite extensive efforts in the literature to comprehend the slip behavior of polymer melts, the relationship between slip and the structure of polymers is not entirely elucidated. Understanding

the slip behavior of polymers is crucial not only for correcting data in rheometers to account for slip effects but also for accurately designing certain industrial processing methods such as extrusions[2–4,11,67,68].

An ideal polymer should have a combination of properties, such as good mechanical characteristics and favourable processing behavior. This the reason for the attractiveness of the bimodal materials[5,68,69]. It is acknowledged that the slip behavior of bimodal polyethylene differs from that of unimodal polyethylene[2,15,68,69]. Since we have the systematic set of materials, we can investigate the impact of bimodal MWD on the slip behavior of polyethylene.

In the presence of slip, the velocity of the melt at the wall becomes non-zero (**Figure 2.8**)[70–72]. Slip provides advantages in certain processing methods, such as extrusion, as it reduces the required pressure to achieve the desired flow rate, leading to saving the energy[3]. Conversely, slip can impact the functionality and accuracy of data in processes like polymer mixing and rheometry[3,70]. The shear stress applied to the polymer chains near the wall is directly proportional to the local velocity gradient[73]. This stress can distort the polymer chains from their equilibrium configuration[73]. When these chains solidify without returning to their equilibrium states, residual stress develops, potentially causing interfacial defects[73].

Simple shear is useful experimentally due to its ease of generation in laboratories and the fact that rheological studies can be conducted without the confounding effects of pressure and strain rate gradients, which occur in capillary flows[2,74]. Simple shear is generated by the rectilinear movement of one plate relative to another stationary plate[2,74]. The velocity profiles of this type of flow are presented in **Figure 2.8.a.** (no-slip condition) and **Figure 2.8.b**. (slip condition)[11]. Another common flow type is capillary flow, where the velocity profile is non-linear. The velocity profiles of capillary flow in the absence and presence of slip are presented in **Figure 2.8.c**. and **Figure 2.8.d**.[75].

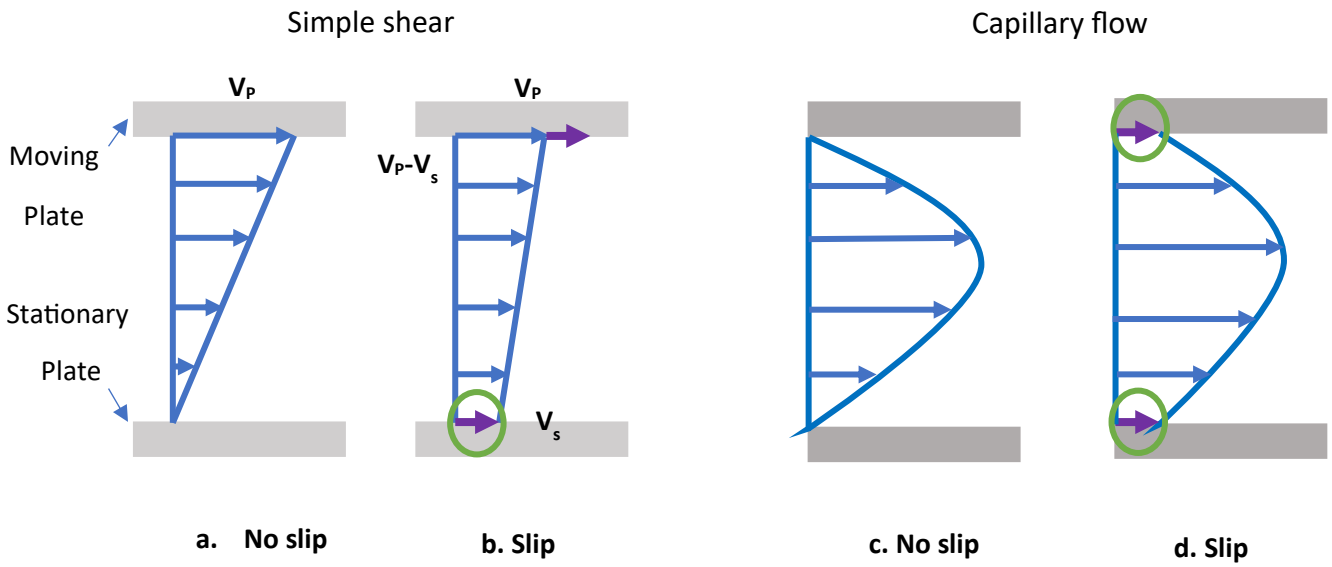

Figure 2.8. Scheme of the velocity profile of a polymer melt in simple shear and capillary flows. a. No-slip condition in simple shear, b. Slip condition in simple shear (inspired from)[11], C. No-slip condition for a capillary flow, and d. The slip condition for a capillary flow (Figures 1C. and 1D. inspired from)[75]. V and V_s are plate velocity and slip velocity, respectively.

2. 6. 2. Slip mechanisms

Entanglements of polymer chains play a crucial role in the characteristics of slip[11]. **Figure 2.9** shows the polymer chains adsorbed to the wall and the bulk chains. Polymer chains close to the wall are adsorbed to the surface through multiple segments in the chain (red circles in **Figure 2.9**). These interfacial chains are also constrained by entanglements with the bulk chains. When flow occurs, the bulk chains are stretched and transfer force to the interfacial chains throughout the entanglements[2,11]. If the force applied to the chains at the wall is larger than the adsorption force, slip occurs at the polymer/wall interface, and it is called true slip (adhesive failure mechanism). If the flow force cannot detach the chains from the wall, the chains act like end-grafted chains (tethered chains). In this case, slip occurs between the bulk and tethered chains and is called apparent slip (cohesive failure mechanism). The slip on low surface energy and non-adsorbing surfaces is close to true slip, while the apparent slip mechanism dominates the slip behavior of entangled polymers over high surface energy walls[2,72]. The case for this study is apparent slip (cohesive failure mechanism) since we use stainless steel as the wall[2].

When slipping over a passive (non-reacting) high-energy surface, three distinct regions of slip with different mechanisms exist: (i) weak, (ii) transition, and (iii) strong slip regions. The observation of these three slip regions enables the definition of two critical shear stress values. The first one denotes the shear stress at which slip initiates, while the second indicates the onset of strong slip[2,4,14,15].

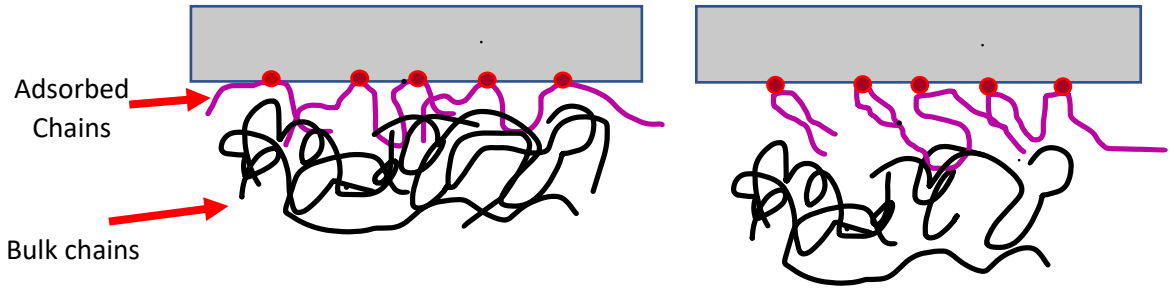

Figure 2.9. The polymer chains adsorbed at the wall surface a. Weak slip, and b. Strong slip after the chains disentanglement in cohesive failure. Polymer chains close to the wall are adsorbed to the surface through red circles. Polymer chains in black are bulk chains and polymer chains in purple are absorbed chains (inspired from[14]).

In the weak slip region, happening close to the no-slip region, the dominant slip mechanism involves the partial disentanglement of a few bulk chains from the tethered chains[2,4,11,14,15]. In the strong slip region, the bulk chains are released from entanglements with tethered chains, and the tethered chains align themselves to the flow direction[2,4,11,14,15]. **Figure 2.9** shows how the chains attach to the wall and are released from the bulk in strong slip[14].

Beyond these two regions, a transition region, from weak to strong slip, also exists. Flow curves (which is the plot of shear stress versus apparent shear rate) in capillary studies of these polymers show non-continuous behavior due to slip-stick instabilities[14]. Slip-stick instability is a periodical oscillation of slip velocity and shear stress[11]. One advantage of simple shear studies, such as the present investigation, lies in the ability to examine the transition region without slip-stick instabilities influencing the shape of the curve[2,12].

2. 6. 3. Sliding plate rheometer

The sliding plate rheometer (SPR) is an apparatus used to investigate the slip behavior of polymers during simple shear flow by generating rectilinear drag flow between two plates[2,12]. The instrument is designed to apply uniform shear stress, temperature, and shear rate to the sample. The main components of SPR are illustrated in **Figure 2.10**. The moving plate is mounted on the bearing and back support, and the gap between it and the stationary plate is adjustable. The sample is positioned between the plates. Under the flow, the shear stress transducer (SST) measures the shear stress corresponding to the applied shear rate[2,12].

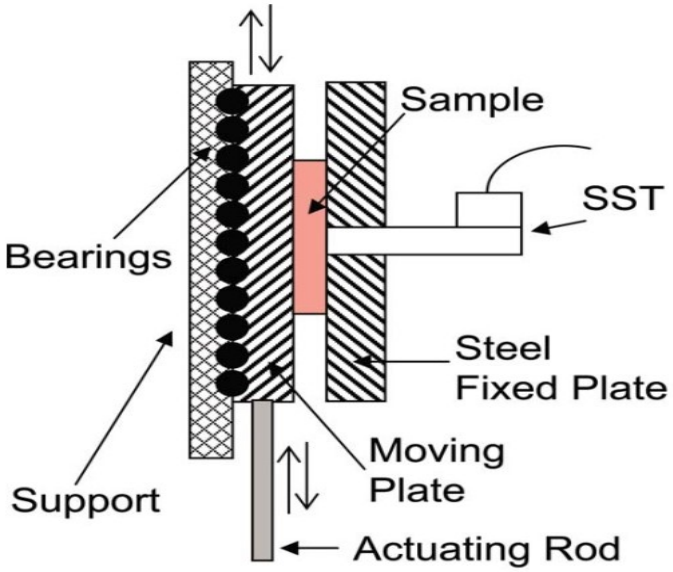

Figure 2.10. Side view of sliding plate rheometer[12]

During a slip test of a sample in SPR, three main phenomena can happen as follow[2,12]:

1. Simple Shear

This is the ideal flow in which the true shear rate is calculated by dividing the plate velocity $(\mathrm{V_p})$ by the gap between the stationary and moving plate (h) as follow[2,12]:

$$\dot{\gamma} = \frac{\mathrm{V_p}}{\mathrm{h}} \quad \text{no slip} \tag{2.1}$$

2. Slip

If slip is present, **Eqn. (2.1)** is no longer valid. In this case, the plate velocity divided by the gap is called the nominal shear rate ($\dot{\gamma}_n$)[2,12]. If both plates are made of the same material with identical surface characteristics, slip velocity (V_S) is the same on both plates, and the nominal shear rate is[12]:

$$\dot{\gamma}_n \equiv \frac{V_p}{h} = \dot{\gamma} + \frac{2V_s}{h} \tag{2.2}$$

3. Melt rupture

Some polymers experience melt rupture at high shear rates. If rupture occurs, the SST cannot record shear stress values[2,12,76]. Melt rupture is a catastrophic disentanglement of polymer chains that occurs within the bulk[2,76]. The distinction between cohesive failure slip and melt rupture lies in the location of disentanglement. In the case of cohesive slip, disentanglement occurs in the vicinity of the surface, whereas in melt rupture, disentanglement occurs within the bulk[76]. Melt rupture is a limiting factor in polyethylene processing, constraining the output volume[2–4,11]. This instability initiates at the polymer-air-steel interface and propagates throughout the sample[16,77]. This instability is not yet fully understood. In this study, we investigate this instability by replacing the stationary plate in the SPR setup with a glass plate. We employ visualization techniques to gain a better understanding of this instability.

During a shear test using SPR, the phenomena mentioned above can occur individually or in combination[12]. The velocity profile of the shear flow differs in the presence of slip, as summarized in **Figure 2.11**. **Eqn. (2.1)** is valid for simple shear without slip[2,12]. However, the presence of slip reduces the shear rate at constant stress (**Eqn. (2.2)**)[2,12]. From the figure, strong slip leaves some debris on the plates due to the high adsorption of a polymeric layer[78].

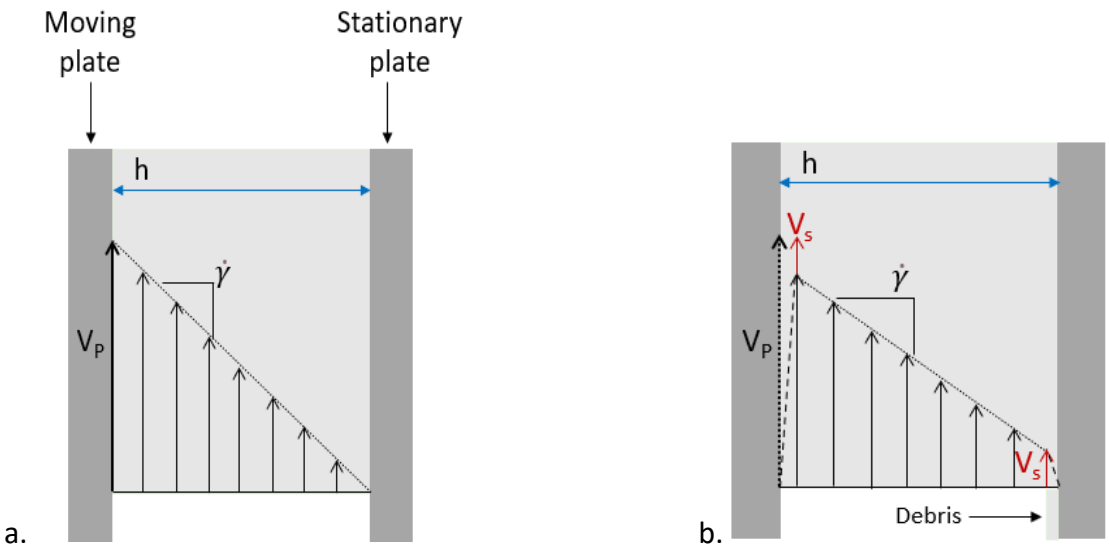

$$\dot{\gamma}_n \equiv \frac{V_p}{h} = \dot{\gamma} \qquad \dot{\gamma}_n \equiv \frac{V_p}{h} = \dot{\gamma} + \frac{V_{ss}}{h} + \frac{V_{sm}}{h}$$

Figure 2.11. Velocity profiles in SPR test in a. Simple shear, b. Simple shear with cohesive slip. $\dot{\gamma}_n$ is the nominal shear rate, h is the gap, and $V_{sm}$and V_{ss} are slip velocities at moving and stationary plates, respectively. The sketch is not to scale. Figures are adapted from[2,12].

In the SPR setup, if the stationary and moving plates are made of the same material (having the same surface energy) with identical surface characteristics, the slip velocity is assumed to be equal on both plates (V_{ss}= V_{sm}) [2,12]. This is the case for our slip studies in **Chapter 4**. Therefore, under constant temperature and pressure conditions, the slip velocity is calculated using the equation below at a constant shear stress (τ)[2,12]:

$$v_S(\tau) = \frac{h}{2}\left(\dot{\gamma}_n(\tau) - \dot{\gamma}(\tau)\right) \tag{2.3}$$

In this equation, $\dot{\gamma}_n(\tau)$ is the nominal shear rate, which is determined by the velocity of the moving plate[2,12], $\dot{\gamma}(\tau)$ the true shear rate in the absence of slip can be obtained from small-amplitude oscillatory shear (SAOS) assuming the Cox-Mertz rule[2–4,12,68].

The main advantages of using SPR for studying slip are:

1. In the SPR, the transition region from weak to strong slip can be studied without slip-stick instability changing the shape of the curve in contrast to capillary rheometers[2,12].

2. The flow is more uniform than in capillary studies without the confounding effects of pressure and shear rate gradient[2,12,71].
3. The control of surface characteristics and more experimental factors is easier to control in SPR[2,12,71].

2. 6. 4. Relaxation mechanisms in slip studies

There are various relaxation mechanisms through which the slip behavior of materials is analyzed[2,79]. The relaxation mechanism differs between polymer chains tethered to the wall and bulk chains, and it depends upon the shear rate level[2,79].

The tube model for polymers indicates a tube-like area around the polymer chains in which the chains are free to move[80]. Any motion larger than the tube diameter is suppressed, while the chain can move along the tube[80]. The primary relaxation mechanism for bulk polymer chains at low shear rates is reptation[2,79]. The snake-like movement along the tube is called reptation. Tethered chains cannot reptate since they are attached to the wall from at least one point along their chain. Therefore, the relaxation mechanism for tethered chains at low shear rates is constraint release (CR)[2,79]. This relaxation mechanism occurs when a chain moves out of its tube to release its constraint for neighbouring chains[81]. Therefore, when the polymer chains in the bulk reptate throughout their tube at low shear rates, the chains at the wall can be released. With the constraint removed, tethered chains can change their conformation locally and relax some stress. Another relaxation mechanism for tethered short chains is arm retraction[79]. The arm retraction mechanism is initially defined for an arm of a star polymer. The tethered chain is like an arm. If the chain retracts back along its tube and pokes out along a new tube, a portion of the old tube is removed along with its constraints[79,82]. **Figure 2.12** represents the constraint release, reptation, and retraction relaxation mechanisms[81].

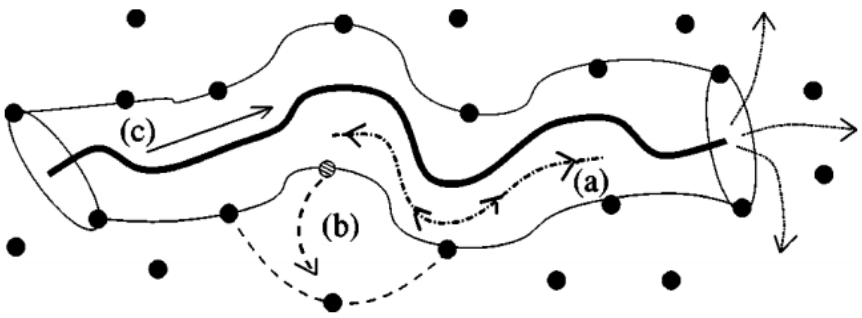

Figure 2.12. Relaxation mechanism of a polymer chains a. reptation b. constraint release c. retraction[81]

At intermediate shear rates, the primary relaxation mechanism is convective constraint release (CCR) for both bulk and tethered chains[2,79]. CCR occurs when the constraint is swept away by the flow (convection) at relatively high shear rates. The time required for the relaxation in this mechanism is much lower than that needed for the chain to reptate throughout the tube[83]. When CCR dominates, the flow can cause both deformation and relaxation. In other words, a bulk chain is being deformed on a timescale in the order of the reciprocal of the bulk shear rate and is relaxed at the same timescale[2,79,84]. This is because the flow determines the convection velocity or CCR relaxation[2,79,84]. However, there is a difference between the two timescales for a chain tethered to the wall. The tethered chains are deformed on a timescale in the order of the reciprocal shear rate at the wall, which is higher than the bulk due to slip[2,79,84]. However, they are relaxed on a timescale in the order of the reciprocal of the bulk shear rate. The latter is because the bulk chains form the tube for the tethered chains[2,79,84]. Therefore, the tethered chains become oriented in the flow direction, and disentanglement from the bulk occurs (strong slip)[2,79,84].

Based on the mechanisms discussed, the tethered chains relax more quickly than they deform in the weak slip region due to arm retraction and CR[2,79,84]. However, in the transition region, the difference in the deformation and relaxation timescales for tethered chains causes them to be oriented in the flow direction and eventually disentangle from the bulk chains[2,79,84].

2. 6. 5. Short chains content

Sabzevari et al.[3] conducted a study on the effect of short chains on the slip behavior of polybutadiene using tracer particle velocimetry in shear. They demonstrated that the addition of weakly entangled short chains to a highly entangled monodisperse sample significantly increased slip at the same shear stress value within their experimental window. Additionally, they reported that the onset of strong slip shifted to lower stress values in the presence of the short chains[3]. In a subsequent study, the same group[4] investigated the slip behavior of two sets of tridisperse polybutadiene in the presence of three components: 1) weakly entangled (set 1)/unentangled chains (set 2), 2) moderately entangled chains, and 3) highly entangled chains. The key distinction between the two sets lies in the first component, where set 1 contains weakly entangled chains (molecular weight = three times the molecular weight between entanglements (M_e)), and set 2 includes an unentangled component (with molecular weight lower than M_e)[4]. Their research revealed that the addition of moderate to high contents of weakly entangled chains (set 2) increased the slip velocity at high shear rates and caused a shift in the onset of strong slip to lower stress values compared to set 1. The authors[4] concluded that the unentangled component was incapable of transferring the viscous force to the tethered chains, leading to a reduction in slip and the occurrence of strong slip at higher shear stresses[2,4].

2. 6. 6. Bimodal molecular weight distribution

Inn[68] investigated the effect of bimodal molecular weight distribution on the slip behavior of metallocene-catalyzed bimodal polyethylene using capillary extrusion under constant piston speed conditions[68]. The bimodal polyethylene with a higher content of low molecular weight chains showed a higher slip velocity before the stick-slip transition and lower oscillation during stick-slip[68]. The author proposed two explanations for this behavior[68]. Firstly, disentanglement occurs at a lower shear stress for low molecular weight chains, facilitating the onset of strong slip[68]. Secondly, this phenomenon could be related to molecular fractionation within the capillary[68]. It has been reported that in the flow of polyethylene within a capillary, low molecular weight chains tend to concentrate near the surface[68]. The migration of short chains close to the

wall towards the surface is plausible, especially for bimodal polymers with a substantial amount of low molecular weight chains[68].

2. 6. 7. Molecular fractionation

Under the flow, it is expected that the chains with different molecular weights will rearrange in a way of achieving the lowest Gibbs free energy. The chains tethered at the wall have lower conformational entropy compared to those in the bulk, and the length of the chains correlates with the degree of entropy loss incurred by their restrictions at the wall. Consequently, longer chains are repelled from the wall surface[14,85,86]. Furthermore, owing to the shear stress gradient, longer chains experience increased free energy of elastic deformation when near the wall, leading to their repulsion[87–89].

Ebrahimi et al.[85] investigated the MWD of both the bulk and the surface layer of an extruded polyethylene pipe sample. They shaved one micron off the sample using a microtome and observed that the surface was enriched with low molecular weight chains[85].

Inn[68,69] studied the surface characteristics of the extrudate of bimodal polyethylene and concluded that the occurrence of wavy extrudates at high shear rates is attributed to the flow of the extrudate over a less viscous and lubricating layer formed by the migration of short chains. They reported the wavy surface only for broad molecular weight distribution materials[68,69]. The formation of a lubricating layer and its role in contributing to slip remains an open question in the literature.

Nimo et al.[90] studied the molecular fractionation of bimodal polyethylene through GPC analysis of the debris. They demonstrated that molecular fractionation can occur under simple shear, even without a bulk shear rate gradient[90]. The possible effects of this fractionation on the structural changes during slip remains an open question.

The slip behavior of bimodal polyethylene differs from that of unimodal polyethylene[2,68,69] , and the slip behavior of bimodal MWD polyethylene is not fully understood[2,68,69]. The presence of short chains changes the slip behavior of polyethylene[2–4,15,69]. Having a set of resins with a systematic change in MWD is crucial to better understand the effect of bimodality[2,68]. There are

no slip studies on bimodal polyethylene using the SPR, i.e., simple shear. In **Chapter 4**, we aim to address this gap by investigating the effect of low molecular content on the slip behavior of bimodal materials. In **Chapter 5**, we present a detailed investigation of the melt rupture of one of our materials using visualization techniques to gain a better understanding of this phenomenon. We demonstrate that melt rupture can occur after reaching a steady-state plateau in slip velocity and simple shear. We hypothesize that time-dependent structural changes during the slip (like molecular fractionation) might lead to the transition from slip to melt rupture. Further studies are required to explore this possibility.

2. 7. Objectives

Many studies have focused either on solid-state or melt-state properties. Here, we are combining both aspects and showing how we can bring two aspects together to design materials. This study focuses on the following objectives:

1. To apply statistical modeling[6] to obtain the ethylene sequence length distribution from experimental molecular weight distribution and short chain branching distribution data.
2. To find the molecular parameters that control bimodal polyethylene's environmental stress crack resistance; and to develop a quick and efficient protocol to rank the developmental materials in terms of environmental stress crack resistance.
3. To explore the effect of low molecular weight chains on the slip behavior of bimodal polyethylene under simple shear.
4. To study the melt rupture of polyethylene, including its characteristics and the conditions under which melt rupture occurs, and to propose mechanisms of melt rupture for further studies.

Chapter 3. Structure of bimodal polyethylene and solid-state properties

In this chapter, using statistical modeling[6], we extract the ethylene sequence length distribution from the experimental molecular weight and short chain branching distributions. We look into the correlations between solid-state properties and the molecular structure. This chapter includes non-isothermal crystallization behavior and successive self-nucleation and annealing results and their correlations with the mechanical properties and structure of our materials. This chapter will be divided into two manuscripts to be submitted. The proposed titles are: 1. Sattari, M., Kwakye-Nimo, S., Karimineghlani, P., Inn, Y., & Wood-Adams, P. M. (2024). Structure and properties of metallocene catalyzed bimodal polyethylene: A. Ethylene sequence length distribution, and successive self-nucleation and annealing behavior. To be submitted. 2. Sattari, M., Kwakye-Nimo, S., Ehounou, E. C. M. J., Karimineghlani, P., Inn, Y., & Wood-Adams, P. M. (2024). Structure and properties of metallocene catalyzed bimodal polyethylene: B. Correlations between structure and mechanical and non-isothermal crystallization behavior. To be submitted.

3. 1. Abstract

The structure of bimodal polyethylene is presented in terms of the ethylene sequence length distribution. This distribution is determined by applying statistical modelling[6] to molecular weight and short chain branching distributions data obtained from gel permeation chromatography (GPC). We found that the ethylene sequence length distribution is the most important structural characteristic of bimodal polyethylene in terms of mechanical properties. The natural draw ratio was used to demonstrate that weight averaged ethylene sequence length is the controlling parameter of environmental stress crack resistance for our materials. Correlations between non-isothermal crystallization behavior and successive self-nucleation and annealing (SSA) results and the structure and mechanical properties of materials are presented, providing quick and convenient methods to rank between materials in terms of environmental stress crack resistance.

3. 2. Introduction

With an estimated global production of 84 million tons annually, polyethylene is the most common plastic resin used in the market[91]. Due to its versatility, low cost and easy processability, polyethylene has a wide range of applications including industrial packaging systems, fiber optic systems and piping[43,92]. Advancement in polymerization and catalysis technology in the early 1990s allowed the emergence of polyethylene resins with bimodal molecular weight distribution[91,93,94]. This type of polyethylene is characterized by increased the stiffness, toughness, and stress crack resistance compared to unimodal resins[95,96]. The end-use behavior of polyethylene, and many other polymers, is determined by its crystallinity and microstructure which are in turn dependent on molecular structure[1].

Crystallization is often studied under idealized isothermal conditions where the parameters of state are maintained constant to facilitate treatment of experimental data[96–98]. Although the treatment of experimental data under non-isothermal crystallization is complex compared to those under isothermal crystallization, the results coincide with practical industrial situations where the kinetics of crystallization depends greatly on instantaneous conditions and rate of change of temperature[96,97] defining the morphology, physical and mechanical properties of final products[96].

3. 2. 1. Molecular Structure of Ethylene Copolymers

Short chain branching (SCB) content and distribution plays an important role in the physical[25,64] and mechanical[25] properties of polyethylene by affecting the crystallization behavior[25]. The mechanical properties of high density polyethylene in particular are strongly affected by a small change on the amount of SCB[25]. The effect of SCB on the melt-state properties on the other hand is not always as profound[23,99].

In the case of bimodal polyethylene, there are two populations of chains: a low-molecular weight (LMW) population and a high-molecular weight (HMW) population[2]. The short chain branching distribution of the two populations can be engineered in the polymerization process[5,25] including via dual-catalyst single-reactor polymerization as for the polyethylenes in this study. The best stress crack resistance can be achieved by placing more short chain branching in the high

molecular weight population as compared to the LMW population or having the same content in the two populations[25,100,101]. The reason for this is that short chain branches on long chains help with the formation of tie chains, connections between two crystallites[25,101,102].

It is challenging to accurately measure short chain branching distribution and therefore multiple methods are available: solvent gradient fractionation[25] followed by off-line nuclear magnetic resonance (NMR) characterization[25], temperature rising elution fractionation (TREF)[64,65], crystallization analysis fractionation (CRYSTAF)[64,65] and more recently the GPC-IR5[25] method. Each of these methods have different strengths and weaknesses[25,64] but all are rather complex experimentally. Therefore, a differential scanning calorimetric (DSC) method, successive self-nucleation and annealing, has been presented as a quick analysis[64,103] of the short chain branching effects on the polyethylene structure. In this paper, we examine how and to what extent we can use this method to understand the structure of polyethylene.

The successive self-nucleation and annealing (SSA) method involves applying self-nucleation by inducing chain orientation which remains[104] in the melt-state due to the memory effect[105] and successive annealing steps at different temperatures followed by a final melting run[62,64,65,106–108] all in a differential scanning calorimetry. The goal is to fractionate crystal lamellae based on their size which is linked to the heterogeneities of the chain[64,100,109,110]. This fractionation results in multiple peaks in the final melting run[64,100,111]. The number of melting peaks is equal to the number of annealing steps plus one comprising unannealed lamellae[64,100,111]. Each melting peak represents an average lamellar thickness[64,100,111]. The higher the melting point is, the thicker are the lamella, which are made of longer ethylene sequence lengths[64,100,111].

Thermal fractionation methods, such as SSA, are based on the crystallization and melting responses of polymers meaning that materials with low crystallinity should not be studied by these methods[64]. In this study, we are characterizing high-density polyethylene with high crystallinity (higher than ~50% at a cooling rate of 2.5 °C/min). Since dissolving polyethylene is difficult and involves hazardous solvents[112,113], solvent-free methods for determining the structure of polyethylene like SSA are of interest even at the expense of accuracy. In the case of polymers with linear chains, SSA fractionation will happen due to chain length[114]. However, the

exact combined effects of MWD and SCBD have not been directly studied due to an absence of materials with a systematic change in MWD and SCBD. Here we address this gap.

3. 2. 2. Crystallization and structure

Alamo et al.[115] found that an increase in the comonomer content at a constant molecular weight significantly lowers the melting temperature and crystallinity of polyethlyene[115]. An increase in molecular weight has a similar effect when the comonomer content is kept constant[115] due to the increased entanglements of the original melt[116]. Alamo et al[115] emphasized the importance of studying the molecular weight and the short chain branching independantly[115]. This requires a set of samples with a systematic change in SCB and MW features as is the case for the current study.

Using molecular dynamics simulations, Hu et al.[41] concluded that crystallization kinetics and morphology are affected by short chain branching content and distribution but not by the length at least up to eight short chain branches per 1000 carbons (SCB/1000C). They reported that up to a critical value of 5 SCB/1000C, there is no difference between placing the short branches on short or long chains in terms of crystallinity. For higher short chain branching contents, the crystallinity of systems with branched long chains is lower than systems with branched short chains[41]. They also showed that SCB increases the number of tie chains between crystallites especially when placed on the long chains[41,117].

In this paper, we examine the effects of molecular weight and short chain branching distributions on the non-isothermal crystallization behavior of a unique set of polyethylene that are bimodal in SCB and MW distributions. The two effects are studied systematically using developmental materials.

3. 2. 3. Environmental stress crack resistance

The bimodal MWD polyethylene used in this study are designed to optimize environmental stress crack growth resistance (ESCR) which is a key property for materials used in piping applications. This is achieved by manipulating the molecular structure to allow for a higher number of tie-chains in the crystal structure[1,118]. Here, we conduct a thorough study of the

molecular structure of bimodal polyethylene through experiment and modeling to shed light on the relationships between molecular structure, crystal structure and mechanical properties including ESCR.

Polyethylene has a semi-crystalline structure with layers of amorphous and crystalline material[35,38,50]. If a chain incorporates in more than one lamellae, a tie chain or covalent bridging occurs[35,36]. Tie chains are believed to play an important role in increasing the toughness and crack resistance of polymers[35,38,39] as they act as load transfer bridges[40].

The number of tie chains increases with increasing short chain branching[39] at the expense of lowering the overall crystallinity[41]. Tie chains can also be increased by designing a bimodal SCBD and MWD[25]. Quantifying tie chains directly whether experimentally is challenging[35,37]. In this study, we develop a protocol using DSC and a statistical model of molecular structure to explore the combined crystallization of low and high molecular populations and the resulting mechanical properties which we link to the presence and amount of tie chains.

Polyethylene failure can be categorized in three major modes: ductile, rapid crack propagation and slow crack growth (SCG)[9]. Among the three modes, slow crack growth is of primary failure mode of polyethylene in pipe applications[8–10]. This time-dependent, brittle mode of failure happens at stresses below the yield stress[7–9]. The time to failure under such a low stress is typically in the range of decades[9]. However, demand for pipes[9,44], novel installation methods that apply higher loads during installation[44–46], and challenging environments including soaps and oils[47] call for materials that can be used for more than 100 years without failure[9].

It is difficult to measure slow crack growth experimentally due to its slow timescale[9]. Such studies are normally conducted with notched specimens[9]. The duration of the test can still last as long as 10,000 hours[8,44]. Tests can be accelerated[8] by a factor of 6 with the application(s) of low surface tension liquids to facilitate the creation of new crack surface[43] or lubricating agents[9], and/or elevated temperatures[9], but it is still very slow. We may also see a change in the failure mechanism[9] with these conditions producing misleading results with respect to its end use behavior. The solution to this problem is to use other mechanical properties that correlate well to the slow crack growth behavior[9]. It has been found that the best parameters to represent the

resistance to ESC for both ethylene-hexene and ethylene-butene copolymers are the strain hardening modulus[50,8,51,42,44] and the natural draw ratio[50,8,51,42] coming from strain hardening tests[9].

There are techniques to improve the ESC resistance by manipulating the molecular structure to induce a higher number of effective tie chains in the crystal structure[18]. Two common approaches are the placement of short chain branches on the HMW portion of the MWD[8,42] and shifting from butene as a comonomer (the most common comonomer in pipe resins) to hexene as a comonomer[28]. The impacts of these changes has been interpreted in terms of tie chains[8,42]. The presence of branches on chains makes it harder for the tie chains to pull out of the crystalline lamellar[42], hexene being more effective that butene since produces a longer branch[42]. However, a thorough study on the effects of MWD and SCBD systematically has not yet been done. In this study, we address this gap. We use a set of ethylene-hexene copolymers with a systematic change in MWD and CCD in which the commoners are placed on the HMW chains. We also examine the relationships between the results of the successive self-nucleation and annealing method[63], SCBD, and strain hardening tests so that DSC can be used to qualitatively rank materials in terms of expected ESCR quickly.

Fawaz et al.[7] studied the effects of molecular structure on slow crack growth. They concluded that increasing the molecular weight and comonomer content increases the number of tie chains resulting in higher slow crack growth resistance. Higher comonomer content leads to thinner lamellae increasing the chance of one chain being incorporated into two lamellae but decreases the overall crystallinity. They also reported that a high molecular weight is needed to ensure lamellar quality and tie chain density. They were however unable to distinguish small effects and concluded that there are many factors affecting the slow crack growth behavior[7]. In order to reduce the complexity, in our studies, we focus on ethylene-hexene bimodal copolymers with the short branches on the longer chains. We are also using a set of materials with a systematic change in the MWD and SCBD.

3. 3. Materials

A set of seven polyethylenes with bimodal SCB and MW distributions is used. These materials are synthesized through a dual-metallocene catalyst system in a single loop-slurry reactor at CPChem as we have previously described these materials[78]. The GPC-IR5 method described previously (including calibration and experimental parameters)[25] was used to obtain the molecular weight and short chain branching distributions of the materials presented in **Figure 3.1a**. For all materials, the high MW population has a higher content of short chain branching. HDPE 4 and HDPE 5 have similar MWDs and the same value of SCB for the low MW population but different SCB content in the high MW population as shown in **Figure 3.1b.** We use this pair to study the effect of this aspect of SCBD. Additionally, HDPE 6 and HDPE 7 (**Figure 3.1.c**) have similar SCB distributions but different MW distributions.

It should be noted that there are uncertainties about the validity of SCBD for M higher than ~$10^{5.4}$ due to the GPC-IR5 method detection limitations[25]. In our analysis, we address this limitation for HDPE 6 and 7 through the model fitting as explained in the supplementary information.

The MWD features[2,78]: weight (M_w) averaged molecular weights, polydispersity index (M_w/M_n)[2,78], in addition to the average SCB ($\mathrm{SCB}_{\mathrm{ave}}$) are presented in **Table 3.1**. Due to the resolution of the IR detector when the polymer concentration in the GPC eluent is very low[25], the short chain branching contents at the high MW end of the distributions of the HDPE 6, 7, 8 and 9 are not available experimentally.

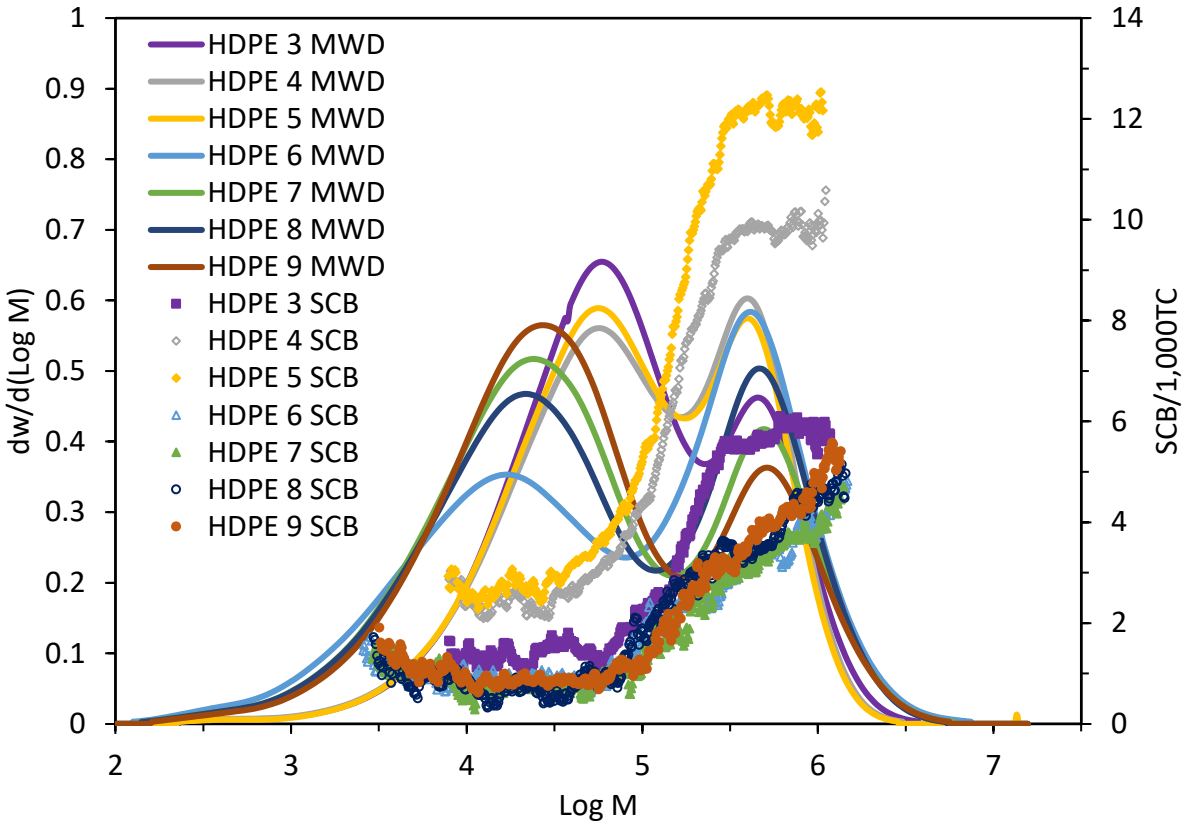
HDPE 3 MWD
HDPE 4 MWD
HDPE 5 MWD
HDPE 6 MWD
HDPE 7 MWD
HDPE 8 MWD
HDPE 9 MWD
HDPE 3 SCB
HDPE 4 SCB
HDPE 5 SCB
HDPE 6 SCB
HDPE 7 SCB
HDPE 8 SCB
HDPE 9 SCB
dw/d(Log M)
SCB/1,000TC
Log M
0
0.1
0.2
0.3
0.4
0.5
0.6
0.7
0.8
0.9
1
0
2
4
6
8
10
12
14
2
3
4
5
6
7

a.

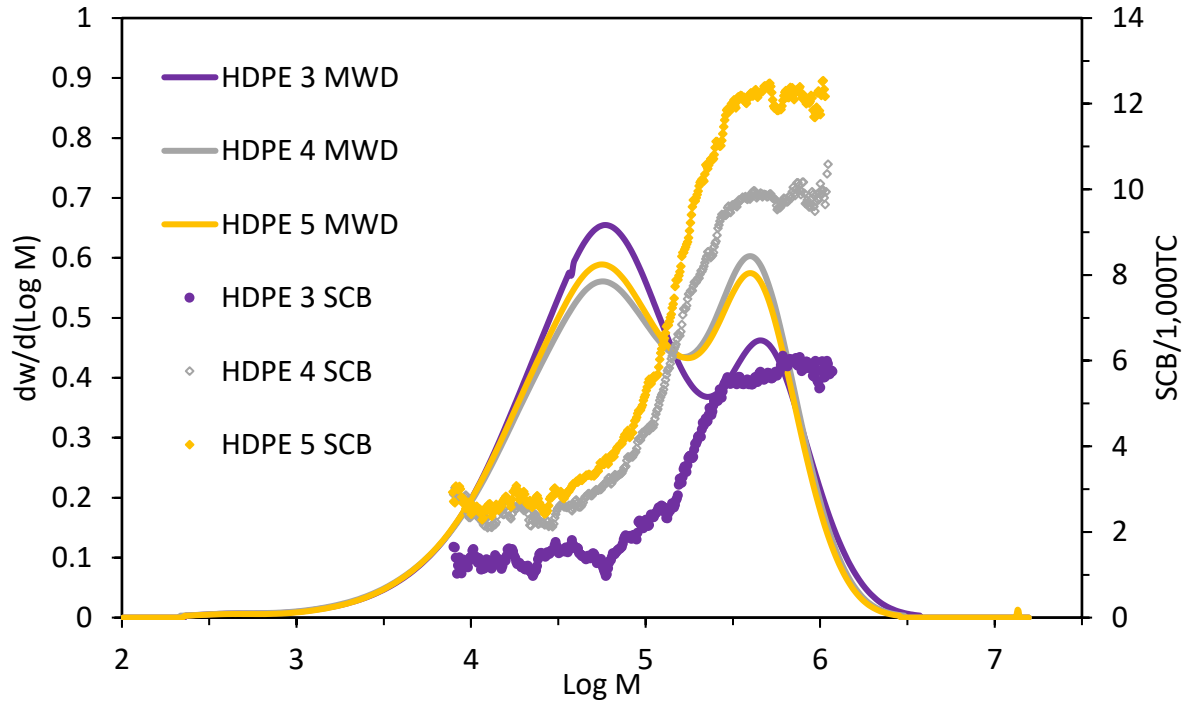
HDPE 3 MWD
HDPE 4 MWD
HDPE 5 MWD
HDPE 3 SCB
HDPE 4 SCB
HDPE 5 SCB
dw/d(Log M)
SCB/1,000TC
Log M
0
0.1
0.2
0.3
0.4
0.5
0.6
0.7
0.8
0.9
1
0
2
4
6
8
10
12
14
2
3
4
5
6
7

b.

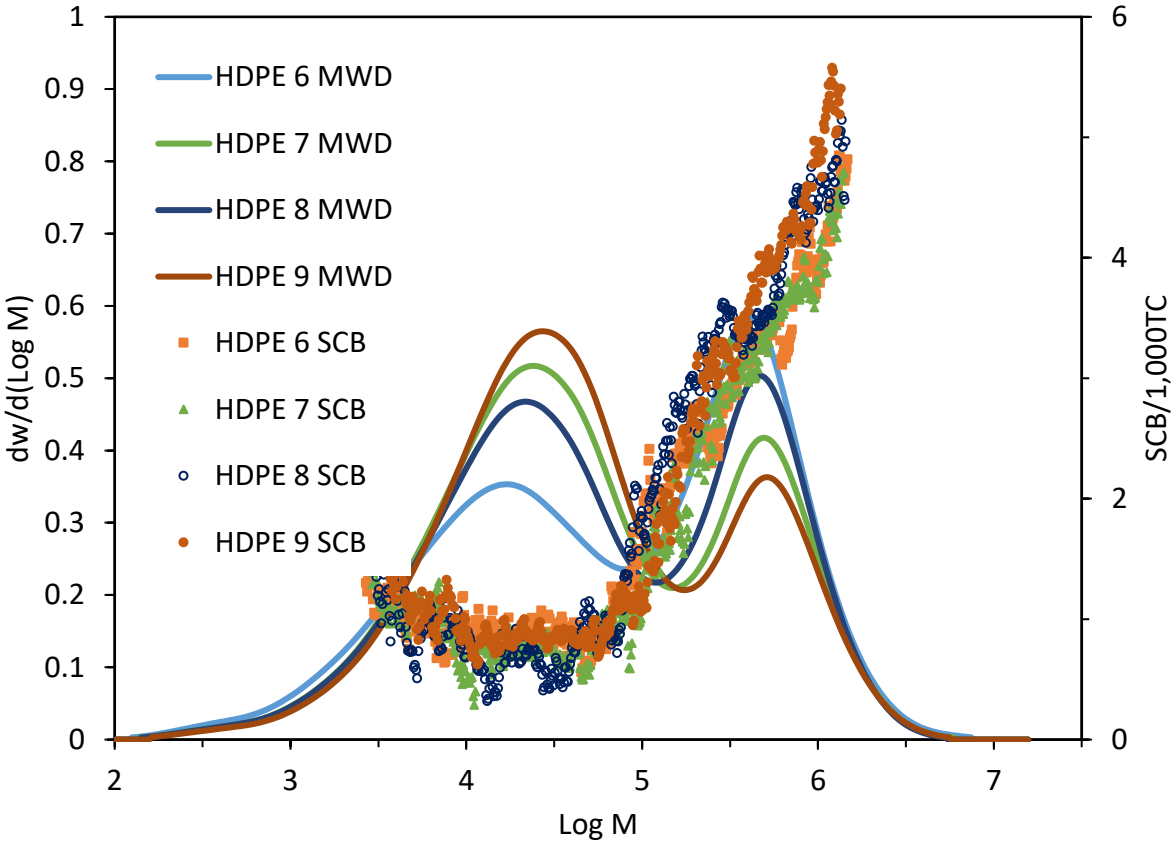

c.

Figure 3.1. Molecular weight and short chain branching distribution of materials: a. All materials b. HDPE 3, HDPE 4, and HDPE 5 c. HDPE 6, HDPE 7, HDPE 8, and HDPE 9

Table 3.1. Molecular weight and short chain branching average of materials

Materials	$\overline{M}_w$ (kg/mol)	$\overline{M}_w/\overline{M}_n$	$SCB_{ave}(^1/_{1000}\,C)$
HDPE 3	202.6	7.8	2.70
HDPE 4	203.1	7.9	5.34
HDPE 5	192.7	7.1	6.34
HDPE 6	283.2	32.8	1.84
HDPE 7	211.0	22.2	1.48
HDPE 8	225.5	23.8	1.80
HDPE 9	202.0	18.6	1.61

3. 4. Experimental

3. 4. 1. Non-isothermal crystallization and melting behavior

Thermal measurements have been carried out using a DSC model TA MDSC Q200 in a nitrogen atmosphere with a sample size of 5 mg in pellet form. Thermal history was first erased by heating the samples to 180 °C and then holding them at this temperature for 10 minutes. Next, they were cooled to 0 °C at the cooling rate (R) of 2.5 °C/min to capture the non-isothermal crystallization behavior. All measurements were repeated three times with new specimens and the average and standard error of the parameters were taken to evaluate the data reproducibility.

3. 4. 2. Successive self-nucleation and annealing method

There are many important experimental parameters in the SSA method as discussed thoroughly elsewhere[63,64]. We have followed the experimental approach of Zhang et al.[119] study with 10 mg specimens where 5°C/min is used for cooling/heating for the self-nucleation and annealing steps and 10°C/min is used for the final melting step. The holding time for both the self-nucleation and annealing steps is 10 minutes. The temperature versus time for SSA experiments is presented in **Figure 3.2**. The most important experimental parameter to be determined is the self-nucleation temperature[63,64]. This temperature should be selected such that the highest number of self-nuclei are created in the absence of spherulitic growth[63,64]. This temperature depends on comonomer content[63,64] so it must be determined for each material. We have applied the SSA analysis to HDPE 3, 4, 5, 6 and 7.

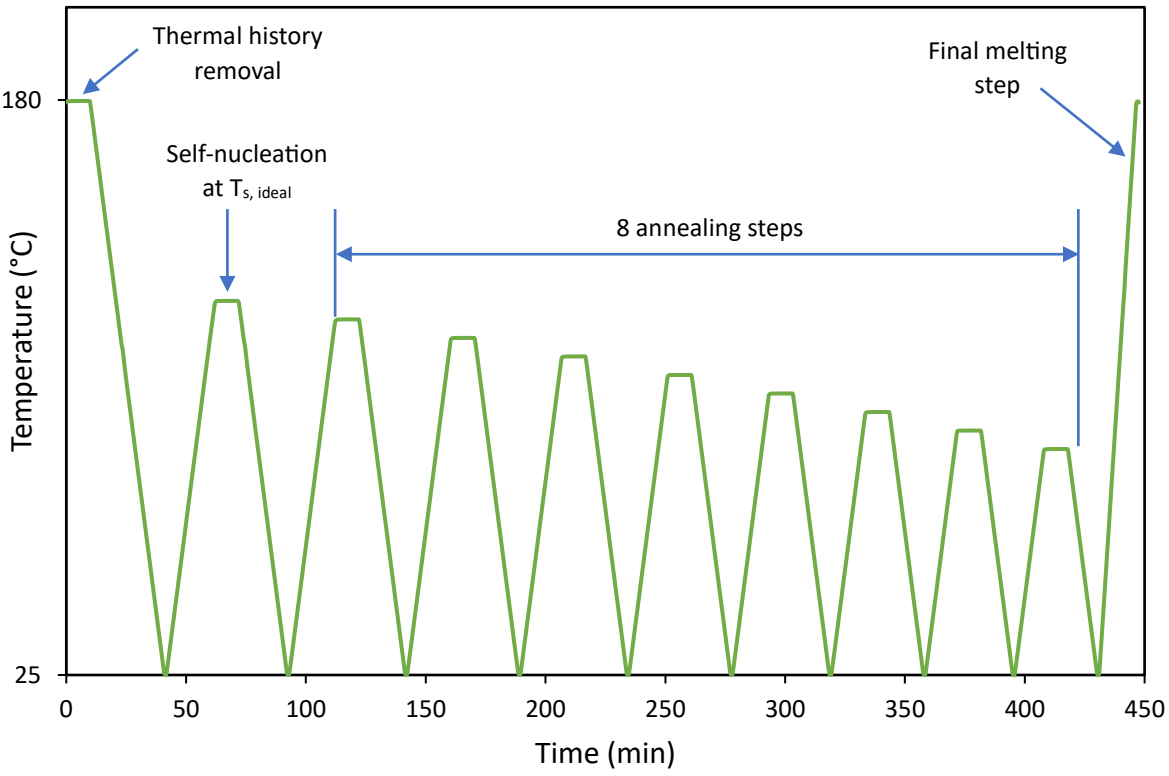

Figure 3.2. Successive self-nucleation and annealing temperature-time protocol

In order to determine $T_{s, ideal}$ for each material, we must perform a set of self-nucleation studies at different T_s using the following protocol of five stages (**Figure 3.3**)[63,64]:

i. Thermal history removal by heating the sample to 180 °C and holding for 10 minutes
ii. Creation of the standard state by cooling down from 180 °C to 25 °C at the rate of $5\,^{\circ C}/_{min}$
iii. Heating up to a possible T_s and holding for 10 minutes
iv. Cooling down to 25 °C at the rate of $5\,^{\circ C}/_{min}$
v. Heating to 180 °C at the rate of $10\,^{\circ C}/_{min}$ to record the melting peak

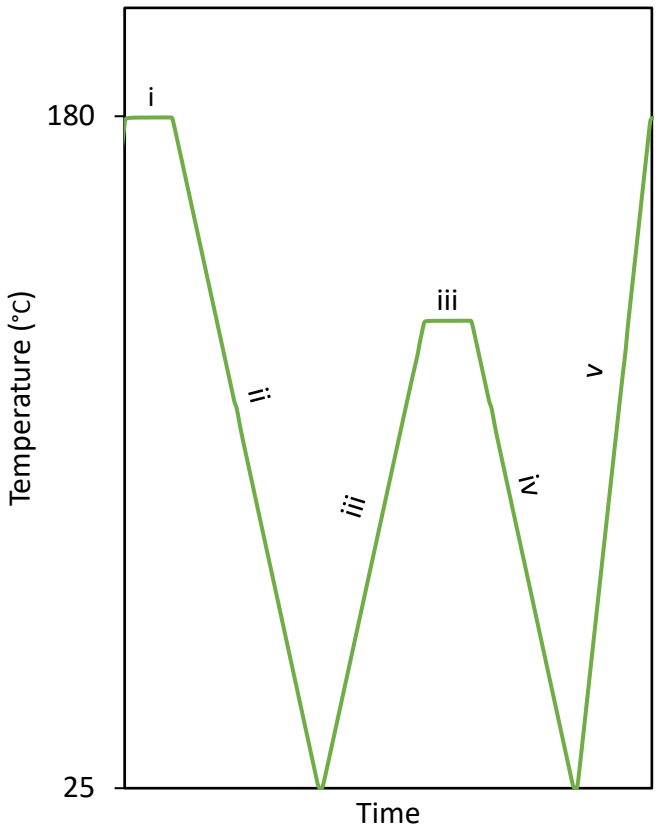

Figure 3.3. Time-temperature protocol for the $T_{s,\ ideal}$ determination. The stages (i, ii, iii, iv and v) are explained in the text.

This procedure is repeated at different possible T_s temperatures around the a common literature value for PE of 131 °C[110] so that the ideal Ts can be determined ($T_{s,\ ideal}$). There are different ways to interpret the results of this protocol[63,64] and thus to determine the $T_{s,\ ideal}$. All are based on indicators that show lamellae growth during the holding time at T_s (stage iii). For materials like polypropylene that are more sensitive to self-nucleation temperature compared with polyethylene, all indicators might be observed[63,64]. Even observation of one indicator is enough to conclude that growth occurred[63,64]:

1. Losing the baseline in stage iv of the self-nucleation protocol[63,64] as shown in **Figure 3.4**. This shows that the growth has already started during the holding time of stage iii.

2. A decrease in the crystallization enthalpy during stage iv compared with that of the standard crystallization (stage ii) shows that growth occurred[63,64] (also observed in **Figure 3.4**).
3. Detection of an additional peak in stage v due to melting of annealed lamella[63,64]. This is challenging to detect for polyethylene especially when the melting peak is broad as is the case for our materials.

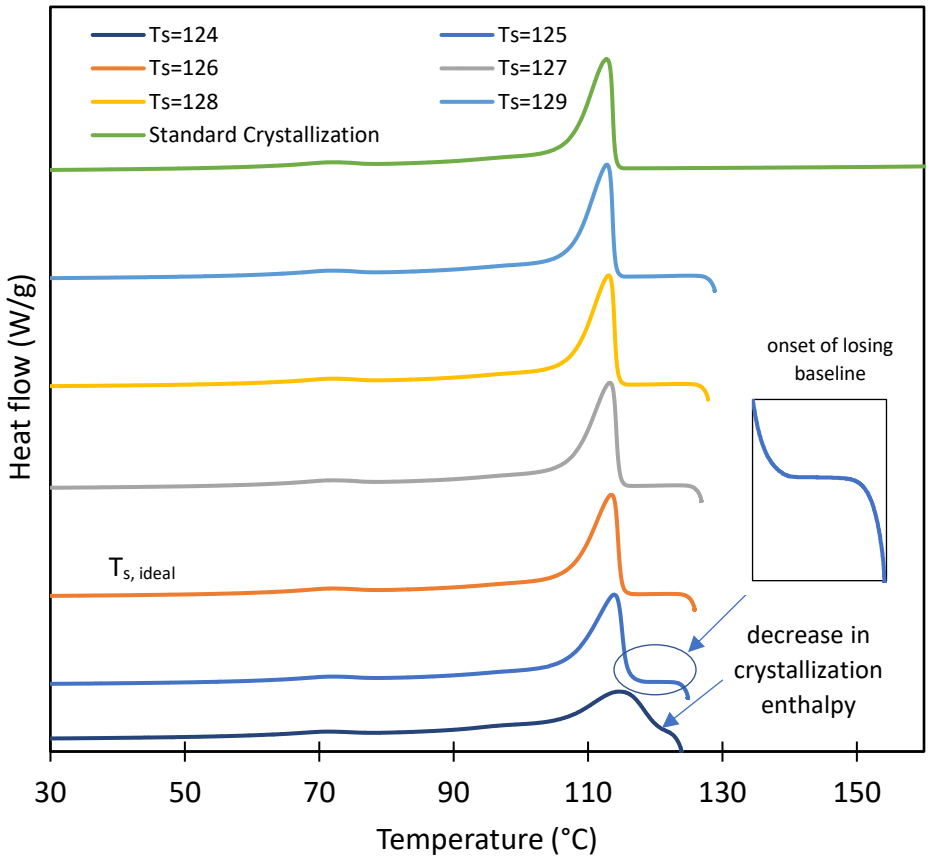

Figure 3.4. Heat flow versus temperature for step iv of $T_{s,ideal}$ selection procedure at different T_s for HDPE 5

In this study, we used methods 1 and 2 to detect the $T_{s,\,ideal}$ since the broad melting peaks of our materials prevent using the third indicator. These results for HDPE 5 are presented in **Figure 3.4**. At T_s=125 °C the baseline is lost and at T_s=124 °C the crystallization enthalpy is lower than T_s=125 °C showing that at 124 °C there is a considerable amount of lamellar growth. Since polyethylene has very fast nucleation[58], choosing a $T_{s,\,ideal}$ without crystal growth is more

important than choosing a temperature that is closest to the growth limit. Thus, for this material, we chose 126°C as the $T_{s,\ ideal}$. We summarize $T_{s,\ ideal}$ for all materials used in the SSA studies in **Table 3.2.**

Table 3.2. $T_{s,\ ideal}$ for all the material used in SSA studies

Materials	$T_{s,\ ideal}$ (°C)
HDPE-3	129
HDPE-4	126
HDPE-5	126
HDPE-6	130
HDPE-7	132

3. 4. 3. Mechanical properties

Strain hardening modulus tests were conducted in an Instron Machine equipped with heating chamber and non-contact extensometer. Polyethylene pellets were compression molded to produce 0.3 mm thickness plaques. The molding and subsequent annealing conditions were followed per ISO 18488. Five (5) specimens per sample were die cut from the plaques with the specimen dimensions consistent with ISO 18488. Test specimen is extended along its major axis at constant speed (20 mm/min) at 80 ^{O}C until the specimen breaks. From the strain hardening test, primary properties such as the natural draw ratio at 80 °C as well as tensile stress at yield, Young's modulus, tensile stress at break, and elongation at break are extracted[120]. NDR can be defined as the strain at the onset of strain hardening in the graph of engineering stress (force divided by the original area) versus the engineering strain[51,53] (**Figure 3.5**). The NDR is related to the ability of the chains' network to extend under the load[51]. It is known that ESC resistance increases with decreasing NDR[51].

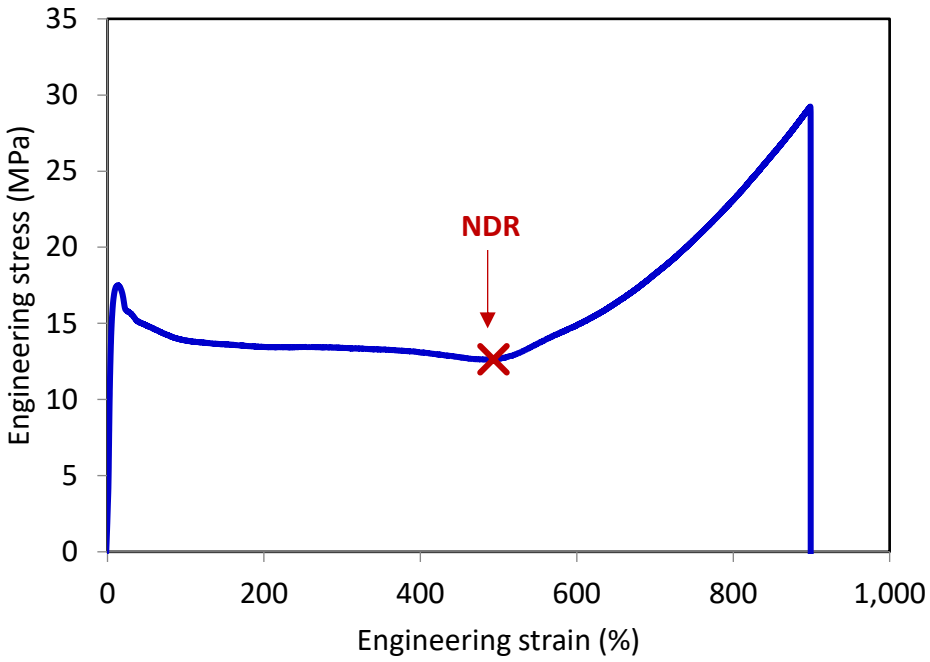

Figure 3.5. Engineering stress versus engineering strain from a strain hardening test demonstrating NDR

3. 5. Results

3. 5. 1. Non-isothermal crystallization

The heat flow versus temperature curve for HDPE 9 at a cooling rate of 2.5 $^{\circ C}/_{min}$ is shown in **Figure 3.6**. We define the baseline by extrapolation of the heat flow curve at higher temperatures than the onset crystallization temperature (T_o) and extending it to lower temperatures. The onset T_o (°C), end (T_e), and peak temperatures (T_p), crystallization enthalpy (ΔH_c), and the relative crystallinity (X_C) for all materials at the rate of 2.5 $^{\circ C}/_{min}$ are extracted from the curves and is presented in **Table 3.3**. The relative crystallinity (X_C) is calculated by dividing the crystallization enthalpy (ΔH_c: obtained from the integral of the curve) by the melting enthalpy of a infinity thick crystal of polyethylene[121–123] (293 J. g^{-1})[122].

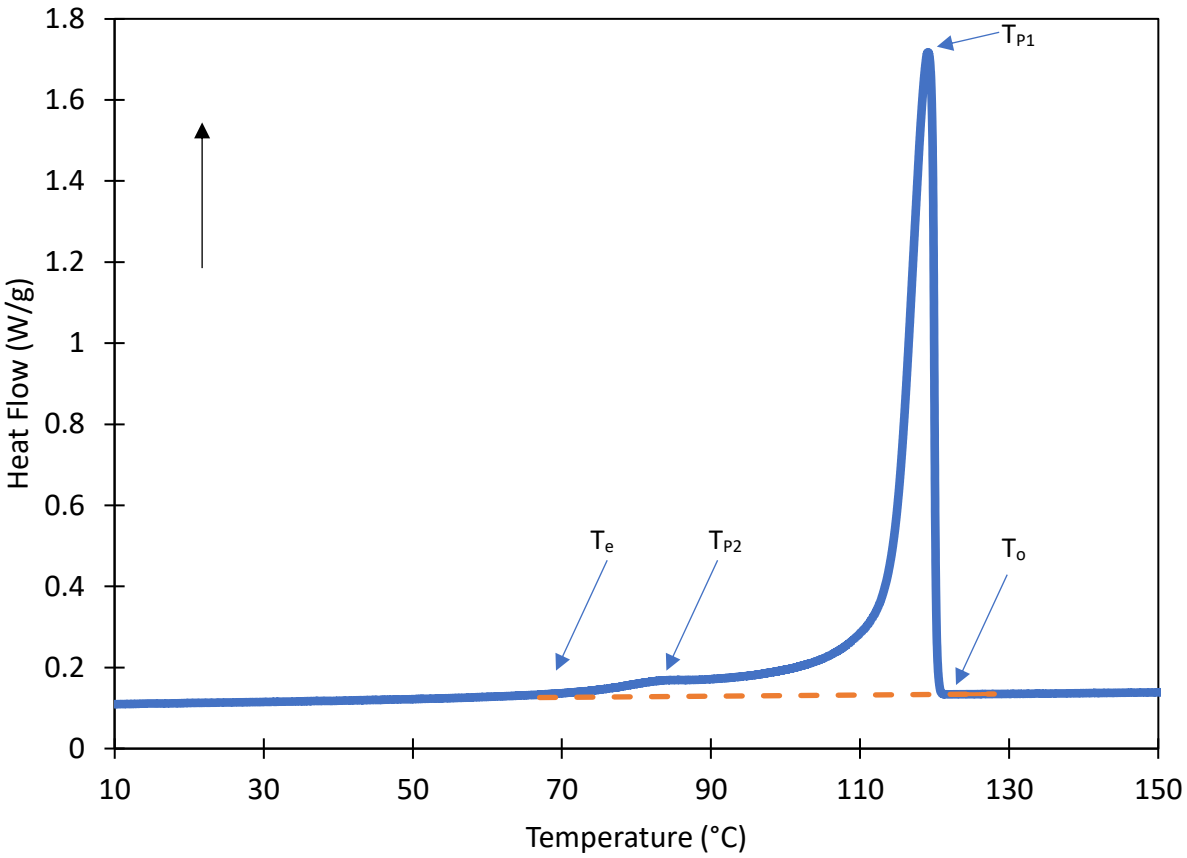

Figure 3.6. Crystallization of HDPE 9 at a rate of 2.5 $^{\circ}{}^{\circ C}/_{min}$ with the baseline shown by the dashed, orange line.

Table 3.3. Non-isothermal crystallization parameters at the rate of 2.5 $^{\circ}C.min^{-1}$

Material	T_0(°C)	T_e (°C)	T_{P1} (°C)	T_{P2} (°C)	X_C (%)
HDPE 3	119.43	50.50	117.17	79.24	61.48
HDPE 4	117.67	44.87	114.70	74.94	53.54
HDPE 5	116.90	42.77	114.13	72.86	50.81
HDPE 6	120.76	36.85	116.94	81.28	67.51
HDPE 7	122.41	38.48	118.36	83.07	72.53
HDPE 8	120.72	41.49	117.66	82.03	69.59
HDPE 9	121.85	56.27	118.77	83.08	71.56

3. 5. 2. Successive self-nucleation and melting

The heating scan of the final melting step in the SSA protocol for HDPE 7 is presented in **Figure 3.7**. Eight distributions consist of multiple Gaussian distributions have been fitted[78] to the SSA curve and shown on **Figure 3.7** (the heating scans for other materials are presented in the supplementary information). The peak temperature and the relative area of the peaks (the area of each resolved peak divided by the summation of the area of all peaks) for all materials are summarized in supplementary information **Table 7.1**.

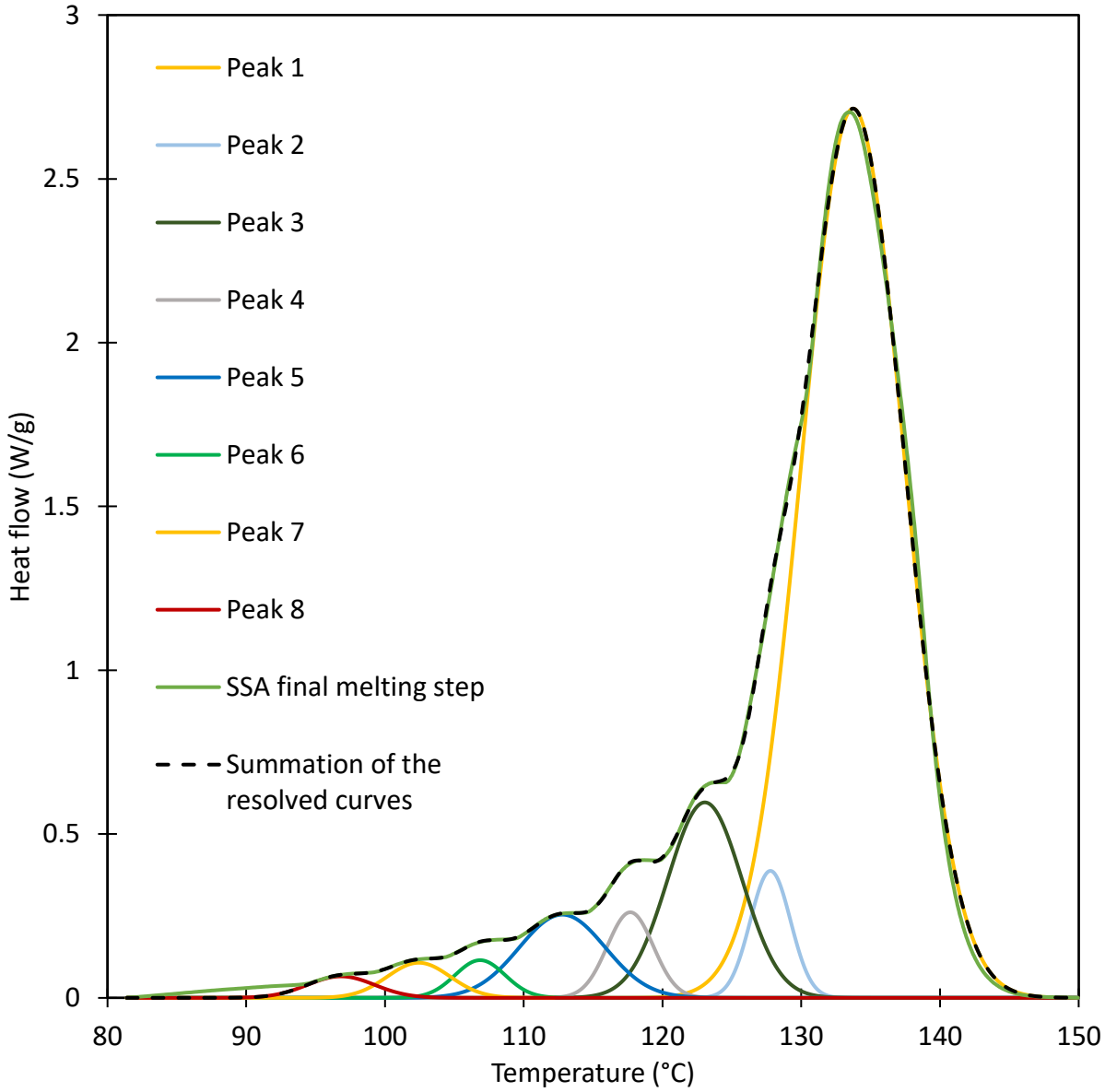

Figure 3.7. The heat flow results of the final melting step in the SSA protocol for HDPE 7

The location and relative area of the peaks in the final melting run of the SSA are two important features[63,64]. The location of each peak in terms of temperature is an indicator of the quality of the crystal or the lamellar thickness: the higher the peak temperature, the better the crystalline quality[63,64]. The second factor is the relative area of the peak showing how much of the overall crystal structure has that particular quality[63,64]. We then present the entire set of SSA results of each material in one value, the average of the lamellar thickness estimated using the modified Gibbs-Thomson equation[62,63,103,111]. There are concerns about using the Gibbs-Thomson equation for lamellar thickness calculation with SSA results[47,48]. However, a qualitative analysis for comparison purposes (as is the case for our study) is well-accepted[62,63,103,111] and validated with direct techniques like transmission electron microscopy and small-angle X-ray scattering[111]. The modified Gibbs-Thomson equation is written as follows[62,63,103,111]:

$$l = \frac{2\sigma T_m^0 \Delta z}{\Delta h (T_m^0 - T_m)} \tag{3.1}$$

Where l is the lamellar thickness, T_m^0 is the equilibrium melting temperature of polyethylene (~414.3 K)[126,127] , T_m is the melting point of each deconvoluted peaks, Δh is the entaply of fusion of C_2H_4 group (8.2 $kJ.mol^{-1}$)[111,128,129], σ is the polyethylene crystal surface energy (5.0 $kJ.mol^{-1}$)[111,128,129], and Δz is the length of C_2H_4 unit in the chain direction (0.254 nm)[127–129].

Using **Eqn. (3.1)**, an average lamellar thickness number is obtained for each peak and then using the relative areas the first ($\bar{l}_1$) moment of the lamellar thickness distributions is calculated (**Table 3.4**). The second ($\bar{l}_2$) and third ($\bar{l}_3$) moments are presented in supplementary information (**Table 7.2**).

Table 3.4. Modified Gibbs-Thomson lamellar thickness first moment for HDPE 3-7 (nm)	
Material	$\bar{l}_1$
HDPE 3	10.28
HDPE 4	7.38
HDPE 5	7.11
HDPE 6	11.19
HDPE 7	14.16

3. 5. 3. Mechanical Properties

The tensile stress at yield, Young's modulus, tensile stress at break, elongation at break, and natural draw ratio (NDR) are presented in **Table 3.5**. Since some specimens broke below a draw ratio of eight, the strain hardening modulus is not reported. We aim to find correlations between MWD and SCBD and these mechanical properties which allow us to rank the materials in terms of ESCR (via NDR). These correlations make optimized design of material possible. The stiffness of the polymer is described by the Young's modulus. The Young's modulus[130,131] and yield stress[131] increase by increasing crystallinity[131] while the stretching ability decreases[130]. Elongation at break is an indicator of the ductility[132].

Table 3.5. Strain hardening test outcome					
Material	Tensile stress at Yield (MPa)	Young's Modulus (MPa)	Tensile stress at Break (MPa)	Elongation at break (%)	NDR %
HDPE 3	7.61	156.5	23.7	665.3	298.6
HDPE 4	5.18	89.4	29.1	579.2	225.0
HDPE 5	3.14	82.3	18.7	519.3	126.3
HDPE 6	8.11	218.2	27.4	636.2	275.6
HDPE 7	10.45	396.5	29.4	783.6	315.0
HDPE 8	8.20	277.9	26.5	660.4	304.0
HDPE 9	9.17	347.8	24.7	834.5	326.8

3. 5. 4. Correlating structure and properties

In order to identify the aspects of molecular structure that determine the properties we used a combination of feature selection[78] and least squares regression analysis considering both linear and logarithmic functions. The best relationship is then identified by the highest R^2 values with the minimum number of independent variables. When a combination of independent variables is required, in addition to the R^2, the probability that the results occurred by chance is evaluated using the F statistic, and a comparison of the fitted coefficients and their errors is performed, with the best combination then reported.

3. 6. Statistical modeling

3. 6. 1. Theoretical background

The molecular structure of polyethylene is commonly described using molecular weight (MW) and short chain branching (SCB) or chemical composition (CC) distributions[6]. The distributions and their features need to be considered in structure-properties relations rather than focusing on the average values, especially in the case of bimodal polyethylene[78,133].

Crystallization of polyethylene is driven by the distribution of ethylene sequence length (ESLD)[6] since comonomers, such as hexene do not typically co-crystalize with ethylene[34,134]. This means that neither SCBD nor MWD, can represent the crystallizability of a polymer[6] on their own. The SCBD obtained experimentally[25] from GPC-IR5 presents the average short chain branching[6] content for chains of molecular weight M. The ESLD represents the weight or number fraction of ethylene sequences in the system with a specific length[6]. In the case of our bimodal polyethylene systems, in which the comonomers are placed on the longer chains at higher content, the use of ESLD to analyze the crystallization behavior is essential[6] since it is possible that longer chains have a lower ethylene sequence length than the shorter chains.

To obtain the ESLD, we used a quantitative model of a unimodal metallocene catalyzed copolymer described in detail elsewhere[6]. This model[6] assumes ideal mixing, which is not exactly the case for polymerization in the loop reactors used to synthesize our materials. However, the

model does provide us with an acceptable approximation of our materials as we will demonstrate later.

Here, we present the relevant parameters and equations of this model[6]. The model is based on two important parameters: the propagation (pp)[6] and ethylene selection probabilities (cp)[6]. The propagation probability defines the chance of a unit adding to the chain, while the ethylene selection probability defines the likelihood that the unit is an ethylene rather than a comonomer (hexene for our study)[6].

The distributions in this model are presented in terms of kinetic chain length (r)[6]. Kinetic chain length is the number of monomeric units (ethylene and hexene for our study) on the chain[135]. The comonomer mole fraction versus kinetic chain length depends only on cp whereas the overall average comonomer mole fraction depends on both cp and pp as follows[6]:

$$\mathrm{F_m(r)} = (1 - \mathrm{cp})\left(1 - \frac{1}{\mathrm{r}}\right) \tag{3.2}$$

$$\overline{\mathrm{F_m}} = \mathrm{pp}(1 - \mathrm{cp}) \tag{3.3}$$

The number average kinetic chain length depends on pp and the weight distribution of kinetic chain length can be written in terms of the number average kinetic chain length as follows[6]:

$$\overline{\mathrm{r_N}} = \frac{1}{1 - \mathrm{pp}} \tag{3.4}$$

$$\mathrm{w(r)} = \frac{\mathrm{r}}{\overline{\mathrm{r_N}}^2}\ \exp\left(-\frac{\mathrm{r}}{\overline{\mathrm{r_N}}}\right) \tag{3.5}$$

The ethylene sequence length distribution depends on both pp and cp[6], in effect a combination of the MWD and the chemical composition distribution:

$$\mathrm{w_{ES}(x)} = \mathrm{x}.(1 - (\mathrm{pp}.\mathrm{cp})^2).(\mathrm{pp}.\mathrm{cp})^{\mathrm{x}-1} \tag{3.6}$$

Where x is the ethylene sequence length. The equations above are for single-metallocene catalyzed polymers[6]. In this study, we are working on bimodal polyethylenes polymerized in the presence of a dual-metallocene catalyst[78]. This means that these materials can be considered as a summation of two single-metallocene catalyzed populations: one of low and another of high

kinetic chain length[78]. Using the weight fraction, we can build the bimodal distributions as follows[21]:

$$\mathrm{d_t(r) = \Sigma m_i d_i(r)} \tag{3.7}$$

Where $d_t(r)$ is an arbitrary weight distribution, $d_i(r)$ is the normalized weight distribution for the *i* component, and m_i is the weight fraction of the *i* component.

3. 6. 2. Extracting cp and pp values

We start from the MWD and SCBD obtained from GPC and GPC-IR5[25]. Both distributions are in terms of molecular weight (M) but at different increments. First, we make the increments the same by interpolating the values of the short chain branching distribution to match the M increments of the MWD.

The MWD from GPC is the logarithmic derivative of the molecular weight versus molecular weight (M)[25]. We need to convert M to kinetic chain length (r) to be able to use the equations described in the theoretical background section. We divided M by 14 (g/mole) so that the number of carbons (N) at each M is achieved:

$$\mathrm{N\,(M) = {M}/{14}} \tag{3.8}$$

Then the number of short chain branches (n_c), number of ethylene sequences (n), the kinetic chain length (r), are given by these equations:

$$\mathrm{n_C(M) = N(M) \times SCB(M) \,/\, 1000} \tag{3.9}$$

$$\mathrm{n\,(M) = n_c(M) + 1} \tag{3.10}$$

$$\mathrm{r = {M}/{28} - 2n_c(M)} \tag{3.11}$$

At this point, **Eqn. (3.11)** is used to convert the ordinal from M to r at each point in the distributions. Now the comonomer mole fraction distribution ($F_m(r)$) is given by[6]:

$$\mathrm{F_m(r) = \frac{n_c(r)}{r}} \tag{3.12}$$

The transformation of SCBD into $F_m(r)$ is presented in **Figure 3.8b**. Two plateaux are observed on the curves, corresponding to the low and high kinetic chain length populations. From these plateaux we can acquire the cp values for each population[6]:

$$(F_m)_{plateau,i} = 1 - cp_i \tag{3.13}$$

In the following, we refer to parameters for the low molecular weight population by the index of L and that of high molecular weight population by H.

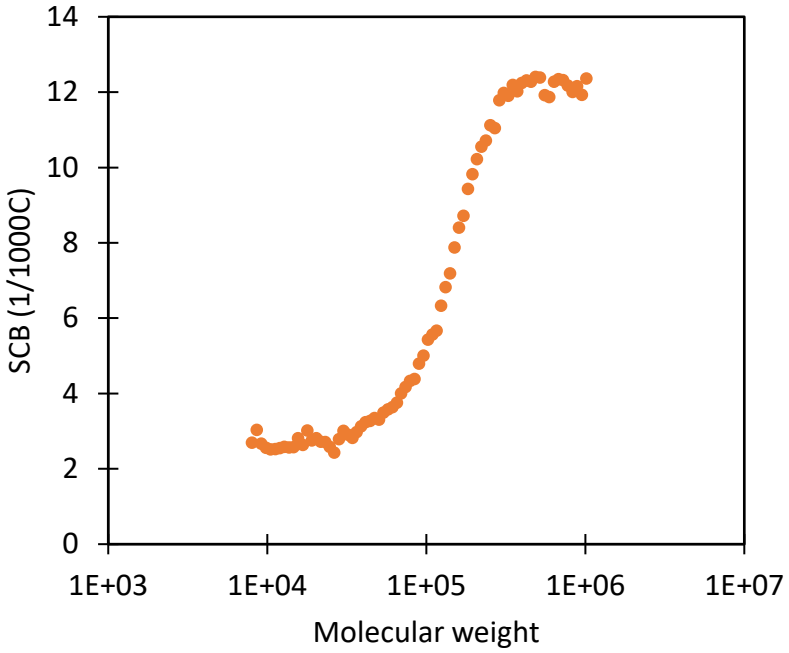

a.

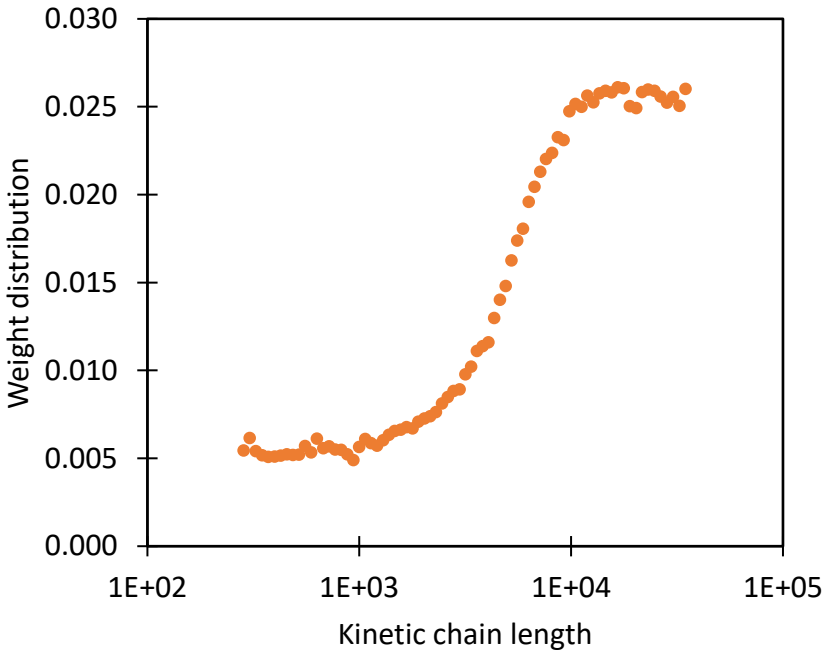

b.

Figure 3.8. Transformation of (a.) experimental SCBD obtained from GPC-IR5[25] into (b) $F_m(r)$

Next, we make use of the experimental MWD to extract the pp values for both populations. Due to the non-ideal mixing in loop reactors, we are unable to obtain a perfect fit, especially of the breadth of the distributions of the low molecular weight population. Therefore, to estimate the pp values, we focus on the location of the two peaks in the kinetic chain length distribution. These two peaks give us an initial estimate of the number average kinetic chain lengths for the two populations which in turn provides the pp values via **Eqn. (3.4)**.

3. 6. 3. Model for Bimodal Polyethylene

We extract the cp and initial guess pp values from the experimental data as explained previously and determine the weight fraction for the low molecular weight population (m_L) by fitting the following equation[21]:

$$w_t(r) = m_L \frac{r}{\overline{r_{N,L}}^2} \exp\left(-\frac{r}{\overline{r_{N,L}}}\right) + m_H \frac{r}{\overline{r_{N,H}}^2} \exp\left(-\frac{r}{\overline{r_{N,H}}}\right) \quad (3.14)$$

$$m_H = 1 - m_L \quad (3.15)$$

Where m_H is the weight fraction for the high molecular weight population. Using the following error function:

$$Error = \sum_r \left(\frac{w_{t,modeling}(r) - w_{t,experiment}(r)}{w_{t,experiment}(r)}\right)^2 \quad (3.16)$$

we optimize m_L using the nonlinear generalized reduced gradient procedure and then loop back to refit the pp values before fitting the final value for m_L. Note that this process is robust with respect to both pp and m_L and insensitive to the initial guess values. We do not incorporate the cp values into this optimization procedure as doing so results in non-unique solutions.

The overall average comonomer mole fraction ($\overline{F_m}$)[6] and the comonomer mole fraction distribution[6] ($F_m(r)$) for the bimodal system, are given by:

$$\overline{\mathrm{F_m}} = \mathrm{m_L\, pp_L}(1 - \mathrm{cp_L}) + \mathrm{m_H\, pp_H}(1 - \mathrm{cp_H}) \quad (3.17)$$

$$\mathrm{F_m(r)} = \frac{\mathrm{m_L\, w_L\,(r)}}{\mathrm{w_t(r)}}(1 - \mathrm{cp_L})\left(1 - \frac{1}{\mathrm{r}}\right) + \frac{\mathrm{m_H\, w_H\,(r)}}{\mathrm{w_t(r)}}(1 - \mathrm{cp_H})\left(1 - \frac{1}{\mathrm{r}}\right) \quad (3.18)$$

For two materials, HDPE 6 and HDPE 7, since the available SCBD is incomplete due to experimental limitations[25], we estimated the SCB of the high molecular weight population from the average short chain branching obtained by NMR (Please see the supplementary information.). The average short chain branching is related to $\overline{F_m}$ as follows. This equation is specific for ethylene-hexene copolymers[50]:

$$\overline{F_m} = m_L \frac{\overline{SCB}_L}{500 - 2\times \overline{SCB}_L} + m_H \frac{\overline{SCB}_H}{500 - 2\times \overline{SCB}_H} \quad (3.19)$$

A comparison of the model and experimental data for HDPE 5 is shown in **Figure 3.9**. Similar plots for the other materials are included in the supporting information and the fitted parameters for all materials are presented in **Table 3.6**.

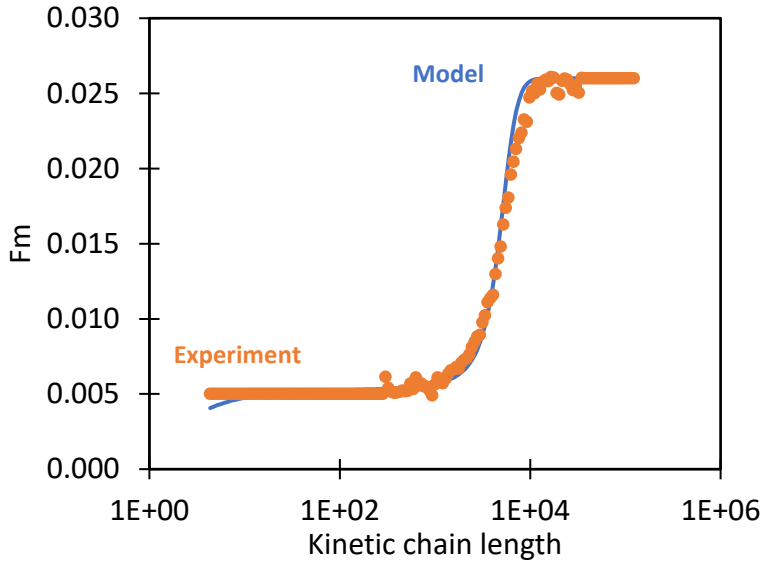

a.

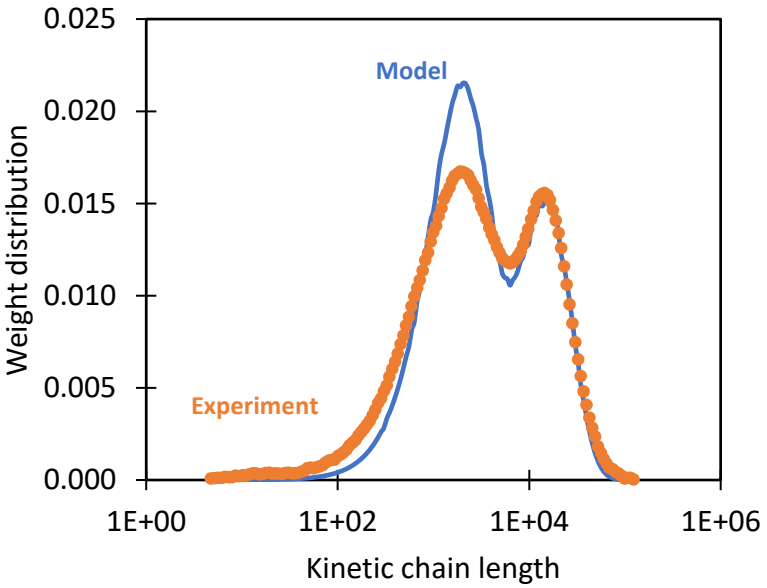

b.

Figure 3.9. Mole fraction (a) and kinetic chain length (b) distributions from modeling and experiment for HDPE 5

Table 3.6. Best fit parameters for molecular structure model.					
Material	w_L	cp_L	cp_H	pp_L	pp_H
HDPE 3	0.63	0.9972	0.98800	0.99903	0.99988
HDPE 4	0.53	0.9955	0.97957	0.99891	0.99985
HDPE 5	0.58	0.9950	0.97400	0.99895	0.99986
HDPE 6	0.41	0.9984	0.99482	0.99704	0.99987
HDPE 7	0.59	0.9987	0.99458	0.99770	0.99990

3. 6. 4. Ethylene sequence length distribution and combined crystallization of high and low molecular weight populations

Assuming that the hexene units do not co-crystalize with the ethylene units in our materials[134,34], then the aspect of molecular structure relevant to crystallization is the ethylene sequence length distribution. Using the optimized model parameters in **Table 3.6**, we can calculate the weight distribution of ethylene sequence lengths ($w_{ES}(x)$) using the following equation[6]:

$$\mathrm{w_{ES}(x) = m_L x.(1-(pp_L.cp_L)^2).(pp_L.cp_L)^{x-1}} + \mathrm{m_H x.(1-(pp_H.cp_H)^2).(pp_H.cp_H)^{x-1}} \quad (3.20)$$

The ethylene sequence distributions are presented in **Figure 3.10**. From the figure, our materials have different ESLD except for HDPE 6 and HDPE 7 which are relatively similar.

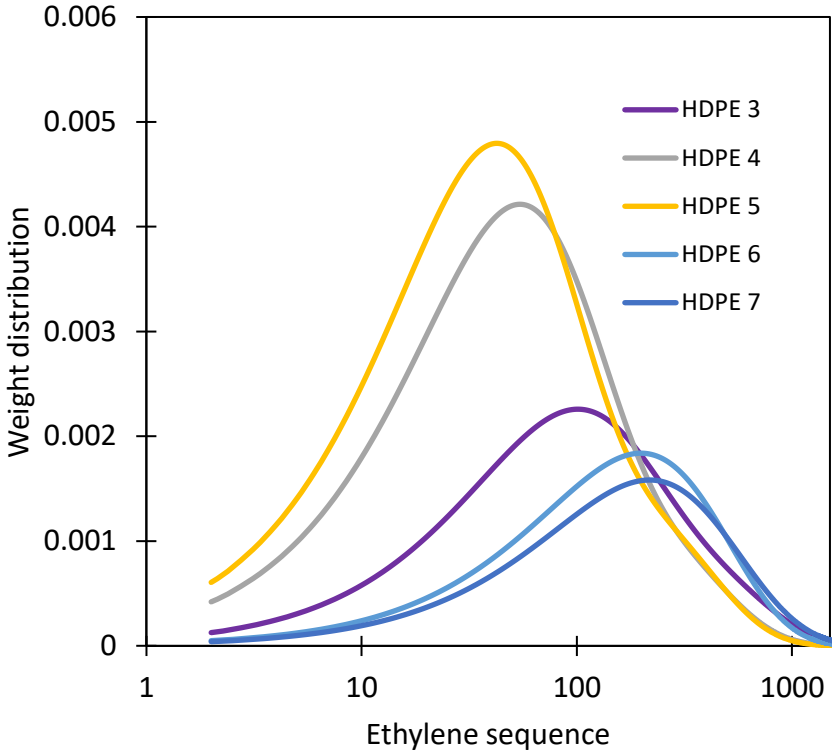

Figure 3.10. Ethylene sequence length distribution for all materials (modelling)

We note that both molecular weight and short chain branching affect $w_{ES}(x)$[6]. The ethylene sequence length and kinetic chain length distributions for HDPE 5 and HDPE 7 are presented in **Figure 3.11**. It is very interesting that although both materials have bimodal kinetic chain length distributions, the ethylene sequence length distributions are not bimodal and rather exhibit tails or shoulders. This is due to the short branches being placed on the longer chains. This emphasizes the importance of consider the ESLD when designing materials for particular crystal morphology[6].

The other interesting feature of **Figure 3.11** is that the high molecular weight population has shorter ethylene sequence lengths for both materials. This is especially obvious for HDPE 5 which has a higher content of short branches. This observation once again hints that ESLD can be very much different from MWD in terms of concluding the effects of sub-populations on the crystallization behavior.

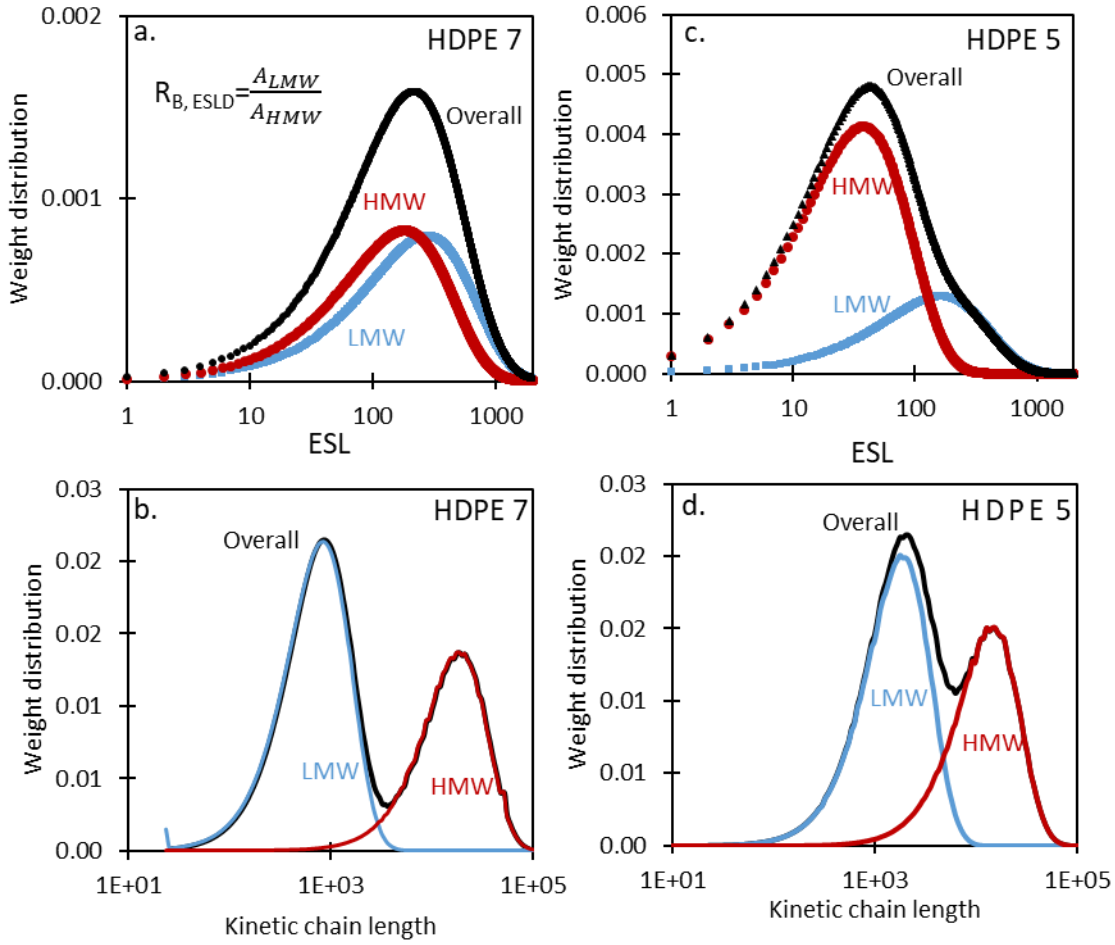

Figure 3.11. ESL (a. HDPE 7 and c. HDPE 5) and kinetic chain length (b. HDPE 7 and d. HDPE 5) distributions (from model). $R_{B,\,ESLD}$ is the bimodal ratio[78] and A_{LMW} and A_{HMW} are peak amplitudes for the low and high molecular weight distributions.

From the ESLD, we extract the bimodal separation ($S_{B,\,ESLD}$)[78], bimodal ratios ($R_{B,\,ESLD}$)[78], and weight average ethylene sequence length ($\overline{ESL_w}$)[6]. The bimodal parameters have been defined previously for molecular weight distribution[78], here we apply the same definition to the ESLD. The results are presented in **Table 3.7**.

Table 3.7. Bimodal separation ($S_{B,\ ESLD}$), bimodal Ratios ($R_{B,\ ESLD}$), and weight average ethylene sequence length			
Material	S_B, ESLD	R_B, ESLD	$\overline{ESL_w}$
HDPE 3	0.46	0.52	393
HDPE 4	0.51	0.31	235
HDPE 5	0.57	0.31	222
HDPE 6	0.06	0.60	402
HDPE 7	0.17	0.96	476

By interpreting the SSA results using the ESLD from the model, we can define a parameter that indicates the probability that the low and high molecular weight populations will exhibit combined crystallization. We begin with the assumption that the short branches are not incorporated into the crystal and thus that crystallization is affected only by the ethylene sequence length distribution. This assumption is consistent with Cao et al.[34] findings for ethylene-hexene copolymer. We also assume that all the ethylene sequence lengths available in the material will be incorporated into the crystalline phase. We acknowledge that, in reality, in our materials, ~30-50 % remains amorphous. However, since the proximity between a particular ethylene sequence and a growing crystal is random throughout the material, we assume that there is no ethylene sequence length dependency of the probability to end up in the crystalline or the amorphous region.

From the ESLD we can calculate the cumulative ethylene sequence distribution (**Figure 3.12**). From **Table 7.1**, we learn that 72% of the crystal structure of HDPE 7 is incorporated in the SSA peak with the highest melting point (peak 1). We assume that this peak is for the thickest lamellar population consisting of the longest ethylene sequences. Therefore, we expect that the longest 72% percent of the ES in **Figure 3.11** created this peak, and the remaining 28% of the ES make up the other 7 peaks (peak 2 through 8). It should be noted that overlap of adjacent SSA peaks introduces error to this approach. As demonstrated in the figure, we can easily extract the ethylene sequence length corresponding to 1-0.72=0.28 giving us the shortest ES involved in the creation of peak 1 from the overall SSA curve. For the case of HDPE 7 and peak 1, the shortest ESL

is 241. We continue this approach by adding sequentially the areas of the other peaks until the shortest ES involved in each combination of peaks is obtained.

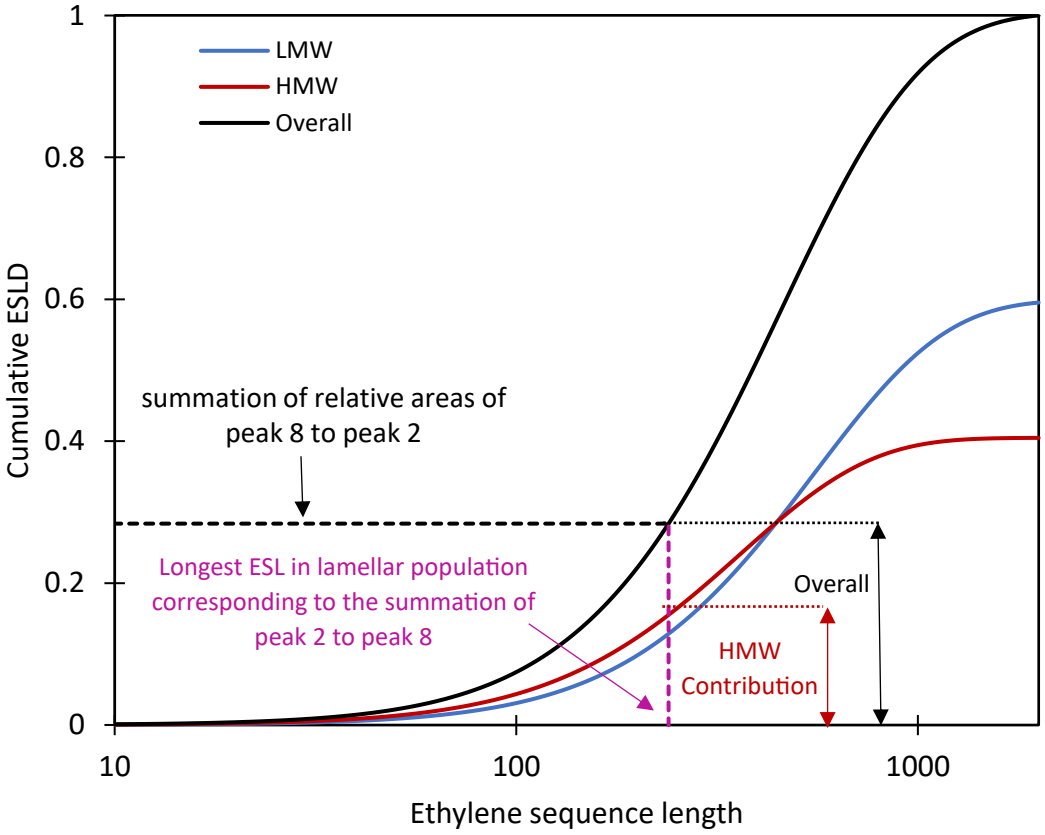

Figure 3.12. Cumulative ESLD for HDPE 7

From **Figure 3.12**, we can also calculate fraction of ethylene sequences corresponding to each SSA crystallization peak comes from each of the low and high molecular weight populations. The results of this analysis are plotted in **Figure 3.13**.

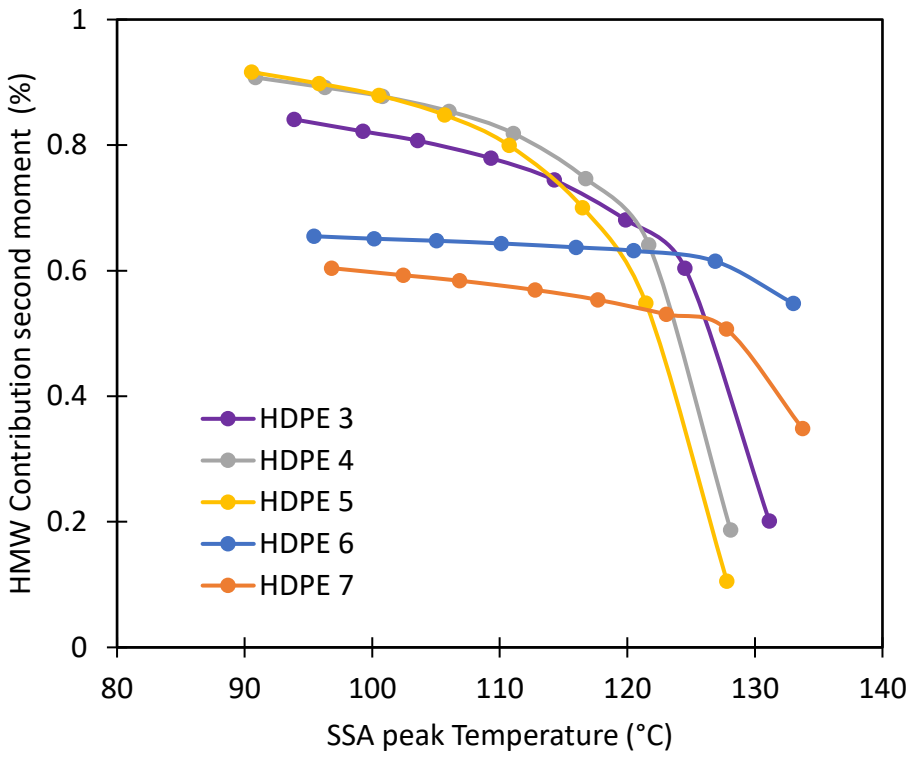

Figure 3.13. Second moment of HMW contribution versus SSA peak temperature

It should be noted that if the HMW contribution is 50%, it shows that both populations contributed equally to the crystalline phase. Any deviation from 50% lower or higher weight fraction, shows that the peak is primarily consisting of crystallized ethylene sequences from the LMW or HMW populations respectively.

The importance of the HMW contribution is that when longer chains are incorporated into a crystal, the probability of tie chains forming increases[41]. Especially when short chain branching is placed on the HMW population, thus interrupting the inclusion of the long chain in a single crystal[41]. We use the second and the third moments of the HMW contribution distribution to evaluate the effect of this phenomenon on the mechanical properties of the materials. These moments are presented in **Table 3.8**. We note that the first moment is simply equal to the weight fraction of the high molecular weight population.

Table 3.8. HMW contribution averages for HDPE 3-7		
Material	Second moment of HMW contribution	Third moment of HMW contribution
HDPE 3	0.53	0.66
HDPE 4	0.66	0.76
HDPE 5	0.69	0.78
HDPE 6	0.59	0.59
HDPE 7	0.42	0.45

3. 7. Discussion

3. 7. 1. Correlations between SSA Results and the molecular features

In this section we investigate the relationship between the SSA results and molecular features. The first moment ($\overline{l_1}$) of the lamellar thickness distribution (nm) correlates with weight average ethylene sequence length ($\overline{ESL_w}$) and $R_{B,\ ESLD}$. The multi-linear regression output is presented in the supplementary information and the relation is:

$$\overline{l_1} = C_1\ R_{B,\ ESLD}{}^{0.42}(\overline{ESL_w})^{0.26} \tag{3.21}$$

Where C_1 is a constant (~ 2.82 nm). The R^2 for this relation is 0.998. This outcome is very interesting since it shows that the SSA behavior is controlled by two important molecular parameters. From this we conclude that SSA experiments are a quick and convenient method to explore structural characteristics of such materials. The other interesting point is that the lamellar thickness correlates with two values that are both extracted from the ESLD showing that this distribution is the key aspect of molecular structure reflected in SSA behavior. **Eqn. (3.21)** shows that longer ethylene sequences and the higher proportion of the longer ethylene sequences, results in thicker lamellae. The controlling parameters for second and third moment of lamellar thickness are presented in the supplementary information.

The second and third moments of HMW contribution to SSA behavior correlated linearly with pp_H (R^2=0.943) and $R_{B,\ ESLD}$ (R^2=0.985) respectively as presented in **Figure 3.14** and **Figure 3.15**. We note that pp_H represents the average molecular weight of the HMW population[6] and

$R_{B,\ ESLD}$ represents the proportion of the ethylene sequences that come from the LMW population[78].

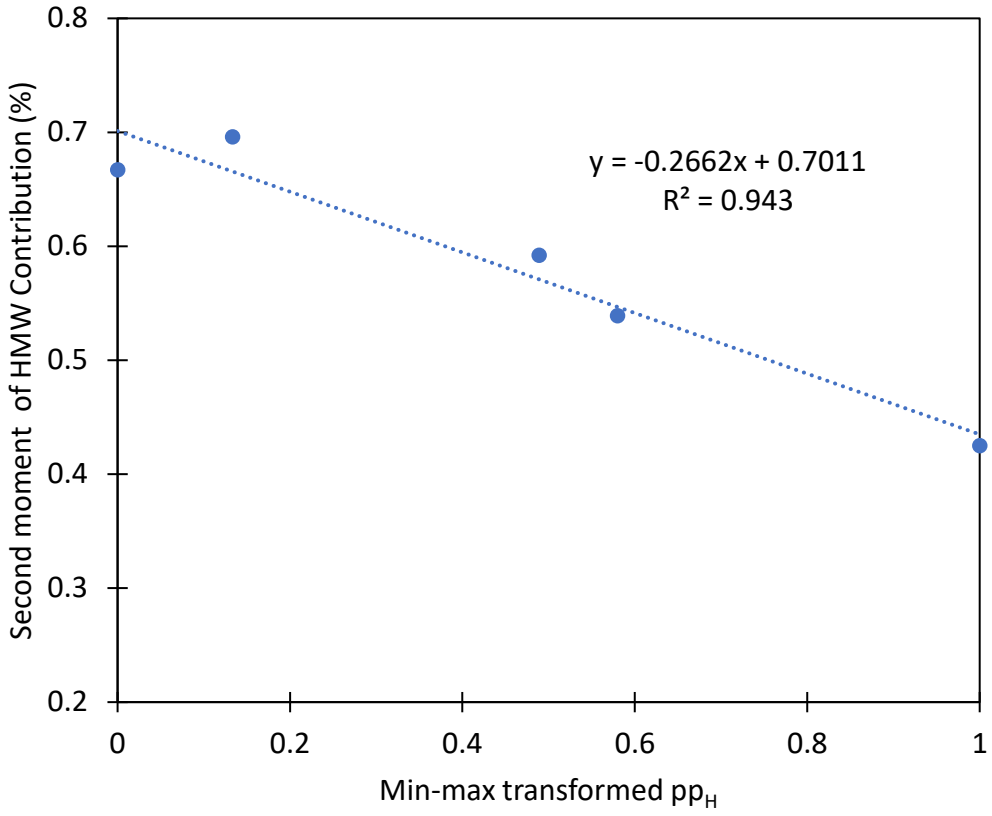

Figure 3.14. Second moment of the HMW contribution to SSA behavior versus propagation probability for the HMW population (pp_H). In order to facilitate plotting, we use a min-max transformation for the x-axis: Min-max transformed pp_H=[pp_H-min(pp_H)]/[max(pp_H)-max(pp_H)]

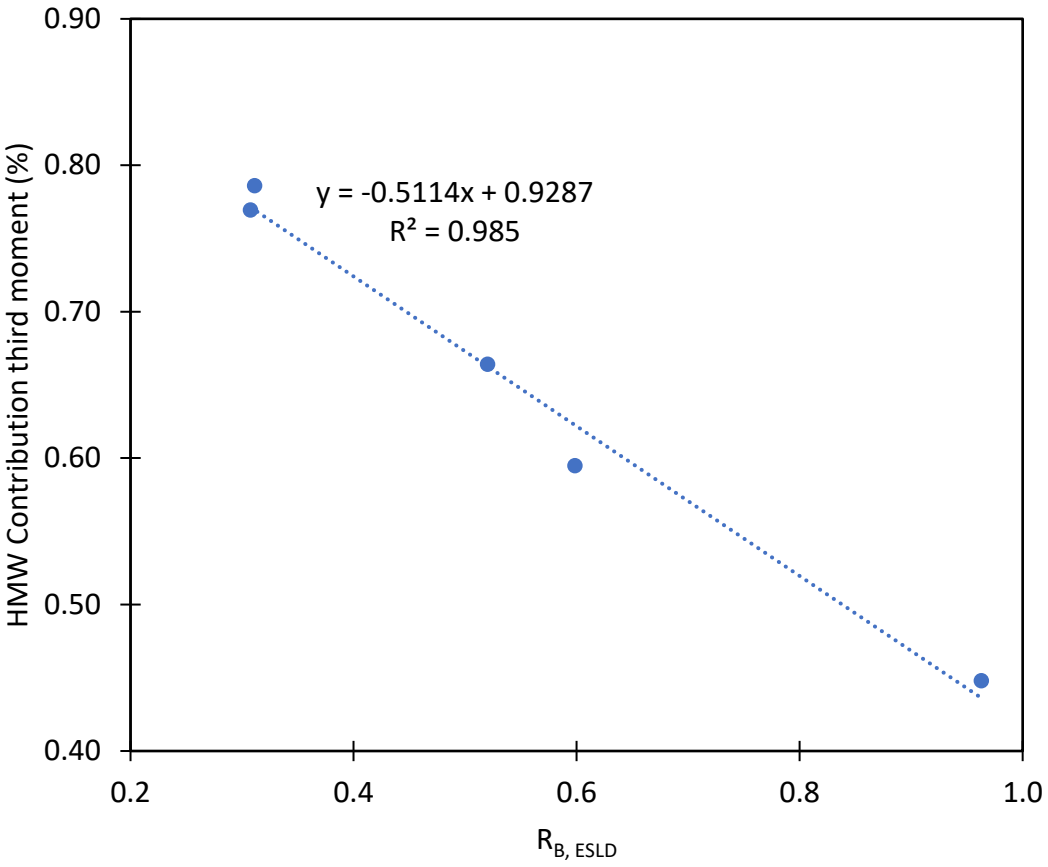

Figure 3.15. Third moment of HMW contribution versus bimodal ratio of ESLD ($R_{B,\ ESLD}$)

3. 7. 2. Correlations between the non-isothermal crystallization properties and molecular features

Here we determine which aspects of molecular structure determine the non-isothermal crystallization behavior in terms of the following parameters: T_{p1}, T_{p2} and X_C. The first peak temperature, T_{p1}, correlates best with $\overline{ESL_w}$ as shown in **Figure 3.16**. This outcome is very interesting since it shows that by a simple and fast DSC run, we can rank between our materials in terms of $\overline{ESL_w}$ using T_{p1}. It also allows us to design a material in terms of $\overline{ESL_w}$ that crystallizes at a particular peak temperature.

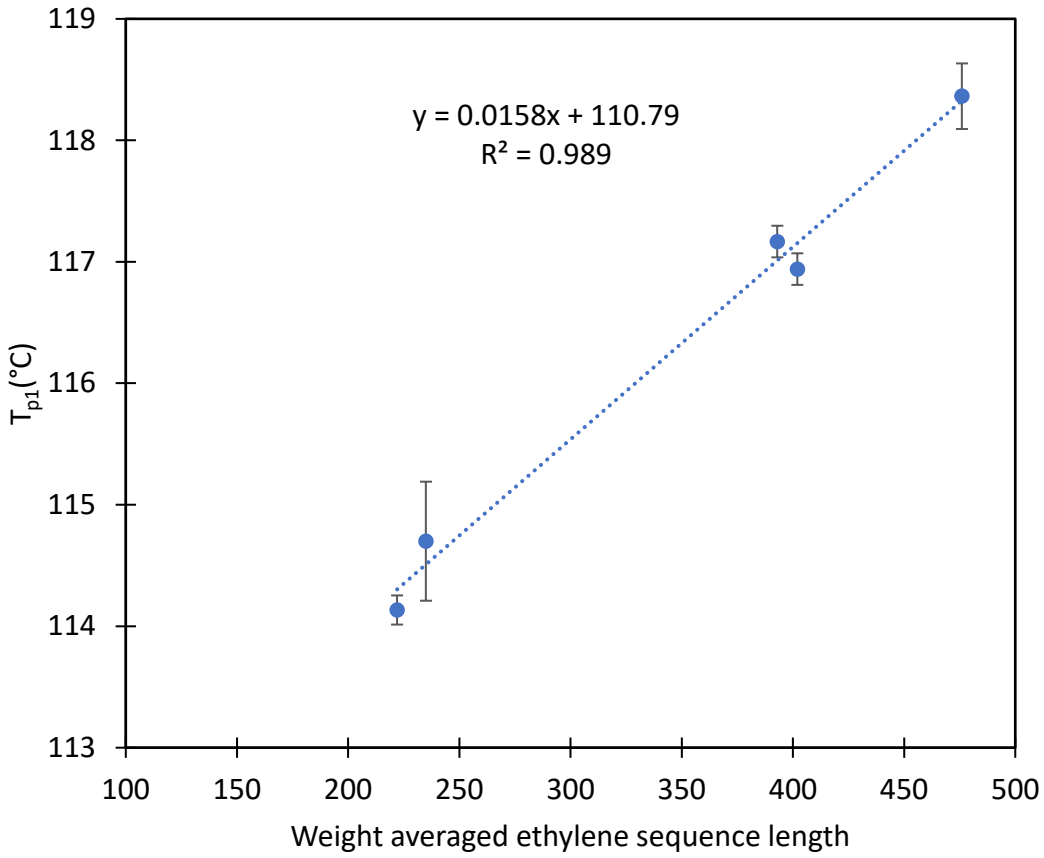

Figure 3.16. T_{P1} versus weight averaged ethylene sequence length

The other crystallization parameters, T_{p2} and X_C both correlate with $\mathrm{SCB}_{\mathrm{ave}}$. The strong correlation between X_C and $\mathrm{SCB}_{\mathrm{ave}}$ (**Figure 3.17**) indicates that the average short chain branching content controls the overall crystallinity of the polymer regardless of the details of the short chain branching distribution.

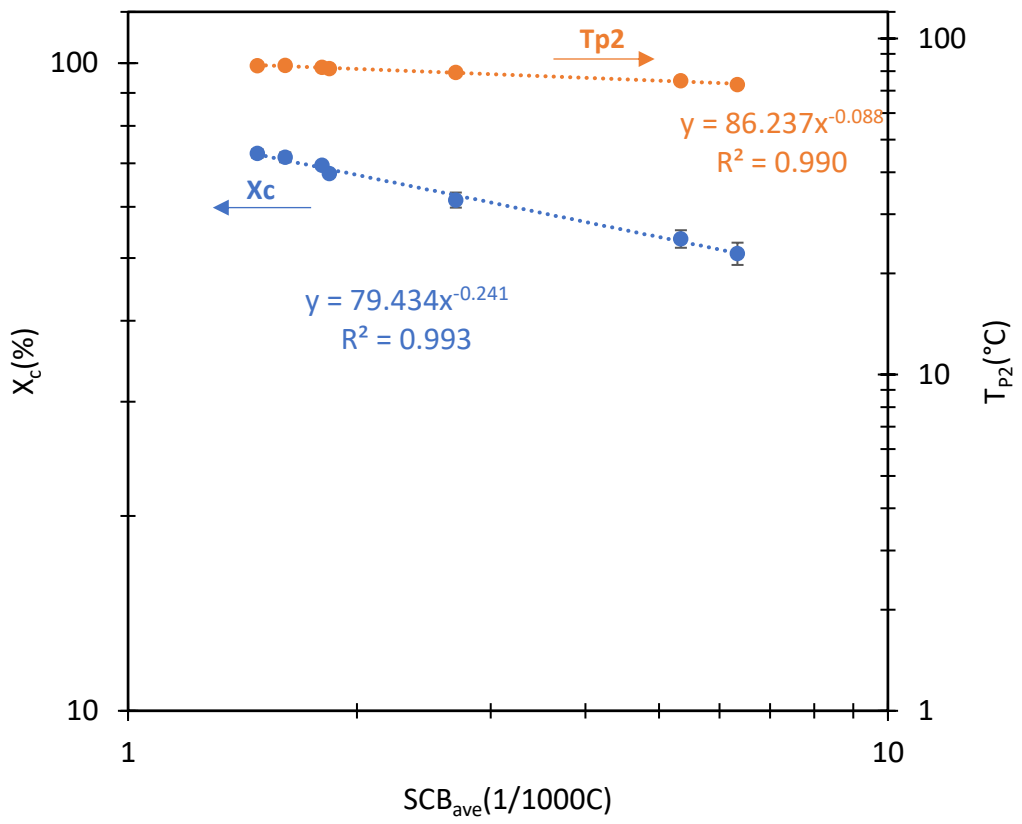

Figure 3.17. X_c and T_{P2} versus SCB_{ave}

The second crystallization peak temperature depends on SCB_{ave} (**Figure 3.17**). This shows that the second peak can be a result of high defect lamellae which form under higher degrees of super-cooling.

3. 7. 3. Correlations between mechanical properties and molecular features

Young's modulus correlates logarithmically and elongation at break correlates linearly with $R_{B,\ ESLD}$ as presented in **Figure 3.18** and **Figure 3.19** respectively.

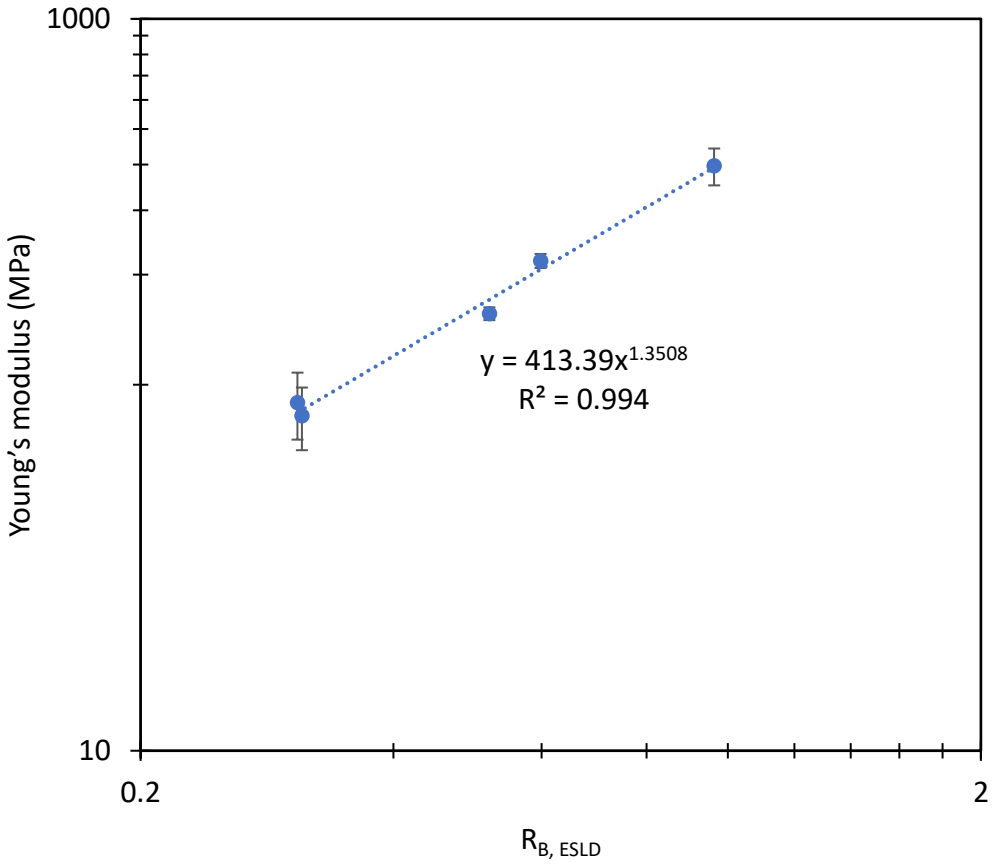

Figure 3.18. Young's modulus versus $R_{B, ESLD}$

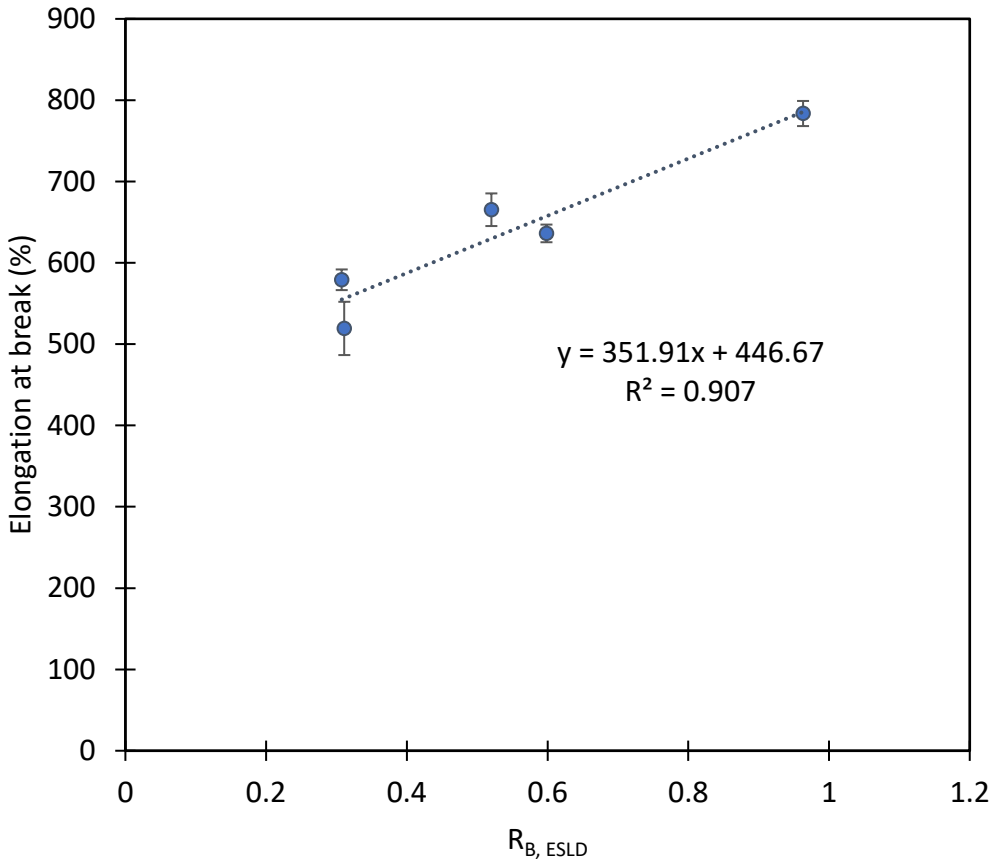

Figure 3.19. Elongation at break (%) versus $R_{B,\ ESLD}$

Tensile stress at yield and NDR correlate linearly with the $\overline{\mathrm{ESL}_w}$ as presented in **Figure 3.20**. The best correlation for NDR, only resulted in an R^2 value of 0.793 while the others were close to 1. It is super interesting that these mechanical properties are correlating with features of ESLD. This means that this distribution, which contains information of both molecular weight and short chain branching distributions[6], is most important to consider in terms of mechanical properties. However, this distribution is not available experimentally and rather requires the combination of experimental MWD and SCBD data with statistical modeling of the structure.

We are using NDR as a proxy of environmental stress crack resistance since we know that the higher the NDR, the lower the ESCR[51]. Therefor, to have materials with a good ESCR, we need to have lower values of $\overline{\mathrm{ESL}_w}$ because a lower average ethylene sequence length allows for the formation of more tie chains. For long chains with shorter ESL, the rest of the chain is available to

be incorporated into other lamellae and thus to form tie chains[7,41]. This correlation between NDR and $\overline{\mathrm{ESL_w}}$ applies for our materials with higher comonomer content on the higher molecular weight population and more studies with a wider range of ESLD is needed. It should be noted that very short ethylene sequences will result in a lower overall crystallinity[41] which will affect all mechanical properties including NDR[7]. We could not find any correlation between tensile stress at break and any molecular parameters.

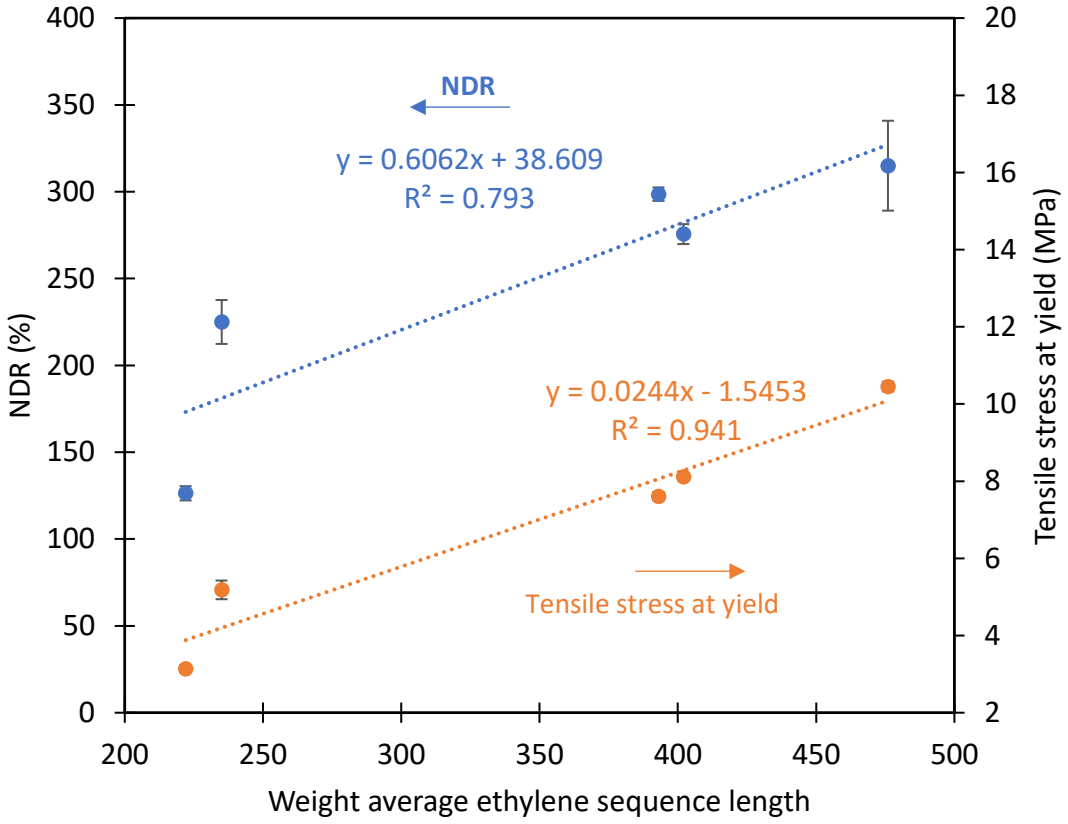

Figure 3.20. NDR and tensile stress at yield versus weight average ethylene sequence length

3. 7. 4. Correlations between the SSA and mechanical results

Next we look at the correlations between the lamellar thickness in the SSA experiments and the HMW contribution to the crystallization with the mechanical properties. The Young's modulus (**Figure 3.21**) and tensile stress at yield (**Figure 3.22**) both increase with increase of the

first moment of lamellar thickness. The correlation is stronger for the Young's modulus with an R^2=0.985.

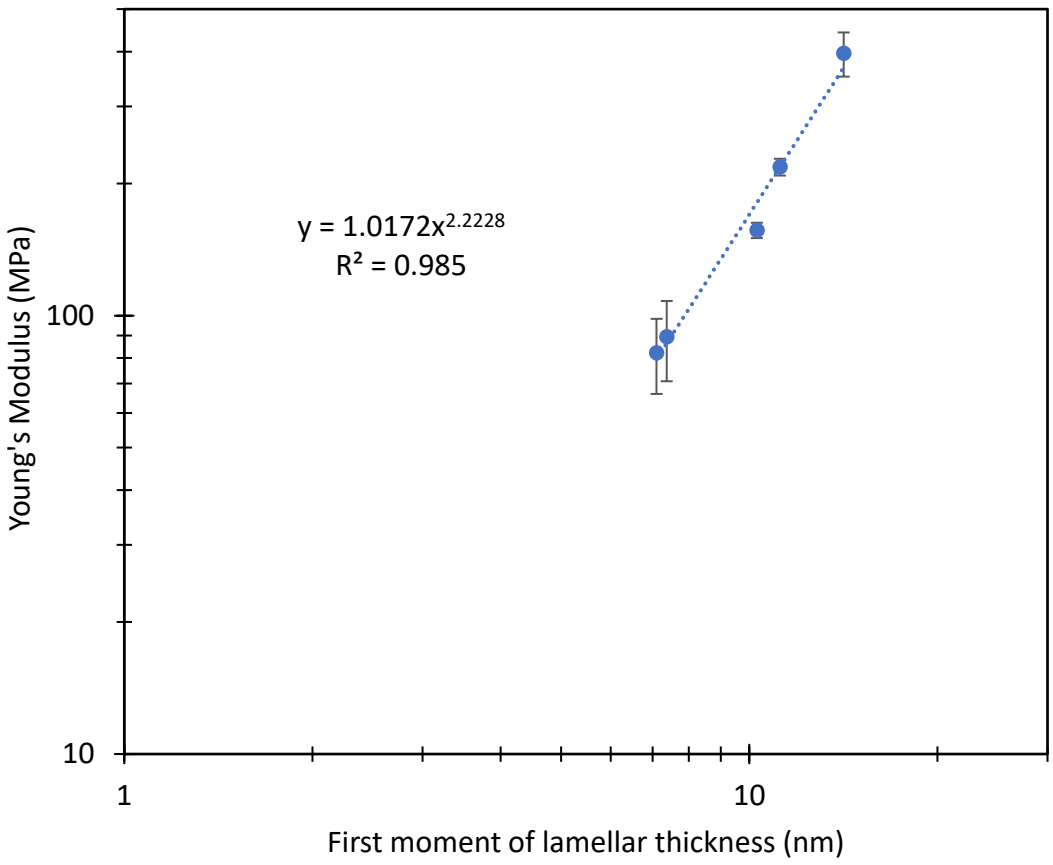

Figure 3.21. Young's modulus versus first moment of lamellar thickness

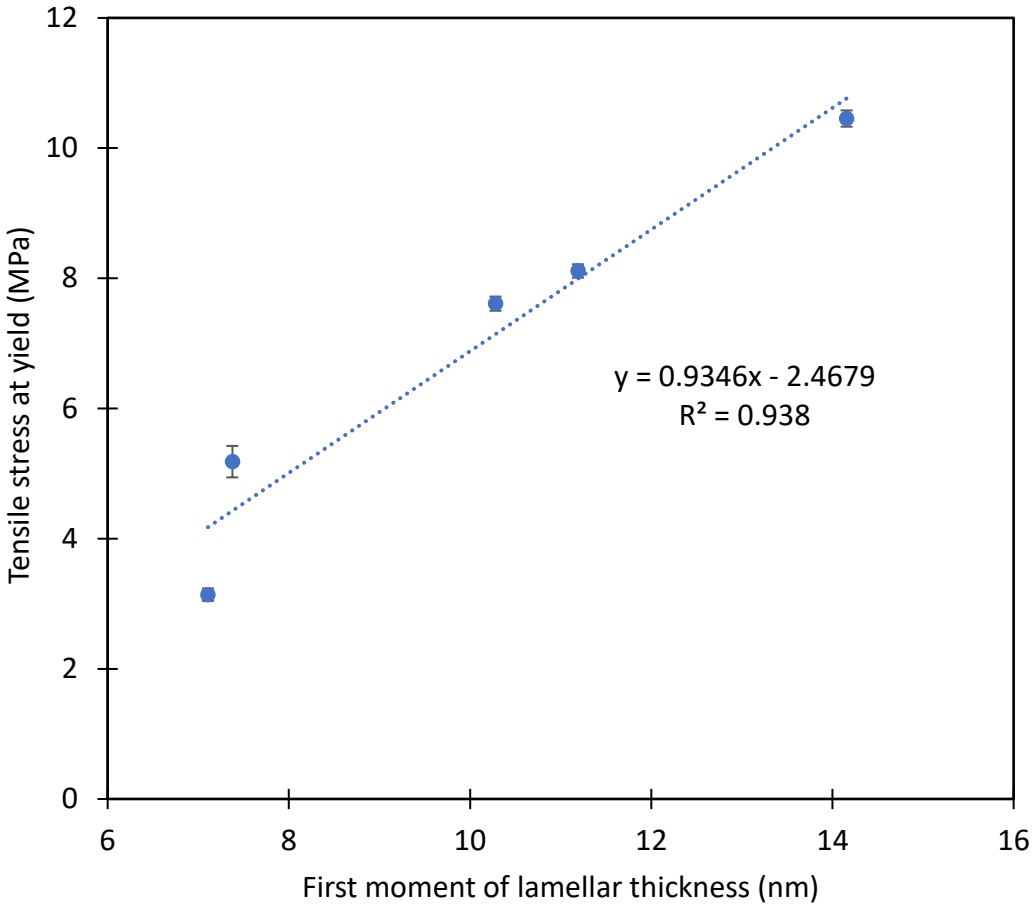

Figure 3.22. Tensile stress at yield versus first moment of lamellar thickness (SSA crystallization)

Interestingly, the elongation at break (**Figure 3.23**) correlates negatively with the second moment of the HMW contribution to the crystallization (R^2=0.981). This is likely due to more tie chains existing with a higher HMW contribution to the crystallization. More tie chains results in a reduction of ductility[132].

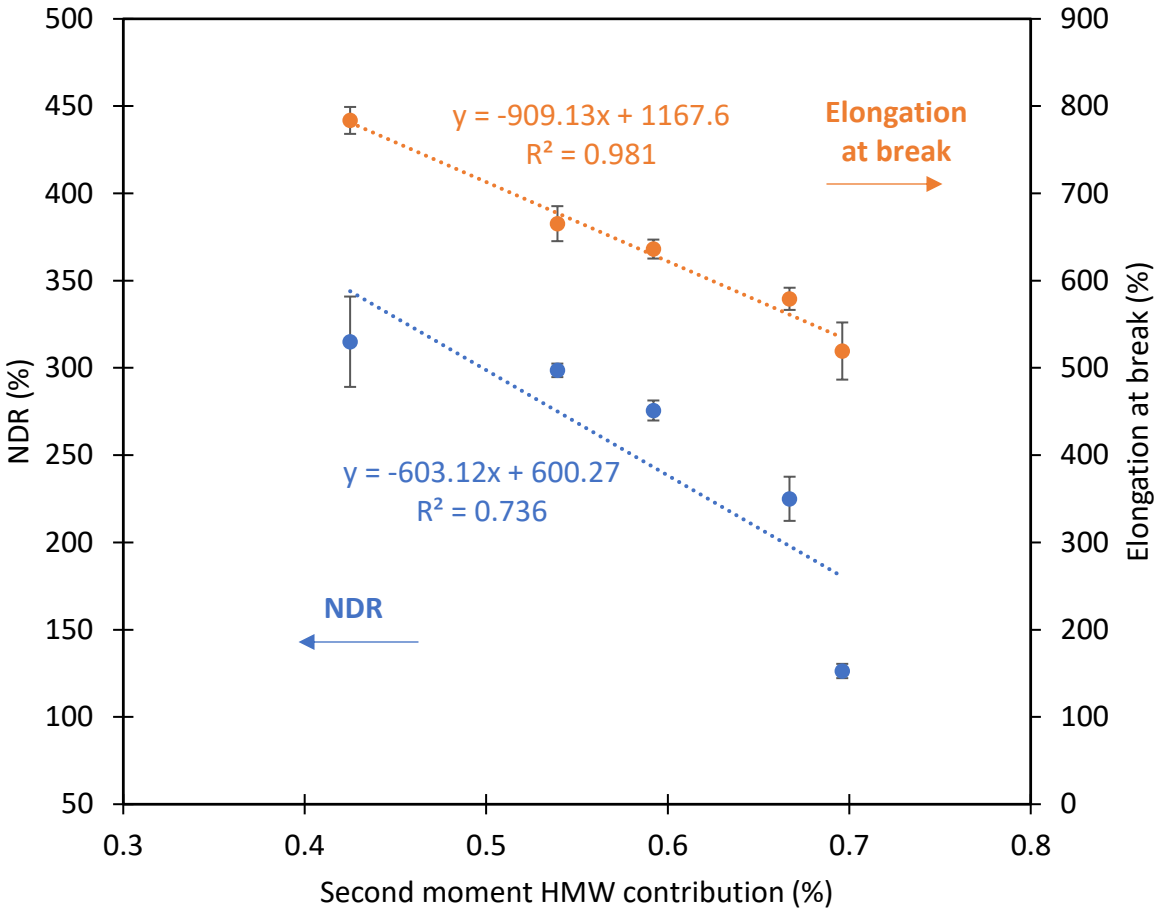

Figure 3.23. NDR and Elongation at break versus second moment of HMW contribution

The best correlation between SSA and NDR is the second moment of HMW contribution to the crystallization (R^2=0.736) as shown in **Figure 3.23**. NDR decreases as the second moment of the HMW contribution increases. As we know, ESCR increases with decreasing NDR[51], we can conclude that a higher high molecular weight contribution to the crystallization indicates a better environmental stress crack resistance. This a result of the presence of more tie chains formation. This is consistent with our observation of a reduction in elongation at break with increasing HMW contribution and its relationship to tie chains.

3. 7. 5. Correlations between the mechanical and non-isothermal crystallization results

The Youngs modulus correlates with the crystallinity (**Figure 3.24**), as expected[130,131]. Tensile stress at yield correlates with T_{P2} (**Figure 3.25**). This indicates that the high defect lamellae, formed at the lower crystallization temperature, likely control the yielding. The best correlation for NDR is with T_{P1} (R^2=0.877). (**Figure 3.26**). This is an interesting result since it shows that we can quickly rank between the materials in terms of NDR using a simple and convenient DSC run. The correlation between elongation at break versus T_{P1} is presented in the supplementary information.

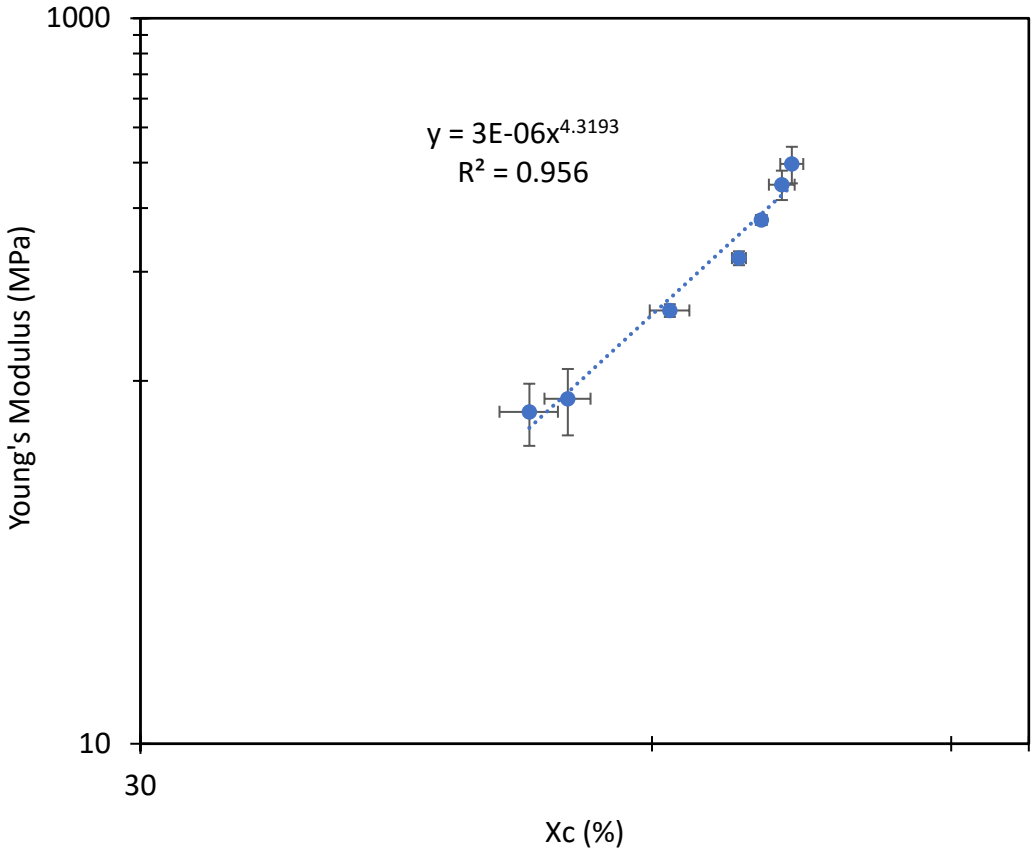

Figure 3.24. Young's Modulus versus X_c

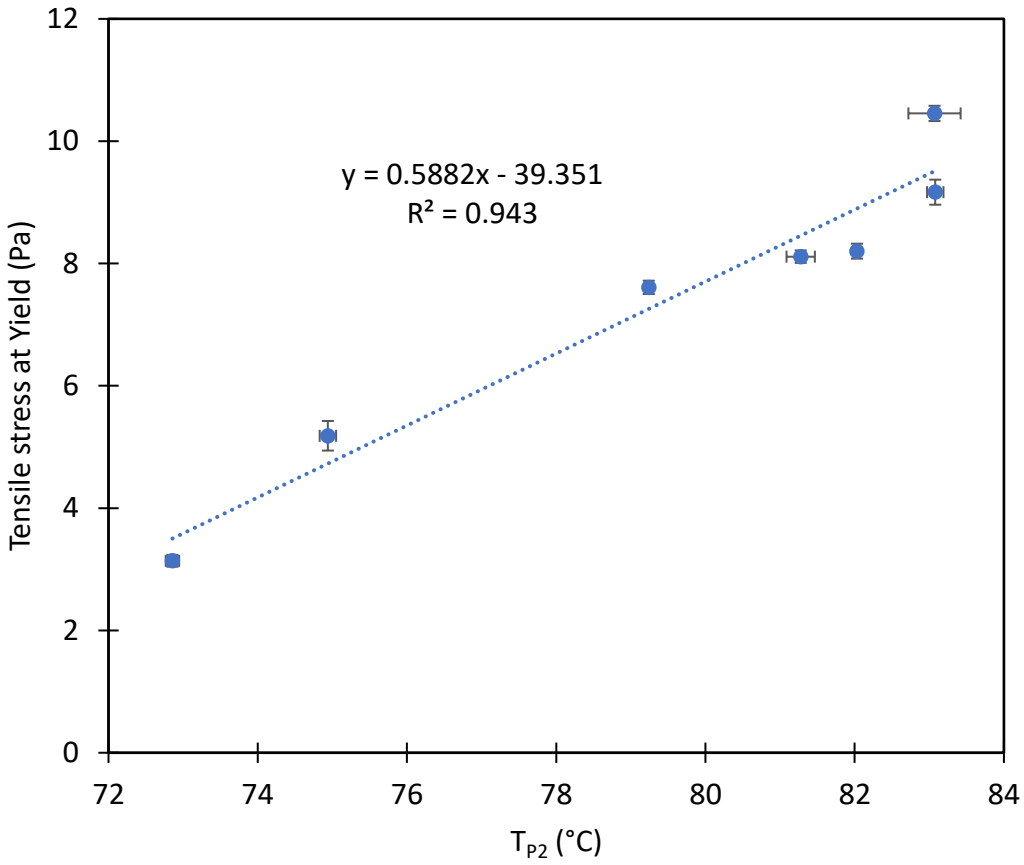

Figure 3.25. Tensile stress at yield versus T_{P2}

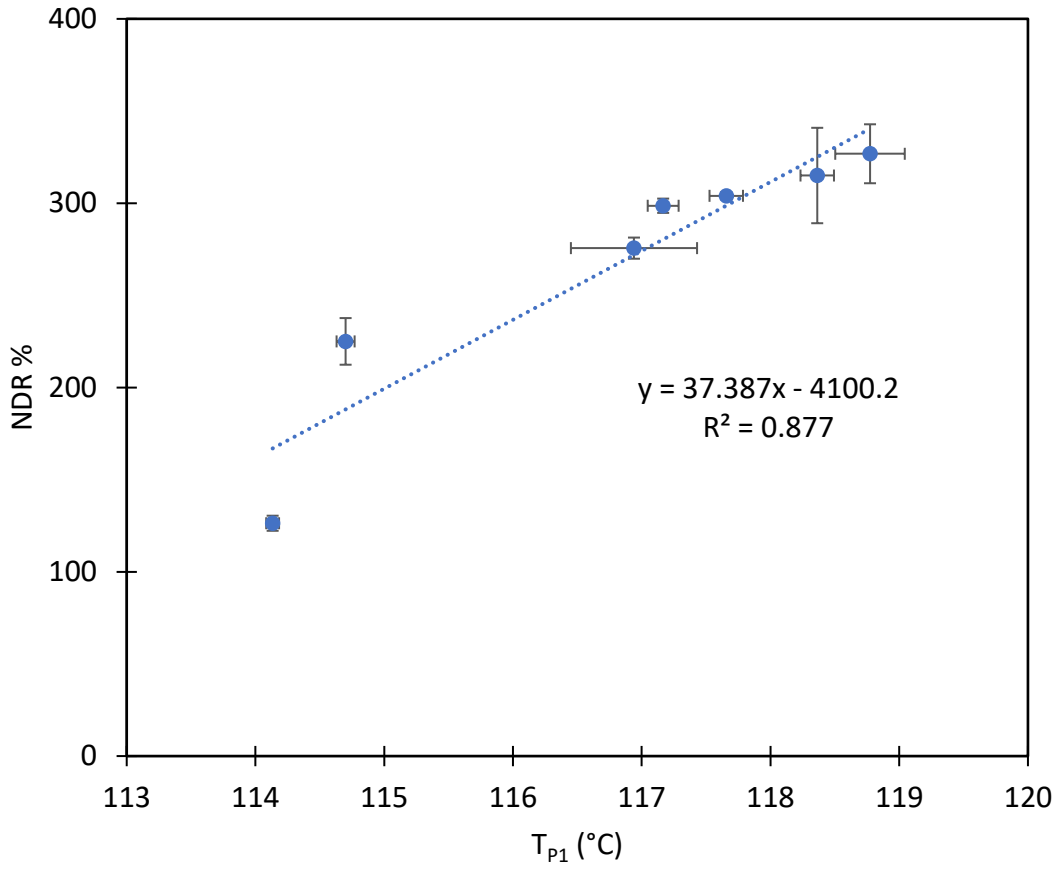

Figure 3.26. NDR versus T_{P1}

Correlations between the SSA results and non-isothermal crystallization results are reported in the supplementary information.

3. 8. Conclusion

We applied statistical modelling[6] to extract the ethylene sequence length distribution of our bimodal materials from experimental measurements of molecular weight and short chains branching distributions. Among the various distributions that describe the structure of bimodal polyethylene, the ethylene sequence length distribution best describes the mechanical properties from the strain hardening test. This means that this distribution, which contains information of both molecular weight and short chain branching distributions[6], is most important to consider in terms of mechanical properties. This is an important approach as the ethylene sequence distribution is not available experimentally.

The NDR correlates with weight averaged ethylene sequence length. We are using natural draw ratio as a proxy of environmental stress crack resistance since we know that the higher the natural draw ratio, the lower the environmental stress crack resistance[51]. Therefor, to have materials with a good environmental stress crack resistance, we need to have lower values of weight averaged ethylene sequence length because a lower average ethylene sequence length allows for the formation of more tie chains. This correlation between natural draw ratio and weight averaged ethylene sequence length applies for our materials with higher comonomer content in the higher molecular weight population and more studies with a wider range of ethylene sequence length distribution would be required to generalize this conclusion. Additionally, the first peak temperature of in the non-isothermal crystallization of our materials correlates with weight averaged ethylene sequence length and thus natural draw ratio. This provides a convenient and quick method to rank developmental materials in terms of environmental stress crack resistance.

The first moment of the lamellar thickness distribution produced in the successive self nucleation annealing and annealing experiments, correlates with weight averaged ethylene sequence length and the bimodal ratio of the ethylene sequence length distribution. From this we conclude that successive self nucleation annealing experiments are a quick and convenient method to explore structural characteristics of such materials. We also showed that the second moment of the contribution of the HMW population to the crystallinity correlates with natural draw ratio showing that the successive self nucleation annealing results can also help us rank between materials in terms of the environmental stress crack resistance.

Finally, it is worth mentioning that the structure analysis in this chapter is based on the assumption that the GPC data acquired is the correct MWD and SCB for the material. This is an assumption for any analysis of this kind[136]. Improvements in the statistical modelling[6] used in this study will improve the analysis outcome. However, our approach can practically estimate ethylene sequence length distribution.

Chapter 4. Wall slip of bimodal polyethylene

This chapter looks into the slip behavior of bimodal polyethylene melts under simple shear. This chapter is based on the following publication: Sattari, M., Inn, Y., & Wood-Adams, P. M. (2022). Wall slip of bimodal polyethylene. Macromolecules, 55(11), 4568-4577.

4. 1. Abstract

Cohesive slip occurs in the flow of linear polyethylene melts over high surface energy walls, changing both the velocity profile and the stress. The slip behavior of bimodal molecular weight distribution (MWD) polymers is different from that of unimodal MWD polymers and is not yet fully understood. Here we study a set of four polyethylenes with a systematic change in MWD making it possible to examine the effect of bimodal molecular weight distribution on the slip behavior. The results show that slip in simple shear occurs over a broad range of stress. Higher short chain content increases slip velocity at all stresses within the transition region before strong slip is fully engaged. At stresses where strong slip is fully engaged, the slip behavior is independent of molecular weight distribution. The stress at which the slip velocity is independent of MWD lowers as the short chain content increases. Disentanglement between the adsorbed and mobile chains is evaluated via the change in friction coefficient with stress. This analysis reveals that the degree of entanglement at the cohesive failure interface drops sharply in the transition region. This region is only accessible in simple shear and not in capillary flows. Finally, melt rupture was observed to occur after the onset of slip for certain conditions.

4. 2. Introduction

The conventional no-slip boundary condition at the wall is known to not always apply to non-Newtonian fluids[3,4,11,67,137]. The occurrence of slip results in various phenomena including a drop in wall shear stress (or pressure drop in a capillary)[3,138], a dependency of the wall shear stress on the gap or diameter at a constant apparent shear rate[3,11] and a discontinuous flow curve for pressure driven capillary data[3,11,74]. Despite a great deal of effort to understand slip behavior of polymer melts, its relation to the structure of polymers is not yet fully understood[3,11,15,139]. A

thorough understanding of the slip behavior of polymers is crucial to correct rheometric data for the effect of slip[3,67] and for the correct design of industrial processes like extrusion[3,4].

Entanglements between polymer chains play a crucial role in the occurrence and characteristics of slip[11]. Polymer chains close to the wall are adsorbed to the surface via multiple chain segments. Other chains within this region may also be strongly entangled with adsorbed chains while not being absorbed on the surface themselves. We refer to these chains as interfacial chains in that they exist in the region between the wall and the bulk flow. They may also be constrained by entanglements with bulk chains. Under flow, the force is transferred between the bulk and interfacial chains through the entanglements[11]. If the flow force applied to the interfacial chains is larger than the adsorption force between the chains and the wall, slip occurs exactly at the polymer/wall interface, and it is called true slip or adhesive failure. If the flow force cannot detach the chains from the wall, the chains act like tethered chains. In this case, slip occurs between the bulk chains and the interfacial chains (cohesive layer) and is called cohesive failure. The slip on low energy and non-adsorbing surfaces is close to true slip, while the slip behavior of entangled polymers over high energy surfaces is dominated by the cohesive slip mechanism[72]. Linear entangled polyethylenes slip even at very small shear stresses[85,140], however, in each system depending upon the instrument precision, there is a stress at which slip is detectable (τ_{C1}). This stress is practically and industrially important because it is the stress where slip starts affecting the macroscopic behavior.

On a passive, high energy surface, there are three slip regimes with different characteristics: (i) weak, (ii) transition and (iii) strong slip. The relaxation mechanisms and the shear stress ranges for the bulk and interfacial chains are different in these regimes which results in a different slip response[72,79,84,140,141]. At low shear stresses, i.e., in the weak slip regime, bulk chains relax via reptation[79,84,141]. The relaxation mechanisms for adsorbed interfacial chains in this regime are constraint release and arm retraction[79,84,141] both happening simultaneously[140,141]. Due to its dynamics, arm retraction has a bigger impact on the short chains than on the long chains[79,141]. In this regime, these two relaxation mechanisms allow for the relaxation of the interfacial chains[79,84,141] and they remain substantially entangled with the bulk chains.[4] Macroscopically, the stress has a power law relation with slip velocity[3,4,72,142,143].

In the transition regime, the dominant relaxation mechanism for both bulk and interfacial chains is convective constraint release (CCR)[79,84,141]. The relaxation time scale for CCR is on the order of $1/\dot{\gamma}$ where $\dot{\gamma}$ is the shear rate[79,81,84,144]. The bulk chains are deformed and relaxed via CCR on the time scale of $1/\dot{\gamma}_{\mathrm{bulk}}$. The interfacial chains are relaxed on the time scale of $1/\dot{\gamma}_{\mathrm{bulk}}$ as the constraints due to the bulk chains are removed and they deform on the time scale $1/\dot{\gamma}_{\mathrm{interfacial}}$. When $\dot{\gamma}_{\mathrm{interfacial}}$ becomes greater than $\dot{\gamma}_{\mathrm{bulk}}$ due to slip, CCR is no longer effective, and the interfacial chains are oriented in the flow direction and disentanglement happens[79,84]. In this regime, entanglement-disentanglement of the bulk and interfacial chains happens[3,4] due to reversible coil to stretch transformation of the interfacial chains[3,4,145]. The slip velocity increases strongly with stress and does not follow a power law[3,4]. While there are some theoretical studies on predicting the slip behavior of materials in the transition region for monodispersed samples under simple shear [79,84,141,146], such an analysis has not been done for polydisperse materials due to the complexity of entanglements between and relaxation of interfacial chains and bulk chains. Generally, polydispersity accelerates the relaxation[79] and thus lowers the stress for the onset of the transition region: short chains disentangle at lower values of stress thus enhancing constraint release relaxation of the long chains resulting in the long chains themselves disentangling at lower stresses.

Under strong slip, beginning at τ_{c2}, the chains relax by contour length fluctuations which is slower for the interfacial chains compared with the bulk chains and the interfacial chains stay oriented in the flow direction[79,141]. In this regime, the interfacial chains are completely and continuously disentangled from the bulk. Once again a power law relation exists between slip velocity and stress, sometimes with a different exponent[3,4,142,143] than that of the weak slip. Under strong slip, the slip velocity is only a function of stress and becomes independent of molecular weight (MW) and MWD[3,4,11,147].

Here we study bimodal polyethylene in which there are two populations of chains in the molecular weight distribution (MWD): high and low molecular weight (MW) populations. Each population will bring some material properties; for example, the high MW population gives mechanical properties while the presence of the short chains leads to better processing

properties[5,68,69,148]. With the advent of new single-reactor production technologies, it is possible to produce bimodal polyethylene with lower capital costs[68,69] opening up many potential applications and the need for thorough characterization of the properties.

There are some slip studies of bimodal polyethylene that have been completed in capillary rheometers, and it is understood that their behavior is different from that of unimodal polyethylene. However, complete understanding of slip behavior of a bimodal MWD polymer is not yet achieved[3,4,15,69,85,85,86]. One challenge has been the lack of access to a set of materials with a systemic change in the MWD. Such materials should be developed in pilot reactors under precise polymerization conditions so that an enough material is produced for the experiments. In this study, we use a set of four metallocene catalyzed bimodal polyethylenes with a systemic change in MWD.

There are limited studies on the slip behavior of bimodal MWD polyethylene primarily coming from our group and that of Hatzikiriakos[15,68,69,85,86]. Ansari et al[15] studied the slip behavior of unimodal and bimodal MWD using a capillary rheometer. They obtained two slip velocity/stress master curves for materials with/without the slip-stick instability. In this work, the authors interpreted the behavior in terms of $\overline{\mathrm{M}}_{\mathrm{w}}$ and $\frac{\overline{\mathrm{M}}_{\mathrm{w}}}{\overline{\mathrm{M}}_{\mathrm{n}}}$ [15]; here we extend this approach to considering aspects of bimodality.

Ebrahimi et al.[85] combined the double reptation model[147] with an entropic molecular fractionation effect to model the slip behavior of unimodal and bimodal polyethylene. Entropic molecular fractionation happens due to the dependency of entropy loss at the polymer-wall interface on chain length. For bimodal materials, their model agreed with capillary experimental data at low shear rates but not at high shear rates due to the shear-induced fractionation effect[85]. Recently, by adding the shear-induced fractionation effect to the model, an agreement between the model and the experimental data is reached for capillary studies[86]. They reported a profound fractionation effect on the slip of bimodal materials while such an effect is minimal for unimodals[85,86]. It should be noted that shear-induced fractionation does not exist under simple shear due to the homogenous shear rate.

Inn[69] compared slip behavior of two unimodal MWD and two bimodal polyethylenes using capillary extrusion under the constant piston speed condition. The MWD curves for all materials were centered around the approximately the same molecular weight. The slip velocities for the bimodal materials before the slip-stick instability were higher than those of the two unimodal materials. The author attributed this behavior to larger content of short chains that are present in the bimodal polymers. We propose two explanations for this effect. First, due to the constraint release caused by the relaxation of the short chains there are a lower number of entanglements restricting the movement of the long chains. In this circumstance, the long chains that are adsorbed on to the wall will disentangle from the bulk chains at a lower stress. The second is related to molecular fractionation in a capillary that has been observed to result in a concentration of the low molecular weight chains close to the wall[69]. Comparing the 3 bimodal materials with each other, they observed an increase in slip velocity before the slip-stick instability with an increase in the short chains content. They also suggested that a larger separation between the low and high molecular weight populations results in higher slip velocity[68].

Sabzevari et al.[3,4] investigated the effect of short chain content on slip using tracer particle velocimetry in shear flow. They compared the slip behavior of binary mixtures of monodispersed polybutadiene: weakly entangled (4.3 Kg/mol) and highly entangled (195.3 Kg/mol) components. The molecular weight between entanglements (M_e) for polybutadiene is 1.65 Kg/mol. They showed that the addition of weekly entangled short chains to a highly entangled monodisperse sample significantly increased slip velocity at the same value of shear stress in their experimental window which happened to be the weak and transition regimes. They also reported that the onset of strong slip shifted to lower stresses with the presence of the short chains[3]. The same group[4] studied the slip behavior of two sets of tridisperse polybutadiene with three components: i) Weakly entangled (set 1)/unentangled chains (Set 2), ii) moderately entangled chains, and iii) highly entangled chains. The difference between the two sets is in the first component where set 1 contains a weakly entangled (M_w=M_e) and set 2 has an unentangled component (M_w<M_e). All tridisperse systems had the same $\bar{M}_w$. Their results showed that the addition of moderate to high contents of weakly entangled chains (set 2) has more effect (compared with set 1) on the slip velocity at high shear rates and causes strong slip to occur at lower stress values. The authors

concluded that unentangled chains are not fully effective in transferring the viscous force, which finally diminishes the slip velocity and makes strong slip happen at higher shear stresses[4].

As discussed in this section, the slip behavior of bimodal polymers is different from that of unimodal while it is not fully understood[3,4,15,69,85,85,86]. The presence of short chains[3,4,15,69] and the distinct separation of the low molecular weight (LMW) and high molecular weight (HMW) populations in bimodal materials[68] is understood to change the slip behavior of materials but there is a lack of a detailed understanding of the effect of bimodality. In particular, there are no slip studies on bimodal polyethylene using simple shear. In this work we will address these issues.

4. 3. Experimental

4. 3. 1. Materials

To study the effect of bimodality on the behavior of a material, it is critical to have a set of bimodal polymers with the below characteristics[68]:

1. A systematic change in the molecular weight distribution.
2. The two populations (short and long chains) are well separated.

A set of four bimodal linear polyethylenes provided by Chevron Phillips Chemical[78] are studied in this work. The absolute molecular weight distributions were obtained by gel permeation chromatography as explained previously[78]. The MWD curves of the four materials are shown in **Figure 4.1**. The two peaks in the MWD are distinctly separated which is a characteristic of metallocene-catalyzed bimodal polyethylene. Additionally, there is a systematic change in the molecular weight distribution of the four materials; as the short chains content increases, the long-chain content decreases.

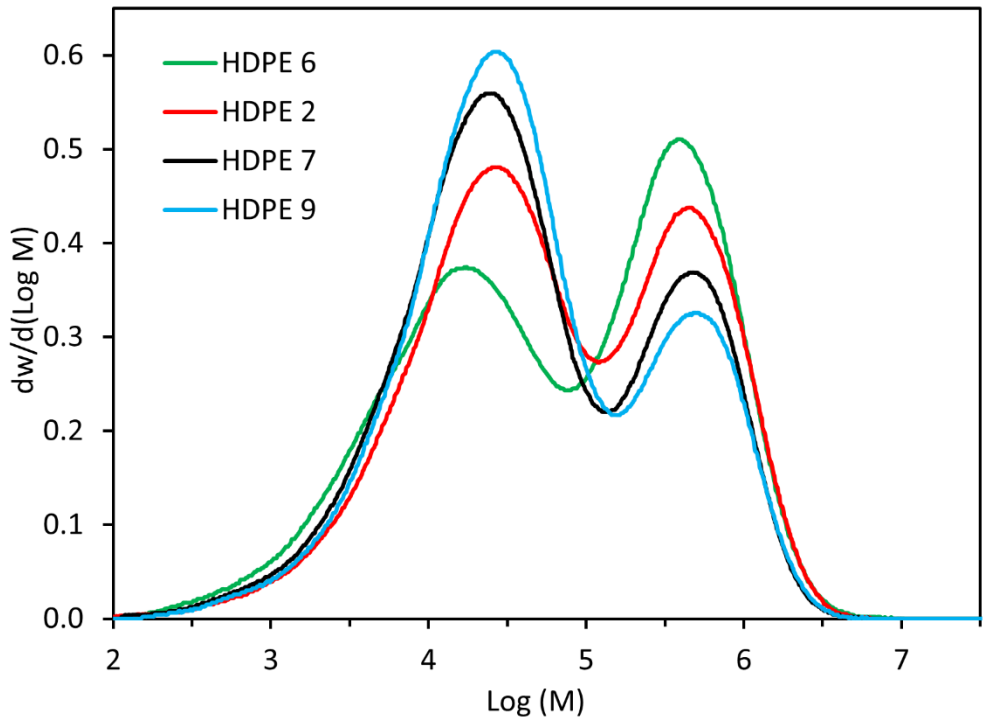

Figure 4.1. The molecular weight distributions of the materials used in this study

The weight and number averaged molecular weights, and the polydispersity indices M_W/Mn, Mz/Mw, and bimodal separation (S_B) and the bimodal ratio (R_B) for the four materials of this study are summarized in **Table 4.1**. The two populations in the MWD have been resolved using the approach described previously[78]. The weight, number and Z averaged MW, and weight fraction of each population are presented in **Table 4.2**.

We use the bimodal separation (S_B) and the bimodal ratio (R_B) to describe the bimodality characteristics of our samples as described previously[78]. The variable S_B is defined as the distance between the means of the two distributions and R_B, is the ratio of the amplitude of the peak of the HMW to that of the LMW:

$$S_B = \frac{\log \bar{M}_{p,H} - \log \bar{M}_{p,L}}{2(\sigma_{p,H} - \sigma_{p,L})} \quad (4.1)$$

$$R_B = \frac{A_{p,H}}{A_{p,L}} \tag{4.2}$$

where $\bar{M}_{p,H}$ and $\bar{M}_{p,L}$ are MW peak values, $\sigma_{p,H}$ and $\sigma_{p,L}$ are the standard deviation from the average, and $A_{p,H}$ and $A_{p,L}$ are the amplitudes for the high and low molecular populations, respectively.

Table 4.1. Characteristics of the MWDs[78]

Sample	$\bar{M}_w(kg/mol)$	$\bar{M}_w/\bar{M}_n$	$\bar{M}_z/\bar{M}_w$	S_B	R_B
HDPE 6	283.2	32.8	3.7	0.73	1.43
HDPE 2	266.1	24.0	3.75	0.75	0.96
HDPE 7	211.0	22.2	4.3	0.85	0.70
HDPE 9	202.0	18.6	4.6	0.86	0.58

Table 4.2. Characteristics of the resolved populations of the materials in **Table 4.3**[78].

		Weight Fraction	$\bar{M}_n$ **(kg/mol)**	$\bar{M}_w$ **(kg/mol)**	$\bar{M}_z$ **(kg/mol)**
Low molecular weight population	HDPE 6	0.57	6.3	66.6	725.3
	HDPE 2	0.66	8.2	67.3	569.2
	HDPE 7	0.71	9.0	53.4	357.5
	HDPE 9	0.74	10.5	54.1	293.1
High molecular weight population	HDPE 6	0.43	374.9	738.8	1,441.1
	HDPE 2	0.34	370.1	682.0	1,220.2
	HDPE 7	0.29	453.9	787.4	1,357.3
	HDPE 9	0.26	474.6	829.5	1,422.6

4. 3. 2. Sliding Plate Rheometer

The sliding plate rheometer (SPR) is an apparatus to study the rheological and slip behavior of polymers during simple shear flow. There is a moving plate mounted on the bearing and back support and a stationary plate. The gap between the two plates (h) is adjustable. The sample is placed between the plates, and the shear stress transducer measures the shear stress [12]. There are two Teflon sidebars on the moving plate that prevent secondary flow[149]. The details of the rheometer are described previously[12].

During the slip test (start-up of simple shear) of polyethylene in SPR, three major phenomena can happen[12]: simple shear, adhesive or cohesive failure (slip), and melt rupture. At high shear rates and strains, polyethylene goes through a catastrophic and non-uniform cohesive failure that happens throughout the material which is called melt rupture. Once the material ruptures, the stress plateau ends and the stress goes toward zero. In this study, our focus is on what happens before the melt rupture.

The velocity profile and the relation between the true and nominal shear rates in the cases of simple shear, and simple shear with cohesive failure are presented in **Figure 4.2**. If there is no slip in the system, the nominal shear rate ($\dot{\gamma}_n(\tau)$=moving plate velocity (V_p) divided by the gap (h)) is equal to the true shear rate ($\dot{\gamma}(\tau)$) (**Figure 4.2a**). However, the presence of slip (**Figure 4.2b**), lowers the true shear rate as compared to the apparent shear rate[12].

In SPR tests, the slip velocity is the same on both the stationary and the moving plate if they are made of the same material and surface roughness as is the case for our rheometer[12,71]. At a constant temperature, pressure and shear stress, the slip velocity (v_s) is calculated as follows[12,150]:

$$v_s(\tau) = \frac{h}{2}\left(\dot{\gamma}_n(\tau) - \dot{\gamma}(\tau)\right) \tag{4.3}$$

In this equation, $\dot{\gamma}_n(\tau)$ is the nominal shear rate, $\dot{\gamma}(\tau)$ is true shear rate corresponding to the no-slip condition at the same stress. The no-slip condition can be obtained from small-amplitude oscillatory shear (SAOS) results assuming the Cox-Mertz rule[3,4,12,68].

The three main advantages of SPR compared to other methods are: 1) In the SPR, the transition regime is detectable while in capillary rheometers this part of the curve is missed due to slip-stick instability[12]. 2) The flow in the SPR is simple shear while in capillary methods it is not: the velocity profile is not linear and strain rate varies with location. 3) The control of surface characteristics and experimental factors like pressure is possible in the SPR[71].

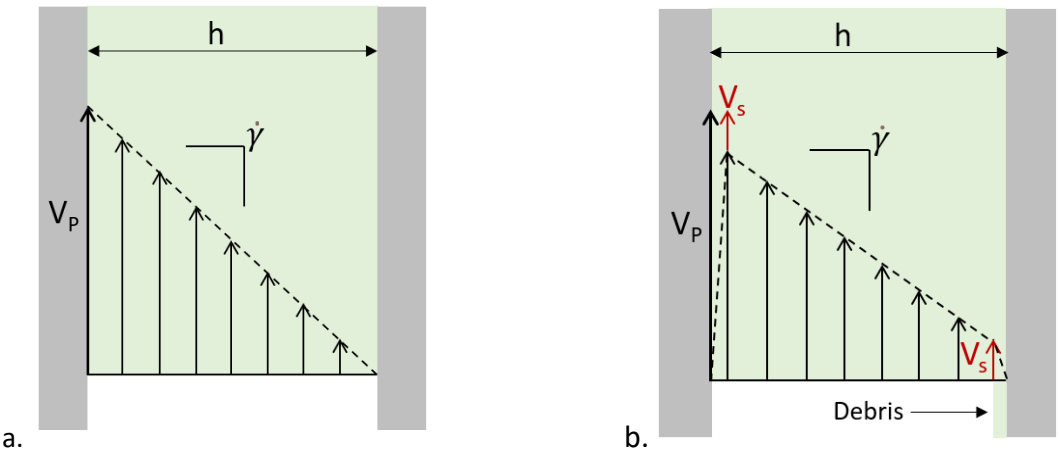

$$\dot{\gamma}_n \equiv \frac{V_p}{h} = \dot{\gamma} \qquad \dot{\gamma}_n \equiv \frac{V_p}{h} = \dot{\gamma} + \frac{2V_s}{h}$$

Figure 4.2. Velocity profiles in the SPR. a. Simple shear, b. Simple shear with cohesive slip. $\dot{\gamma}_n$ is nominal shear rate, h is the gap and V_s is the slip velocity. The sketch is not to scale. Inspired by[12].

4. 3. 3. Sample preparation and Sliding Plate Rheometer tests

The samples for small-amplitude oscillatory shear (SAOS) tests were compression molded at a temperature of $190℃$ for 5 minutes under a pressure of 50 MPa. The SAOS tests were conducted using Anton-Paar's MC502 rheometer with a plate-plate geometry of 25 mm diameter at a 1 mm gap. The small-amplitude oscillatory shear (SAOS) tests at 190 °C over the frequency range of 0.01-500 rad/s are described previously[78]. The cubic spline method is applied to interpolate between the SAOS data points.

For SPR tests, rectangular specimens are compression molded at 190 °C under 50 MPa of pressure for 5 minutes. The SPR tests have been conducted at 190 °C and the gap between the stationary and moving plate is 1 mm. Once the sample is loaded, and the targeted temperature is reached in the oven an additional 10 minutes is allowed to ensure isothermal equilibrium within the sample. The stress transducer was calibrated before each test at the targeted temperature. SPR tests were conducted at various moving plate velocities. After each test is conducted, the stationary and moving plate are removed from the rheometer and cleaned. The plates are first

cleaned using an oven cleaner for 10 minutes and then rinsed with water. After that, to ensure all the polymer chains are removed, the surface of the plates is cleaned with a torch (flame temperature 2054 °C, BernzomaticÂ® 14.1 oz MAP-ProÂ® hand torch) three times. Then the plates are washed again with oven cleaner for another 20 minutes and finally the oven cleaner is removed my rinsing multiple times with water.

Plate speeds (i.e., nominal shear rates) were selected for each material such that specific states of stress were experienced in order to capture the interesting features of the slip velocity versus shear stress curve for the four materials. Tests at each nominal shear rate were repeated at least five times and the averaged value of stress is reported to ensure data reliability. For each repeat a fresh specimen was used. Results are reported with error bars representing standard error.

The surface energies are measured using Dataphysics OCA20 (software and microscope) with the Owens, Wendt, Rabel and Kaelble (OWRK) method[151]. In this method, it is assumed that the total surface energy (γ_t) of a substance comes from two independent interactions: polar (γ_p) and dispersive (γ_d)[152,153]. The governing equation in OWRK method is as follows[152,153]:

$$\frac{(1+cos(\theta))\gamma^l}{2\sqrt{\gamma_d{}^l}} = \sqrt{\gamma_p{}^s}.\sqrt{\frac{\gamma_p{}^l}{\gamma_d{}^l}} + \sqrt{\gamma_d{}^s} \qquad (4.4)$$

where γ^l is the liquid surface tension, γ^s s the liquid surface energy and θ is the contact angle. The liquid properties are known and the two unknown values ($\gamma_p{}^s$ and $\gamma_d{}^s$) are obtained from the slope and the intersection of linear fitting of $\frac{(1+cos(\theta))\gamma^l}{2\sqrt{\gamma_d{}^l}}$ versus $\sqrt{\frac{\gamma_p{}^l}{\gamma_d{}^l}}$ [152,153]. Drops (two microlitre) of diiodomethane, ethylene glycol, water and formamide are placed via syringe onto the substrate and the contact angle is measured with a camera and determined by the software. Each liquid is repeated at least three times using different droplets and the average contact angle for each liquid is then used to infer the substrate surface energy.

4. 4. Results and discussions

The linear viscoelastic studies of these materials have been previously published[78]. Examples of the output of an SPR test is a shear stress transient curve as shown in **Figure 4.3**. The shear stress in the presence of the slip at the various nominal shear rates is the averaged value of the plateau of the shear transient curve. We note that the shape of the transient depends on nominal shear rate. In the case of 2.5 (s^{-1}), there is a nonlinear stress overshoot on the transient curve.

The overshoot and slow decline to steady state are due to the non-linear viscoelastic response and also slip, both of which are time dependant. Nonlinear viscoelasticity in this case is related to orientation of the chains[154]. Clearly, the time-dependent slip development can also contribute to the shear stress transient [12,155].

We have used the standardized residuals technique as described previously[156] to detect the plateau region. The standardized residual is defined as follows:

$$r_i = \frac{e_i}{\sqrt{\sigma^2}} = \frac{e_i}{\sqrt{\frac{1}{n-1}\sum_{i=1}^{i=n}(e_i-\bar{e})^2}} \tag{4.5}$$

where σ is the standard deviation, n is the number of points (shear stress values), e_i is the real residual[156] which is the difference between data point i and the average of the data points from n=1 (long time end of the plateau) to n=i. By plotting the standardized residuals versus time and moving from longer times towards shorter times, the first monotonic increase or decrease in the standardized residual curve identifies the start of the plateau (**Figure 4.3c**).

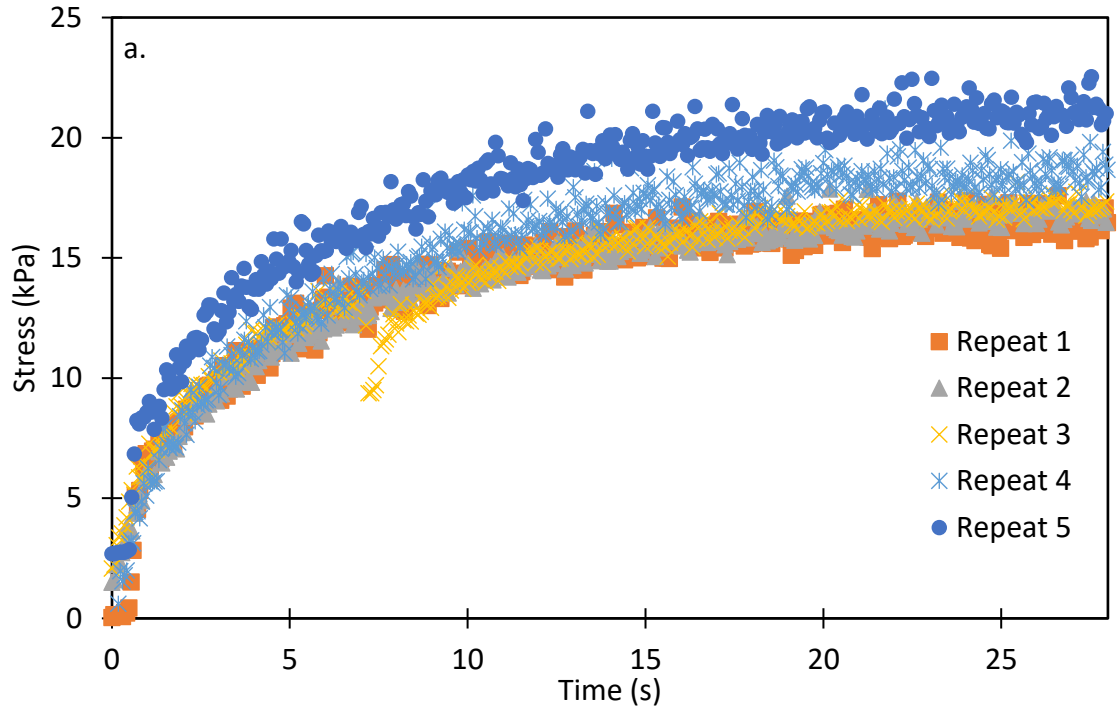
a.
Stress (kPa)
Time (s)
0
5
10
15
20
25
Repeat 1
Repeat 2
Repeat 3
Repeat 4
Repeat 5

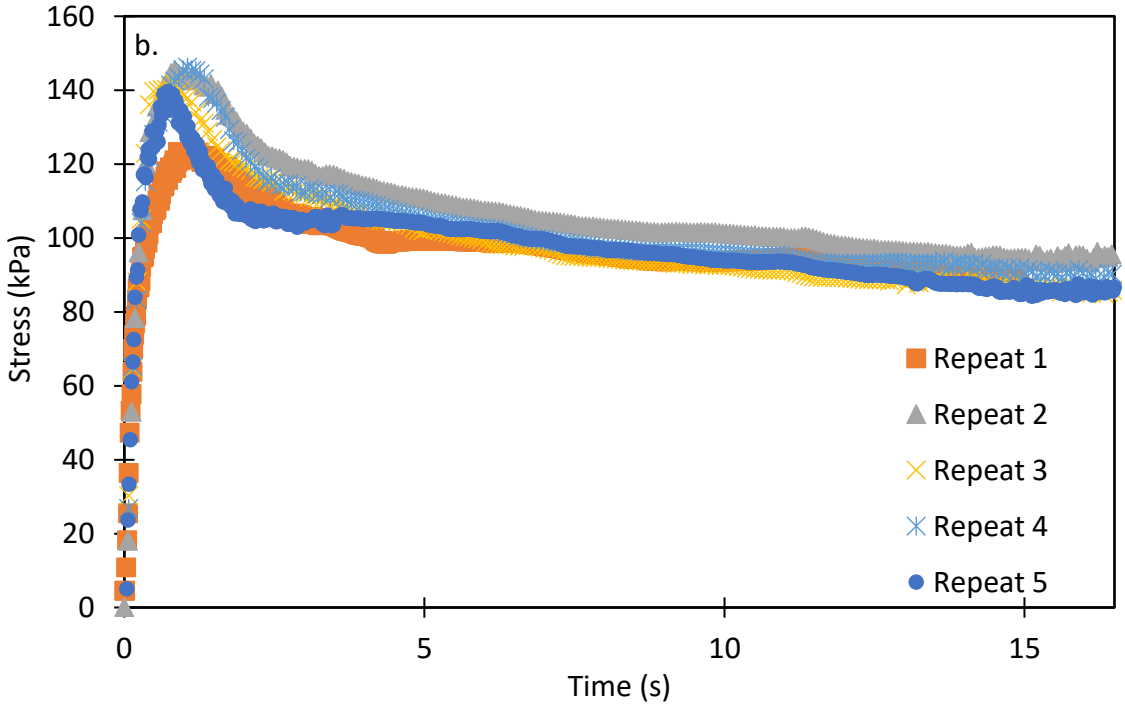
b.
Stress (kPa)
Time (s)
0
20
40
60
80
100
120
140
160
5
10
15
Repeat 1
Repeat 2
Repeat 3
Repeat 4
Repeat 5

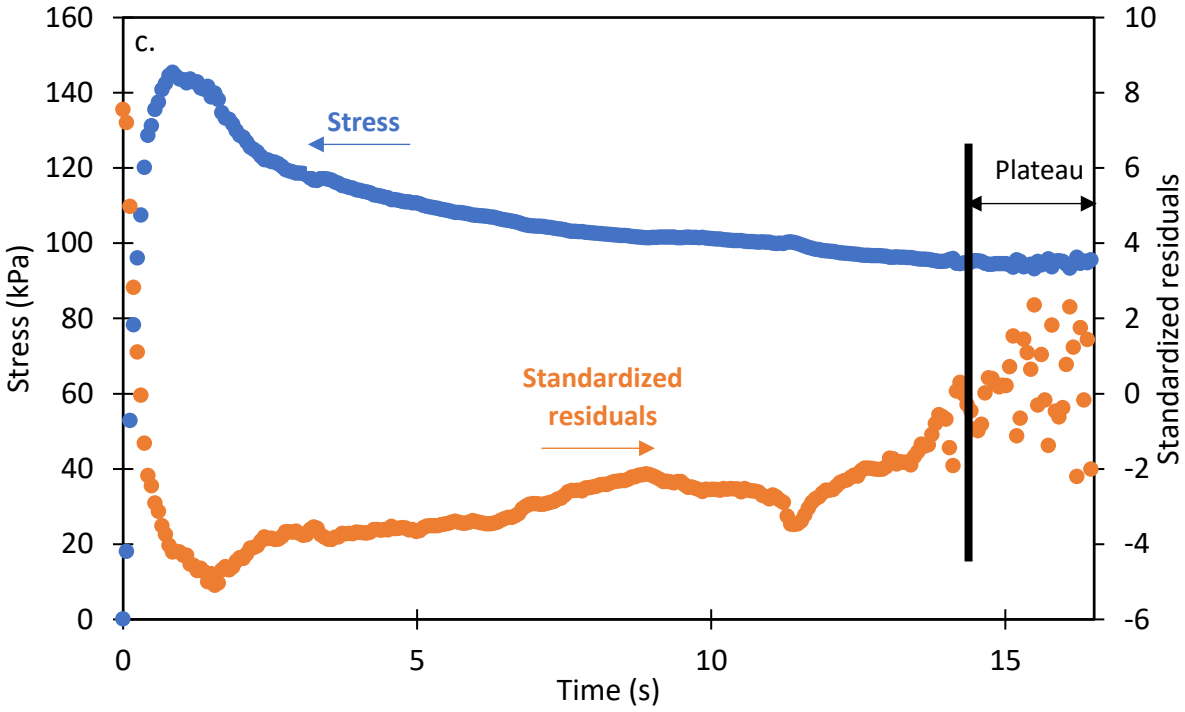

Figure 4.3. Shear stress transient curves for HDPE 6 at 190 °C, at a. 0.05 s^{-1} , b. 2.5 s^{-1} and c. showing the standardized residuals of one curve at 2.5 s^{-1}. The solid black line indicates the plateau region identified from the residuals.

The shear stress in the absence of slip is obtained from small amplitude oscillatory shear (SAOS) tests assuming the Cox-Merz rule. Obtaining the shear stress versus true shear rate from SAOS data is now well accepted in the literature and differences with the SPR results are interpreted as being due to slip [3,4,12,68,157]. The stress in the presence of slip (SPR results) and in the absence of slip (SAOS results) are put together for the four materials in **Figure 4.4**.

It can be seen from **Figure 4.4** that, for all the materials, there is a noticeable difference between the stresses in the presence/absence of slip over a wide range of nominal shear rate. This difference starts at a relatively low value of nominal shear rate. This shows that slip is present at a wide range of stress for the four bimodal polyethylene materials used in this study. Note that the observation of debris on the plate is additional evidence for the presence of slip (**Figure 4.5**).

The experimental shear stress window is not always the same for different materials. The onset of slip shifts to lower stress as the short chain content increases in our samples. The upper

limit for the experimental window is dictated by melt rupture which occurs at higher stresses. For the HDPE 7 and HDPE 9 which have the highest short chain content (**Figure 4.1**), it is not possible to extend the curves toward higher nominal shear rates as we did for HDPE 6 and HDPE 2 due to melt rupture.

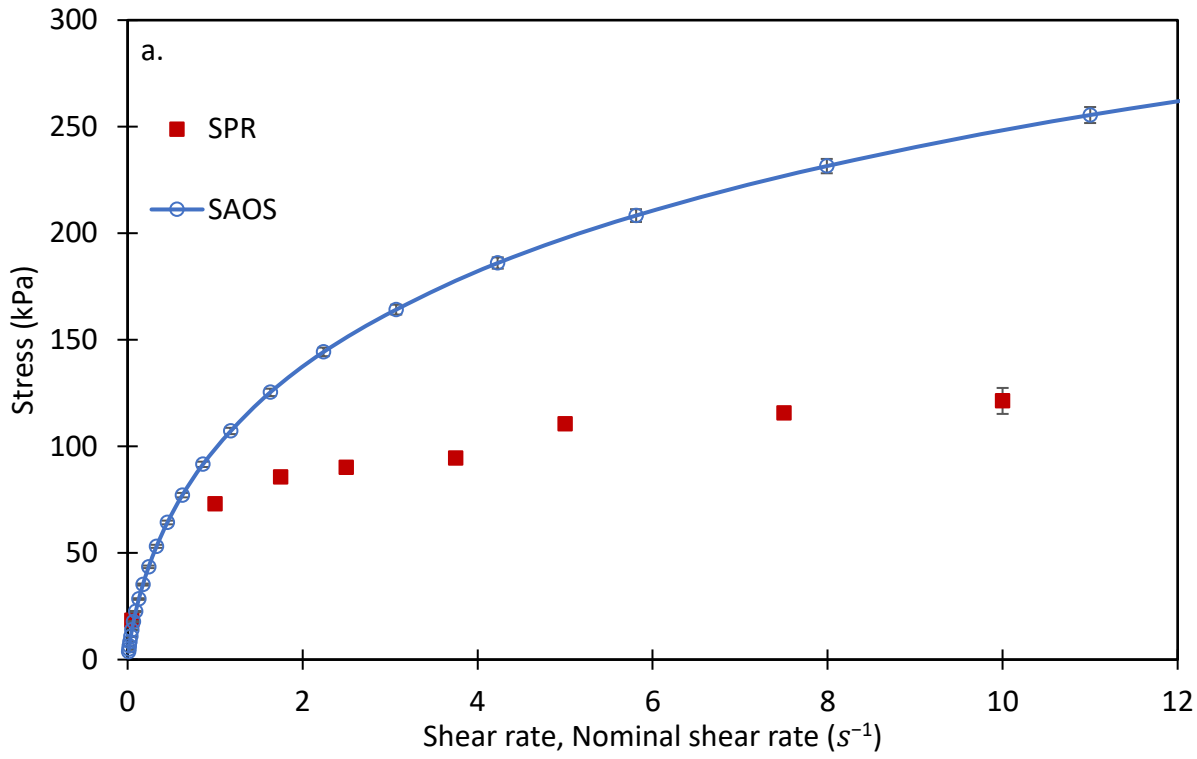

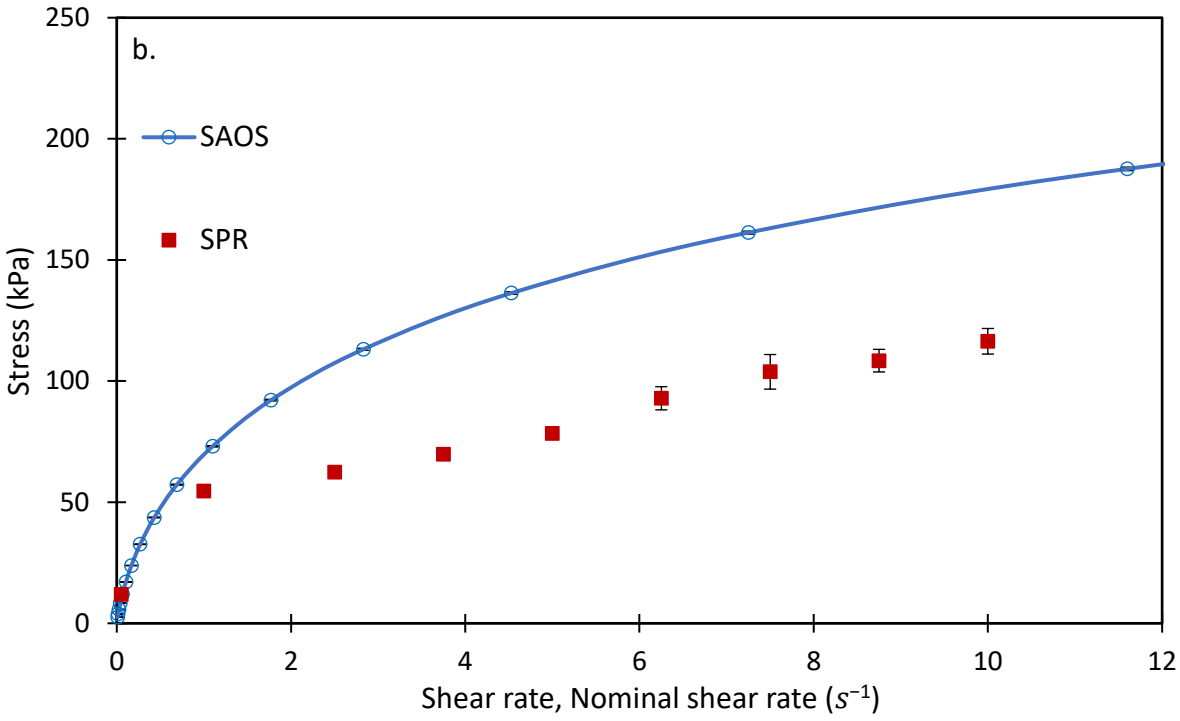
b.
SAOS
SPR
Stress (kPa)
250
200
150
100
50
0
0
2
4
6
8
10
12
Shear rate, Nominal shear rate (s^{-1})

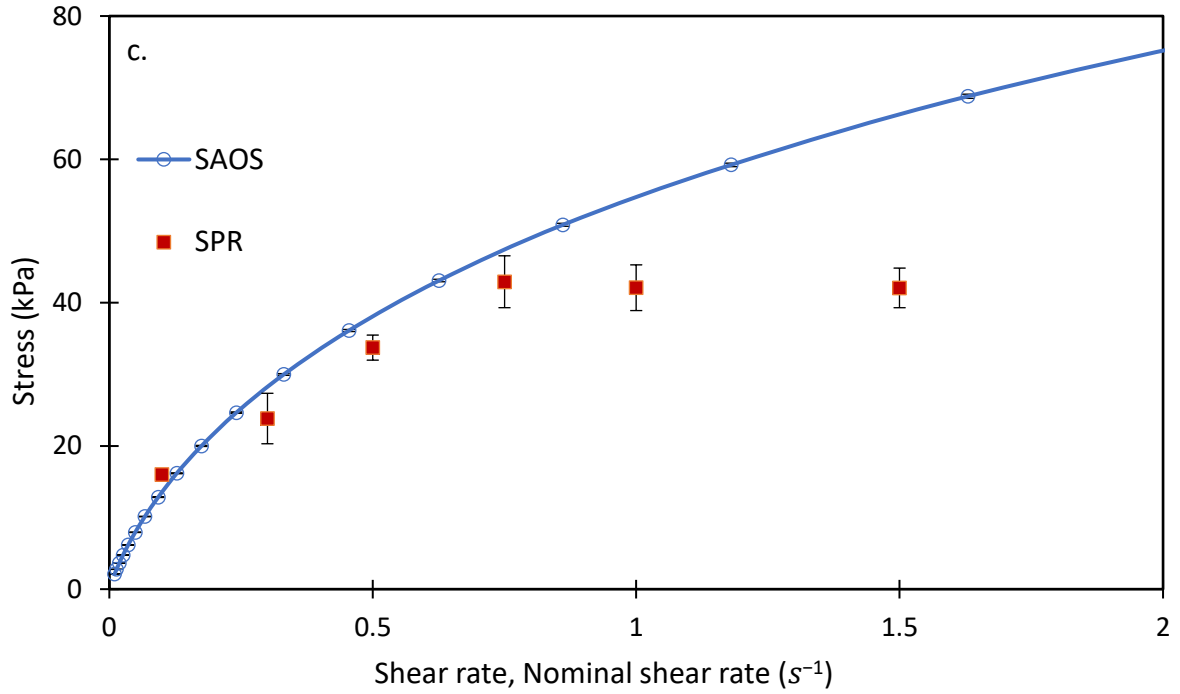
c.
SAOS
SPR
Stress (kPa)
80
60
40
20
0
0
0.5
1
1.5
2
Shear rate, Nominal shear rate (s^{-1})

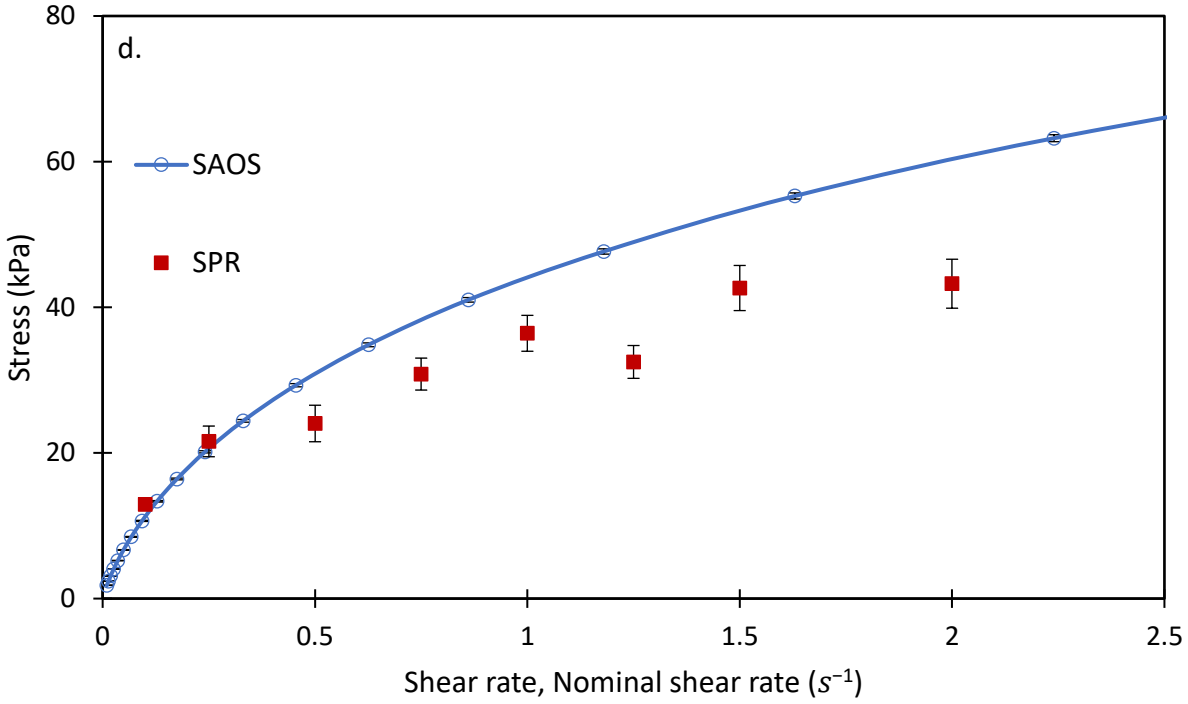

Figure 4.4. Stress in the presence of slip (SPR results) and in the absence of slip (SAOS results) [78] at 190 °C. a. HDPE 6, b. HDPE 2, c. HDPE 7, and d. HDPE 9. SPR tests at each nominal shear rate were repeated at least five times using fresh specimens. Trend lines are shown for SAOS data. Error bars represent standard error.

In an experiment, if the specimen slips without going through melt rupture, the shape of the specimen does not change much and, after the test, some debris are left on the plates. Photos of the stationary and moving plates under such a condition are shown in **Figure 4.5a** and **Figure 4.5b** However, in the case of melt rupture, the shape of the specimen changes and significant material remnants are observed on the two plates (**Figure 4.5c and Figure 4.5.d**). Note also, that if the specimen ruptures, the the plateau in the shear stress transient curve ends, and stress goes toward zero.

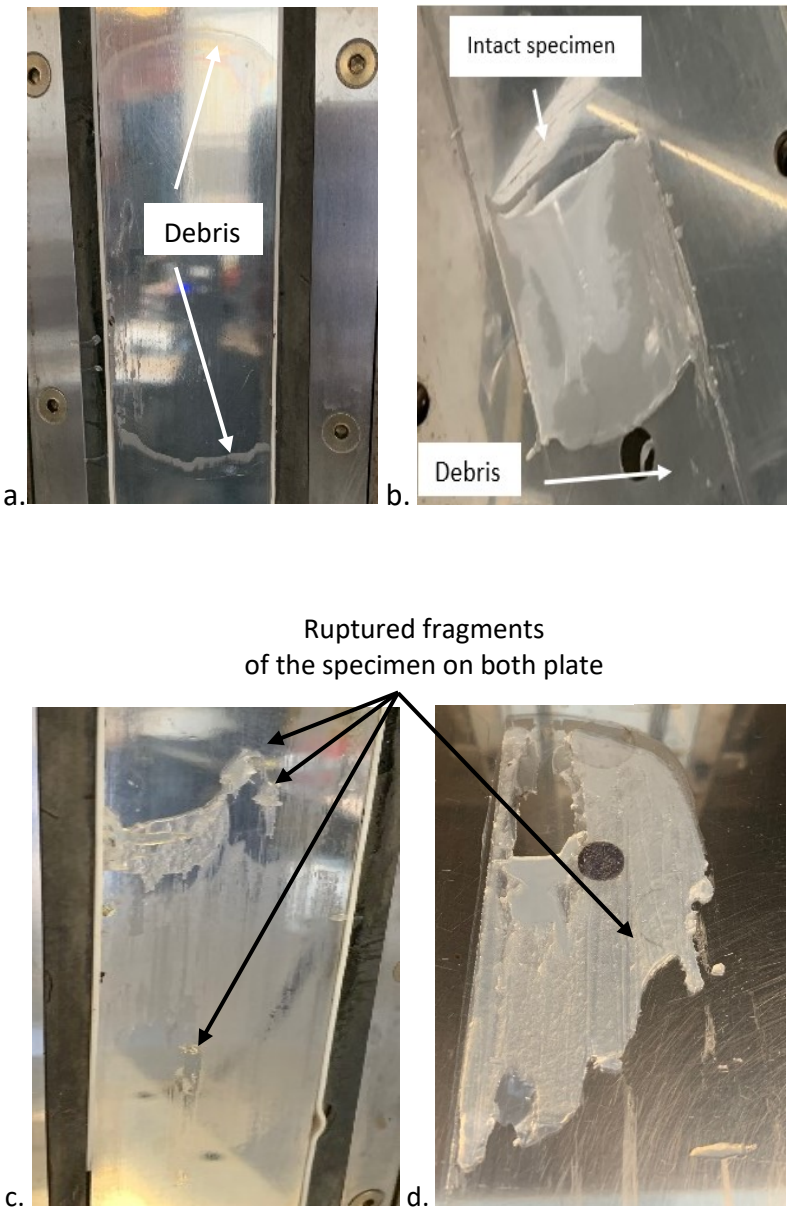

Figure 4.5. Photos of specimens after shearing for 60 s at the nominal rate of 1 s^{-1} at 190 °C: HDPE 7 under slip a. moving plate and b. stationary plate and HDPE 9 under melt rupture c. moving plate and d. stationary plate.

To further investigate the slip and melt rupture, the stationary plate is replaced with a glass plate and the flow is recorded using a camera. A glass plate is a good replacement for steel as it is also a high-energy surface with a surface energy (53±7 $\mathrm{mJ.m^{-2}}$) close to that of steel (60±9 $\mathrm{mJ.m^{-2}}$) with the results shown in **Figure 4.6**.

Figure 4.6 shows three images taken from the recording at different times under conditions where slip occurs first followed later by melt fracture. In **Figure 4.6b** we can see debris left on the plates during slip at the nominal shear rate of 0.75 s^{-1}. The same thing was observed for nominal shear rates of 0.25 and 0.5 s^{-1}. **Figure 4.6c** shows the specimen after melt rupture. The change in the shape of the specimen and cohesive failure at different locations in the specimen can be observed.

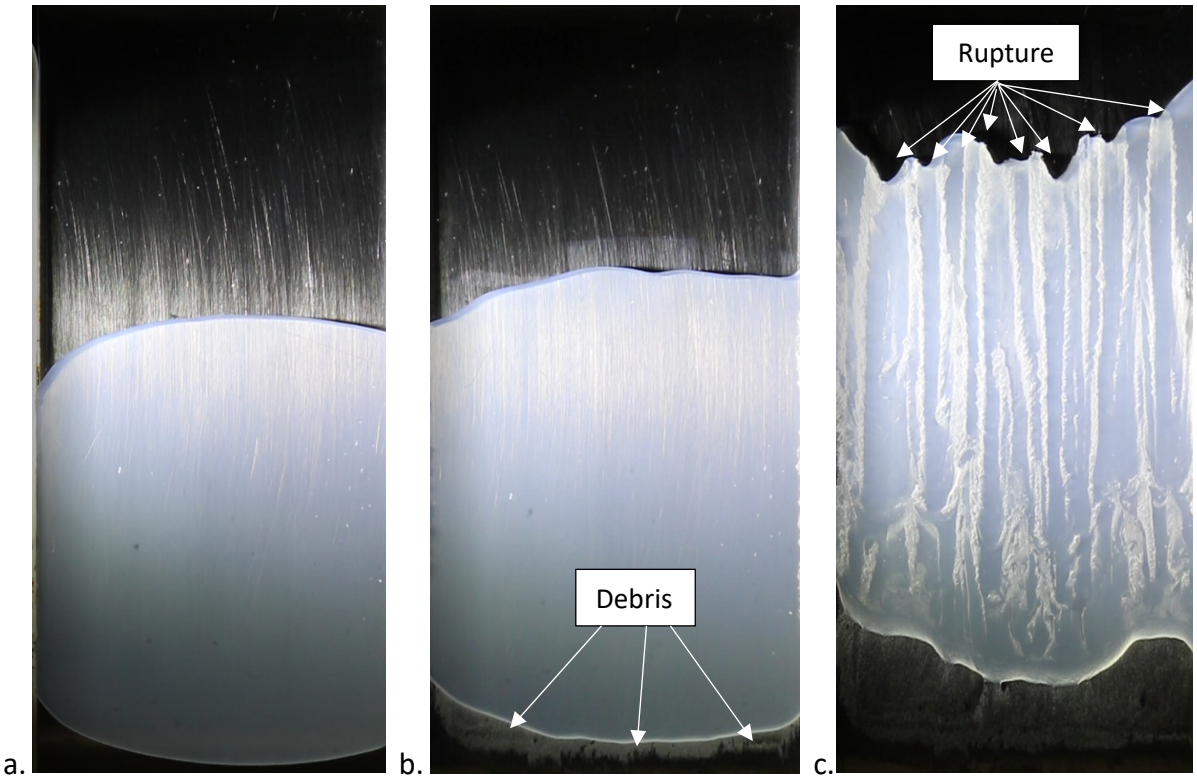

Figure 4.6. Images during shear flow of HDPE 7 at a rate of 0.75 s^{-1} at 190 °C: a. before the experiment starts, b. during experiment before melt rupture but after slip starts, and c. after melt rupture

In order to calculate the slip velocity, we apply **Eqn. (4.3)** to the curves presented in **Figure 4.4** resulting in **Figure 4.7**. The measured slip velocity in all cases is lower than its maximum value. The maximum slip velocity versus the nominal shear rate (**Figure 7.4a**) and versus stress (**Figure 7.4b**) for HDPE 2 is presented in the supplementary information. It should be noted that the nominal shear rate is not uniquely related to stress (even in the strong slip regime) because of the effect of viscosity which is different for different materials.

The first interesting feature of the slip velocity vs stress curve (**Figure 4.7**) is that the presence of short chains shifts the curve to lower stresses. This is consistent with previously published results for capillary flow at low flow rates (before the stick-slip instability) for bimodal polyethylene[15,68,69].

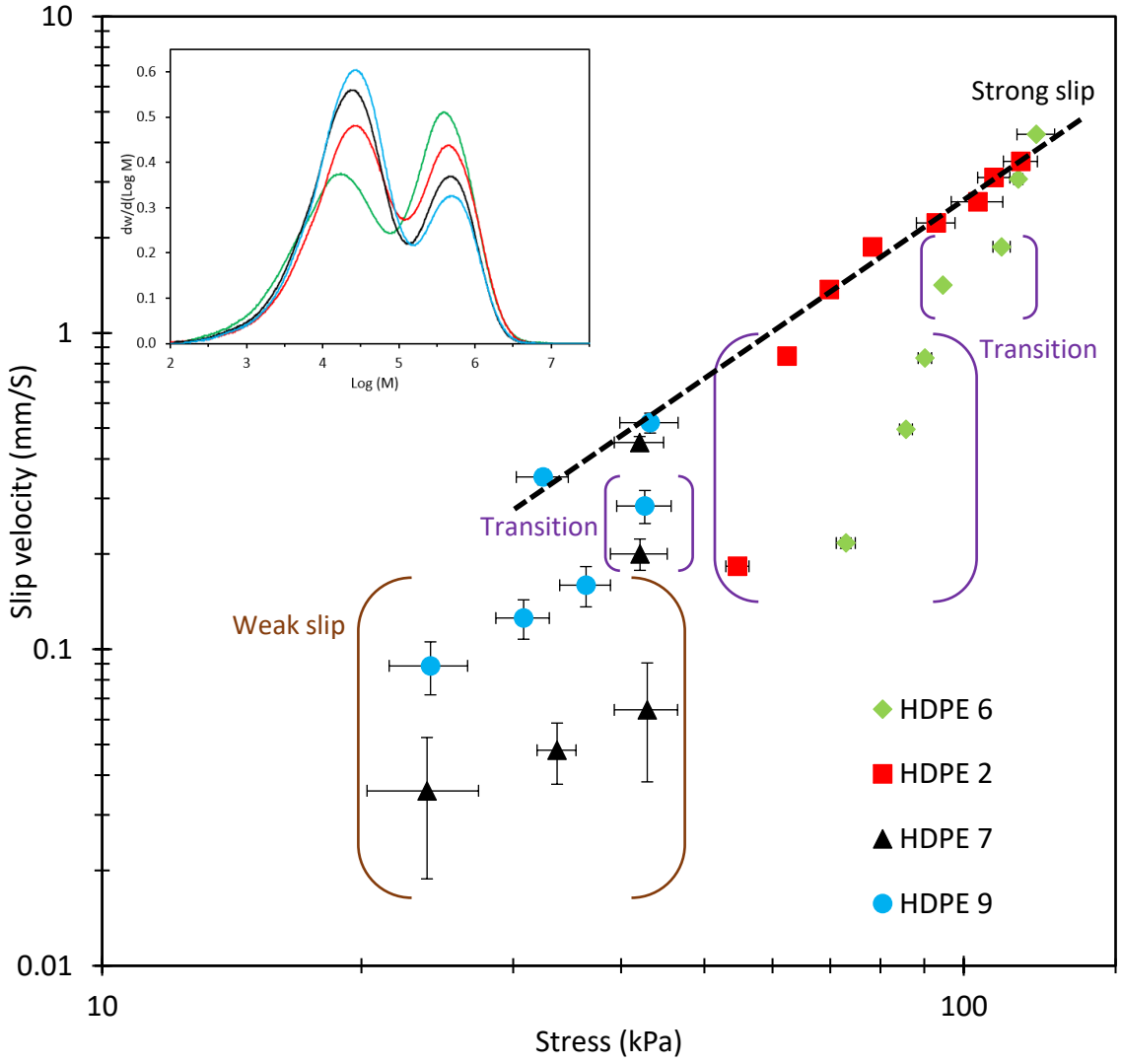

Figure 4.7. Slip velocity versus stress at 190 °C using the data of **Figure 4.4** and **Eqn. (4.3)** for HDPE 6, HDPE 2, HDPE 7, and HDPE 9. Error bars represent standard error.

The shift of the slip velocity curve to lower stresses with increased short chain content is possibly due to[68,69,79,85,86]: 1) Short chains at the cohesive failure interface disentangling from the bulk at lower stresses in response to convective constraint release. 2) Short chains in the bulk

enhancing the relaxation of the tethered chains via constraint release. 3) Surface-driven molecular fractionation is easier for short chains having higher mobility under the experimental time-frame contributing to the effects 1 and 2 above. 4) This fractionation can also cause a low viscosity layer close to the wall which might act as a lubricant in the slip process[68,69]. Inn[68,69] observed a wavy extrudate surface in the capillary studies of bimodal polyethylene at relatively low flow rates before the stick-slip instability and gross melt fracture. This wavy surface is similar to that observed in the flow of heavy oil lubricated by water[158,159]. Inn concluded that this wavy surface could be due to the slip of the polymer melt over a low viscosity layer close to the wall[68,69]. The existence and role of this low viscosity layer is still an open subject in the literature.

We can observe different slip regions in the slip velocity curves. The weak slip and transition regions and the strong slip line are indicated in **Figure 4.7**. We can see that the short chain content affects the slip behavior of the materials at all values of stress within the transition region before strong slip is fully engaged. After the strong slip is fully engaged, the slip behavior of the materials is independent of molecular weight distribution and is only a function of stress: under strong slip, the monomer friction coefficient, which depends only on monomer chemistry, determines the slip behavior. This is consistent with the results of capillary rheometer studies in the high flow rate branch (after the stick-slip instability) for polyethylene[15]. The importance of this study is that it is conducted under simple shear with no effect of pressure or shear rate gradient on the slip results. In capillary rheometers, the pressure inside the capillary reduces the slip velocity and this effect is more profound at higher rates where strong slip occurs. Additionally, the shear rate varies across the diameter of the capillary perhaps contributing to the segregation of low molecular weight chains at the surface. Our results show that the slip is truly independent of MWD without the confounding effects of pressure and shear rate gradients. This behavior has also been reported in slip studies of bi and tri dispersed polybutadiene under simple shear[3,4] and we now can extend this conclusion to bimodal polyethylene with the presence of a broad distribution of short and long chains.

In **Figure 4.7**, there is one data point for HDPE 9 that does not follow the trend. This point is at a stress of 32 kPa (corresponding to nominal shear rate of 1.25 s^{-1}) and has a higher slip

velocity compared with the data point at 42 kPa (corresponding to nominal shear rate of 1.5 s^{-1}), see **Figure 4.4d** The slip velocity at this point is very reproducible (variation of 15%).

Another interesting feature of **Figure 4.7** is the slope of the transition regimes for the different materials. The transition regime slope for HDPE 7 and HDPE 9 is steeper compared with that of HDPE 2 and HDPE 6. This means that materials with a higher content of short chains pass through the transition regime over a smaller range of stress. This is due to short chains disentangling at lower values of stress thus enhancing constraint release relaxation of the long chains resulting in the long chains themselves disentangling at lower stresses. Molecular fractionation may also happen more readily for materials with higher short chains as discussed before.

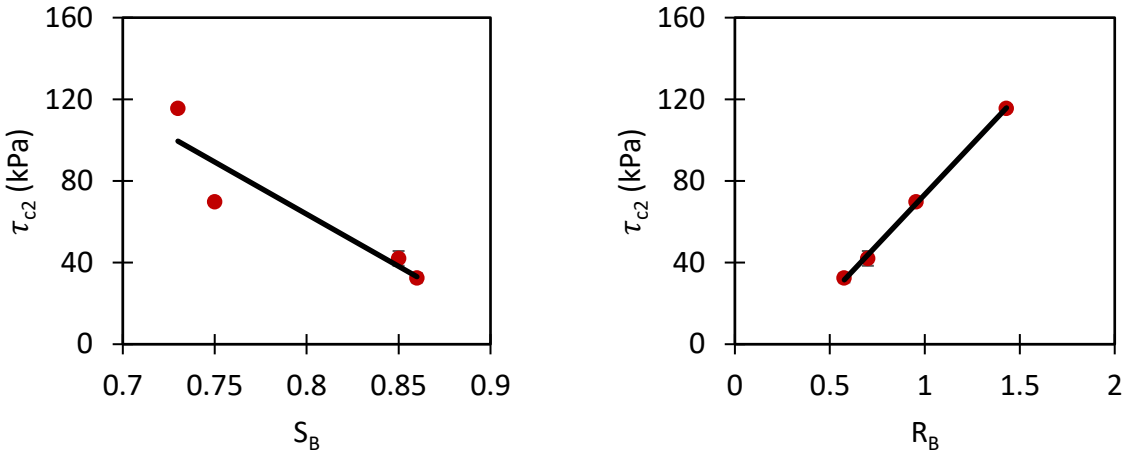

a. b.

Figure 4.8. Relationship between the end of the transition region and the bimodal parameters for the experimental materials at 190 °C using the data of **Figure 4.4** (a) τ_{c2} versus S_B (b) τ_{c2} versus R_B. Error bars represent standard error.

In **Figure 4.8**, the stress at which strong slip starts (τ_{c2}) shows a negative correlation with the bimodal parameter S_B (**Figure 4.8a**) and a positive correlation with R_B (**Figure 4.8b**). Note that for our set of materials these two parameters are strongly correlated ($S_B \propto \frac{1}{R_B}$) and therefore we cannot separate the two effects. In our set of materials, as S_B increases, the weight fraction of the low molecular weight population also increases (**Table 4.2**). This causes the decrease in the

value of the critical stress due disentanglement occurring at a lower stress as constraint release is enhanced.

An alternative approach to analyze the slip behavior is through the friction coefficient coming from the following equation[142,160,161]:

$$\tau = \mathrm{v_s k} \tag{4.6}$$

In this equation, τ is the shear stress, $\mathrm{v_s}$ is the slip velocity and k is the friction coefficient. The friction coefficient versus stress for the four materials is presented in **Figure 7.5** reduction in friction coefficient with stress is indicative of disentanglement. The friction coefficient in the weak slip regime is almost constant for HDPE 7 which shows that short chains do not disentangle from the bulk chains in this regime. For HDPE 9, the friction coefficient appears to decrease slightly in the weak slip regime. This material has the highest short chain content and we can see that disentanglement starts slowly in the weak slip regime. The interesting feature of **Figure 7.5** is that in the transition regime, the friction coefficient drops significantly with stress for all materials as more and more interfacial chains are disentangled. This is consistent with our former discussion about the difference in the CCR stress relaxation time-scale for bulk and interfacial chains that causes the disentanglement in this regime. We can see in the fully disentangled, strong slip region the friction coefficient of the 4 materials approaches the same line.

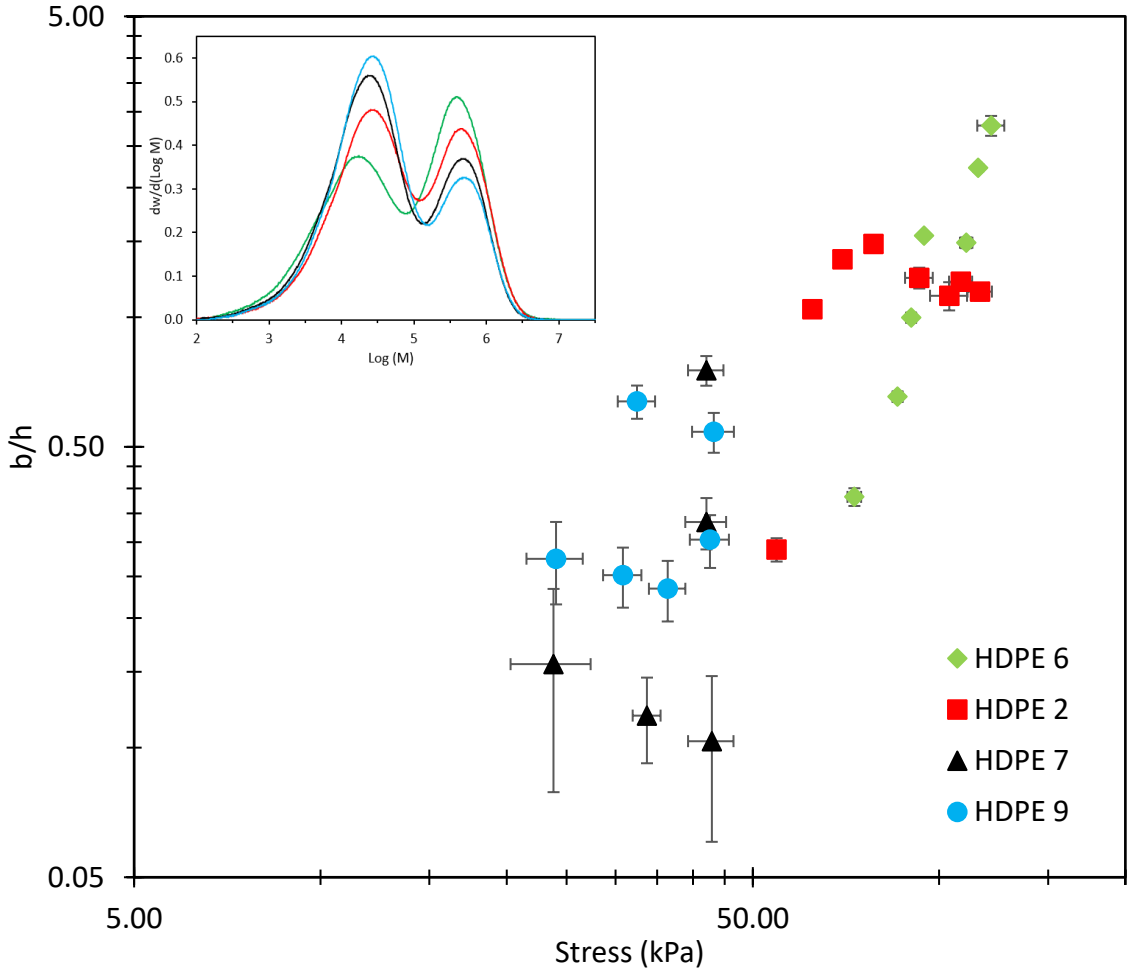

Figure 4.9. Slip length versus stress at 190 °C using the data of **Figure 4.4** and **Eqn. (4.7)** for HDPE 6, HDPE 2, HDPE 7 and HDPE 9. Error bars represent standard error.

The slip length (b) is defined as the distance from the wall at which the extrapolation of the velocity approaches zero. Under simple shear, slip length is[73,162]:

$$b = {}^{v_s}/_{\dot{\gamma}} = {}^{\eta}/_{k} \tag{4.7}$$

where v_s is the slip velocity and $\dot{\gamma}$ is the true shear rate, η is the viscosity and k is the friction coefficient. The importance of the slip length is that it provides a characteristic length that can be compared with the length-scale of the flow[163], in our case the gap between the plates (h) or the capillary diameter in Poiseuille flow. When ${}^{b}/_{h} \ll 1$ the slip is not significant from a macroscopic perspective and ${}^{b}/_{h}$ close to one indicates that there is considerable slip in the system[3,164]. **Figure**

4.9 shows $^{b}/_{h}$ versus shear stress for the four materials. Interestingly, HDPE 7 and HDPE 9 reach strong slip at a value of $^{b}/_{h}$ close to 0.7 while HDPE 6 and HDPE 2 at 2.2 and 1.2, respectively. This shows that the presence of short chains should be considered in the design of flow systems as they change the $^{b}/_{h}$ ratio required for the strong slip.

4. 5. Conclusions

Slip occurs over a broad range of stress for bimodal molecular weight distribution polyethylene under simple shear. Higher short chain contents shift the slip velocity versus stress curve to lower stresses due to a reduction in disentanglement stress and the resulting relaxation of chains and molecular fractionation. Different slip regimes in the slip velocity curves were observed: weak, transition and strong slip regimes. The short chain content affects the slip behavior of the materials at all values of stress within the transition region before strong slip is fully engaged: the higher the content of short chain, the higher is the slip velocity in the weak and transition regime. The change in the slip velocity with stress in the transition region is more abrupt for HDPE 7 and HDPE 9 (high short chain content) compared with those of HDPE 6 and HDPE 2. After strong slip is fully engaged, the slip behavior of the materials is independent of molecular weight distribution and is only a function of stress. The stress at which the slip velocity becomes independent of MWD decreases as the short chain content increases. The friction coefficient drops significantly in the transition region with stress for all materials as more and more interfacial chains are disentangled. HDPE 7 and HDPE 9 reach to strong slip at a lower value of $^{b}/_{h}$ as compared with HDPE 6 and HDPE 2. In our experiments, it became obvious that materials go through melt rupture after slipping at high shear rates and strains and that melt rupture happens at lower stresses for materials having a higher short chain content.

Chapter 5. A visual investigation of polyethylene melt rupture in simple shear with slip

In **Chapter 4**, We noticed that melt rupture happens frequently for our materials. In this chapter we replace the stationary plate in the SPR setup with the glass plate and investigate melt rupture using visualization techniques. This chapter is based on a manuscript that is now submitted: Sattari, M., Inn, Y., & Wood-Adams, P. M. (2024). A visual investigation of polyethylene melt rupture in simple shear with slip. Submitted to Polymer.

5. 1. Abstract

Melt rupture of a metallocene catalyzed bimodal molecular weight distribution polyethylene is studied under simple shear via flow visualization techniques. It was found that melt rupture is a time-dependent phenomenon that can occur after steady state plateau in slip velocity and stress. The rupture happens at the three-phase (polymer-air-plate) common line and propagates through the specimen. The common line recedes slightly and stops slipping just before the onset of rupture. The surface characteristics (roughness and coating) play an important role in the rupture behavior of the material. The presence of polytetrafluoroethylene lubrication (low surface energy coating) changes the nature of the slip mechanism towards adhesive failure and accelerates melt rupture in terms of time-to-rupture-onset (at the same nominal shear rate). Surface roughness also reduced the time to rupture onset but without affecting the nature of the slip. A time-dependent phenomenon at the interface like fractionation or changes in conformation and entanglement density of the interfacial chains could be the reason for the transition from slip to melt rupture.

5. 2. Introduction

At high amount of deformation rates and/or strains in the polymer melt flows, the polymer melt might experiences a nonuniform and catastrophic cohesive failure that is called melt rupture[2,76]. Melt rupture can be characterised using time-to-rupture at a particular stress, which quantifies the durability of polymer melts[76,165–167]. This measure of time-to-rupture is

crucial industrially since it reveals limitations in processing methods when the aim is to avoid rupture or shift it to higher stress and/or longer time[76].

In the case of extrusion, studying melt rupture is challenging because of the confounding effects of pressure[2,76,168] and shear rate gradients through the capillary[2] and die swell at the exit[169]. Studies under simple shear have this advantage to study the flow independent of those effects[2]. The flow

Polymer melt rupture has been studied broadly under the elongational flows[165–167,170]; however, there are limited studies on melt rupture under simple shear. It is worthwhile mentioning that, two different phenomena are defined in the literature of the extensional flows[76]: Considère criterion failure and melt rupture. Considère criterion failure is where a localized or nonhomogeneous deformation starts. The Melt rupture, on the other hand, is defined as the physical rupture of the melt of polymers[165]. Under simple shear, the stress and deformation can be homogenous (in the steady state region) until the onset of rupture[76].

Andrade et al.[171] observed a correlation between the number of steady states in the Hencky strain versus time curve in tensile creep of low-density polyethylene (LDPE) and the type of failure. According to them, at relatively high creep stresses, one steady state is observed, and the failure is cohesive while at lower stresses, two steady states and ductile fracture are observed. The time-dependent disentanglement of long branches and short chains leads to a second, temporary steady state shortly before failure[171].

It is commonly believed that the linear rheological behavior in shear flows often can be described by universal molecular parameters such as entanglement number and rouse relaxation time[172]. This universality can be extended to the non-linear regime using common constitutive equations to account for the strain dependency with some success in shear flows[172]. However, this is less effective for extensional flows which exhibit “non-universality”[172] attributed to the effects of elongated chains on the reduction in monomer friction coefficient or changes in the topological interactions during the flow[172,173]. Here in this study, we are studying a time-dependent melt rupture in shear flow for a bimodal polyethylene that cannot be explained by the universal approach.

Under large extensional strain rates where the deformation rate is higher than the reciprocal of the Rouse relaxation time, a viscoelastic melt acts as a solid and elastic failure happens[174,175]. Huang et al.[175] showed that such failure in uniaxial extensional flow of polystyrene does not happen at pre-existing defects in the material but at random locations on the specimen edges. They attributed this to random thermal fluctuations at the edge which might change the local entanglement density[175], an open subject in the literature. The chains at the edge are subjected to additional orientation[175] as compared to the bulk meaning that thermal fluctuations are more likely to lead to local failure[176]. We will show that their observations in extension are consistent with ours under simple shear. Huang[177] studied the failure mechanism of monodisperse polystyrene in uniaxial filament stretching. She reported that the maximum stretch ratio of the entanglement strand controls the failure stress rather than the frictional resistance against sliding. She also concluded that since the failure stress is independent of the number of entanglements per chain, the failure mechanism should not be disengagement but probably chain scission[177]. More recently, Huang et al.[178] mapped free radicals created due to chain session using a profluorescent nitroxide probe. They demonstrated that chain scission happens during melt failure in uni-axial, extensional creep and that the number of scission events are increased at the edges and in voids of the specimen. They also showed that the scission occurs within 50 micro-meter from the surface[178]. Interestingly, the thickness is close to the thickness of slip debris observed in our previous work[90]. The competition and interplay of chain session and disentanglement in melt failure is still an open subject in the literature. Wingstrand et al.[179] investigated studies of the effects of flow-induced crystallization in HDPE fracture in filament stretching and concluded that this crystallization type stabilized filaments and can prevent melt failure. In fact, the crystal nuclei can incorporate some chain segments creating an infinite relaxation time by acting like a cross-link[179]. Flow-induced crystallization happens under both extensional[179–181] and under shear[182] flows, depending on the degree of chain stretch induced in the particular flow[183].

In capillary flows, surface and gross melt fracture are observed more frequently for metallocene-catalyzed bimodal polyethylene compared with conventional[184,185] broad MWD polyethylene even if they show similar rheological shear and extensional response[17]. The addition

of a processing aid did not reduce the melt fracture of the metallocene-catalyzed bimodal polyethylene[17]. The effects of processing aids on different types of polyethylene are reviewed elsewhere[186].

Although it remains an open subject, many researchers report that sharkskin is a die exit phenomenon, and gross melt fracture is due to the extensional deformation[17,187] in the capillary entry region[17,188]. In our studies, we observe melt rupture under simple shear, showing that extensional flow is not essential for it to occur. We will show that the failure we observe in simple shear is a bulk rupture, closer to gross melt fracture rather than sharkskin in capillary studies.

Hatzikiriakos et al.[189] reported that coating a die with either a slip or adhesion promoter, increases the quality of the extrudate appearance, i.e. reduces surface defects such as sharkskin. They proposed that slip and pressure effects interplay to cause this unexpected behavior[189]. This further illustrates the complexity of melt instabilities and the need for additional understanding of slip and melt failures and their interrelationships. We remove the confounding effects of pressure by working in simple shear rather than capillary flow. Lee et al. [184] reported that stress in the region of the flow curve where gross melt fracture is observed is independent of temperature and molecular weight for linear low density polyethylene. They did not observe slip (flow curve being independent of the capillary diameter) and concluded that slip does not cause gross melt fracture[184].

Kim and Dealy[187] used carbon black tracers and confirmed that gross melt fracture originates at the die entry region, and at a critical extensional stress that is a material property[187]. Broadening the MWD in the range of $2 < {Mw}/{Mn} < 7$ (this range is lower than characteristic of a bimodal polyethylene) and increasing the LCB (in the range of 0.009-0.063 LCB/1000C, metallocene catalyzed polyethylene) linearly increases the critical tensile stress. This critical stress was found to be independent of molecular weight[190]. Doerpinghaus et al.[185] compared the effects of long chain branching of metallocene polyethylene (0.79 LCB/1000C) with conventional LDPE (39 LCB/1000C) and reported that both metallocene and conventional long chain branching decreases the onset wall shear stress for gross melt fracture, and increases the severity of the gross melt fracture; however the effect of LCB in LDPE was more profound[185]. They also observed

that the degree of strain hardening in uniaxial extensional flow is positively correlated to the severity of gross melt fracture in capillary flows[185].

Melt rupture of polyethylene melt under simple shear is a catastrophic cohesive failure[2,76] that is different from the cohesive failure that takes place during the cohesive (apparent) slip of polyethylene melts[2,72,76]. In the case of cohesive (apparent) slip, the tethered chains to the wall are disentangled from the bulk chains. These tethered chains generate a failure plane close to the wall and making a thin layer of polyethylene on the vicinity of the wall[11,76]. Upon this, the bulk chains slips over the tethered polyethylene layer and the bulk flow otherwise continues[2,72,76]. The cohesive failure leading to rupture occurs within the bulk (far from the wall) and results in a non-uniform flow or even the flow stops in the case of simple shear[2,76].

Dhori et al.[77,16,191] investigated the displacement on of the common lines (the contact line among the melt, wall, and air (**Figure 5.1**)) in viscoelastic flow both by experimental work and modelling[77,16,191]. According to their entropy inequality analysis, it is the elastic component of the Helmholtz free energy that defines the movement of the common line whether it advances (low deformations) or recedes (high deformations). The Helmholtz free energy depends on deformation, surface tension, surface mass density and surface chemical potential of the air, polymer, and the plates[77,16,191]. At high deformations, when Helmholtz free energy exceeds a critical value, the common line moves drastically and melt rupture happens[77,16,191]. Their simple shear experimental research was on linear low density polyethylene lacking flow visualization techniques[16,76] and here we contribute to better understanding of melt rupture. They did not report any slip for the material they studied[16] and rupture was interpreted as dewetting[77,16,191]. This cannot be the case for cohesive slip occurring in the case of our bimodal polyethylene[2,90].

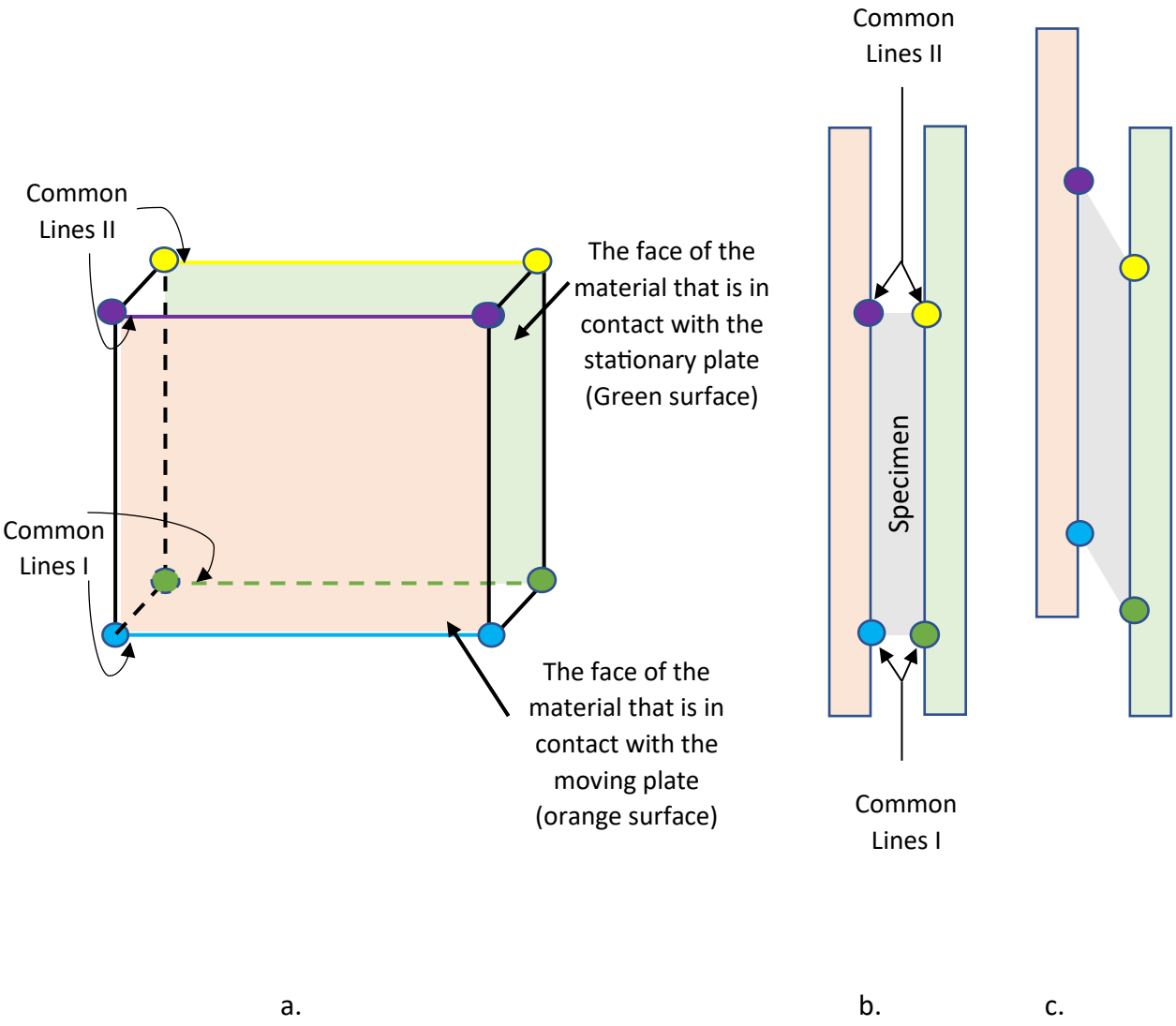

Figure 5.1. Schematic of specimen geometry showing 3D a. and side views b. before and c. after shearing the specimen. The common lines in a. are points in b. and c. The figure is not to scale.

Schematics of the side view of a specimen before (**Figure 5.1b**) and after simple shear (**Figure 5.1c**) is presented in **Figure 5.1**. There are four three-phase-contact points illustrated with circles. These points are lines on the three-dimensional view (**Figure 5.1a**). The green and yellow circles are in contact with the stationary plate and the blue and purple circles are in contact with the moving plate. After shearing, the material tilts toward the moving direction. As a result, the gap is not filled at the purple or green points, so rupture initiates at either the yellow and blue

points or both[77,16,191]. If moving and stationary plates are made of the same material, rupture should happen at both points simultaneously due to symmetry but in the case of different plate materials, rupture may initiate from either of the planes. For the first time, we investigated the effect of the plate materials, roughness, and coating on initiation of and the behavior during rupture of bimodal polyethylene by direct visualization and image analysis techniques.

In response to shearing, materials either deform and/or slip which is governed by the equation below[12]:

$$\dot{\gamma}_{\mathrm{n}} = \dot{\gamma} + {}^{V_{ss}}/_{h} + {}^{V_{sm}}/_{h} \tag{5.1}$$

In this equation $\dot{\gamma}_{\mathrm{n}}$ is the nominal shear rate or the moving plate velocity over the gap, h, $\dot{\gamma}$ is the true shear rate, V_{ss} is the slip velocity on the stationary plate, and V_{sm} is the slip velocity on the moving plate. The two slip velocities are different if the plates have different surface properties such as surface energy and roughness[12]. In the case of a full slip, $\dot{\gamma}$, is zero, there is no deformation, and the nominal shear rate will be equal to the summation of the slip velocities divided by the gap (**Figure 5.2b**). In case the material does not slip, all shearing will be converted into deformation as presented in **Figure 5.2c**. The specimen can experience both deformation and slip and, in this case, the more the material slips, the lower the deformation (**Figure 5.2d**).

In visualization studies of simple shear, one transparent plate (glass) is used, and the flow is recorded through it. In this study, the stationery plate is the glass plate. If the material deforms, ideally, four common lines should appear on the front view of the specimen through the glass stationary plate. However, due to practical limitations in distinguishing between shadows, common lines, and debris, not all four borders are clearly detectable in the recordings. We also note that minor secondary flows[12] occur in our visual experiments which further complicates the measurement of the little deformation in our mixed-plate systems (please see the supplementary information.).

In the current study, we calculate the slip velocity based on the movement of common lines I in **Figure 5.1**. It should be noted that in a 3D view (**Figure 5.1a**), common lines I and II consist of two lines each. In our experiments where we visualize the flow through the stationary

plate, even under flow, it is not practically possible to distinguish between the two lines in each pair due to the very small amount of deformation and the limitations mentioned previously. Therefore, we refer to each pair as “common lines I” and “common lines II”. The movement of common lines I is the most evident in the recordings and its velocity is equal to V_{ss}. It should be noted that the movement of common lines II reflects both deformation and slip and is more difficult to analyze. By assuming zero deformation $(\dot{\gamma} = 0)$, the maximum possible V_{sm} can be calculated using **Eqn. (5.1)**. In this study, for the first time, we investigate how rupture front propagation affects the balance of slip behavior during melt rupture.

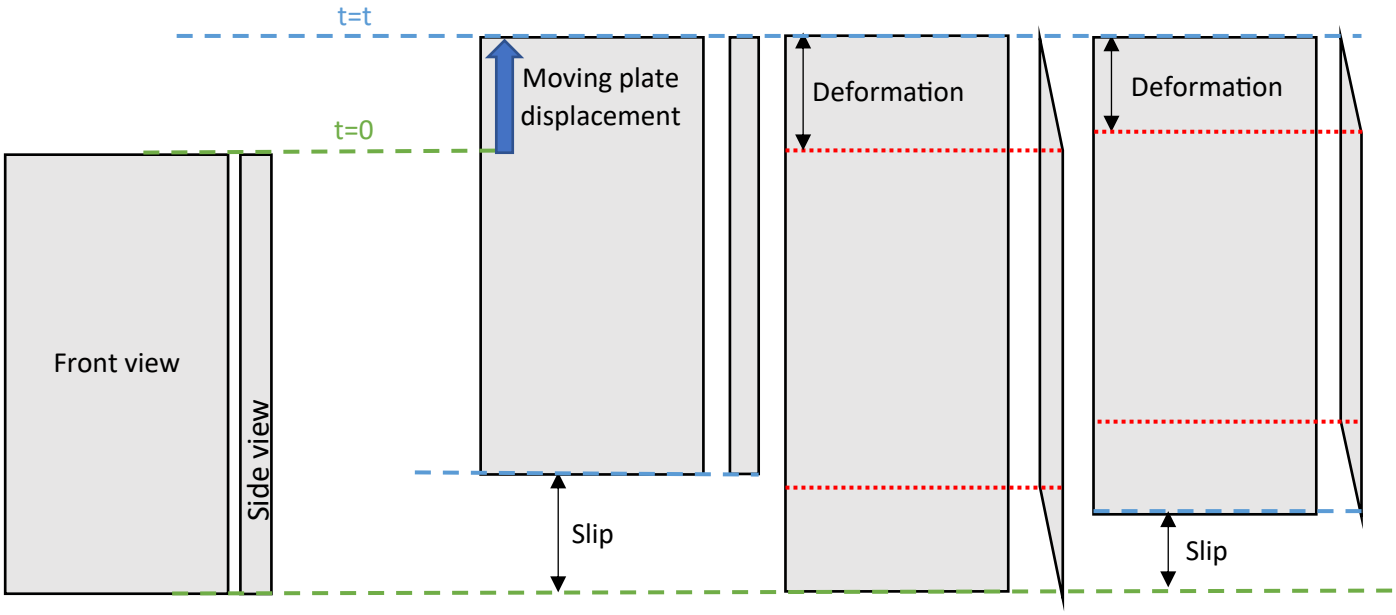

a. Initial specimen

b. After slip

The specimen slips without deformation in response to the moving plate displacement.

c. After deformation

The specimen deforms without slip. Ideally, four borders can be seen from the front view (through the stationary plate and the molten specimen).

d. After combined slip and deformation

The specimen slips and deforms. The higher the slip, the lower the deformation and vice versa. Ideally, four borders can be seen from the front view.

Figure 5.2. Schematic of the front and side views of a specimen under simple shear: a. Before the experiment starts and after displacement of the moving plate, b. Under full slip, c. Under deformation without slipping, d. Under slip and deformation. The figure is not to scale.

Wall slip of polymer melts is believed to be related to several instabilities in both capillary and simple shear flows[76] including die drool,[88] sharkskin[192] and melt rupture[2]. Such instabilities

are observed for metallocene-catalyzed polyethylene whether unimodal[169] or bimodal[68] MWD more frequently than other conventional polyethylenes[184,185]. During the start-up of simple shear of molten polyethylene, three important phenomena can happen separately or simultaneously: simple shear flow, adhesive or cohesive failure close to the wall (slip) and melt rupture[2,12,76]. The stress transient cannot be used to properly distinguish and study combined slip and rupture since once the material ruptures, stress goes to zero[2,76]. Here we use flow visualization to provide a more detailed picture. We investigate melt rupture and slip of a bimodal polyethylene on different surfaces and examine if slip is related to time-to-rupture-onset of the material. We will show that after a certain amount of time, the material stops slipping (starting from a contact line) and this leads to non-homogeneous deformation and rupture.

5. 3. Materials and method

5. 3. 1. Material

We studied a bimodal polyethylene provided by Chevron Phillips Chemical. The molecular weight distribution[2] and relaxation spectra[78] are presented in **Figure 5.3**, and the slip[2] and linear viscoelasticity[78] behaviors are reported previously (HDPE 9)[2,78]. Among the materials studied previously[2], HDPE 9 went through melt rupture at all shear rates within the experimental window in time[2] and for this reason it was selected for this study.

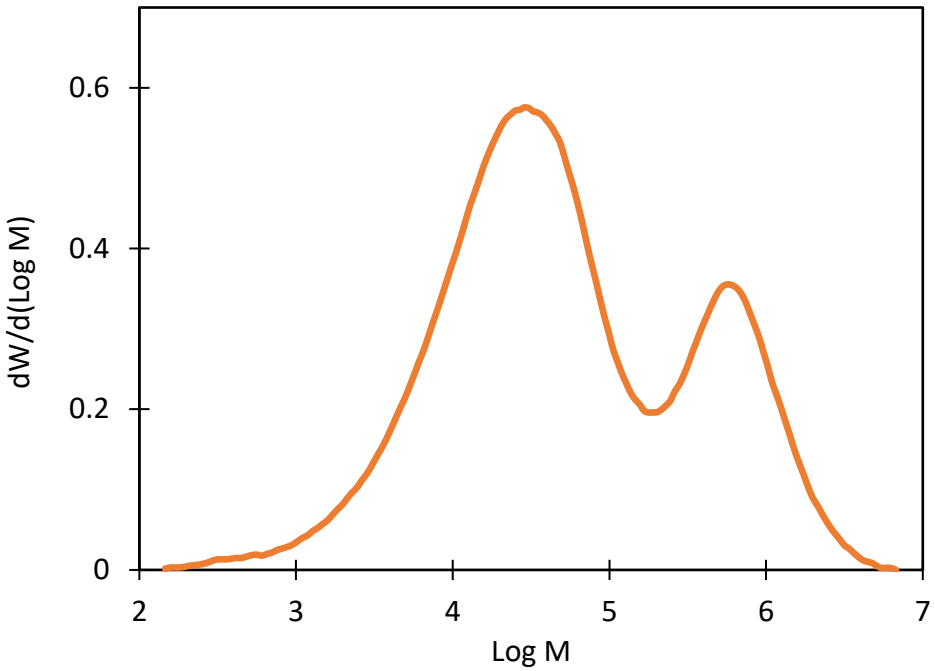

a.

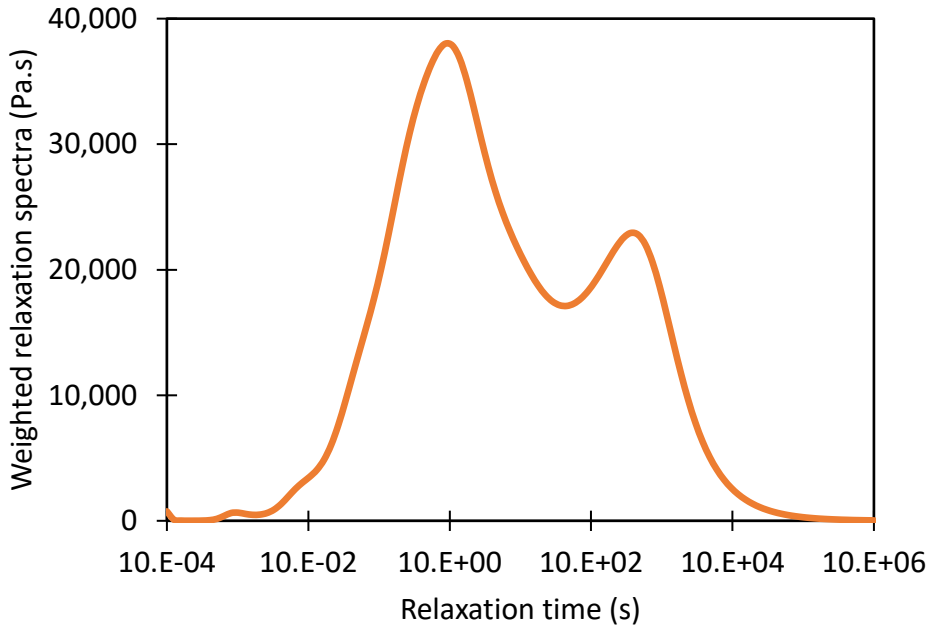

b.

Figure 5.3. The molecular weight distribution[2](a), and relaxation spectra[78] (b) for HDPE 9

5. 3. 2. Visualization studies under simple shear

The experiments are carried out in a sliding plate rheometer[2]. To visualize the slip and melt rupture, the stationary plate is replaced with a glass plate and the flow is recorded with a

camera (Canon EOS rebel T7 DSLR equipped with Canon EF-S 60mm F/2.8 macro USM lens with a frame rate of 30 FPS). The visualization studies were conducted at nominal shear rates of 1, 2, 4 and 10 s^{-1} at a gap of 1 mm.

To study the effect of plate surface energy on the melt rupture behavior, the glass and/or the steel plate are coated with Polytetrafluoroethylene (PTFE) using LPS® Dry Film PTFE Lubricant spray. The PTFE spray is an aerosol containing volatile carrier solvents that evaporate from the substrate in approximately one minute after application at room temperature according to the manufacturer. The coating is sprayed by scanning over the plate surface from a distance of ~20 cm followed by 5 minutes of drying in air. This process is repeated three times to ensure a uniform coating prior to use. It is worthwhile mentioning that during flow with slip, the coating is swept along with the melt and therefor this type of PTFE coating acts more like a lubricant than a permanent coating, similar to the behavior of processing aids in extrusion[193]. Similar coatings have previously been shown to have a reproducible functionality[71].

A sandblasted glass is used to study the effect of the surface roughness on melt rupture. One side of the glass plate is sand blasted using ~120 grit sand for approximately 15 seconds resulting in an average roughness (Ra: the average of deviations of surface profile from the mean value[194]) of 1.27 µm ±0.46.

Rupture experiments are carried out at 190 °C. After each experiment, the set-up is opened, and the plates are cleaned[2] before being subjected to the next PTFE coating application as needed. Four sets of experiments were conducted using different combinations of surface energy and roughness at rates of 1, 2, 4 and 10 s^{-1} as summarized in the **Table 5.1**.

Table 5.1. Different plate combinations included in this study			
Index	Stationary Plate	Moving plate	Notation in this paper
1	Stainless steel	Stainless steel	Steel-Steel
2	Glass	Stainless steel	Glass-Steel
3	Glass	PTFE coated stainless steel	Glass-Csteel
4	PTFE coated glass	PTFE coated stainless steel	Cglass-Csteel
5	Glass with a rough surface	Stainless steel	Rglass-Steel

5. 3. 3. Slip velocity measurements

The slip velocity is determined using the video analysis software, AdobeAfterEffect® with the MochaPro® plugin. For the visualization studies, the stress transducer cannot be installed so we do not have the stress to calculate the slip velocity as we did for the steel-steel set up in the previous study[2].

The sample borders are defined for the software using the magnet tool of MochaPro® and after specimen movement tracking, the shape data is extracted. This provides the coordination of the sample border in each frame. The slip velocity is calculated using the displacement of common lines I in **Figure 5.1** as this border contrasts acceptably with the moving plate.

The software provides the shape of the specimen in terms of discrete points in each frame. The points making up common lines I are extracted and the border displacement in the flow direction is calculated at each frame step for at least five evenly spaced points. The average displacement of the five points multiplied by the frame rate is reported as the transient slip velocity. The slip velocity is calculated from the plateau of the transient slip velocity curve. For longer videos, rates of one and two s^{-1}, every third or tenth frame is analysed respectively.

Note that distances measured in terms of fraction of frame size are converted to lengths using a scaling factor. The scaling factor is determined by tracking a nut on the moving plate at a known plate speed.

Since we do not have a measurement of stress, this method cannot be a replacement for rheometric experiments. However, it gives an acceptable estimation of slip velocity on the stationary plate and is suitable to study large scale phenomenon like melt rupture. The difference between the nominal shear rate and the slip velocity on the stationary plate gives the maximum possible slip on the moving plate which would happen in the absence of deformation (**Eqn. (5.1)**).

5. 3. 4. Rupture front velocity measurements

We used Fiji® software to measure the rupture front velocity. In each frame analysed, a region of interest (ROI) is manually fitted to the rupture front position providing coordinates of the front. The scaling described previously is used and the rupture front velocity is calculated by multiplying the displacement by the frame rate.

5. 3. 5. CT-scan measurements

The 3D shapes of the ruptured fragments were captured using 3D x-ray microscopy tomography (CT) with a ZEISS Xradia 520 Versa. The objective magnification and source voltage was 0.4X and 70kV respectively with a voxel resolution of 50-55 microns. The 1600 projection images were collected and reconstructed on Zeiss software. The 3D thickness maps were then built in Dragonfly Pro 2020 software, Object Research Systems (ORS) Inc.

5. 4. Result and Discussion

5. 4. 1. Slip velocity measurements

The slip velocity on the stationery plate and the maximum slip velocity on the moving plate for all setups are presented in **Table 5.2**. From the table, the slip velocity on the glass (stationary) plate is higher than on the steel (moving) plate at all the rates and in all the setups. The surface energies of glass and steel are quite similar, 53 ± 7 and 60 ± 9 $mJ.m^{-2}$ respectively[2]. The observed difference in slip velocities then, indicates that such a small difference in surface energy is has a surprisingly large effect on the slip behavior of our materials. We find this difference between the slip velocities on the steel and glass plates very interesting and invites more studies on the effects of interfaces on the slip behavior of bimodal polyethylene to understand the exact state of orientation and entanglement of the interfacial chains in these

materials under slip. This difference between the slip velocities on the steel and glass plates and the lack of a stress trace, unfortunately makes it difficult to compare these results with those in the steel-steel setup that we reported previosuly[2].

The difference between the slip velocity on the two plates is highest at the rate of 10 s^{-1}; the maximum difference is smaller with a coated steel plate.

Surface roughness did not affect the slip velocity on glass with the possible exception of a rate of 10 s^{-1}. Surface roughness is expected to reduce slip velocity through an increase in interfacial area and mechanical interlocking[195]. However, with cohesive slip, increased adhesion to the plate could result in a more compact adsorbed layer that is less entangled with the bulk flow.

Table 5.2. Slip velocity on stationary, and the maximum slip velocity on the moving plates (mm/s)

Apparent Rate (s^{-1})	1		2		4		10	
Setup: Stationary plate-moving plate	V_{ss}	$V_{sm,max}$	V_{ss}	$V_{sm,max}$	V_{ss}	$V_{sm,max}$	V_{ss}	$V_{sm,max}$
Glass- Steel	0.56	0.44	1.06	0.94	2.25	1.75	6.85	3.15
Glass-Coated steel	0.54	0.46	1.15	0.85	2.51	1.49	6.46	3.54
Coated glass-Coated steel	0.54	0.46	1.06	0.94	2.27	1.73	5.45	4.55
Rough glass-steel	0.57	0.43	1.11	0.89	2.30	1.70	6.51	3.49

5. 4. 2. Rupture type and location of initiation

We conducted visualization studies on four different set ups that are presented is in **Table 5.1** (setups 2-5). We observed that melt rupture, initiation, common line and the type of rupture changes with the change of the interface. We defined three types of melt ruptures: finger-like (**Figure 5.4**), progressive (**Figure 5.5**) and edge-initiated ruptures. In all cases, rupture started after some time of steady slip (**Figure 5.4b**).

In the figure-like rupture type, the rupture initiates from different locations on the common lines at different times (**Figure 5.4c** and **Figure 5.4d**) and these fronts propagate and maybe join each other (**Figure 5.4e** and **Figure 5.4f**) until the rupture front reaches the end of the sample (**Figure 5.4g**).

In the case of the progressive rupture, rupture happens along the entire common line at the same time and propagates through the sample (**Figure 5.5b**).

The third type of the rupture which happens at relatively lower nominal shear rates is edge rupture. This type of rupture initiates from the PTFE bars that are installed to avoid secondary flows[2,12]. We refer to this type of rupture as the border rupture.

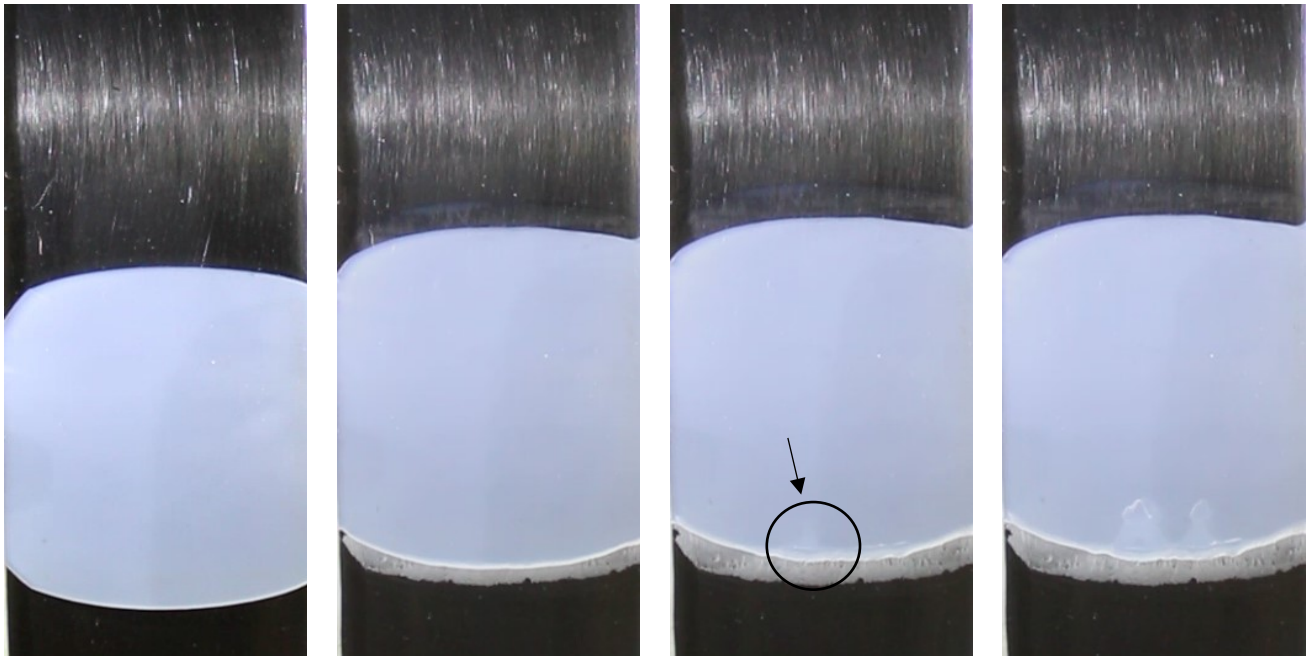

a. Before experiment starts (time=0 s)

b. Under flow with slip (time=4.8 s)

c. the onset of rupture with a finger-like streamline (time=5.9 s)

d. Creation of a second finger-like streamline (time=6.2 s)

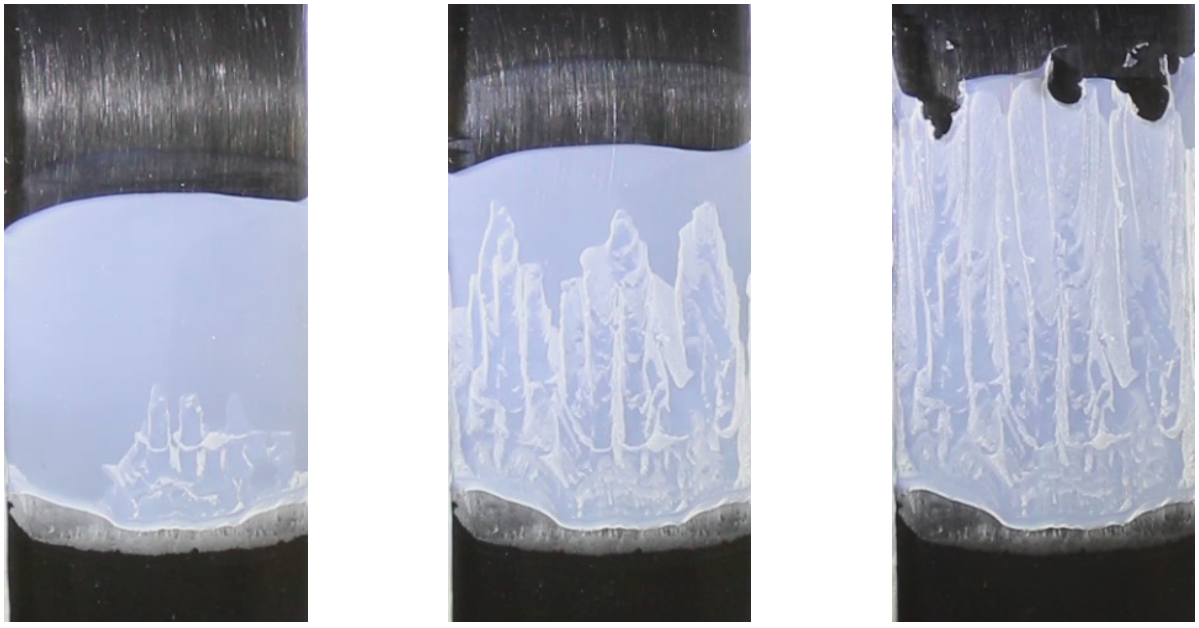

e. Rupture propagation and merging the finger-like streamlines (time=7.6 s)

f. Rupture propagation (time=14.2 s)

g. Rupture takes almost all the specie man

Figure 5.4. Finger-like rupture: Glass-Steel set up at the rate of 2 s^{-1}

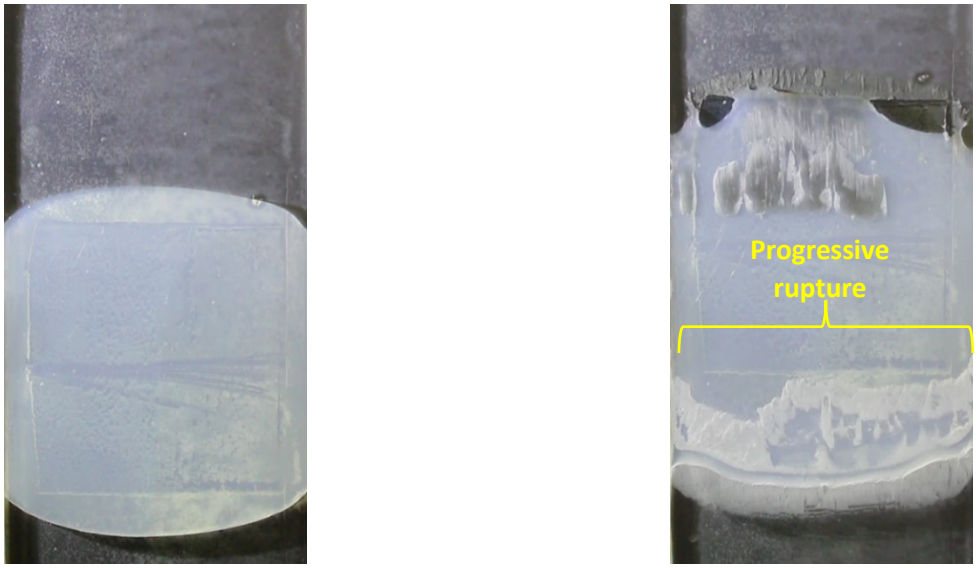

a. Before experiment starts (time=0 s)

b. Progressive rupture from steel plate (time=4.3 s)

Figure 5.5. Progressive and finger-like rupture: Glass-Csteel set up at the rate of 4 s^{-1}

If rupture starts on the steel plate, it will initiate from the blue point in **Figure 5.1c**, and for the case of initiation on the glass plate, it starts from the yellow point[16,77] as explained in the introduction. This behavior has been explored previously without slip with the rupture being attributed to adhesive failure[16,77]. It is interesting that we have the same observations in the presence of cohesive slip.

The rupture type and onset time for rupture is summarized in **Table 5.3**. In the glass-stationary plate / steel-moving plate setup, the rupture initiates solely on the steel surface. In this setup, after the experiment, the specimen is left on the glass plate and only the surface originally in contact with the steel plate is rough as shown in **Figure 5.6**. This confirms that the rupture initiated at the steel plate.

When rupture initiates from both stationary and moving plates, the specimen is split into two parts. Each part has a rough, rupture surface and a smooth surface which was originally in contact with the plate.

a.  b. 

Figure 5.6. Images of the specimen deformed at a nominal rate of 1 s^{-1}, showing the side of specimen that was in contact with glass (a) and the rupture surface originally in contact with steel (b).

With the coated steel plate (glass-Csteel setup), we observed the initiation of rupture on both steel and glass plates. The rupture initiates at different times on the two plates though with it occurring first on the coated steel plate at low rates (1 and 2 s^{-1}) and occurring first on the glass plate at higher rates of 4 and 10 s^{-1}. These observations are interesting because with the glass-steel system we do not observe rupture initiation on glass under any rate. The coating also changes the rupture type from finger-like to mostly progressive on the steel plate while the glass plate-initiated rupture was mostly finger-like. The coating had little if any effect on the slip velocity at the steel surface and there appears to be no correlation between slip velocity and rupture type or initiation location. This indicates that while slip velocity always occurs before rupture, it is certainly not the only parameter affecting it.

In the third setup, both stationary and moving plates were coated with PTFE (CGlass-CSteel setup). In this case, as with the Glass-CSteel setup, rupture initiated on both plates. The coated glass plate, however, initiated edge rupture at lower nominal shear rates of 1 and 2 s^{-1} and progressive rupture at higher nominal shear rates of 4 and 10 s^{-1}.

In the Cglass-Csteel setup the slip on the coated glass was lower than that on the bare glass in the glass-Csteel setup while the maximum slip on the coated steel increased. This is a type of rebalancing due to both coated surfaces being similar in terms of surface energy.

In the third set up, surprisingly, the rupture at the glass initiated at an earlier time than that on the steel. In other setups, the rupture either first or only initiated on steel. This shows that both the substrate surface and coating play a role on the rupture behavior of the materials. We recall that the coating is swept along with the slipping melt acting more like a lubricant than a permanent coating.

In the roughened glass-stationary plate / steel-moving plate setup, surprisingly, the specimen ruptured solely on the steel plate just as in the glass-steel setup.

Table 5.3. Rupture type and onset time (s) for rupture for different setups								
Rate (s^{-1})	1		2		4		10	
	Onset time for rupture	Rupture Type	Rupture Time (s)	Rupture Type	Rupture Time (s)	Rupture Type	Rupture Time (s)	Rupture Type
Glass stationary plate- Steel moving plate setup								
Glass	N/A	N/A	N/A	N/A	N/A	N/A	N/A	N/A
Steel	13.40	Finger-like	5.93	Finger-like	2.30	Finger-like	0.93	Finger-like
Glass stationary plate- Coated steel moving plate setup								
Glass	7.00	initiated on borders then finger-like	5.87	Finger-like	1.73	Finger-like	0.73	Finger-like
Coated Steel	6.97	initiated on borders then progressive	4.97	Progressive	2.53	Progressive and then finger-like	1.03	Progressive
Coated glass stationary plate- Coated steel moving plate setup								
Coated Glass	3.97	edge rupture	2.43	edge rupture	1.63	Progressive then finger-like	0.60	Progressive then finger-like
Coated Steel	5.57	initiated on edges then progressive	3.60	initiated on edges then progressive	2.13	Progressive	0.87	Progressive
Rough glass stationary plate- Steel moving plate setup								
Rough Glass	N/A	N/A	N/A	N/A	N/A	N/A	N/A	N/A
Steel	9.23	Finger-like	4.50	Finger-like	2.00	Finger-like	0.6	Finger-like

5. 4. 3. Onset time for rupture

The onset time for rupture versus apparent shear rate in different setups is presented in **Figure 5.7** where we see a power law relationship. In cases that rupture occurs at both surfaces, the shorter time is taken as the onset time. From these data we conclude that coating lowers the time-to-rupture onset whether it is on the steel moving plate or both plates (**Figure 5.7a**). This conclusion is important since it shows that lubricating the surface might change the rupture behavior separate to the effects on the slip velocity. Similarly, roughening the glass plate reduced the onset time for rupture although it did not lower the slip velocity (**Figure 5.7b**). An interesting feature about the **Figure 5.7** is the effect of the surface characteristics of the plates on the power law exponent. Coating, whether on glass or steel decreases the power law exponent while, roughening the glass surface does not change the exponent.

Previously we have shown that the slip of these bimodal polyethylenes[90] is primarily cohesive, leaving debris behind, but with some adhesive failure occurring as well. The slip mechanism approaches adhesive failure on coated plates[71] (while still exhibiting some cohesive nature). The change in slip mechanism may be contributing to the change in onset time for rupture and power law exponent seen in **Figure 5.7a**. During cohesive slip, progressive disentanglement of the bulk chains from the adsorbed chains at the wall perhaps reduces the chance of the catastrophic cohesive failure of melt rupture. There is no such gradual transition in adhesive slip.

In the case of the rough glass, we see a reduction in the onset time for rupture with no observable effect on slip velocity.

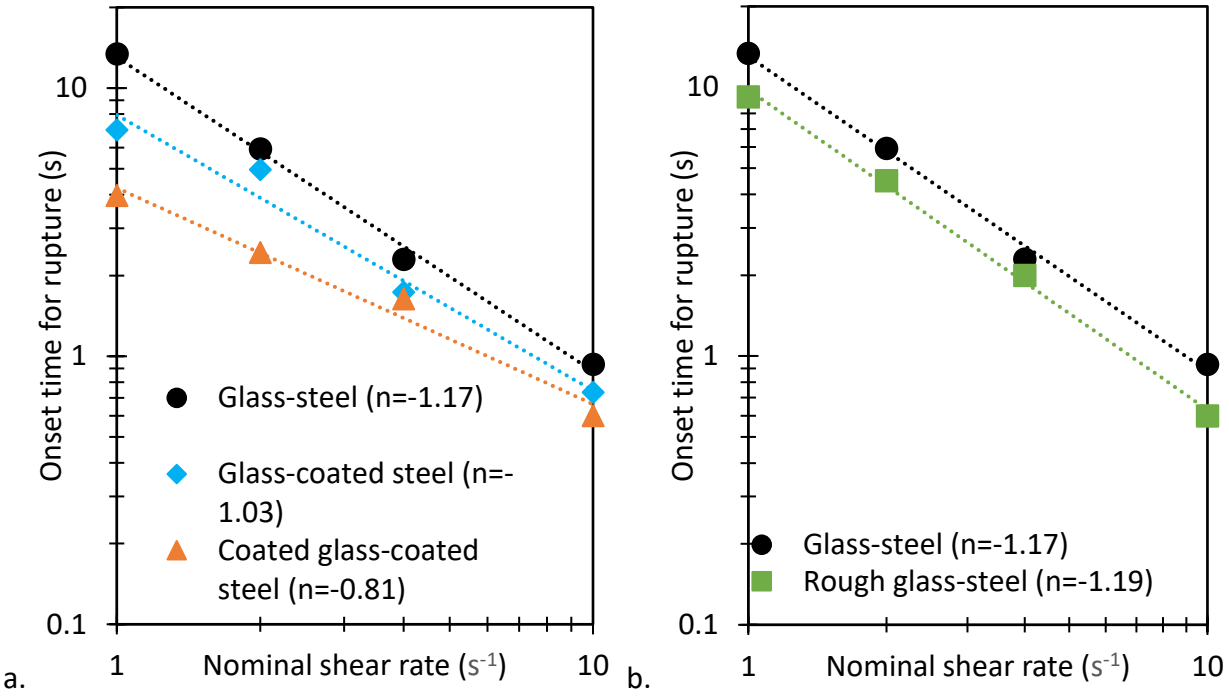

Figure 5.7. Onset time for rupture versus nominal shear rate. Effect of coating (a), and of roughening (b)

Another interesting observation is that just before rupture is about to happen, the common line recedes. This is consistent with the predictions of Dhori et al.[16,77] about melt rupture in the absence of cohesive slip. In our case, slip continues while the common line recedes, until rupture starts and then it stops.

It is interesting to look at the movement of the common lines I and II, before and after melt rupture. These lines move due to slip and therefore give us a measure of slip velocity. The transient velocity of the two lines is presented in **Figure 5.8**. Before the onset of rupture, the velocities of the two borders are essentially the same and equal to the slip velocity on the stationary plate. After rupture happens, common line I stops moving and common line II continues moving. This means that as of rupture onset, we have measurable, nonuniform deformation and the specimen will have ruptured and intact portions, as shown in **Figure 5.8**. The velocity of common line II remains constant until the rupture front has passed through most of the sample and then becomes erratic and slowly decreases. This likely means that the state of deformation and slip velocity remains the same in the intact portion of the specimen through

most of the rupture process. The increase in the length of the specimen during rupture, is balanced by a decrease in the thickness of the ruptured portion. This was confirmed by CTscan analysis of the final ruptured specimen.

The fact that rupture starts after slipping and after a steady plateau is reached in the slip velocity (**Figure 5.8**) and stress[2] transient curves is very interesting. During the rupture process, the material behind the rupture front stops slipping. This indicates that there is a time-dependent, structural phenomenon, probably at the interface, leading to situation where slip is insufficient to mediate stress. Interfacial molecular fractionation,[90,133] chain conformation and entanglement densities are likely factors at play. These phenomena are time-dependent and localised at the interface. We have previously observed surface fractionation of short chains under slip with these bimodal polyethylenes.[90,133] It is possible that the accumulation of short chains changes the interface such that melt rupture is more favorable than cohesive slip, both related to disentanglement. A change of conformation and thus entanglement density of interfacial chains is known to happen during the transition to strong slip through disentanglement, but it is also possible that the structuring continues to change while undergoing strong slip leading eventually to rupture.

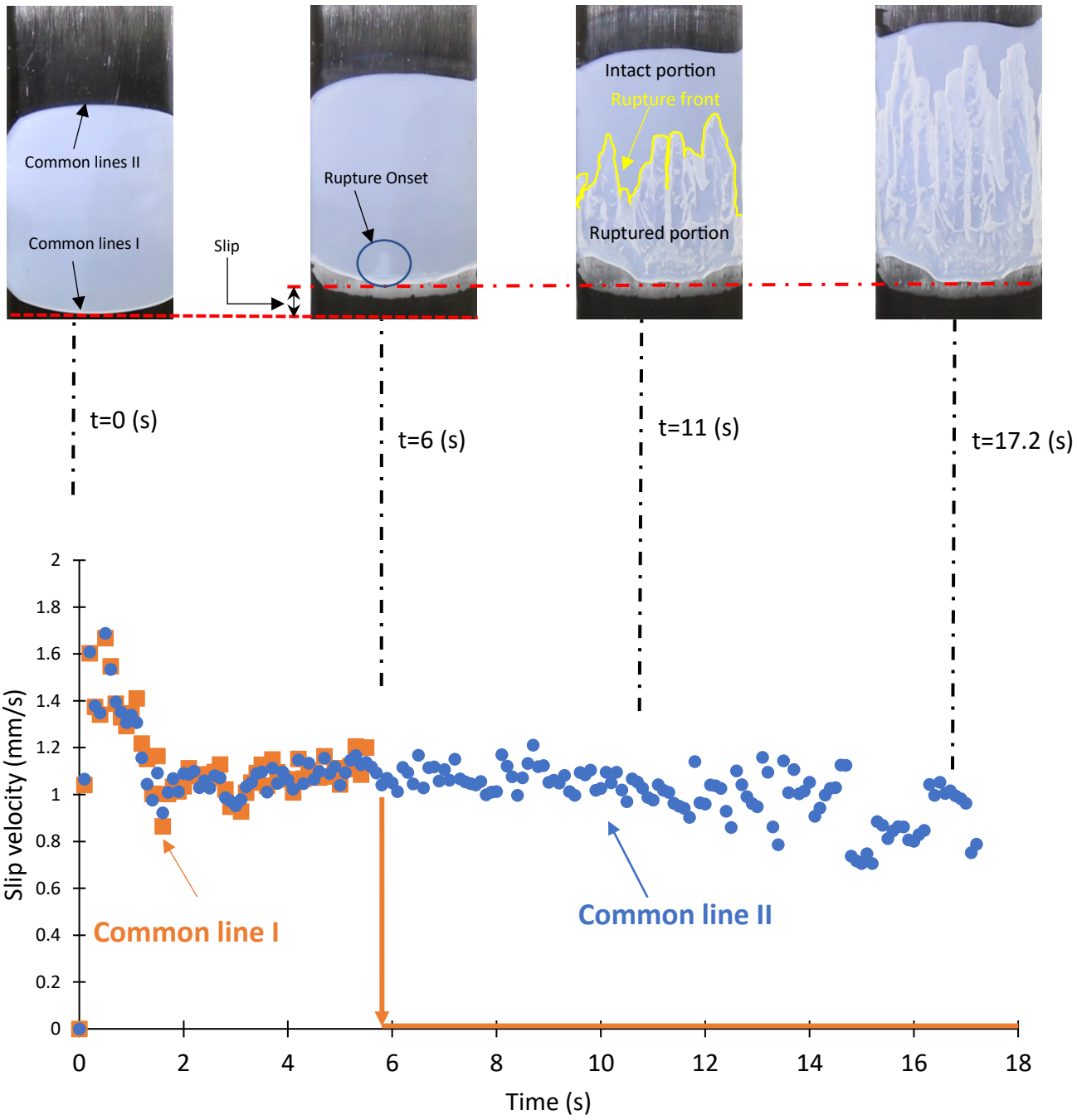

Figure 5.8. Slip velocity transient curve for the rate of 2 s^{-1} for the glass stationary plate-steel moving plate setup

5. 4. 4. Rupture front velocity

In the glass-steel setup, the rupture type is finger-like as shown in **Figure 5.9**. The displacement of the finger-like front 2 (**Figure 5.9**) is presented in **Figure 5.10**. In **Figure 5.10**, the

discontinuity in the curve or step changes in the displacement is shown by an arrow. These step changes are due to merging of the fronts. When two fronts are approaching to each other (**Figure 5.9a**), after some time they merge (**Figure 5.9b**) and a step change in displacement happens (**Figure 5.9c**). The rupture front velocity versus time for three different fronts are presented in **Figure 5.11**. When rupture starts, the rupture front velocity is very high, and it decreases approaching the moving plate velocity over time. This behavior is observed for conditions under which finger-like rupture occurs.

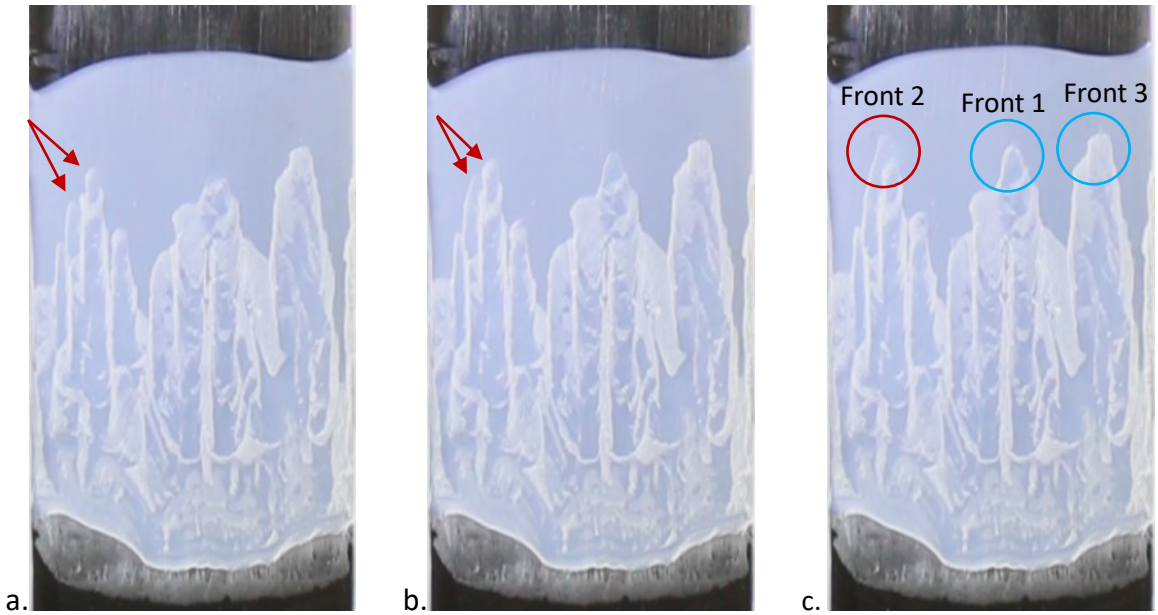

Figure 5.9. Merging of two finger-like rupture fronts at a rate of 2 s^{-1} for the glass stationary plate-steel moving plate setup: a. two finger-like fronts approaching, b. two finger-like fronts merging, and c. step-change in displacement by merging (red circle)

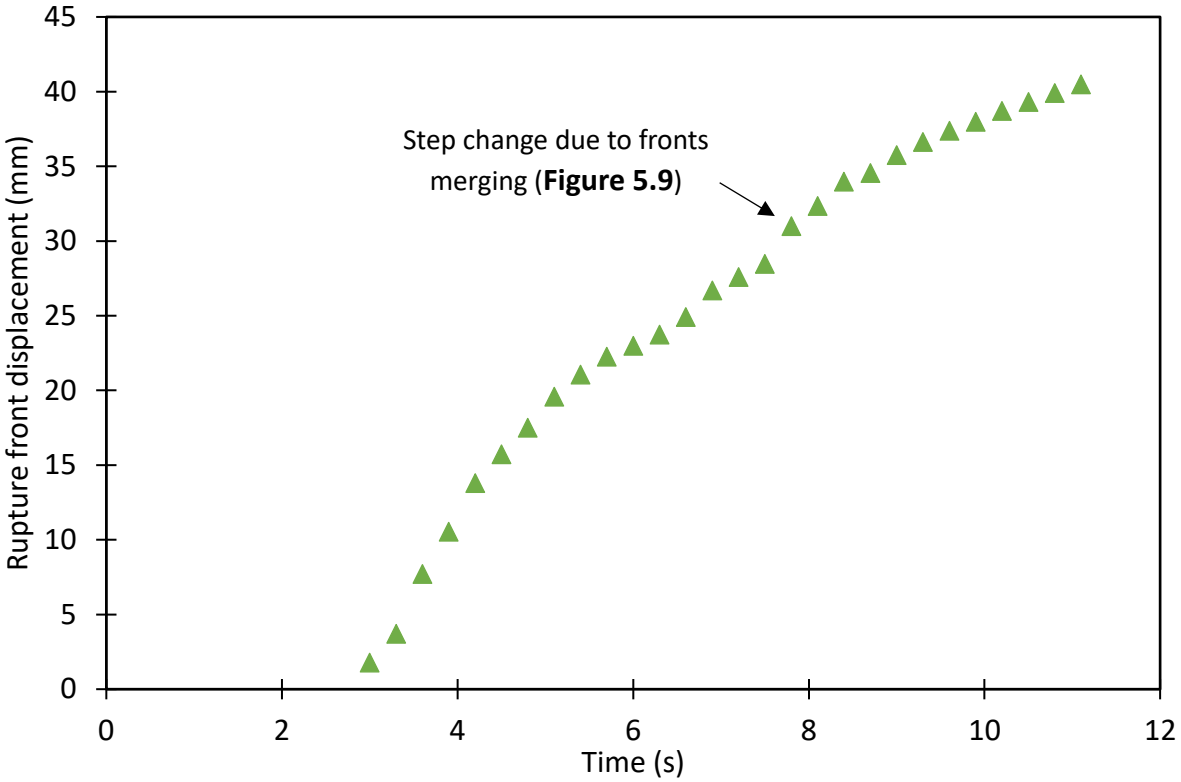

Figure 5.10. The displacement of the finger-like front 2 (**Figure 5.9**) versus time for the rate of 2 s^{-1} for the glass stationary plate-steel moving plate setup

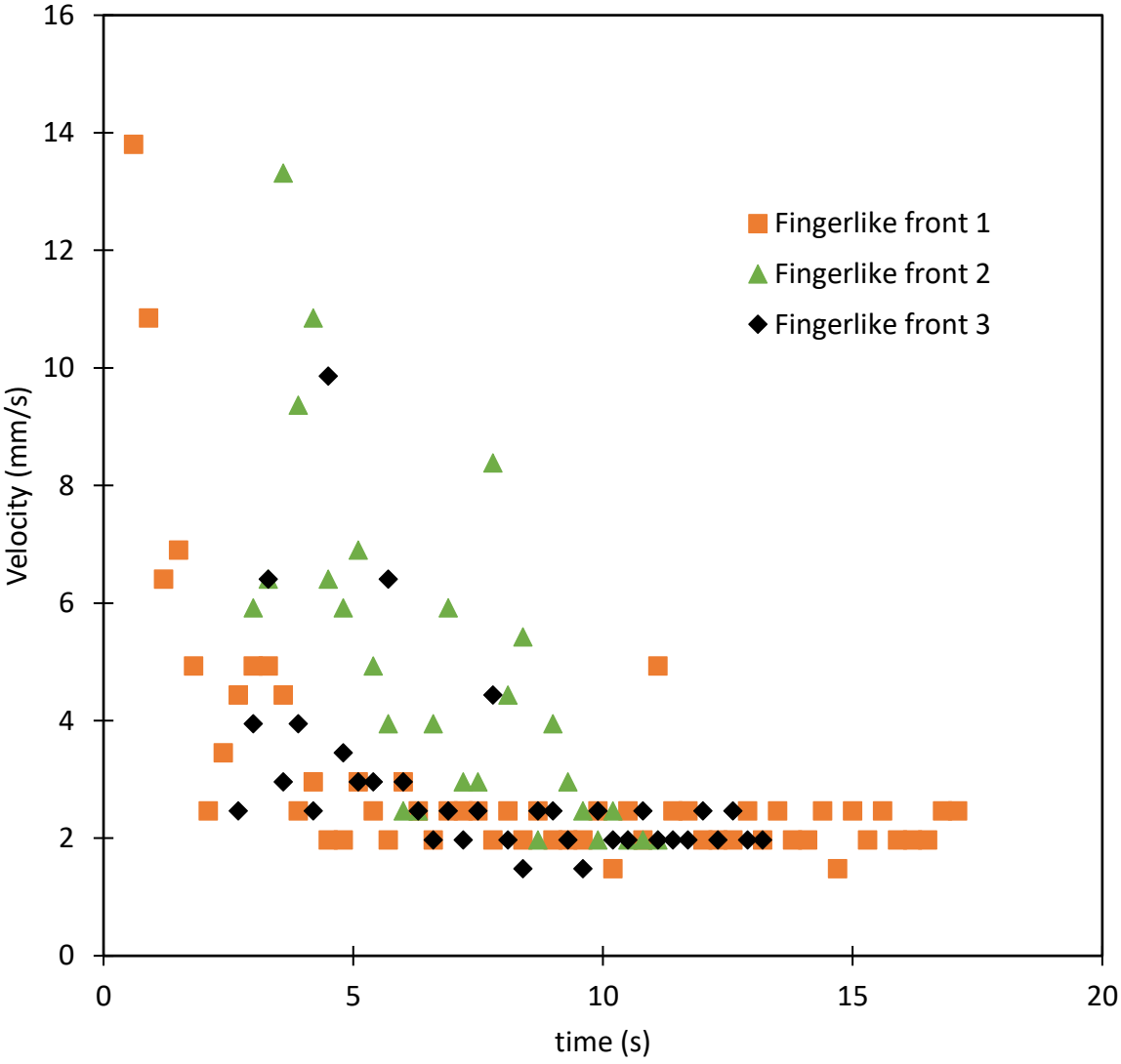

Figure 5.11. Transient rupture front propagation velocity of three different finger-like fronts at a rate of 2 s^{-1} for the glass stationary plate-steel moving plate setup

5. 4. 5. CT-scan imaging

To better understand the deformation that happens during melt rupture, the ruptured specimen is collected after cooling down and CTscan imaging is conducted. The thickness map of a ruptured specimen for the glass-steel setup and the rate of 2 s^{-1} is presented in **Figure 5.12**. At the borders the thickness is close to the gap (1 mm) and it decreases as we move in the rupture

direction. The interesting feature in these results is that they confirm that the observed melt rupture is a bulk defect rather than a surface defect. In capillary studies, it is commonly accepted that defects that are within 10% of the thickness/diameter are surface defects[184]. In **Figure 5.12**, the rupture extends to at least 50% of the cross-section indicating a bulk defect and is thus closer to gross melt fracture than sharkskin observed in capillary studies.

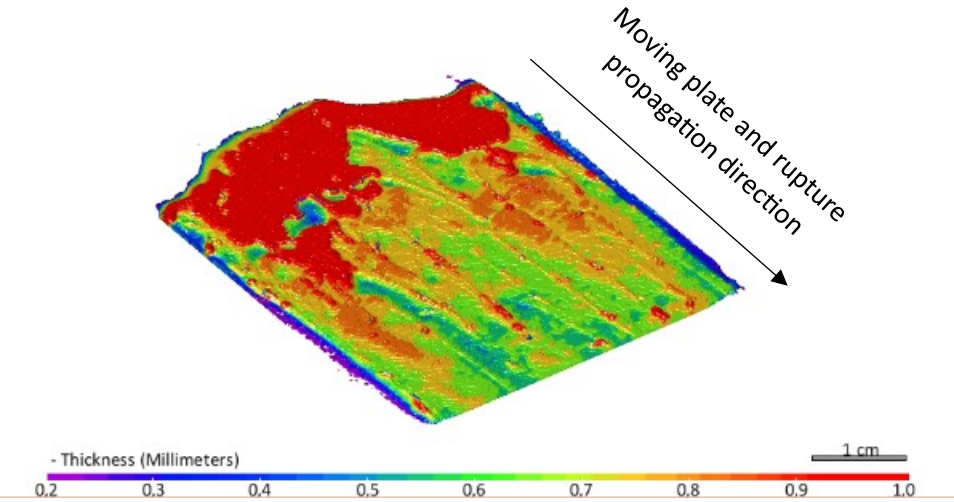

Figure 5.12. CT-Scan image of the ruptured specimen the rate of 2 s^{-1} for the glass stationary plate-steel moving plate setup

In the case that rupture initiates on both plates, the specimen splits into two fragments. The two fragments of the ruptured specimen for the Cglass-csteel set up are presented in **Figure 5.13** where the rupture propagation and moving plate directions are shown by the black and blue arrows respectively. It should be noted that the rupture starting on the coated glass plate (**Figure 5.13a**) propagates in the opposite direction of the moving plate. We also note that its front gradually passes through the bulk thickness (**Figure 5.13a**). This can be compared to the rupture front initiated on the coated steel plate (**Figure 5.13b**) which rapidly passes through to ~50% of the specimen thickness.

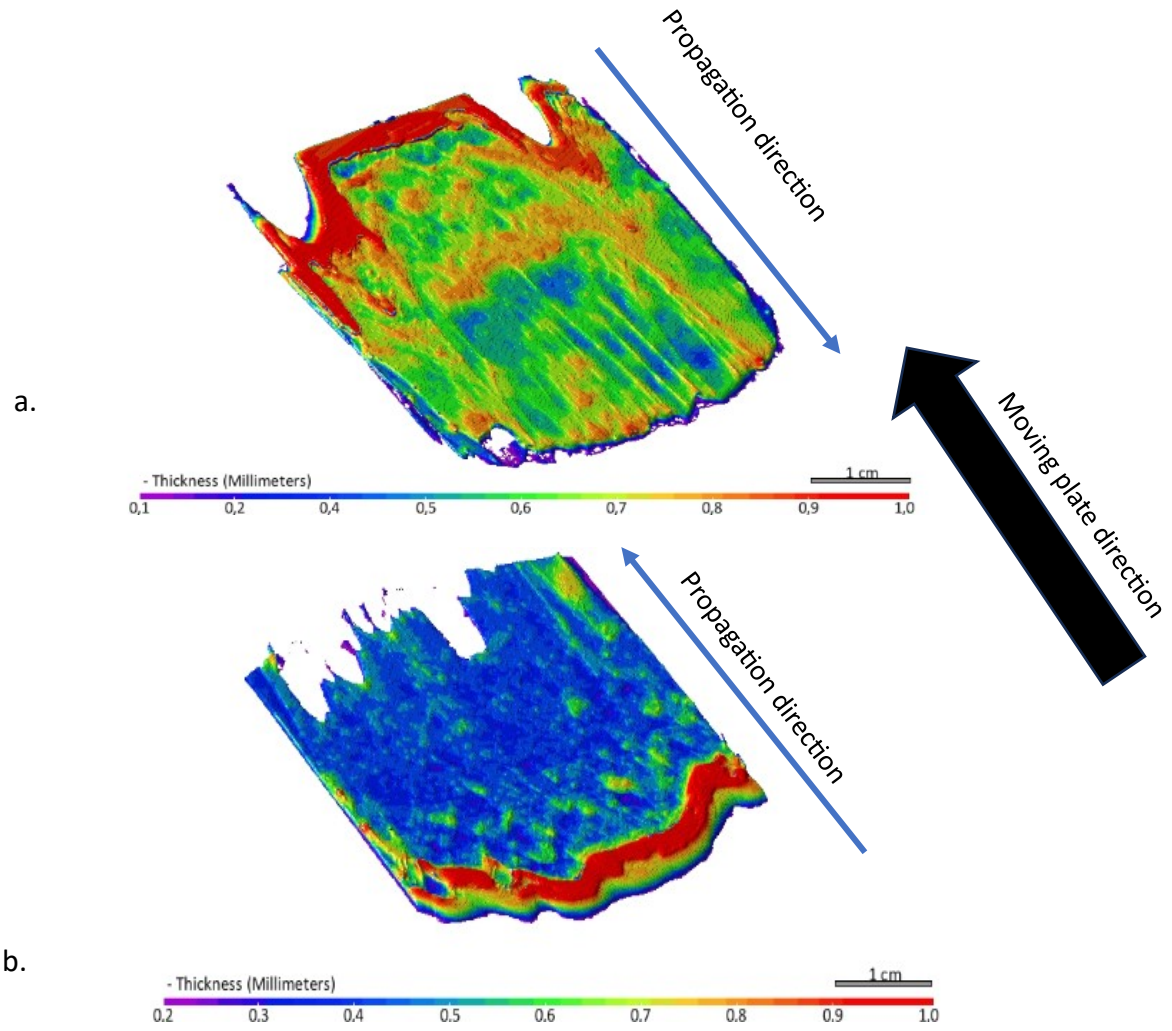

Figure 5.13. CT-Scan image of the ruptured specimen at a rate of 4 s^{-1} for the coated glass stationary plate-coated steel moving plate setup: a. The rupture surface initiated on the coated glass plate. b. The rupture surface initiated on the coated steel plate. Only the ruptured surfaces are shown.

5. 4. 6. Steel-steel setup

In our previous slip studies[2], the moving and stationary plates are both stainless steel and a shear stress transducer records the stress. The output of flow studies with the transducer is the stress transient curve (**Figure 5.14**). In the stress transient, there is a stress overshoot at short times that happens due to non-linear viscoelasticity and is modified in shape by slip. With slip, the steady state stress is lower than that under the no-slip condition, here estimated from small amplitude oscillatory shear (SAOS) data assuming the Cox-Merz rule[2] (**Figure 5.14**).

After the stress plateau, melt rupture happens (for the case of HDPE 9) and stress drops to zero. The time that it takes for the stress to drop to zero can be related to the propagation of the rupture front. It should be noted that we expect that in the steel-steel setup, rupture initiates from both stationary and moving plates due to boundary condition symmetry. Therefore, the time that it takes until the stress drops to zero could be related to two fronts reaching the active face of the transducer. However, we cannot say exactly at what point the stress signal starts being affected by the rupture front(s) and whether it is one front or two reaching the transducer. This depends on the initial placement of the specimen relative to the transducer and slip and varies slightly from test to test.

It should be noted that in an SPR test, two different phenomena can cause the stress to drop to zero: melt rupture and the sample slipping past the transducer[76]. In order to distinguish between the two phenomena, after each experiment, the rheometer set up is manually opened[76] and occurrence of the melt rupture is visually confirmed. For the case of HDPE 9, rupture happens at all nominal shear rates studied[2].

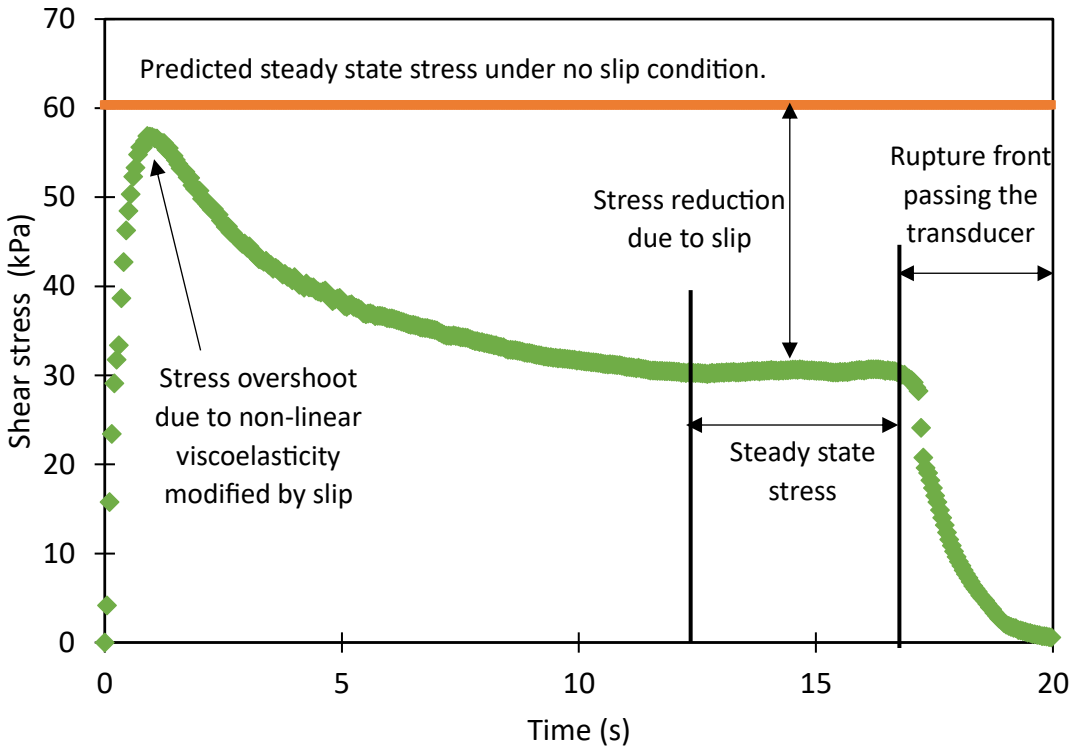

Figure 5.14. Shear stress versus time curve for the material HDPE 9 at a nominal shear rates of 2 s^{-1}

The duration from when a SPR test start (zero time) to when the stress plateau ends (time-to-stress-plateau-end) versus the nominal shear rate has been presented in the supplementary information.

To study the ruptured surfaces in the steel-steel setup, we conducted one experiment at the rate of 4 s^{-1}. We confirmed that the rupture initiated from both plates and two fragments were collected from the moving and stationary plates. The thickness maps of the ruptured fragments are presented in **Figure 5.15**. The thickness decreases in the rupture direction which is consistent with our observations in other set-ups. From these images, it seems that the rupture type is finger-like in both directions.

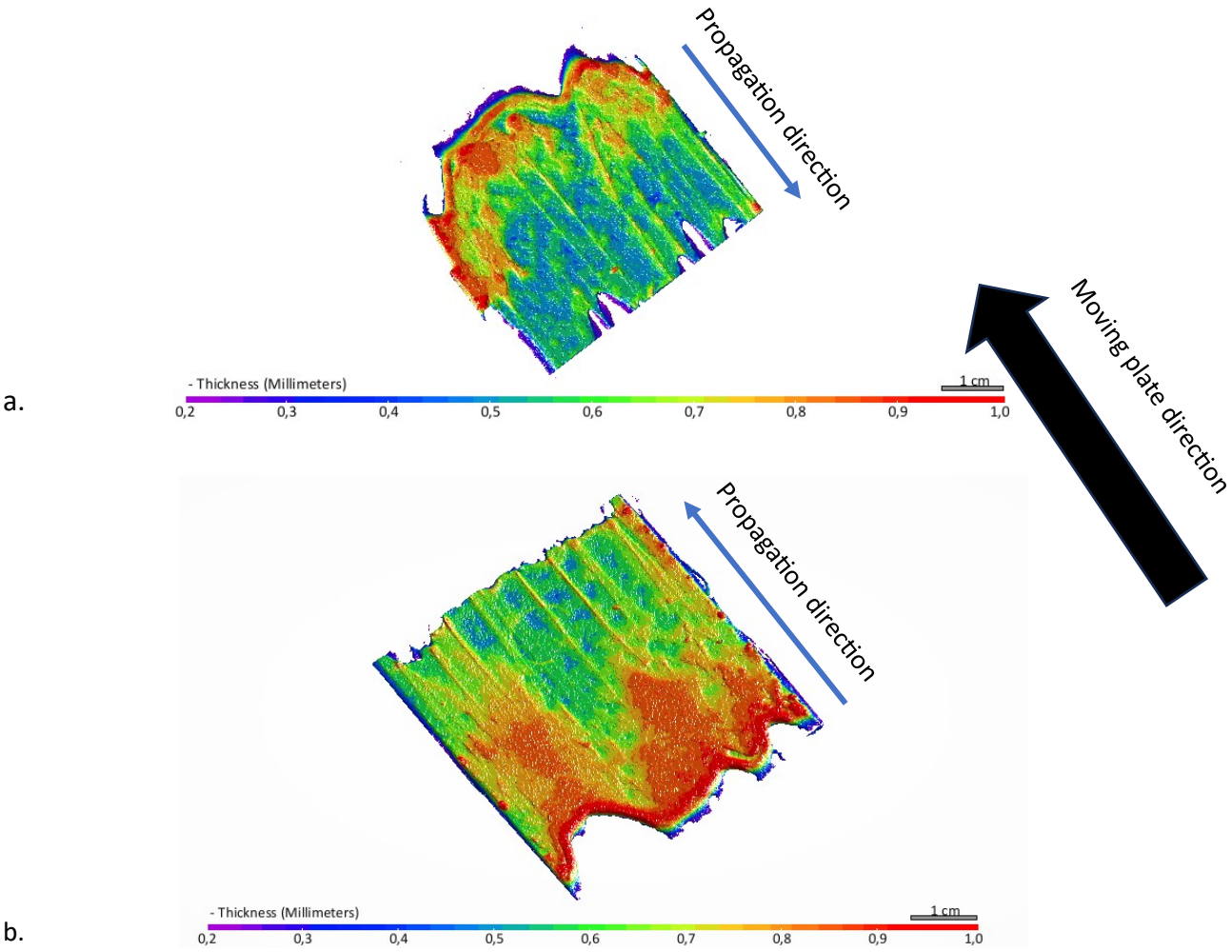

Figure 5.15. CT-Scan image of the ruptured specimen the rate of 4 s^{-1} for the steel-steel setup: a. The rupture surface initiated on the stationary plate. b. The rupture surface initiated on the moving plate. Only the ruptured surfaces are shown.

5. 5. Conclusion

Melt rupture of a bimodal polyethylene has been found to be a time-dependent phenomena that can happen after the steady state plateau in slip velocity and stress. Rupture happens at the three phase (polymer-air-plate) common line of rectilinear shear and propagates through the specimen. The rupture behavior over two surfaces, glass, and steel, was found to be very different. Rupture initiates on the steel side but not on the glass side of an uncoated, mixed plate sliding plate rheometer setup. The surface characteristics, roughness, and coating, play an important role in the rupture behavior of the material. The low surface energy PTFE coating aggravates the melt rupture in terms of time-to- rupture-onset (versus nominal shear rate) and changes the rupture type. A time-dependent phenomenon at the interface like fractionation, a

change in the entanglement density and/or a conformational change of the interfacial chains could be the reason for the switch from slip to melt rupture. We note that on uncoated steel and glass the slip is primarily cohesive in nature and switches to more adhesive-like slip with the coating. Thus, the type of slip may be an important factor influencing the type and kinetics of rupture.

Chapter 6. Conclusions and future work

The effect of the bimodal structure of polyethylene is studied in both solid and melt-states. In the solid-state studies, the effect of the structure was examined through the ethylene sequence length distribution. We observed that longer ethylene sequences originate from the low molecular weight population. This is due to the higher content of short branches in the high molecular weight population. The long ethylene sequence length in the low molecular weight population results in increased crystallinity, while the branched high molecular weight population forms tie chains, enhancing environmental stress crack resistance. In our materials, there is a relatively high content of low molecular weight population.

Additionally, the presence of this substantial amount of low molecular weight chains alters the melt-state properties. It significantly increases slip velocity and may induce structural changes during slip, potentially resulting in melt rupture. These structural changes could involve molecular fractionation, changes in entanglement density, or alterations in the interfacial configuration of chains. All of these phenomena are more likely for low molecular weight chains[2,68,90] and more studies are needed to better understand the structural changes during slip.

This thesis produced methods that can be applied to similar design problems with other polymers, and it illustrates that simultaneously optimising both solid-state and melt-state properties are extremely difficult. The findings of this thesis help resin manufacturers design the structure of bi-modal polyethylene for specific purposes. The detailed findings of this study are presented in the following section.

6. 1. Detailed Conclusions

In **Chapter 3**, we employed statistical modeling[6] to derive the ethylene sequence length distribution of our bimodal materials from experimental measurements of molecular weight and short chain branching distributions. Among the various distributions describing the structure of bimodal polyethylene, the ethylene sequence length distribution best characterizes the mechanical properties observed in the strain hardening test.

The natural draw ratio correlates with the weight-averaged ethylene sequence length. We use the natural draw ratio as a proxy for environmental stress crack resistance, given that a higher natural draw ratio corresponds to lower environmental stress crack resistance. Therefore, to produce materials with good environmental stress crack resistance, lower values of weight averaged ethylene sequence length are needed, as it facilitates the formation of more tie chains. This correlation is true for our materials with higher comonomer content in the higher molecular weight population. Further studies with a broader range of ethylene sequence length distributions would be required to generalize this conclusion. Additionally, the first (higher) peak temperature in the non-isothermal crystallization studies of our materials correlates with the weight averaged ethylene sequence length and, consequently, with the natural draw ratio. This offers a convenient method to rank developmental materials in terms of environmental stress crack resistance.

The first moment of the lamellar thickness distribution generated in successive self nucleation and annealing experiments correlates with the weight averaged ethylene sequence length and with the bimodal ratio of the ethylene sequence length distribution. From this, we believe that successive self-nucleation annealing experiments provide a quick and convenient method to explore the structural characteristics of such materials. Furthermore, we demonstrated that the second moment of the contribution of the high molecular weight population to crystallinity correlates with the natural draw ratio, indicating that the results of successive self-nucleation annealing can assist in ranking materials in terms of environmental stress crack resistance.

In **Chapter 4**, we studied the slip behavior of bimodal polyethylene under simple shear. Slip occurs across a wide range of stress in bimodal molecular weight distribution polyethylene under simple shear. The bimodal structure of polyethylene significantly influences its slip behavior through its low molecular weight content. This effect occurs in the weak and transition slip regions, as well as the stress at which strong slip starts. A higher content of low molecular weight shifts the slip velocity versus stress curve towards lower stresses. This shift is attributed to a decrease in disentanglement stress, leading to the relaxation of chains and molecular fractionation. Various slip regimes are evident in the slip velocity curves: weak, transition, and

strong slip regimes. The low molecular weight content impacts the material slip behavior across all stress values within the weak and transition region before the strong slip. A higher content of low molecular weight population corresponds to an elevated slip velocity in the weak and transition slip regimes. Once strong slip is fully established, the slip behavior becomes independent of molecular weight distribution, solely relying on stress.

The stress level at which the slip velocity becomes independent of molecular weight distribution decreases with an increase in short-chain content. The degree of entanglement between the interfacial and bulk chains drops sharply in the transition region based on friction of coefficient analysis.

Under simple shear, shear gradient induced molecular fractionation does not exist. The results of slip studies under simple shear can help better separate the effect of shear flow and shear gradient induced fractionation on the slip.

During the slip studies, we observed frequent occurrences of melt rupture in our materials. We looked deeper into this phenomenon using visualization techniques in **Chapter 5**. Melt rupture in bimodal polyethylene was identified as a time-dependent event that can occur after reaching the steady-state plateau in slip velocity and stress. The rupture occurs in the vicinity of the regions that join the three phases (polymer-air-plate) and propagates through the specimen.

The rupture behavior exhibited notable differences over two surfaces, namely glass and steel. Rupture initiation was observed on the steel side but not on the glass side of an uncoated mixed plate SPR setup. The presence of a low surface energy (PTFE) coating exacerbated melt rupture in terms of time-to-rupture-onset (at the same nominal shear rates). A time-dependent phenomenon at the interface, such as fractionation, change in entanglement density, or a conformational change in the interfacial chains, could explain the transition from slip to melt rupture. These phenomena mentioned above are more likely to happen when there is a high content of low molecular weight population in the system, which is the case for our materials. It should be noted that since we did not have a record of stress in the visualization studies, we used the nominal shear rate to study the time-to-rupture-onset.

6. 2. Future work

In **Chapter 3**, we demonstrated that the features of ethylene sequence length distribution control environmental stress cracking resistance and other mechanical properties. Further studies with a broader range of ethylene sequence length distribution are needed to generalize these findings. Specifically, designing materials with a broader range of shapes and types of ethylene sequence length distribution. For example, polyethylene materials having higher values of $R_{b,\ ESLD}$ would help better understand the effects of bimodality.

In **Chapter 4**, we showed that in our materials with a high content of low molecular weight chains, slip behavior is highly affected by this content. More studies with materials having lower low molecular weight content are needed to determine the optimum low molecular weight content that results in a more stable melt flow. These studies should consider the possible changes in the crystallinity and the mechanical properties as well.

In **Chapter 5**, we demonstrated that melt rupture could occur after a steady-state slip velocity and stress. Our hypothesis is that this is due to the interfacial changes that happen during slip. More studies are needed to better understand these interfacial structural changes. These studies could include characterisation methods to provide information about the interfacial chain orientation, like sum frequency generation (SFG)[196].

Bibliography

(1) Richards, R. B. Polyethylene-structure, Crystallinity and Properties. *J. Appl. Chem.* **1951**, *1* (8), 370–376. https://doi.org/10.1002/jctb.5010010812.

(2) Sattari, M.; Inn, Y.; Wood-Adams, P. M. Wall Slip of Bimodal Polyethylene. *Macromolecules* **2022**, *55* (11), 4568–4577.

(3) Sabzevari, S. M.; Cohen, I.; Wood-Adams, P. M. Wall Slip of Bidisperse Linear Polymer Melts. *Macromolecules* **2014**, *47* (9), 3154–3160. https://doi.org/10.1021/ma500451g.

(4) Sabzevari, S. M.; Cohen, I.; Wood-Adams, P. M. Wall Slip of Tridisperse Polymer Melts and the Effect of Unentangled versus Weakly Entangled Chains. *Macromolecules* **2014**, *47* (22), 8033–8040. https://doi.org/10.1021/ma501320d.

(5) *Multimodal Polymers with Supported Catalysts: Design and Production*; Albunia, A. R., Prades, F., Jeremic, D., Eds.; Springer International Publishing: Cham, 2019. https://doi.org/10.1007/978-3-030-03476-4.

(6) Costeux, S.; Anantawaraskul, S.; Wood-Adams, P. M.; Soares, J. B. Distribution of the Longest Ethylene Sequence in Ethylene/α-Olefin Copolymers Synthesized with Single-Site-Type Catalysts. *Macromolecular theory and simulations* **2002**, *11* (3), 326–341.

(7) Fawaz, J.; Deveci, S.; Mittal, V. Molecular and Morphological Studies to Understand Slow Crack Growth (SCG) of Polyethylene. *Colloid Polym Sci* **2016**, *294* (8), 1269–1280. https://doi.org/10.1007/s00396-016-3888-5.

(8) Robledo, N.; Domínguez, C.; García-Muñoz, R. A. Alternative Accelerated and Short-Term Methods for Evaluating Slow Crack Growth in Polyethylene Resins with High Crack Resistance. *Polymer Testing* **2017**, *62*, 366–372.

(9) Almomani, A.; Mourad, A.-H. I.; Deveci, S.; Wee, J.-W.; Choi, B.-H. Recent Advances in Slow Crack Growth Modeling of Polyethylene Materials. *Materials & Design* **2023**, 111720.

(10) Domínguez, C.; Robledo, N.; Paredes, B.; García-Muñoz, R. A. Strain Hardening Test on the Limits of Slow Crack Growth Evaluation in High Resistance Polyethylene Resins: Effect of Comonomer Type. *Polymer Testing* **2020**, *81*, 106155.

(11) Hatzikiriakos, S. G. Wall Slip of Molten Polymers. *Progress in Polymer Science* **2012**, *37* (4), 624–643. https://doi.org/10.1016/j.progpolymsci.2011.09.004.

(12) Park, H. E.; Lim, S. T.; Smillo, F.; Dealy, J. M.; Robertson, C. G. Wall Slip and Spurt Flow of Polybutadiene. *Journal of Rheology* **2008**, *52* (5), 1201–1239. https://doi.org/10.1122/1.2964199.

(13) Musil, J.; Zatloukal, M. Historical Review of Die Drool Phenomenon in Plastics Extrusion. *Polymer Reviews* **2014**, *54* (1), 139–184. https://doi.org/10.1080/15583724.2013.860987.

(14) Hatzikiriakos, S. G. Slip Mechanisms in Complex Fluid Flows. *Soft Matter* **2015**, *11* (40), 7851–7856. https://doi.org/10.1039/C5SM01711D.

(15) Ansari, M.; Inn, Y. W.; Sukhadia, A. M.; DesLauriers, P. J.; Hatzikiriakos, S. G. Wall Slip of HDPEs: Molecular Weight and Molecular Weight Distribution Effects. *Journal of Rheology* **2013**, *57* (3), 927–948. https://doi.org/10.1122/1.4801758.

(16) Dhori, P. K.; Giacomin, A. J.; Slattery, J. C. Common Line Motion II: Sliding Plate Rheometry. *Journal of non-newtonian fluid mechanics* **1997**, *71* (3), 215–229.

(17) Ansari, M.; Hatzikiriakos, S. G.; Sukhadia, A. M.; Rohlfing, D. C. Melt Fracture of Two Broad Molecular Weight Distribution High-Density Polyethylenes. *Polymer Engineering & Science* **2012**, *52* (4), 795–804.
(18) Ansari, M.; Inn, Y. W.; Sukhadia, A. M.; DesLauriers, P. J.; Hatzikiriakos, S. G. Melt Fracture of HDPEs: Metallocene versus Ziegler–Natta and Broad MWD Effects. *Polymer* **2012**, *53* (19), 4195–4201.
(19) Sperling, L. H. *Introduction to Physical Polymer Science*; John Wiley & Sons, 2005.
(20) Peacock, A. J.; Calhoun, A. *Polymer Chemistry: Properties and Application*; Carl Hanser Verlag GmbH Co KG, 2012.
(21) Raj, R. Experimental Validation of the Molecular Weight Distribution (MWD) and Chemical Composition Distribution (CCD) Deconvolution Method for Polyolefins Made with Ziegler-Natta Catalysts. Master of Science, University of Alberta, 2021. https://era.library.ualberta.ca/items/b71010ef-2451-43a0-8ef6-784787837373 (accessed 2023-11-13).
(22) Boyron, O.; Taam, M.; Boisson, C. Chemical Composition of Hexene-Based Linear Low-Density Polyethylene by Infrared Spectroscopy and Chemometrics. *Macro Chemistry & Physics* **2019**, *220* (24), 1900376. https://doi.org/10.1002/macp.201900376.
(23) Wood-Adams, P. M.; Dealy, J. M.; Degroot, A. W.; Redwine, O. D. Effect of Molecular Structure on the Linear Viscoelastic Behavior of Polyethylene. *Macromolecules* **2000**, *33* (20), 7489–7499.
(24) Xu, X.; Xu, J.; Feng, L.; Chen, W. Effect of Short Chain-Branching Distribution on Crystallinity and Modulus of Metallocene-Based Ethylene–Butene Copolymers. *Journal of applied polymer science* **2000**, *77* (8), 1709–1715.
(25) Yu, Y. A Short-Chain Branching Distribution Determination Technique for Polyethylene Using IR5-Detected GPC. *Macromolecular Symposia* **2020**, *390* (1), 1900014.
(26) Soares, J. B. P.; Kim, J. D.; Rempel, G. L. Analysis and Control of the Molecular Weight and Chemical Composition Distributions of Polyolefins Made with Metallocene and Ziegler−Natta Catalysts. *Ind. Eng. Chem. Res.* **1997**, *36* (4), 1144–1150. https://doi.org/10.1021/ie960479x.
(27) Starck, P.; Malmberg, A.; Löfgren, B. Thermal and Rheological Studies on the Molecular Composition and Structure of Metallocene- and Ziegler–Natta-catalyzed Ethylene–A-olefin Copolymers. *J of Applied Polymer Sci* **2002**, *83* (5), 1140–1156. https://doi.org/10.1002/app.10152.
(28) Ramachandran, R.; Beaucage, G.; Kulkarni, A. S.; McFaddin, D.; Merrick-Mack, J.; Galiatsatos, V. Persistence Length of Short-Chain Branched Polyethylene. *Macromolecules* **2008**, *41* (24), 9802–9806.
(29) Bovey, F. A.; Schilling, F. C.; McCrackin, F. L.; Wagner, H. L. Short-Chain and Long-Chain Branching in Low-Density Polyethylene. *Macromolecules* **1976**, *9* (1), 76–80.
(30) Costeux, S.; Wood-Adams, P.; Beigzadeh, D. Molecular Structure of Metallocene-Catalyzed Polyethylene: Rheologically Relevant Representation of Branching Architecture in Single Catalyst and Blended Systems. *Macromolecules* **2002**, *35* (7), 2514–2528. https://doi.org/10.1021/ma011432c.

(31) Anantawaraskul, S. Chemical Composition Distribution of Binary and Multicomponent Copolymers. PhD Thesis, McGill University, 2003. https://escholarship.mcgill.ca/concern/theses/cr56n165j.
(32) Moteki, Y.; Okabe, M.; Takahashi, M.; Matsuda, H. Study of Polyolefin Gel in Organic Solvents IX. Ethylene Sequence Distribution of Ethylene–Propylene Random Copolymer and Crystalline Junction Size in Its Thermoreversible Gel. *Polymer journal* **1994**, *26* (9), 1002–1012.
(33) Zhang, F.; Liu, J.; Fu, Q.; Huang, H.; Hu, Z.; Yao, S.; Cai, X.; He, T. Polydispersity of Ethylene Sequence Length in Metallocene Ethylene/A-olefin Copolymers. I. Characterized by Thermal-fractionation Technique. *J Polym Sci B Polym Phys* **2002**, *40* (9), 813–821. https://doi.org/10.1002/polb.10145.
(34) Cao, Y.; Zhao, L.; Wang, J.; Shao, Y.; He, X. Molecular Dynamics Simulation of Extension-Induced Crystallization of Branched Bimodal HDPE: Unraveling the Effects of Short-Chain Branches. *Physical Chemistry Chemical Physics* **2021**, *23* (35), 19862–19871.
(35) Nilsson, F.; Lan, X.; Gkourmpis, T.; Hedenqvist, M. S.; Gedde, U. W. Modelling Tie Chains and Trapped Entanglements in Polyethylene. *Polymer* **2012**, *53* (16), 3594–3601.
(36) Gu, K.; Onorato, J. W.; Luscombe, C. K.; Loo, Y.-L. The Role of Tie Chains on the Mechano-Electrical Properties of Semiconducting Polymer Films. *Advanced Electronic Materials* **2020**, *6* (4), 1901070.
(37) McDermott, A. G.; DesLauriers, P. J.; Fodor, J. S.; Jones, R. L.; Snyder, C. R. Measuring Tie Chains and Trapped Entanglements in Semicrystalline Polymers. *Macromolecules* **2020**, *53* (13), 5614–5626.
(38) Lu, Y.; Lyu, D.; Xiong, B.; Chen, R.; Men, Y. Inter-Fibrillar Tie Chains Determined Critical Stress of Large Strain Cavitation in Tensile Stretched Isotactic Polypropylene. *Polymer* **2018**, *138*, 387–395.
(39) Seguela, R. Critical Review of the Molecular Topology of Semicrystalline Polymers: The Origin and Assessment of Intercrystalline Tie Molecules and Chain Entanglements. *J Polym Sci B Polym Phys* **2005**, *43* (14), 1729–1748. https://doi.org/10.1002/polb.20414.
(40) Zhou, H.; Wilkes, G. L. Creep Behaviour of High Density Polyethylene Films Having Well-Defined Morphologies of Stacked Lamellae with and without an Observable Row-Nucleated Fibril Structure. *Polymer* **1998**, *39* (16), 3597–3609.
(41) Hu, Y.; Shao, Y.; Liu, Z.; He, X.; Liu, B. Effect of Short-Chain Branching on the Tie Chains and Dynamics of Bimodal Polyethylene: Molecular Dynamics Simulation. *European Polymer Journal* **2018**, *103*, 312–321.
(42) DesLauriers, P. J.; Lamborn, M. J.; Fodor, J. S. Correlating Polyethylene Microstructure to Stress Cracking; Correlations to Post Yield Tensile Tests. *Polymer* **2018**, *153*, 422–429.
(43) Thuy, M.; Pedragosa-Rincón, M.; Niebergall, U.; Oehler, H.; Alig, I.; Böhning, M. Environmental Stress Cracking of High-Density Polyethylene Applying Linear Elastic Fracture Mechanics. *Polymers* **2022**, *14* (12), 2415.
(44) Deveci, S.; Fang, D. Correlation of Molecular Parameters, Strain Hardening Modulus and Cyclic Fatigue Test Performances of Polyethylene Materials for Pressure Pipe Applications. *Polymer Testing* **2017**, *62*, 246–253.
(45) Polak, M. A. Analysis of Polyethylene Pipe Behaviour in Horizontal Directional Drilling Field Tests. *Canadian Journal of Civil Engineering* **2005**, *32* (4), 665–677.

(46) Lueke, J. S.; Ariaratnam, S. T. Rehabilitation of Underground Infrastructure Utilizing Trenchless Pipe Replacement. *Practice periodical on structural design and construction* **2001**, *6* (1), 25–34.
(47) Zhang, Y.; Jar, P.-Y. B.; Xue, S.; Han, L.; Li, L. Measurement of Environmental Stress Cracking Resistance of Polyethylene Pipe: A Review. In *ASME Asia Pacific Pipeline Conference*; American Society of Mechanical Engineers, 2019; Vol. 58912, p V001T10A001.
(48) Deblieck, R. A.; Van Beek, D. J. M.; Remerie, K.; Ward, I. M. Failure Mechanisms in Polyolefines: The Role of Crazing, Shear Yielding and the Entanglement Network. *Polymer* **2011**, *52* (14), 2979–2990.
(49) Zhang, Y.; Xiang, A.; Lu, X.; Zhou, H.; Yin, D.; Tian, H. Research on Slow Crack Growth Resistance of Polyethylene Pipe Based on Strain Hardening Modulus. *Vinyl Additive Technology* **2022**, *28* (1), 226–234. https://doi.org/10.1002/vnl.21885.
(50) Xiong, B.; Lame, O.; Chenal, J.-M.; Rochas, C.; Seguela, R.; Vigier, G. Amorphous Phase Modulus and Micro–Macro Scale Relationship in Polyethylene via in Situ SAXS and WAXS. *Macromolecules* **2015**, *48* (7), 2149–2160.
(51) Gobetti, A.; Ramorino, G. Application of Short-Term Methods to Estimate the Environmental Stress Cracking Resistance of Recycled HDPE. *Journal of Polymer Research* **2020**, *27* (11), 353.
(52) van der Stok, E.; Scholten, F. Strain Hardening Tests on PE Pipe Materials. *Proceedings of Plastic Pipes XVI (Barcelona, 24.–26.09. 2012)* **2012**.
(53) Séguéla, R. On the Natural Draw Ratio of Semi-Crystalline Polymers: Review of the Mechanical, Physical and Molecular Aspects. *Macro Materials & Eng* **2007**, *292* (3), 235–244. https://doi.org/10.1002/mame.200600389.
(54) van der Stok, E. J. W. Testing Parameters Influencing the Strain Hardening Modulus. *Proceeding of Plastic Pipes* **2018**, *19*, 24–28.
(55) Wang, Z.; Zhai, W.; Yang, B.; Xin, M.; Li, M.; Yin, X. B. Polyethylene Resins Slow Crack Growth Testing Based on Strain Hardening Modulus and Crystallinity. In *2020 3rd International Conference on Electron Device and Mechanical Engineering (ICEDME)*; IEEE, 2020; pp 569–572.
(56) Kurelec, L.; Teeuwen, M.; Schoffeleers, H.; Deblieck, R. Strain Hardening Modulus as a Measure of Environmental Stress Crack Resistance of High Density Polyethylene. *Polymer* **2005**, *46* (17), 6369–6379.
(57) Sattari, M.; Mirsalehi, S. A.; Khavandi, A.; Alizadeh, O.; Naimi-Jamal, M. R. Non-Isothermal Melting and Crystallization Behavior of UHMWPE/SCF/Nano-SiO2 Hybrid Composites. *J Therm Anal Calorim* **2015**, *122* (3), 1319–1330. https://doi.org/10.1007/s10973-015-5003-4.
(58) Zhuravlev, E.; Madhavi, V.; Lustiger, A.; Androsch, R.; Schick, C. Crystallization of Polyethylene at Large Undercooling. *ACS Macro Lett.* **2016**, *5* (3), 365–370. https://doi.org/10.1021/acsmacrolett.5b00889.
(59) *Thermal Analysis of Polymers: Fundamentals and Applications*, 1st ed.; Menczel, J. D., Prime, R. B., Eds.; Wiley, 2009. https://doi.org/10.1002/9780470423837.
(60) Hosoda, S.; Nozue, Y.; Kawashima, Y.; Suita, K.; Seno, S.; Nagamatsu, T.; Wagener, K. B.; Inci, B.; Zuluaga, F.; Rojas, G.; Leonard, J. K. Effect of the Sequence Length Distribution on the Lamellar Crystal Thickness and Thickness Distribution of Polyethylene: Perfectly

Equisequential ADMET Polyethylene vs Ethylene/α-Olefin Copolymer. *Macromolecules* **2011**, *44* (2), 313–319. https://doi.org/10.1021/ma102072p.
(61) Müller, A. J.; Lorenzo, A. T.; Arnal, M. L. Recent Advances and Applications of "Successive Self-Nucleation and Annealing" (*SSA*) High Speed Thermal Fractionation. *Macromolecular Symposia* **2009**, *277* (1), 207–214. https://doi.org/10.1002/masy.200950325.
(62) Arnal, M. L.; Balsamo, V.; Ronca, G.; Sánchez, A.; Müller, A. J.; Canizales, E.; Urbina de Navarro, C. Applications of Successive Self-Nucleation and Annealing (SSA) to Polymer Characterization. *Journal of thermal analysis and calorimetry* **2000**, *59* (1), 451–470.
(63) Müller, A. J.; Michell, R. M.; Pérez, R. A.; Lorenzo, A. T. Successive Self-Nucleation and Annealing (SSA): Correct Design of Thermal Protocol and Applications. *European Polymer Journal* **2015**, *65*, 132–154.
(64) Müller, A. J.; Arnal, M. L. Thermal Fractionation of Polymers. *Progress in polymer science* **2005**, *30* (5), 559–603.
(65) Arnal, M. L.; Sanchez, J. J.; Müller, A. J. Miscibility of Linear and Branched Polyethylene Blends by Thermal Fractionation: Use of the Successive Self-Nucleation and Annealing (SSA) Technique. *Polymer* **2001**, *42* (16), 6877–6890.
(66) Gholami, F.; Pircheraghi, G.; Rashedi, R.; Sepahi, A. Correlation between Isothermal Crystallization Properties and Slow Crack Growth Resistance of Polyethylene Pipe Materials. *Polymer Testing* **2019**, *80*, 106128.
(67) Ghahramani, N.; Georgiou, G. C.; Mitsoulis, E.; Hatzikiriakos, S. G. JG Oldroyd's Early Ideas Leading to the Modern Understanding of Wall Slip. *Journal of Non-Newtonian Fluid Mechanics* **2021**, *293*, 104566.
(68) Woo Inn, Y. Melt Fracture and Wall Slip of Metallocene-Catalyzed Bimodal Polyethylenes in Capillary Flow. *Journal of Rheology* **2013**, *57* (2), 393–406. https://doi.org/10.1122/1.4774397.
(69) Inn, Y. W. Melt Fracture, Wall Slip, and Flow-Induced Fractionation of Bimodal Polyethylenes. *AIP Conference Proceedings* **2015**, *1662* (1), 030004. https://doi.org/10.1063/1.4918879.
(70) Mostafa Sabzevari, S.; D. McGraw, J.; Wood-Adams, P. Short Chains Enhance Slip of Highly Entangled Polystyrenes during Thin Film Dewetting. *RSC Advances* **2016**, *6* (94), 91163–91170. https://doi.org/10.1039/C6RA15606A.
(71) Hatzikiriakos, S. G.; Dealy, J. M. Wall Slip of Molten High Density Polyethylene. I. Sliding Plate Rheometer Studies. *Journal of Rheology* **1991**, *35* (4), 497–523. https://doi.org/10.1122/1.550178.
(72) Mhetar, V.; Archer, L. A. Slip in Entangled Polymer Melts. 1. General Features. *Macromolecules* **1998**, *31* (24), 8607–8616. https://doi.org/10.1021/ma980163w.
(73) Léger, L.; Hervet, H.; Massey, G.; Durliat, E. Wall Slip in Polymer Melts. *J. Phys.: Condens. Matter* **1997**, *9* (37), 7719–7740. https://doi.org/10.1088/0953-8984/9/37/006.
(74) Dealy, J. M.; Wang, J. *Melt Rheology and Its Applications in the Plastics Industry*; Springer Science & Business Media, 2013.
(75) Perezgonzalez, J.; Marín-Santibáñez, B. M.; Gonzalez, F. R.; Gonzalez-Santos, J. G. Rheo-Particle Image Velocimetry for the Analysis of the Flow of Polymer Melts; 2012. https://doi.org/10.5772/36502.

(76) Sattari, M.; Inn, Y. W.; Wood-Adams, P. M. Melt Rupture of Bimodal Molecular Weight Polyethylene in Simple Shear with Slip; Society of Plastics Engineers: Denver, United States, 2023.
(77) Dhori, P. K.; Slattery, J. C. Common Line Motion I: Implications of Entropy Inequality. *Journal of non-newtonian fluid mechanics* **1997**, *71* (3), 197–213.
(78) Kwakye-Nimo, S.; Inn, Y.; Yu, Y.; Wood-Adams, P. M. Linear Viscoelastic Behavior of Bimodal Polyethylene. *Rheol Acta* **2022**, *61* (6), 373–386. https://doi.org/10.1007/s00397-022-01340-5.
(79) Joshi, Y. M.; Lele, A. K.; Mashelkar, R. A. Molecular Model for Wall Slip: Role of Convective Constraint Release. *Macromolecules* **2001**, *34* (10), 3412–3420.
(80) McLeish, T. C. B. Tube Theory of Entangled Polymer Dynamics. *Advances in physics* **2002**, *51* (6), 1379–1527.
(81) Graham, R. S.; Likhtman, A. E.; McLeish, T. C.; Milner, S. T. Microscopic Theory of Linear, Entangled Polymer Chains under Rapid Deformation Including Chain Stretch and Convective Constraint Release. *Journal of Rheology* **2003**, *47* (5), 1171–1200.
(82) Milner, S. T.; McLeish, T. C. B. Parameter-Free Theory for Stress Relaxation in Star Polymer Melts. *Macromolecules* **1997**, *30* (7), 2159–2166.
(83) Mead, D. W.; Larson, R. G.; Doi, M. A Molecular Theory for Fast Flows of Entangled Polymers. *Macromolecules* **1998**, *31* (22), 7895–7914. https://doi.org/10.1021/ma980127x.
(84) Stepanyan, R.; Slot, J. J. M.; Molenaar, J.; Tchesnokov, M. A Simple Constitutive Model for a Polymer Flow near a Polymer-Grafted Wall. *Journal of Rheology* **2005**, *49* (5), 1129–1151. https://doi.org/10.1122/1.2000968.
(85) Ebrahimi, M.; Ansari, M.; Inn, Y. W.; Hatzikiriakos, S. G. Surface Fractionation Effects on Slip of Polydisperse Polymer Melts. *Physics of Fluids* **2016**, *28* (9), 093101. https://doi.org/10.1063/1.4962564.
(86) Najm, M.; Hatzikiriakos, S. G. Flow-Induced Fractionation Effects on Slip of Polydisperse Polymer Melts. *Physics of Fluids* **2020**, *32* (7), 073109. https://doi.org/10.1063/5.0017996.
(87) Musil, J.; Zatloukal, M. Experimental Investigation of Flow Induced Molecular Weight Fractionation during Extrusion of HDPE Polymer Melts. *Chemical Engineering Science* **2011**, *66* (20), 4814–4823. https://doi.org/10.1016/j.ces.2011.06.047.
(88) Musil, J.; Zatloukal, M. Experimental Investigation of Flow Induced Molecular Weight Fractionation Phenomenon for Two Linear HDPE Polymer Melts Having Same Mn and Mw but Different Mz and Mz+1 Average Molecular Weights. *Chemical Engineering Science* **2012**, *81*, 146–156. https://doi.org/10.1016/j.ces.2012.06.049.
(89) Schreiber, H. P.; Storey, S. H. Molecular Fractionation in Capillary Flow of Polymer Fluids. *Journal of Polymer Science Part B: Polymer Letters* **1965**, *3* (9), 723–727. https://doi.org/10.1002/pol.1965.110030908.
(90) Kwakye-Nimo, S.; Inn, Y.; Yu, Y.; Wood-Adams, P. M. Polymer Fractionation at an Interface in Simple Shear with Slip. *Macromolecules* **2022**, *55* (15), 6609–6619. https://doi.org/10.1021/acs.macromol.2c01102.
(91) Spalding, M. A.; Chatterjee, A. *Handbook of Industrial Polyethylene and Technology: Definitive Guide to Manufacturing, Properties, Processing, Applications and Markets Set*; John Wiley & Sons, 2017.

(92) Choudhury, I. A.; Hashmi, M. S. J. *Encyclopedia of Renewable and Sustainable Materials*; elsevier, 2020.
(93) Song, S.; Wu, P.; Ye, M.; Feng, J.; Yang, Y. Effect of Small Amount of Ultra High Molecular Weight Component on the Crystallization Behaviors of Bimodal High Density Polyethylene. *Polymer* **2008**, *49* (12), 2964–2973. https://doi.org/10.1016/j.polymer.2008.04.050.
(94) Alt, F. P.; Böhm, L. L.; Enderle, H.-F.; Berthold, J. Bimodal Polyethylene – Interplay of Catalyst and Process. *Macromolecular Symposia* **2001**, *163* (1), 135–144. https://doi.org/10.1002/1521-3900(200101)163:1<135::AID-MASY135>3.0.CO;2-7.
(95) Makaryan, I. A.; Sedov, I. V. State of the Global Market of Bimodal Polyethylenes and the Basic Technologies for Their Production. *Russ J Gen Chem* **2021**, *91* (3), 571–581. https://doi.org/10.1134/S1070363221030282.
(96) Krumme, A.; Lehtinen, A.; Viikna, A. Crystallisation Behaviour of High Density Polyethylene Blends with Bimodal Molar Mass Distribution: 2. Non-Isothermal Crystallisation. *European polymer journal* **2004**, *40* (2), 371–378.
(97) Di Lorenzo, M. L.; Silvestre, C. Non-Isothermal Crystallization of Polymers. *Progress in Polymer Science* **1999**, *24* (6), 917–950. https://doi.org/10.1016/S0079-6700(99)00019-2.
(98) Chew, S.; Griffiths, J. R.; Stachurski, Z. H. The Crystallization Kinetics of Polyethylene under Isothermal and Non-Isothermal Conditions. *Polymer* **1989**, *30* (5), 874–881.
(99) Wood-Adams, P. M.; Dealy, J. M. Using Rheological Data to Determine the Branching Level in Metallocene Polyethylenes. *Macromolecules* **2000**, *33* (20), 7481–7488.
(100) Sun, X.; Shen, G.; Shen, H.; Xie, B.; Yang, W.; Yang, M. Co-Crystallization of Blends of High-Density Polyethylene with Linear Low-Density Polyethylene: An Investigation with Successive Self-Nucleation and Annealing (SSA) Technique. *Journal of Macromolecular Science, Part B* **2013**, *52* (10), 1372–1387.
(101) Krishnaswamy, R. K.; Yang, Q.; Fernandez-Ballester, L.; Kornfield, J. A. Effect of the Distribution of Short-Chain Branches on Crystallization Kinetics and Mechanical Properties of High-Density Polyethylene. *Macromolecules* **2008**, *41* (5), 1693–1704.
(102) Hosoda, S.; Uemura, A. Effect of the Structural Distribution on the Mechanical Properties of Linear Low-Density Polyethylenes. *Polymer journal* **1992**, *24* (9), 939–949.
(103) Lorenzo, A. T.; Arnal, M. L.; Müller, A. J.; Boschetti de Fierro, A.; Abetz, V. High Speed SSA Thermal Fractionation and Limitations to the Determination of Lamellar Sizes and Their Distributions. *Macromolecular Chemistry and Physics* **2006**, *207* (1), 39–49.
(104) Auriemma, F.; Alfonso, G. C.; De Rosa, C. Polymer Crystallization I. *Springer2017* **2017**.
(105) Sangroniz, L.; Cavallo, D.; Müller, A. J. Self-Nucleation Effects on Polymer Crystallization. *Macromolecules* **2020**, *53* (12), 4581–4604.
(106) Perez-Camargo, R. A.; Liu, G.; Meabe, L.; Zhao, Y.; Sardon, H.; Müller, A. J.; Wang, D. Using Successive Self-Nucleation and Annealing to Detect the Solid–Solid Transitions in Poly (Hexamethylene Carbonate) and Poly (Octamethylene Carbonate). *Macromolecules* **2021**, *54* (20), 9670–9680.
(107) Li, X.; Li, X.; Wang, Y.; Zhu, P.; Wang, D.; Müller, A. J.; Dong, X. Effect of Initial Molecular Weight on the Structural Evolution of Polyamide 1012 during High-Temperature Thermal Treatments as Revealed by Successive Self-Nucleation and Annealing. *Macromolecules* **2022**, *55* (17), 7674–7682.

(108) Zaldua, N.; Liénard, R.; Josse, T.; Zubitur, M.; Mugica, A.; Iturrospe, A.; Arbe, A.; De Winter, J.; Coulembier, O.; Müller, A. J. Influence of Chain Topology (Cyclic versus Linear) on the Nucleation and Isothermal Crystallization of Poly (l-Lactide) and Poly (d-Lactide). *Macromolecules* **2018**, *51* (5), 1718–1732.
(109) Michell, R. M.; Müller, A. J.; Deshayes, G.; Dubois, P. Effect of Sequence Distribution on the Isothermal Crystallization Kinetics and Successive Self-Nucleation and Annealing (SSA) Behavior of Poly (ε-Caprolactone-Co-ε-Caprolactam) Copolymers. *European polymer journal* **2010**, *46* (6), 1334–1344.
(110) Liu, Q.; Liu, S.; Lv, Y.; Huang, Y.; Kong, M.; Yang, Q.; Li, G. Photo-Degradation of Polyethylene under Stress: A Successive Self-Nucleation and Annealing (SSA) Study. *Polymer Degradation and Stability* **2020**, *172*, 109060.
(111) Lorenzo, A. T.; Arnal, M. L.; Müller, A. J.; Lin, M.-C.; Chen, H.-L. SAXS/DSC Analysis of the Lamellar Thickness Distribution on a SSA Thermally Fractionated Model Polyethylene. *Macromolecular Chemistry and Physics* **2011**, *212* (18), 2009–2016.
(112) Wong, S. L.; Ngadi, N.; Abdullah, T. A. T. Study on Dissolution of Low Density Polyethylene (LDPE). *Applied Mechanics and Materials* **2015**, *695*, 170–173.
(113) Barlow, A.; Wild, L.; Ranganath, R. Gel Permeation Chromatography of Polyethylene. I. Calibration. *J. Appl. Polym. Sci.* **1977**, *21* (12), 3319–3329. https://doi.org/10.1002/app.1977.070211211.
(114) Li, X.; Wang, L.; Wang, D.; Muller, A. J.; Dong, X. Competition between Chain Extension and Crosslinking in Polyamide 1012 during High-Temperature Thermal Treatments as Revealed by Successive Self-Nucleation and Annealing Fractionation. *Macromolecules* **2021**, *54* (16), 7552–7563.
(115) Alamo, R. G.; Viers, B. D.; Mandelkern, L. Phase Structure of Random Ethylene Copolymers: A Study of Counit Content and Molecular Weight as Independent Variables. *Macromolecules* **1993**, *26* (21), 5740–5747.
(116) Alamo, R. G.; Chan, E. K. M.; Mandelkern, L.; Voigt-Martin, I. G. Influence of Molecular Weight on the Melting and Phase Structure of Random Copolymers of Ethylene. *Macromolecules* **1992**, *25* (24), 6381–6394.
(117) Gao, R.; He, X.; Shao, Y.; Hu, Y.; Zhang, H.; Liu, Z.; Liu, B. Effects of Branch Content and Branch Length on Polyethylene Crystallization: Molecular Dynamics Simulation. *Macromolecular Theory and Simulations* **2016**, *25* (3), 303–311.
(118) Jabbari-Farouji, S.; Lame, O.; Perez, M.; Rottler, J.; Barrat, J.-L. Role of the Intercrystalline Tie Chains Network in the Mechanical Response of Semicrystalline Polymers. *Phys. Rev. Lett.* **2017**, *118* (21), 217802. https://doi.org/10.1103/PhysRevLett.118.217802.
(119) Zhang, M.; Wanke, S. E. Quantitative Determination of Short-Chain Branching Content and Distribution in Commercial Polyethylenes by Thermally Fractionated Differential Scanning Calorimetry. *Polymer Engineering & Science* **2003**, *43* (12), 1878–1888.
(120) Alsharaballi, A. Evaluating Measurement of Strain Hardening Method for Mechanical Assessment of Geomembrane Service Life in MSW Landfills. PhD Thesis, University of South Carolina, 2019. https://search.proquest.com/openview/e4f1aee47f402bce34b417764454bbb9/1?pq-origsite=gscholar&cbl=51922&diss=y.

(121) Shen, H.; Xie, B.; Yang, W.; Yang, M. Non-Isothermal Crystallization of Polyethylene Blends with Bimodal Molecular Weight Distribution. *Polymer testing* **2013**, *32* (8), 1385–1391.
(122) Shin, K.; Woo, E.; Jeong, Y. G.; Kim, C.; Huh, J.; Kim, K.-W. Crystalline Structures, Melting, and Crystallization of Linear Polyethylene in Cylindrical Nanopores. *Macromolecules* **2007**, *40* (18), 6617–6623.
(123) Xu, D.; Bin, Y.; Tang, P. Crystallization and Phase Separation of Branched Low Molecular Weight Polyethylene/Ultrahigh Molecular Weight Polyethylene Blend under a Controlled Temperature Gradient. *Macromolecules* **2010**, *43* (12), 5323–5329.
(124) Crist, B.; Mirabella, F. M. Crystal Thickness Distributions from Melting Homopolymers or Random Copolymers. *Journal of Polymer Science Part B: Polymer Physics* **1999**, *37* (21), 3131–3140.
(125) Lu, L.; Alamo, R. G.; Mandelkern, L. Lamellar Thickness Distribution in Linear Polyethylene and Ethylene Copolymers. *Macromolecules* **1994**, *27* (22), 6571–6576.
(126) Höhne, G. W. H. Another Approach to the Gibbs–Thomson Equation and the Melting Point of Polymers and Oligomers. *Polymer* **2002**, *43* (17), 4689–4698.
(127) Matsko, M. A.; Vanina, M. P.; Echevskaya, L. G.; Zakharov, V. A. Study of the Compositional Heterogeneity of Ethylene–Hexene-1 Copolymers by Thermal Fractionation Technique by Means of Differential Scanning Calorimetry. *Journal of thermal analysis and calorimetry* **2013**, *113*, 923–932.
(128) Zhao, N.; Cheng, R.; He, X.; Liu, Z.; Liu, B. A Novel SiO2-Supported Cr–V Bimetallic Catalyst Making Polyethylene and Ethylene/1-Hexene Copolymers with Bimodal Molecular Weight Distribution. *Macromolecular Chemistry and Physics* **2014**, *215* (18), 1753–1766.
(129) Zhao, N.; Cheng, R.; Dong, Q.; He, X.; Liu, Z.; Zhang, S.; Terano, M.; Liu, B. Tuning the Short Chain Branch Distribution of Ethylene and 1-Hexene Copolymers by SiO2-Supported Silyl Chromate Catalyst with Different Al-Alkyl Co-Catalysts. *Polyolefins Journal* **2014**, *1* (2), 93–105.
(130) Szlachetka, O.; Witkowska-Dobrev, J.; Bary\la, A.; Dohojda, M. Low-Density Polyethylene (LDPE) Building Films–Tensile Properties and Surface Morphology. *Journal of Building Engineering* **2021**, *44*, 103386.
(131) Bohm, L. L.; Enderle, H. F.; Fleißner, M. High-density Polyethylene Pipe Resins. *Advanced Materials* **1992**, *4* (3), 234–238. https://doi.org/10.1002/adma.19920040317.
(132) Staff, A. *Awwa Manual, Volume 55: Pe Pipe: Design and Installation*; American Water Works Association, 2005.
(133) Sattari, M.; Kwakye-Nimo, S.; Inn, Y. W.; Wood-Adams, P. M. Shear Flow of Bimodal Polyethylene: Slip and Surface Fractionation. In *AIP Conference Proceedings*; AIP Publishing, 2023; Vol. 2997.
(134) Rojas, G.; Inci, B.; Wei, Y.; Wagener, K. B. Precision Polyethylene: Changes in Morphology as a Function of Alkyl Branch Size. *J. Am. Chem. Soc.* **2009**, *131* (47), 17376–17386. https://doi.org/10.1021/ja907521p.
(135) Long, M. *Application of Radioisotopes to Polymer Chemistry: Investigation of Radiolabelled Atom Transfer Polymerization*; The University of Manchester (United Kingdom), 2016.

(136) Soares, J. B. P. Polyolefin Microstructural Deconvolution Methods: The Good, the Bad, and the Ugly. *Can J Chem Eng* **2023**, *101* (9), 4955–4978. https://doi.org/10.1002/cjce.24833.
(137) Boukany, P. E.; Wang, S.-Q. Exploring Origins of Interfacial Yielding and Wall Slip in Entangled Linear Melts during Shear or after Shear Cessation. *Macromolecules* **2009**, *42* (6), 2222–2228. https://doi.org/10.1021/ma802644r.
(138) Black, W. B.; Graham, M. D. Wall-Slip and Polymer-Melt Flow Instability. *Phys. Rev. Lett.* **1996**, *77* (5), 956–959. https://doi.org/10.1103/PhysRevLett.77.956.
(139) Tapadia, P. S.; Joshi, Y. M.; Lele, A. K.; Mashelkar, R. A. Influence of Stereoregularity on the Wall Slip Phenomenon in Polypropylene. *Macromolecules* **2000**, *33* (2), 250–252. https://doi.org/10.1021/ma991480l.
(140) Chatzigiannakis, E.; Ebrahimi, M.; Hatzikiriakos, S. G. On the Molecular Weight Dependence of Slip Velocity of Polymer Melts. *Journal of Rheology* **2017**, *61* (4), 731–739. https://doi.org/10.1122/1.4984759.
(141) Joshi, Y. M.; Lele, A. K. Dynamics of End-Tethered Chains at High Surface Coverage. *Journal of Rheology* **2002**, *46* (2), 427–453.
(142) Adjari, A.; Brochard-Wyart, F.; de Gennes, P.-G.; Leibler, L.; Viovy, J.-L.; Rubinstein, M. Slippage of an Entangled Polymer Melt on a Grafted Surface. *Physica A: Statistical Mechanics and its Applications* **1994**, *204* (1–4), 17–39.
(143) Mhetar, V.; Archer, L. A. Slip in Entangled Polymer Solutions. *Macromolecules* **1998**, *31* (19), 6639–6649. https://doi.org/10.1021/ma971339h.
(144) Marrucci, G. Dynamics of Entanglements: A Nonlinear Model Consistent with the Cox-Merz Rule. *Journal of Non-Newtonian Fluid Mechanics* **1996**, *62* (2), 279–289. https://doi.org/10.1016/0377-0257(95)01407-1.
(145) Wang, S.-Q.; Drda, P. Molecular Instabilities in Capillary Flow of Polymer Melts: Interfacial Stick-Slip Transition, Wall Slip and Extrudate Distortion. *Macromolecular Chemistry and Physics* **1997**, *198* (3), 673–701. https://doi.org/10.1002/macp.1997.021980302.
(146) Tchesnokov, M. A.; Molenaar, J.; Slot, J. J. M.; Stepanyan, R. A Molecular Model for Cohesive Slip at Polymer Melt/Solid Interfaces. *The Journal of chemical physics* **2005**, *122* (21), 214711.
(147) Ebrahimi, M.; Ansari, M.; Hatzikiriakos, S. G. Wall Slip of Polydisperse Linear Polymers Using Double Reptation. *Journal of Rheology* **2015**, *59* (3), 885–901. https://doi.org/10.1122/1.4917543.
(148) Zhong, F.; Thomann, R.; Mülhaupt, R. Tailoring Mono-, Bi-, and Trimodal Molar Mass Distributions and All-Hydrocarbon Composites by Ethylene Polymerization on Bis(Imino)Pyridine Chromium(III) Supported on Ultrathin Gibbsite Single Crystal Nanoplatelets. *Macromolecules* **2019**, *52* (7), 2701–2711. https://doi.org/10.1021/acs.macromol.9b00091.
(149) Xu, J.; Costeux, S.; Dealy, J. M.; De Decker, M. N. Use of a Sliding Plate Rheometer to Measure the First Normal Stress Difference at High Shear Rates. *Rheol Acta* **2007**, *46* (6), 815–824. https://doi.org/10.1007/s00397-006-0156-5.

(150) Hayes, K. A.; Buckley, M. R.; Qi, H.; Cohen, I.; Archer, L. A. Constitutive Curve and Velocity Profile in Entangled Polymers during Start-Up of Steady Shear Flow. *Macromolecules* **2010**, *43* (9), 4412–4417. https://doi.org/10.1021/ma100162c.
(151) Owens, D. K.; Wendt, R. C. Estimation of the Surface Free Energy of Polymers. *Journal of applied polymer science* **1969**, *13* (8), 1741–1747.
(152) Gao, Y.; Guo, R.; Fan, R.; Liu, Z.; Kong, W.; Zhang, P.; Du, F. Wettability of Pear Leaves from Three Regions Characterized at Different Stages after Flowering Using the OWRK Method. *Pest Management Science* **2018**, *74* (8), 1804–1809. https://doi.org/10.1002/ps.4878.
(153) Zhu, Y.; Yu, C.; Li, Y.; Zhu, Q.; Zhou, L.; Cao, C.; Yu, T.; Du, F. Research on the Changes in Wettability of Rice (Oryza Sativa.) Leaf Surfaces at Different Development Stages Using the OWRK Method. *Pest Management Science* **2014**, *70* (3), 462–469. https://doi.org/10.1002/ps.3594.
(154) Dealy, J. M.; Read, D. J.; Larson, R. G. *Structure and Rheology of Molten Polymers: From Structure to Flow Behavior and Back Again*, 2nd ed.; Carl Hanser Verlag GmbH & Co. KG: München, 2018. https://doi.org/10.3139/9781569906125.
(155) Masubuchi, Y.; Vlassopoulos, D.; Ianniruberto, G.; Marrucci, G. Wall Slip in Primitive Chain Network Simulations of Shear Startup of Entangled Polymers and Its Effect on the Shear Stress Undershoot. *Journal of Rheology* **2021**, *65* (2), 213–223. https://doi.org/10.1122/8.0000194.
(156) Yuryev, Y.; Wood-Adams, P. Rheological Properties of Crystallizing Polylactide: Detection of Induction Time and Modeling the Evolving Structure and Properties. *Journal of Polymer Science Part B: Polymer Physics* **2010**, *48* (7), 812–822.
(157) Vega, J. F.; Martínez-Salazar, J.; Trujillo, M.; Arnal, M. L.; Müller, A. J.; Bredeau, S.; Dubois, Ph. Rheology, Processing, Tensile Properties, and Crystallization of Polyethylene/Carbon Nanotube Nanocomposites. *Macromolecules* **2009**, *42* (13), 4719–4727. https://doi.org/10.1021/ma900645f.
(158) Joseph, D. D. Steep Wave Fronts on Extrudates of Polymer Melts and Solutions: Lubrication Layers and Boundary Lubrication. *Journal of non-newtonian fluid mechanics* **1997**, *70* (3), 187–203.
(159) Joseph, D. D.; Liu, Y. J. Letter to the Editor: Steep Wave Fronts on Extrudates of Polymer Melts and Solutions. *Journal of Rheology* **1996**, *40* (2), 317–319.
(160) Brochard-Wyart, F.; De Gennes, P.-G.; Hervert, H.; Redon, C. Wetting and Slippage of Polymer Melts on Semi-Ideal Surfaces. *Langmuir* **1994**, *10* (5), 1566–1572.
(161) Grzelka, M.; Antoniuk, I.; Drockenmuller, É.; Chennevière, A.; Léger, L.; Restagno, F. Slip and Friction Mechanisms at Polymer Semi-Dilute Solutions/Solid Interfaces. *Macromolecules* **2021**, *54* (10), 4910–4917. https://doi.org/10.1021/acs.macromol.0c02804.
(162) Brochard, F.; De Gennes, P. G. Shear-Dependent Slippage at a Polymer/Solid Interface. *Langmuir* **1992**, *8* (12), 3033–3037.
(163) Wang, S.-Q.; Drda, P. A. Stick−Slip Transition in Capillary Flow of Polyethylene. 2. Molecular Weight Dependence and Low-Temperature Anomaly. *Macromolecules* **1996**, *29* (11), 4115–4119. https://doi.org/10.1021/ma951512e.

(164) Ravindranath, S.; Wang, S.-Q. What Are the Origins of Stress Relaxation Behaviors in Step Shear of Entangled Polymer Solutions? *Macromolecules* **2007**, *40* (22), 8031–8039. https://doi.org/10.1021/ma071495g.
(165) Barroso, V. C.; Maia, J. M. Time Dependent Effects on the Rupture of Molten Linear Polymers in Extension. *Journal of Non-Newtonian Fluid Mechanics* **2005**, *126* (2), 93–103. https://doi.org/10.1016/j.jnnfm.2004.03.012.
(166) Malkin, A. Ya.; Petrie, C. J. S. Some Conditions for Rupture of Polymer Liquids in Extension. *Journal of Rheology* **1997**, *41* (1), 1–25. https://doi.org/10.1122/1.550881.
(167) Vinogradov, G. V.; Dreval, V. E.; Borisenkova, E. K.; Kurbanaliev, M. K.; Shalganova, V. G. Uniaxial Extension of Linear Flexible-Chain Polymers in an Extremely Broad Range of Stresses and Strain Rates. *Rheol Acta* **1981**, *20* (5), 433–442. https://doi.org/10.1007/BF01503264.
(168) Huang, J.-C.; Leong, K.-S. Shear Viscosity, Extensional Viscosity, and Die Swell of Polypropylene in Capillary Flow with Pressure Dependency. *Journal of applied polymer science* **2002**, *84* (6), 1269–1276.
(169) Migler, K. B.; Son, Y.; Qiao, F.; Flynn, K. Extensional Deformation, Cohesive Failure, and Boundary Conditions during Sharkskin Melt Fracture. *Journal of Rheology* **2002**, *46* (2), 383–400.
(170) Malkin, A. Ya.; Arinstein, A.; Kulichikhin, V. G. Polymer Extension Flows and Instabilities. *Progress in Polymer Science* **2014**, *39* (5), 959–978. https://doi.org/10.1016/j.progpolymsci.2014.02.006.
(171) Andrade, R. J.; Maia, J. M. A Study on the Flow, Failure, and Rupture Mechanisms of Low-Density Polyethylene in Controlled-Stress Uniaxial Extensional Flow. *Journal of Rheology* **2011**, *55* (5), 925–937.
(172) Matsumiya, Y.; Watanabe, H. Non-Universal Features in Uniaxially Extensional Rheology of Linear Polymer Melts and Concentrated Solutions: A Review. *Progress in Polymer Science* **2021**, *112*, 101325.
(173) Huang, Q. When Polymer Chains Are Highly Aligned: A Perspective on Extensional Rheology. *Macromolecules* **2022**, *55* (3), 715–727.
(174) Wang, Y.; Boukany, P.; Wang, S.-Q.; Wang, X. Elastic Breakup in Uniaxial Extension of Entangled Polymer Melts. *Physical review letters* **2007**, *99* (23), 237801.
(175) Huang, Q.; Alvarez, N. J.; Shabbir, A.; Hassager, O. Multiple Cracks Propagate Simultaneously in Polymer Liquids in Tension. *Physical review letters* **2016**, *117* (8), 087801.
(176) Sgouros, A. P.; Lakkas, A. T.; Megariotis, G.; Theodorou, D. N. Mesoscopic Simulations of Free Surfaces of Molten Polyethylene: Brownian Dynamics/Kinetic Monte Carlo Coupled with Square Gradient Theory and Compared to Atomistic Calculations and Experiment. *Macromolecules* **2018**, *51* (23), 9798–9815.
(177) Huang, Q. Exploring the Mechanism of Fracture for Entangled Polymer Liquids in Extensional Flow. *Physics of Fluids* **2019**, *31* (8), 083105.
(178) Huang, Q.; Hassager, O.; Madsen, J. Spatial Radical Distribution in Fractured Polymer Glasses and Melts Visualized Using a Profluorescent Nitroxide Probe. *Macromolecules* **2022**, *55* (21), 9431–9441.

(179) Wingstrand, S. L.; Hassager, O.; Parisi, D.; Borger, A. L.; Mortensen, K. Flow Induced Crystallization Prevents Melt Fracture of HDPE in Uniaxial Extensional Flow. *Journal of Rheology* **2018**, *62* (4), 1051–1060.
(180) McHugh, A. J.; Guy, R. K.; Tree, D. A. Extensional Flow-Induced Crystallization of a Polyethylene Melt. *Colloid and Polymer Science* **1993**, *271*, 629–645.
(181) Swartjes, F. H. M.; Peters, G. W.; Rastogi, S.; Meijer, H. E. Stress Induced Crystallization in Elongational Flow. *International Polymer Processing* **2003**, *18* (1), 53–66.
(182) Boutaous, M.; Bourgin, P.; Zinet, M. Thermally and Flow Induced Crystallization of Polymers at Low Shear Rate. *Journal of Non-Newtonian Fluid Mechanics* **2010**, *165* (5–6), 227–237.
(183) Mackley, M. R.; Keller, A. Flow Induced Crystallization of Polyethylene Melts. *Polymer* **1973**, *14* (1), 16–20.
(184) Lee, H.; Kim, D. H.; Son, Y. Anomalous Rheological Behavior of Polyethylene Melts in the Gross Melt Fracture Regime in the Capillary Extrusion. *Polymer* **2006**, *47* (11), 3929–3934.
(185) Doerpinghaus, P. J.; Baird, D. G. Comparison of the Melt Fracture Behavior of Metallocene and Conventional Polyethylenes. *Rheol Acta* **2003**, *42* (6), 544–556. https://doi.org/10.1007/s00397-003-0309-8.
(186) Hatzikiriakos, S. G.; Migler, K. B. *Polymer Processing Instabilities: Control and Understanding*; CRC Press, 2004.
(187) Kim, S.; Dealy, J. M. Gross Melt Fracture of Polyethylene. I: A Criterion Based on Tensile Stress. *Polymer Engineering & Science* **2002**, *42* (3), 482–494.
(188) Kometani, H.; Kitajima, H.; Matsumura, T.; Suga, T.; Kanai, T. Visualization of Flow Instabilities for High Density Polyethylene. *International Polymer Processing* **2006**, *21* (1), 32–40.
(189) Hatzikiriakos, S. G.; Dealy, J. M. Effects of Interfacial Conditions on Wall Slip and Sharkskin Melt Fracture of HDPE. *International Polymer Processing* **1993**, *8* (1), 36–43.
(190) Kim, S.; Dealy, J. M. Gross Melt Fracture of Polyethylene. II: Effects of Molecular Structure. *Polymer Engineering & Science* **2002**, *42* (3), 495–503.
(191) Dhori, P. K.; Jeyaseelan, R. S.; Giacomin, A. J.; Slattery, J. C. Common Line Motion III: Implications in Polymer Extrusion. *Journal of non-newtonian fluid mechanics* **1997**, *71* (3), 231–243.
(192) Graham, M. D. The Sharkskin Instability of Polymer Melt Flows. *Chaos* **1999**, *9* (1), 154–163. https://doi.org/10.1063/1.166386.
(193) Achilleos, E. C.; Georgiou, G.; Hatzikiriakos, S. G. Role of Processing Aids in the Extrusion of Molten Polymers. *J Vinyl Addit Technol* **2002**, *8* (1), 7–24. https://doi.org/10.1002/vnl.10340.
(194) Cinquino, M.; Prontera, C. T.; Zizzari, A.; Giuri, A.; Pugliese, M.; Giannuzzi, R.; Monteduro, A. G.; Carugati, M.; Banfi, A.; Carallo, S. Effect of Surface Tension and Drying Time on Inkjet-Printed PEDOT: PSS for ITO-Free OLED Devices. *Journal of Science: Advanced Materials and Devices* **2022**, *7* (1), 100394.
(195) Van Dam, J. P. B.; Abrahami, S. T.; Yilmaz, A.; Gonzalez-Garcia, Y.; Terryn, H.; Mol, J. M. C. Effect of Surface Roughness and Chemistry on the Adhesion and Durability of a Steel-Epoxy Adhesive Interface. *International Journal of Adhesion and Adhesives* **2020**, *96*, 102450.

(196) De Lima, B. M.; Hayes, P. L.; Wood-Adams, P. M. Influence of Polymer Molecular Weight on Chain Conformation at the Polystyrene/Silver Interface. *Langmuir* **2021**, *37* (33), 10036–10045. https://doi.org/10.1021/acs.langmuir.1c01211.

Chapter 7. Appendices

7. 1. Supplementary information for Chapter 3

7. 1. 1. Estimation of the plateau value for the short chain branching of the high molecular weight population for HDPE 6 and HDPE 7

For two materials of HDPE 6 and HDPE 7, there is uncertainty about the validity[1] of co-monomer mole fraction at kinetic chain lengths higher than 10^4. For these materials the value of the commoner for the high molecular weight population is estimated from the overall average short chain branching via **Eqn. (3.19)** followed by a re-optimization of the weight fraction. Additional iterations did not change the results.

7. 1. 2. Additional fitting comparisons for short chain branching and molecular weight distributions

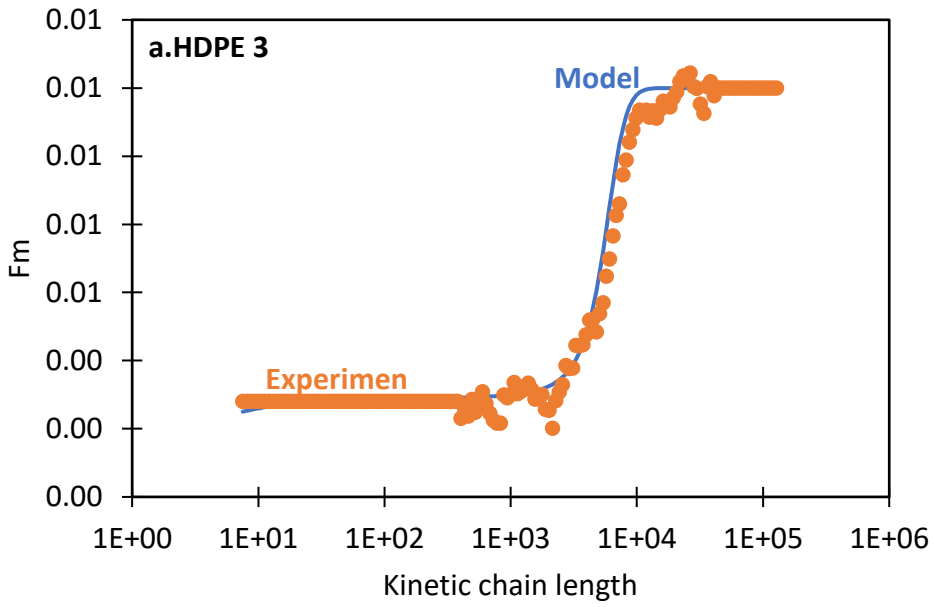

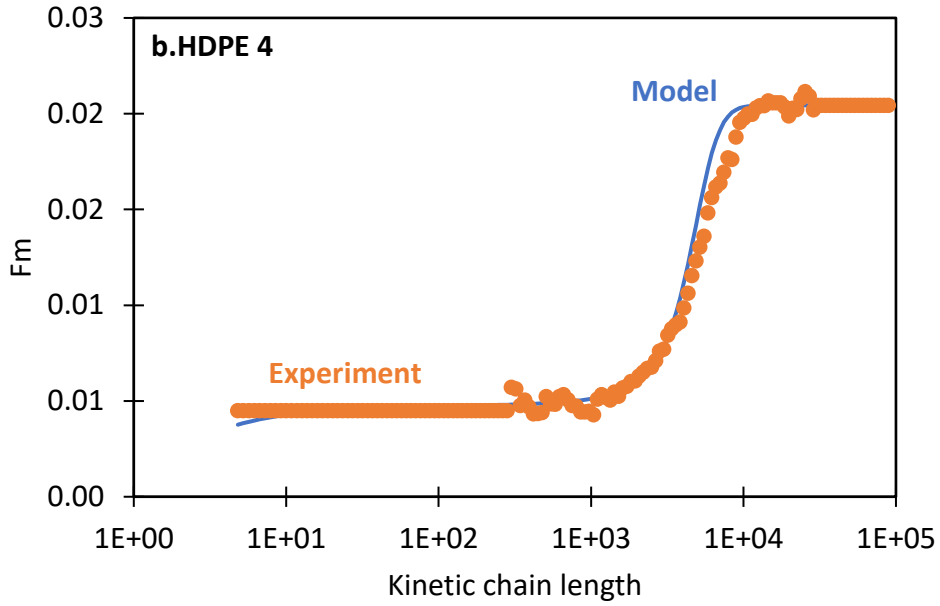
b.HDPE 4
Model
Experiment
Fm
0.03
0.02
0.02
0.01
0.01
0.00
1E+00
1E+01
1E+02
1E+03
1E+04
1E+05
Kinetic chain length

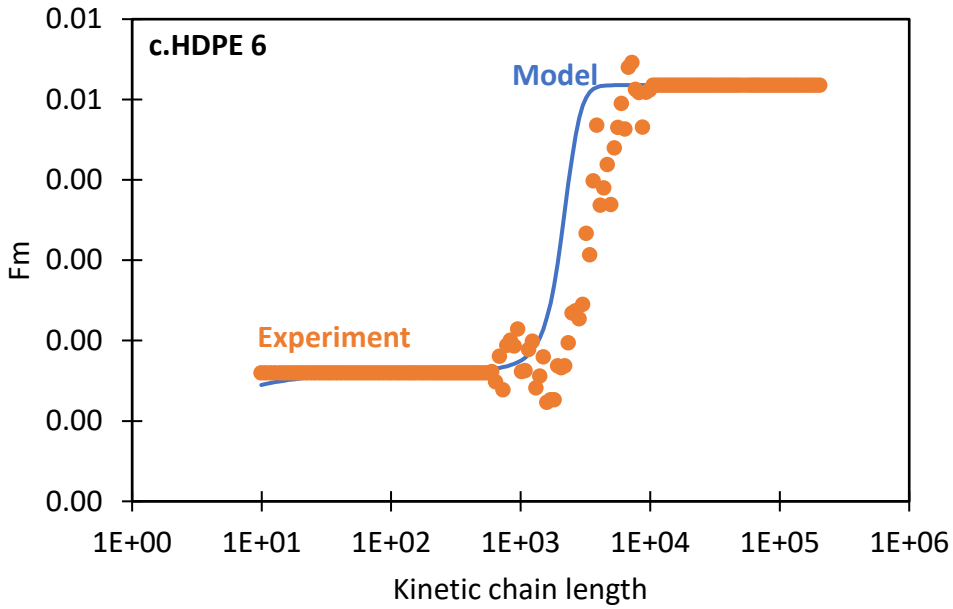
c.HDPE 6
Model
Experiment
Fm
0.01
0.01
0.00
0.00
0.00
0.00
1E+00
1E+01
1E+02
1E+03
1E+04
1E+05
1E+06
Kinetic chain length

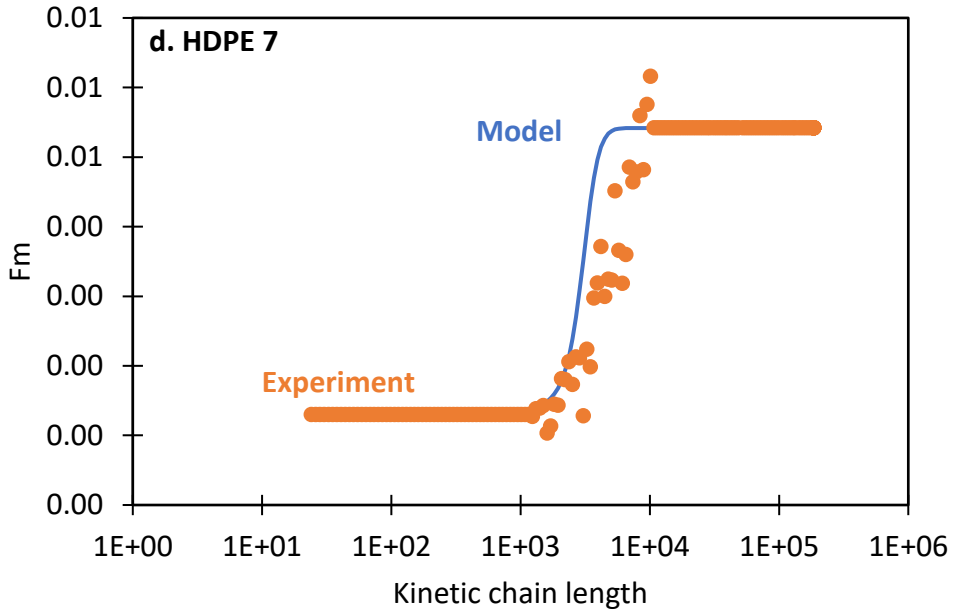
d. HDPE 7
Model
Experiment
Fm
0.01
0.01
0.01
0.00
0.00
0.00
0.00
1E+00
1E+01
1E+02
1E+03
1E+04
1E+05
1E+06
Kinetic chain length

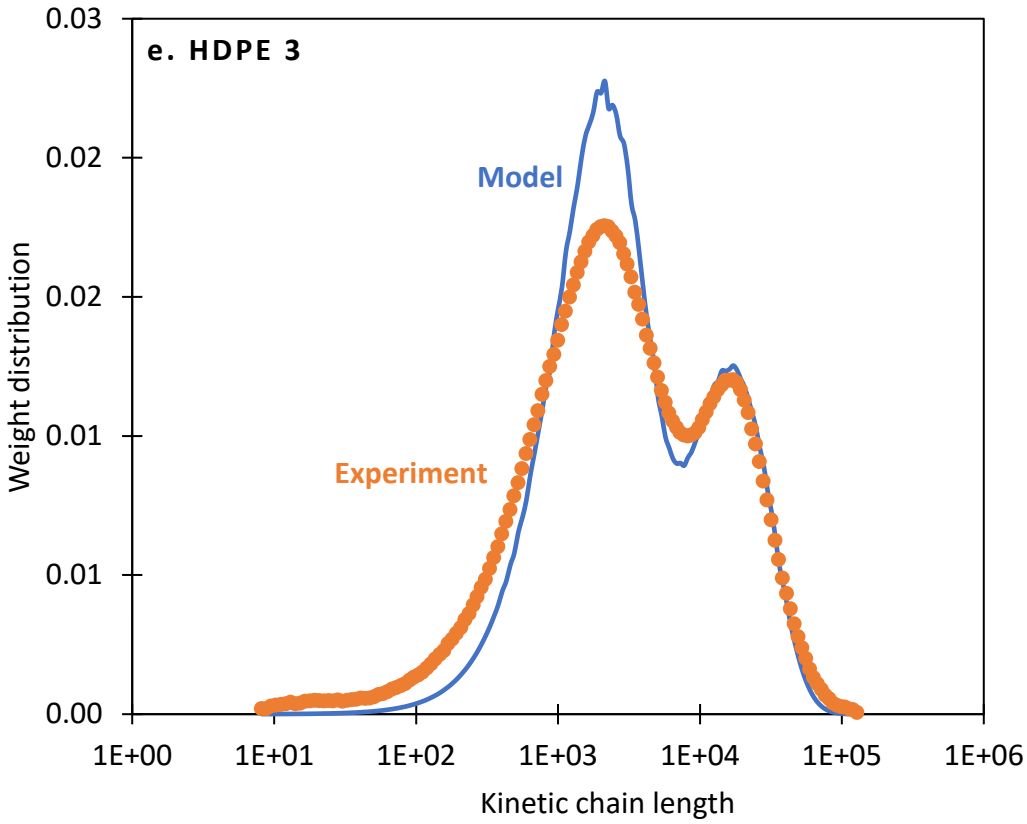
e. HDPE 3
Model
Experiment
Weight distribution
0.03
0.02
0.02
0.01
0.01
0.00
1E+00
1E+01
1E+02
1E+03
1E+04
1E+05
1E+06
Kinetic chain length

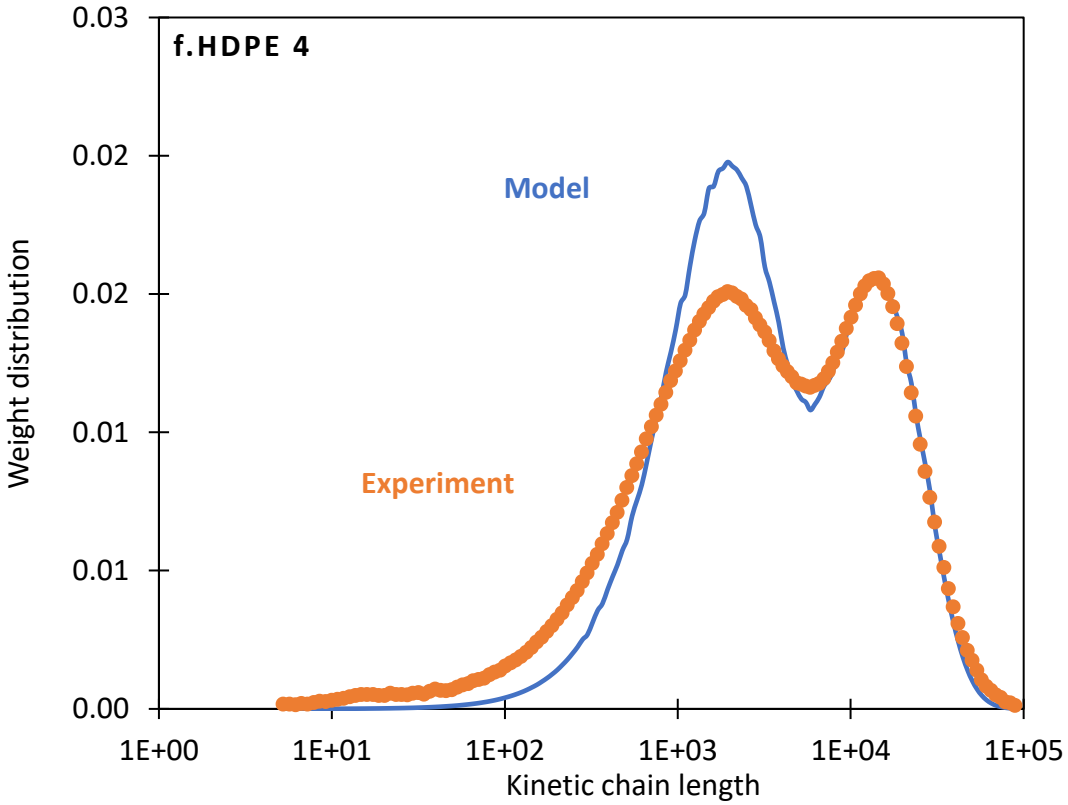
f.HDPE 4
Model
Experiment
Weight distribution
Kinetic chain length
0.03
0.02
0.02
0.01
0.01
0.00
1E+00
1E+01
1E+02
1E+03
1E+04
1E+05

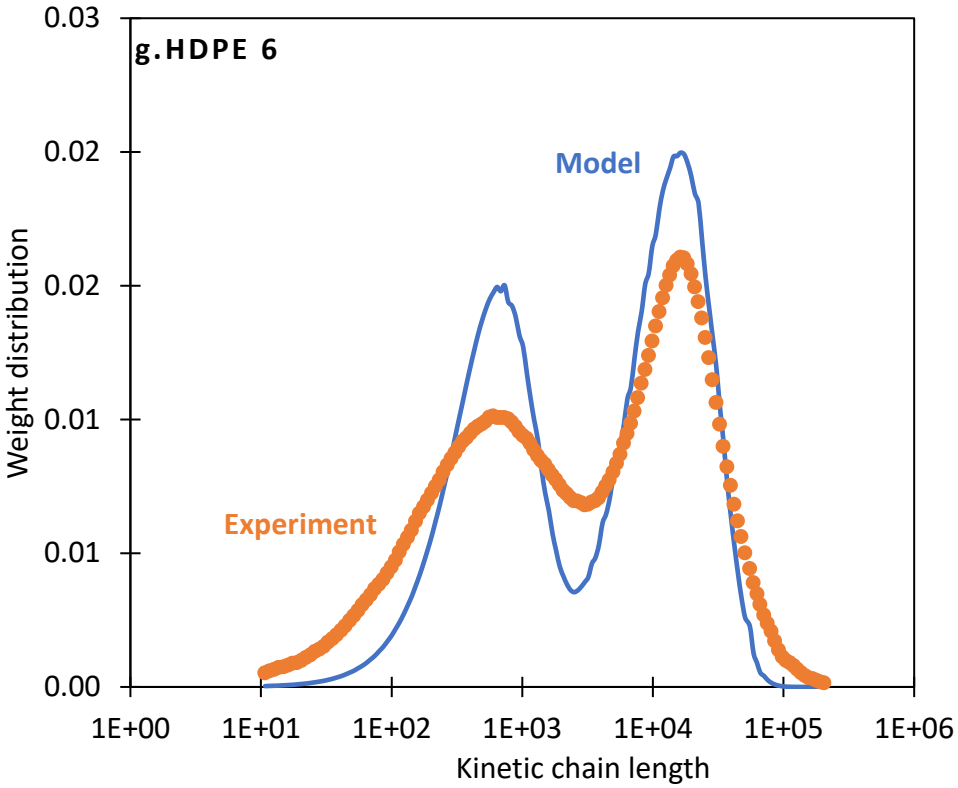
g.HDPE 6
Model
Experiment
Weight distribution
0.03
0.02
0.02
0.01
0.01
0.00
1E+00
1E+01
1E+02
1E+03
1E+04
1E+05
1E+06
Kinetic chain length

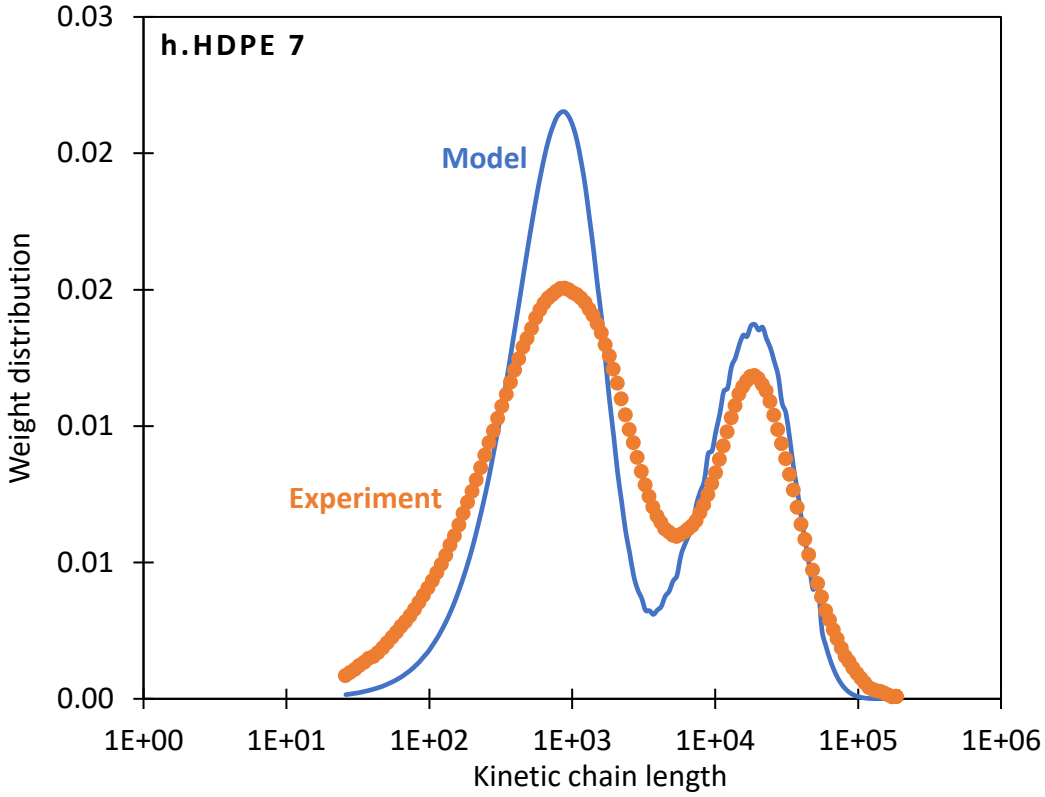

Figure 7.1. Mole fraction: a. HDPE 3, b. HDPE 4, c. HDPE 6, d. HDPE 7, and kinetic chain length: e. HDPE 3, f. HDPE 4, g. HDPE 6, h. HDPE 7 distributions from modeling and experiment

7. 1. 3. Additional heat flow results of the final melting step in the SSA protocol

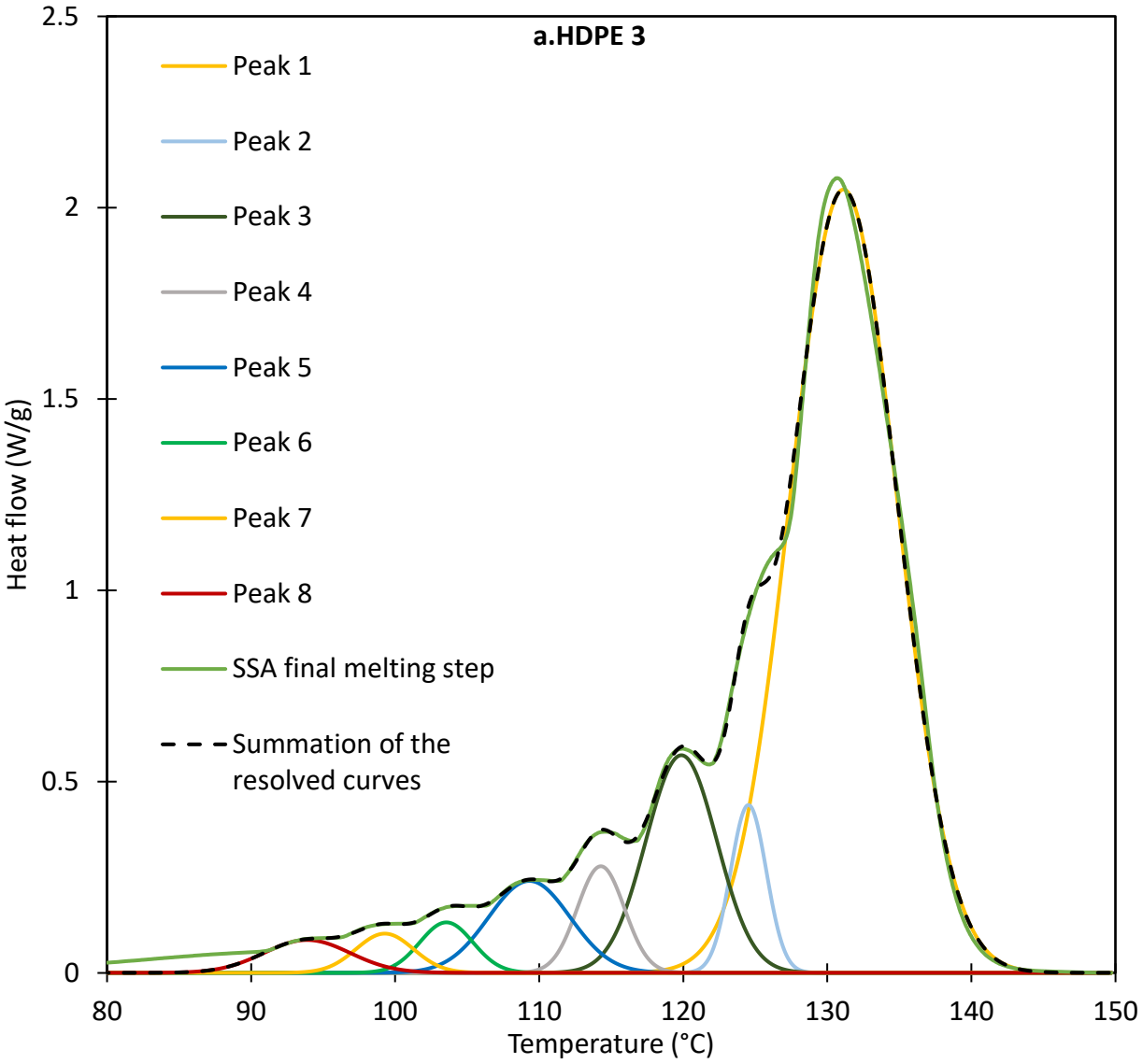

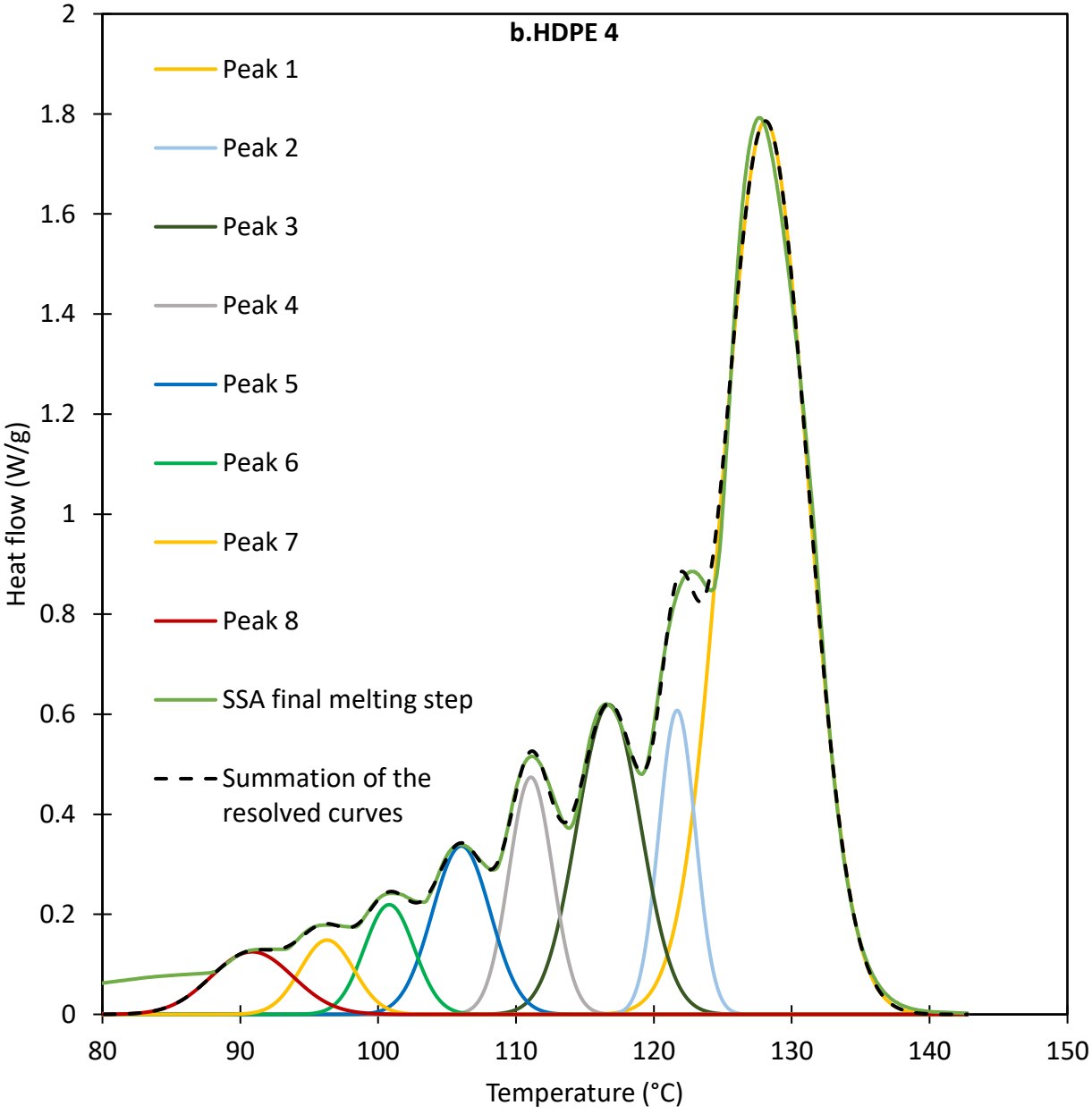
b.HDPE 4
Peak 1
Peak 2
Peak 3
Peak 4
Peak 5
Peak 6
Peak 7
Peak 8
SSA final melting step
Summation of the resolved curves
Heat flow (W/g)
Temperature (°C)
0
0.2
0.4
0.6
0.8
1
1.2
1.4
1.6
1.8
2
80
90
100
110
120
130
140
150

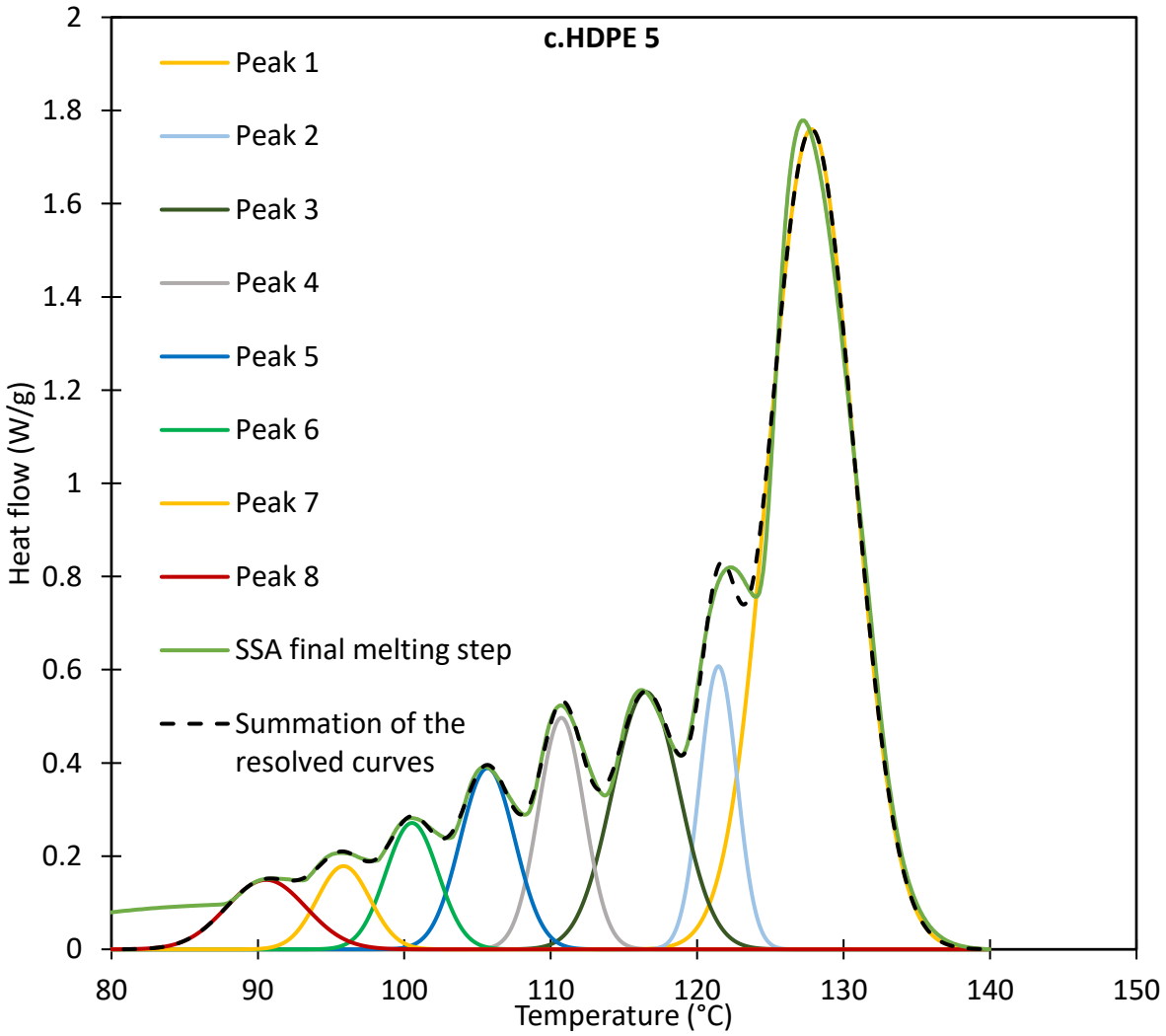
c.HDPE 5
Peak 1
Peak 2
Peak 3
Peak 4
Peak 5
Peak 6
Peak 7
Peak 8
SSA final melting step
Summation of the resolved curves
Heat flow (W/g)
Temperature (°C)
0
0.2
0.4
0.6
0.8
1
1.2
1.4
1.6
1.8
2
80
90
100
110
120
130
140
150

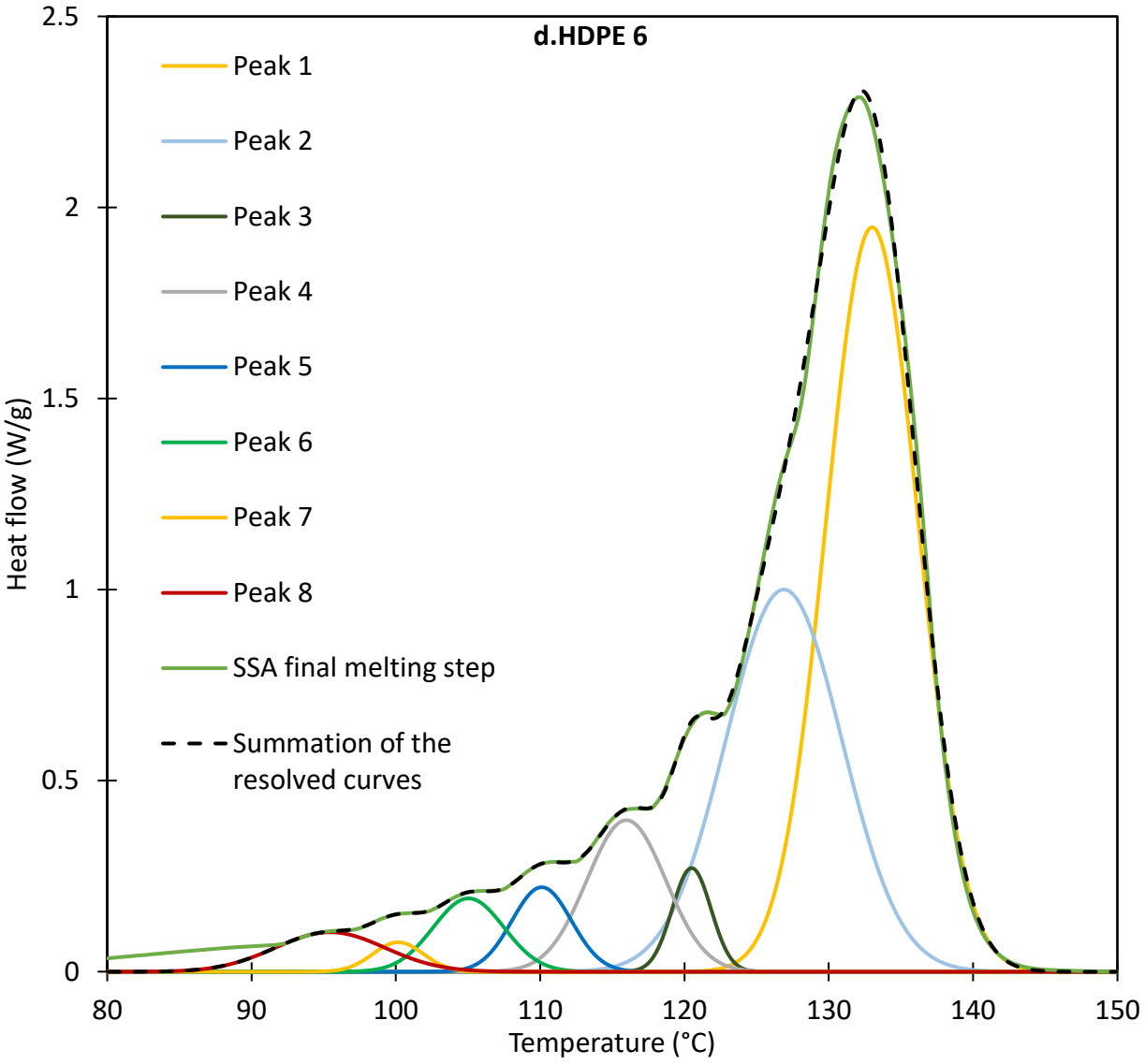

Figure 7.2. The heat flow results of the final melting step in the SSA protocol: a. HDPE 3, b. HDPE 4, c. HDPE 5 and d. HDPE 6

Table 7.1. The peak temperatures and the relative area of the SSA peaks for HDPE 3-7										
	HDPE 6		HDPE 7		HDPE 3		HDPE 4		HDPE 5	
	Relative Area	Temperature (°C)	Relative Area	Temperature (°C)	Relative Area	Temperature (°C)	Relative Area	Temperature (°C)	Relative Area	Temperature (°C)
Peak 1	0.47	133.01	0.72	133.74	0.67	131.12	0.53	128.10	0.52	127.81
Peak 2	0.31	126.89	0.04	127.78	0.05	124.53	0.08	121.69	0.08	121.46
Peak 3	0.03	120.50	0.11	123.05	0.12	119.87	0.14	116.74	0.13	116.50
Peak 4	0.08	115.97	0.03	117.68	0.04	114.28	0.07	111.08	0.08	110.73
Peak 5	0.03	110.11	0.06	112.78	0.06	109.32	0.07	106.04	0.07	105.68
Peak 6	0.04	105.04	0.01	106.85	0.02	103.56	0.04	100.81	0.05	100.53
Peak 7	0.01	100.16	0.02	102.43	0.02	99.28	0.03	96.30	0.03	95.85
Peak 8	0.03	95.45	0.01	96.83	0.02	93.89	0.04	90.86	0.04	90.56

Table 7.2. Modified Gibbs-Thomson lamellar thickness averages for HDPE3-7 (nm)		
Material	$\bar{l}_2$	$\bar{l}_3$
HDPE 3	11.60	12.25
HDPE 4	8.42	9.06
HDPE 5	8.17	8.83
HDPE 6	13.13	14.28
HDPE 7	16.01	16.79

7. 1. 4. Property structure correlations

Table 7.3. The multi-linear regression output for the first lamellar thickness moment (Y) (nm) and $R_{B,\ ESLD}$ (X Variable 1), and weight averaged ethylene sequence length (X Variable 2). Log-Log transformation is applied.

SUMMARY OUTPUT

Regression Statistics	
Multiple R	0.99916
R Square	0.998321
Adjusted R Square	0.996643
Standard Error	0.007321
Observations	5

ANOVA

	df	*SS*	*MS*	*F*	*Significance F*
Regression	2	0.063744	0.031872	594.7154	0.001679
Residual	2	0.000107	5.36E-05		
Total	4	0.063852			

	Coefficients	*Standard Error*	*t Stat*	*P-value*	*Lower 95%*	*Upper 95%*	*Lower 95.0%*	*Upper 95.0%*
Intercept	0.45092	0.234502	1.922883	0.194415	-0.55806	1.459901	-0.55806	1.459901
X Variable 1	0.420757	0.061627	6.827508	0.020786	0.155599	0.685916	0.155599	0.685916
X Variable 2	0.264086	0.085834	3.076719	0.091389	-0.10523	0.633398	-0.10523	0.633398

Table 7.4. The multi-linear regression output for the second lamellar thickness moment (Y) (m) and short chain branching average (X Variable 1) and $R_{B,\ ESLD}$ (X Variable 2). Log-Log transformation is applied.

SUMMARY OUTPUT

Regression Statistics	
Multiple R	0.999973
R Square	0.999947
Adjusted R Square	0.999893
Standard Error	0.001297
Observations	5

ANOVA

	df	*SS*	*MS*	*F*	*Significance F*
Regression	2	0.063181	0.03159	18776.52	5.33E-05
Residual	2	3.36E-06	1.68E-06		
Total	4	0.063184			

	Coefficients	*Standard Error*	*t Stat*	*P-value*	*Lower 95%*	*Upper 95%*	*Lower 95.0%*	*Upper 95.0%*
Intercept	-7.75317	0.001344	-5768.45	3.01E-08	-7.75895	-7.74738	-7.75895	-7.74738
X Variable 1	-0.21565	0.009085	-23.7367	0.00177	-0.25475	-0.17656	-0.25475	-0.17656
X Variable 2	0.319829	0.012113	26.4043	0.001431	0.267712	0.371945	0.267712	0.371945

Table 7.5. The multi-linear regression output for the third lamellar thickness moment (Y) (m) and M_z/M_w (X Variable 1) and weight averaged ethylene sequence length (X Variable 2). Log-Log transformation is applied.

SUMMARY OUTPUT

Regression Statistics	
Multiple R	0.999742
R Square	0.999484
Adjusted R Square	0.998967
Standard Error	0.003924
Observations	5

ANOVA

	df	*SS*	*MS*	*F*	*Significance F*
Regression	2	0.059605	0.029803	1935.451	0.000516
Residual	2	3.08E-05	1.54E-05		
Total	4	0.059636			

	Coefficients	*Standard Error*	*t Stat*	*P-value*	*Lower 95%*	*Upper 95%*	*Lower 95.0%*	*Upper 95.0%*
Intercept	-9.29639	0.056239	-165.301	3.66E-05	-9.53837	-9.05441	-9.53837	-9.05441
X Variable 1	0.745722	0.053865	13.84424	0.005177	0.513959	0.977484	0.513959	0.977484
X Variable 2	0.392784	0.031822	12.34302	0.0065	0.255864	0.529705	0.255864	0.529705

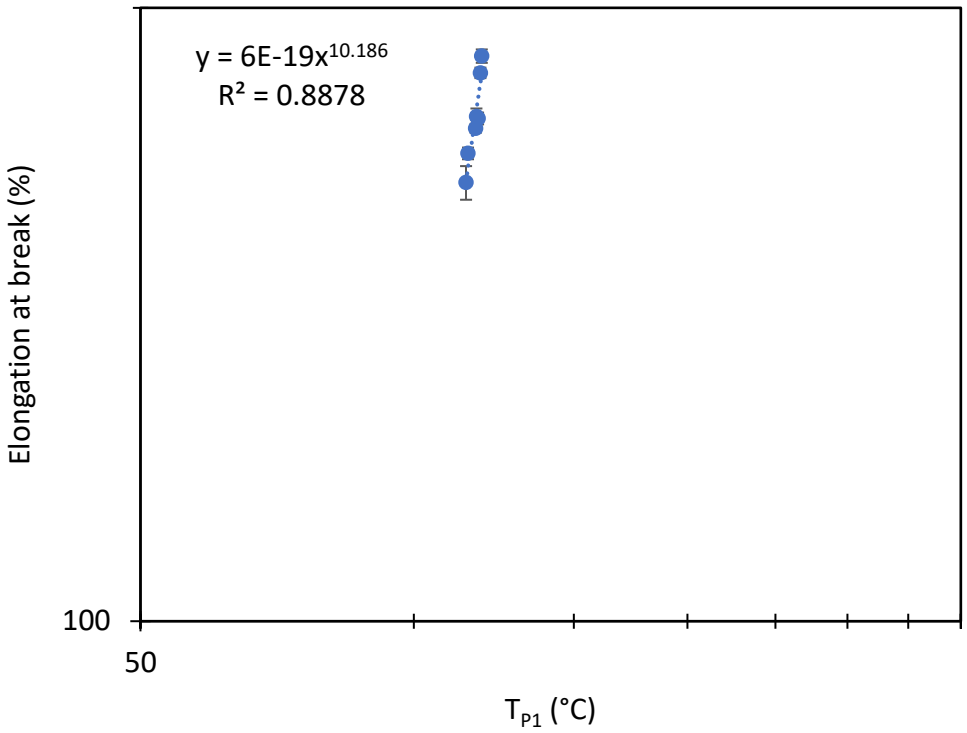

Figure 7.3. Elongation at break versus T_{P1}

Table 7.6. Correlations between the SSA and thermal results			
Property	key parameter	R^2	Scale
First moment of lamellar thickness	X_c	0.9758	logarithmic
Second moment of lamellar thickness	X_c	0.9858	logarithmic
Third moment of lamellar thickness	X_c	0.9905	logarithmic
Second moment of HMW Contribution	T_{P1}	0.9175	Linear
Third moment of HMW Contribution	X_c	0.9571	Linear

7. 2. Supplementary information for Chapter 4

Table 7.7. The average value of the plateau in the shear stress transient at different nominal shear rates for the four materials[2]

HDPE 6	Nominal Shear Rate (s^{-1})	0.05	1.00	1.75	2.50	3.75	5.00	7.50	10.00	
	Shear Stress (kPa)	18.32	72.96	85.68	90.13	94.52	110.63	115.66	121.35	
	Shear Stress Standard Error	0.96	1.85	1.47	1.61	0.25	2.55	1.42	6.09	
	True Shear Rate (s^{-1})	-	0.57	0.76	0.83	0.92	1.26	1.38	1.52	
HDPE 2	Nominal Shear Rate (s^{-1})	0.05	1.00	2.50	3.75	5.00	6.25	7.50	8.75	10.00
	Shear Stress (kPa)	11.94	54.63	62.36	69.81	78.33	92.88	103.82	108.42	116.43
	Shear Stress Standard Error	0.88	1.69	0.52	1.26	1.22	4.78	7.13	4.66	5.28
	True Shear Rate (s^{-1})	-	0.63	0.81	1.01	1.26	1.80	2.31	2.56	3.04
HDPE 8	Nominal Shear Rate (s^{-1})	0.10	0.30	0.50	0.75	1.00	1.50			
	Shear Stress (kPa)	16.02	23.82	33.72	42.91	42.08	42.05			
	Shear Stress Standard Error	0.75	3.52	1.75	3.62	3.19	2.77			
	True Shear Rate (s^{-1})	-	0.23	0.40	0.62	0.60	0.60			
HDPE 9	Nominal Shear Rate (s^{-1})	0.10	0.25	0.50	0.75	1.00	1.25	1.50	2.00	
	Shear Stress (kPa)	12.94	21.59	24.04	30.83	36.43	32.50	42.65	43.24	
	Shear Stress Standard Error	0.63	2.11	2.51	2.19	2.46	2.25	3.10	3.36	
	True Shear Rate (s^{-1})	-	-	0.32	0.50	0.68	0.55	0.93	0.96	

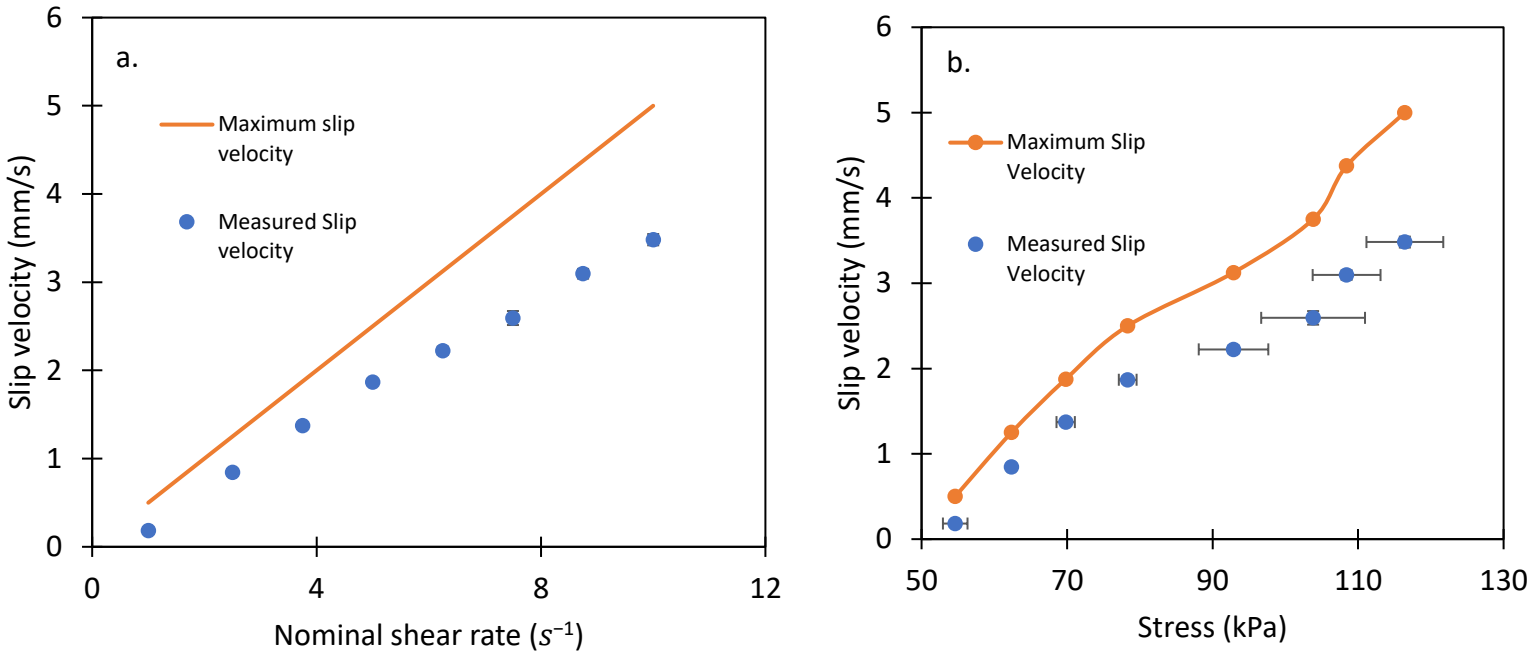

Figure 7.4. Measured slip velocity and its maximum value versus the nominal shear rate (a) and against stress (b) for HDPE 2^2

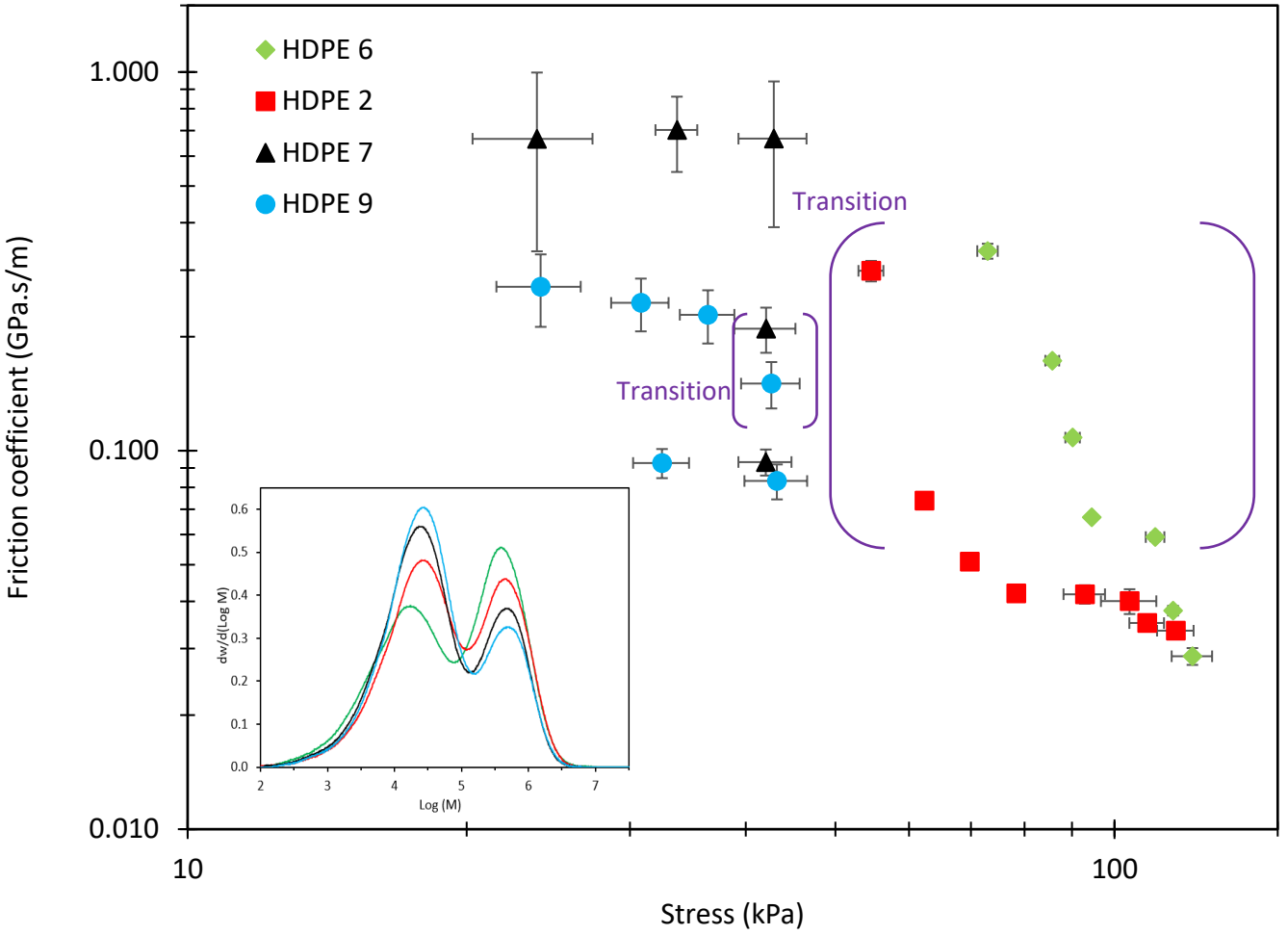

Figure 7.5. Friction coefficient versus stress at 190 °C using the data of **Figure 4.4** and **Eqn. (4.6)** for HDPE 6, HDPE 2, HDPE 7, and HDPE 9. Error bars represent standard error[2].

7. 3. Supplementary information for Chapter 5

7. 3. 1. Roughness measurements

The surface roughness of rupture specimens from the glass-steel setup was measured using a Vecco Dektar 150 stylus surface profilometer. The stylus tip is 12.5 μm in diameter and applies a force of 10^{-5} N to the surface. Mean roughness (Ra: the average of deviations of the surface profile from the mean value[3], (**Figure 7.6a**)) and the root mean square roughness (Rq: the root mean square of deviations of the surface profile from the mean value[3] (**Figure 7.6b**)), are calculated and reported. For each sample, the profile measurements are taken in the cross-section direction at various points along the specimen length (flow direction). No correlation with the apparent rate is observed.

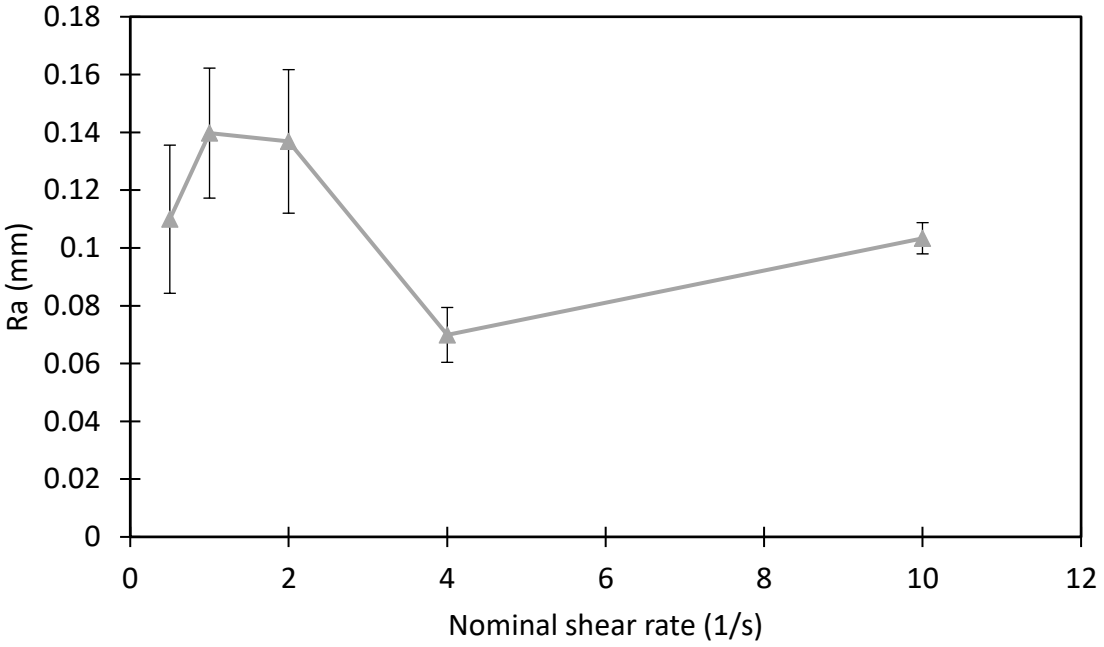

a.

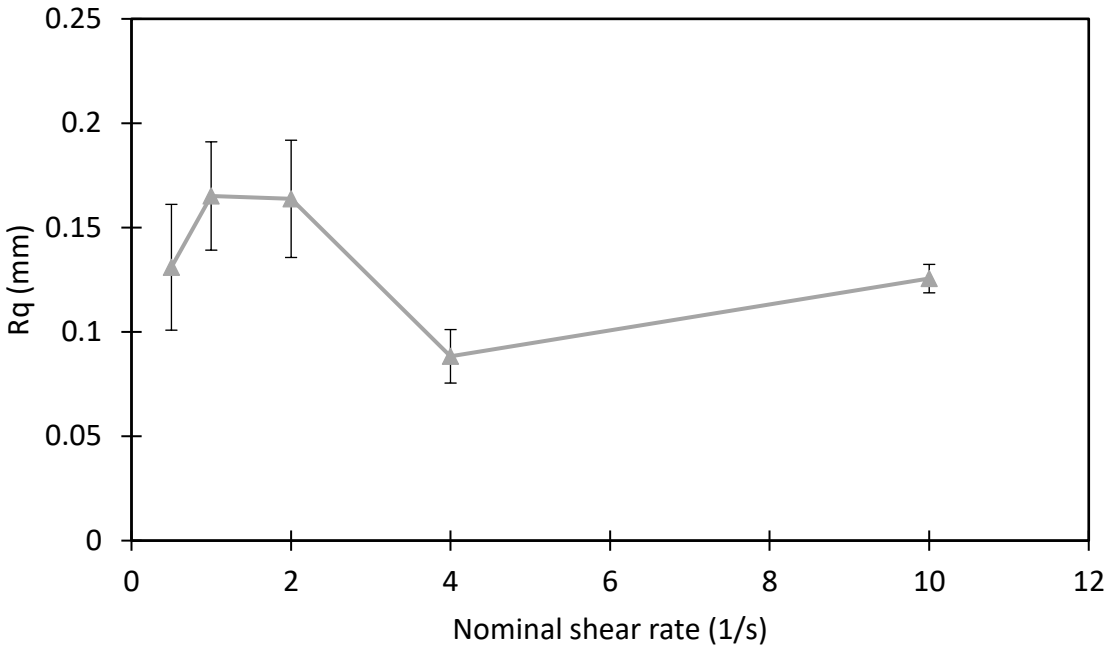

b.

Figure 7.6. The surface roughness of rupture specimens from the glass-steel setup: a. Ra: the average of deviation of the surface profile from the mean value, b. Rq: the root mean square of the deviation of the surface profile from the mean value

7. 3. 2. Time-to-stress-plateau-end

There is a power law relation between the time-to-stress-plateau-end and nominal shear rate^{4} in the steel-steel setup. However, at this point, we are not able to attribute this parameter to any properties of the specimen due to two reasons: 1. From the visualization, we learned that the slip velocity of the intact portion of the specimen remains almost constant until the end of rupture and time-to-stress-plateau-end includes some part of the rupture propagation as well as the time to rupture onset. 2. We know that non-linear viscoelasticity adds complexity to the interpretation of the transient curve.

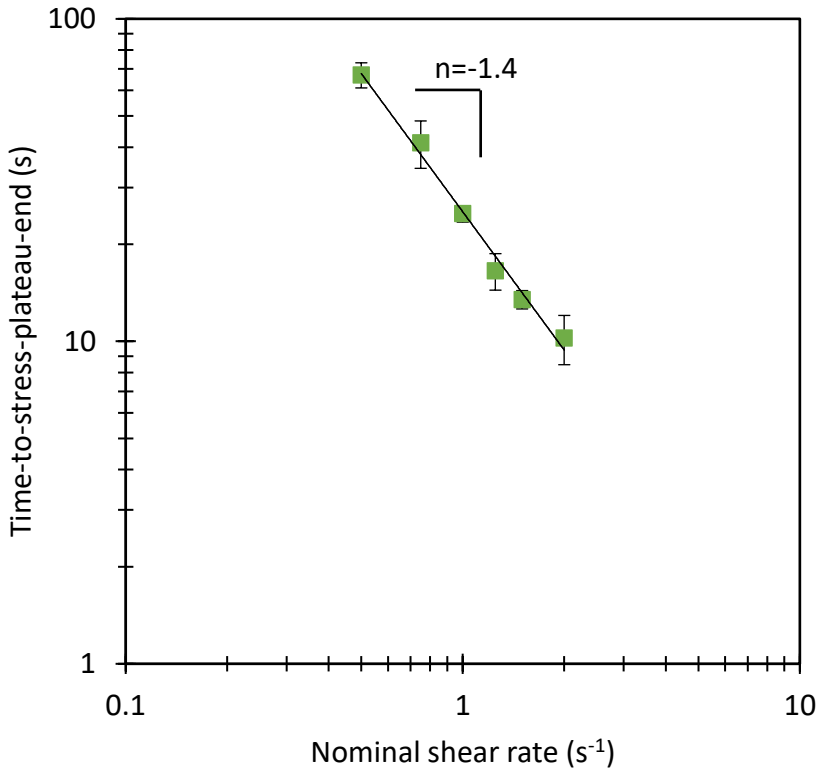

Figure 7.7. Time-to-stress-plateau-end versus nominal shear rate for HDPE 9[4] in steel-steel setup coming from the stress transient curves in our previous study[2]

7. 3. 3. Source of error

In addition to the experimental limitations and difficulties recording the flow in an oven explained previously, we encountered another source of error. We noticed that minor secondary flows are happening in our visual experiments. This is because when the stationary steel plate is replaced with a glass plate, the nuts on the SPR setup cannot be tightly fastened using the high-torque limited screws (150 lb-in). We replaced the screw with a lower torque-limited screw which eventually limits its efficiency. Since the slip is remarkably high in our samples, this limited secondary flow does not affect the slip velocity significantly but may affect the little deformation we have in our system prior to rupture. All with the other limitations, this prevents us from extracting deformation values from the videos.

7. 4. bibliography for appendices

(1) Yu, Y. A Short-Chain Branching Distribution Determination Technique for Polyethylene Using IR5-Detected GPC. *Macromolecular Symposia* **2020**, *390* (1), 1900014.
(2) Sattari, M.; Inn, Y.; Wood-Adams, P. M. Wall Slip of Bimodal Polyethylene. *Macromolecules* **2022**, *55* (11), 4568–4577.
(3) Cinquino, M.; Prontera, C. T.; Zizzari, A.; Giuri, A.; Pugliese, M.; Giannuzzi, R.; Monteduro, A. G.; Carugati, M.; Banfi, A.; Carallo, S. Effect of Surface Tension and Drying Time on Inkjet-Printed PEDOT: PSS for ITO-Free OLED Devices. *Journal of Science: Advanced Materials and Devices* **2022**, *7* (1), 100394.
(4) Sattari, M.; Inn, Y. W.; Wood-Adams, P. M. Melt Rupture of Bimodal Molecular Weight Polyethylene in Simple Shear with Slip; Society of Plastics Engineers: Denver, United States, 2023.